Vers la mesure de la violation de la symétrie CP dans les oscillations de neutrinos avec l'expérience T2K

Towards the measurement of CP violation in neutrino oscillations with the T2K experiment

Thèse de doctorat de l'université Paris-Saclay

École doctorale n° 576, Particules, hadrons, énergie et noyau : instrumentation, image, cosmos et simulation (PHENIICS)
Spécialité de doctorat: physique des particules
Unité de recherche: Université Paris-Saclay, CEA, Département de Physique des Particules, 91191, Gif-sur-Yvette, France
Référent: Faculté des sciences d'Orsay

Thèse présentée et soutenue à Paris-Saclay,
le 1er juillet 2021, par

Laura-Iuliana MUNTEANU

Composition du jury:

Andrea Giuliani Directeur de Recherche, Université Paris-Saclay	Président
Anselmo Meregaglia Chargé de Recherche, HDR, Université de Bordeaux	Rapporteur & Examinateur
Alessandra Tonazzo Professeure, Université de Paris	Rapporteure & Examinatrice
Margherita Buizza-Avanzini Chargée de Recherche, Institut Polytechnique de Paris	Examinatrice
Francesca Di Lodovico Professor, King's College London	Examinatrice
Federico Sanchez Nieto Professeur Ordinaire, Université de Genève	Examinateur

Direction de la thèse:

Marco Zito Ingénieur-chercheur, HDR, Université Paris-Saclay, CEA IRFU	Directeur de thèse
Sara Bolognesi Ingénieure-chercheuse, HDR, Université Paris-Saclay, CEA IRFU	Co-Directrice de thèse

Thèse de doctorat

NNT: 2021UPASP049

Acknowledgements

I should warn the reader that this section will be full of superlatives, but none of them are employed lightly. At the end of these three years, I am happy to say that, looking back, one of the main feelings that I experience is gratitude.

The work presented in this thesis is the result of three very formative years. I have had the chance to work in an incredibly constructive environment, despite an ongoing pandemic. I hope, in this section, to give credit to the many people who have made this journey possible, and without whom I know I would not have enjoyed it as much.

First of all, I would like to thank my supervisors, Sara Bolognesi and Marco Zito. I would like to thank Marco for his help and support throughout my three years as a PhD student, for his constructive criticism and deep insights into neutrino physics. I would also like to thank Sara for being the best possible supervisor a student could have. Thank you for your encouragement, for your visionary skills in physics, for the opportunities you gave me, and for being a wonderful person overall.

It is very important to note that none of the work presented in this document would have been possible without the hard work, over many years, of many T2K collaborators. I am very lucky to have been part of T2K, and to have had the chance, before the pandemic, to attend several collaboration meetings in Japan. I have no hesitation in encouraging new members to join this wonderful collaboration - T2K is not only one of the leading experiments in neutrino physics today, but it is also a very pleasant working environment. I have met many inspiring collaborators, on both a professional and a personal level, and I feel extremely fortunate to have been able to contribute to the ongoing success of the experiment.

Most of my work was done as part of the Near Detector fitting group, part of the Oscillation Analysis group. I would like to express my gratitude to Mark Scott, Clarence Wret, John Walker, Jacob Morrison and Asher Kaboth for helping me along the way and providing answers to my many questions about the BANFF and the near detector fit in general. I would also like to thank my co-analyzer for the Neutrino 2020 analysis, Joe Walsh, for sharing the joys and sorrows of the BANFF fit and working together towards improving it. I am also deeply grateful to the new BANFF convener, Ciro Riccio, and the new analyzers, Tristan Doyle and Yongheng Xu, for continuing this line of work. More generally, I'd like to extend my thanks to the Neutrino 2020 Oscillation Analysis group conveners, Patrick Dunne and Christophe Bronner, as well as the far detector analyzers, Lukas Berns, Ed Atkin, Kevin Wood, Siva Prasad Kasetti and Will Parker, for their work and collaboration towards producing a remarkable result, paving the way for future analyses in neutrino oscillation physics. I'd also like to thank Kendall Mahn, for her leadership, and continuing support during my time in T2K.

The work presented in this thesis has actually begun before my official PhD start date. In 2018, between March and June, I did my Master's internship on the ND280 upgrade project. The time I spent working on this topic during my internship exceeded all of my expectations and made me very excited to continue working on T2K. I would like to thank two people in particular - Davide Sgalaberna and Stephen Dolan. I'd like to thank Davide for his contagious excitement about the ND280 Upgrade, for being so proactive and for involving me in many projects. I'd like to also thank Stephen, even beyond the ND280 Upgrade project, for his continuous support, for sharing his deep knowledge of neutrino interactions physics with me, and for providing me with countless opportunities to learn new things. I am particularly happy to see that the work I initially joined in the Sim&Opt group has bloomed into the Physics&Performance group which has achieved remarkable results. For continuing this work, and keeping me involved, I'd like to thank Adrien Blanchet, Margherita Buizza Avanzini, Claudio Giganti and my supervisor and current convener, Sara Bolognesi. In addition to the people I've had the pleasure of working with for the physics sensitivity studies for the Upgrade, I'd like to thank the IRFU members heavily involved in the Resitive MicroMegas development and test-beam analyses. The ND280 Upgrade has become a very dear project to me, and I am extremely excited to see it installed and taking data.

Over the last year, I've joined the Hyper-Kamiokande collaboration and worked in the Long Baseline Physics Working Group. I'd like to thank the previous Osc3++ analyzer, Tommaso Boschi, for teaching me the ins and outs of the framework. I'd also like to extend my thanks to Megan Friend, Mark Scott and Sara Bolognesi, as conveners, and to Tom Dealtry and Zhenxiong Xie, as co-analyzers, for their collaboration and support during my time in Hyper-Kamiokande. I hope one day to be able to continue working on this exceptional experiment and see its coveted results!

I am very happy to have been a part of the accelerator neutrino group at CEA/IRFU/DPhP - my heartfelt thanks go to Sara, Marco, Samira, Guillaume, Sandrine, Paul, Georges, Sergey, Pierre and Mathieu. I am extremely lucky to have been part of such a supportive, constructive and friendly group. You have all certainly set the bar very high! I'd also like to thank Samira, in particular, for her support, for our data-taking trip to Japan, for listening to my sorrows and sharing hers, for helping me organize my defense and for being a good friend, in general!

I'd also like to thank the members of the LPNHE Neutrino group in Paris, with whom I had wonderful and fruitful collaborations throughout my PhD: Claudio, Boris, Mathieu, Marco and Adrien. In addition, I would like to express my gratitude towards several other members of the LPNHE, whom I've known since before my PhD, and have kindled my love for particle physics (and cosmology): Eli Ben-Haim, Matthew Charles and Delphine Hardin. I want to thank them for teaching me and believing in me - you have certainly helped me reach this point!

As I am writing these lines after my PhD defense, I'd like to acknowledge the input of the examination committee to this document. I thank Alessandra Tonazzo and Anselmo Meregaglia, my referees, for reading my thesis carefully and thoroughly and helping me improve its aspect. I would also like to thank the members of the jury (Andrea Giuliani, Margherita Buizza Avanzini, Francesca Di Lodovico, Federico Sanchez Nieto) for their insightful questions on the day of the defense.

None of this would have been possible without the help and support of my friends. I'd like to thank Dounia, for sharing the joys and sorrows of the life of a PhD student with me, for her support, and for saving my life (literally!) at one point. I am also deeply grateful to Valeriu and Valeria, Ileana and Ana, and to Kévin - I apologize for being so absent during these three years, but I care deeply about all of you and I would not have been able to power through without your friendship!

I could not imagine being here today without the support of my family. I'd like to thank my parents, Svetlana and Petru, for giving me all of the right conditions in which I could explore the world, for giving me opportunities and for their endless love. I am also grateful for my Belgian family - I'd like to thank Nenea Slavic, Tanti Liuba, Nelu and Veronica, for keeping in touch with me during this period and for cheering for me at every occasion. On the same note, I am very grateful towards Agnès and Jean-Pierre, my boyfriend's parents, for supporting me throughout this journey.

Finally, I wish to thank Maxime, who has been there for me more than anyone else, and who decided three years of neutrino physics weren't enough and has agreed to come with me to Geneva for my next job, at CERN. You have been with me every step of the way, providing me with endless love, care and support. Thank you for your bottomless patience, for helping me go on even when it seemed like I did not have the strength to do so, and for believing in me. Thank you for filling every day with joy and laughter, even in the darkest times. I could not have hoped for a better life partner. Thank you!

And now lots, and lots, of rest.

Résumé

Les neutrinos sont les particules les plus abondantes dans l'Univers, après les photons. Leur existence a été postulée en 1930 par W. Pauli pour expliquer le spectre continu de l'énergie des électrons issus des désintégrations radioactives bêta. Pauli avait postulé que cette particule (qu'il avait initialement appelé le "neutron", et qui a ensuite été nommée "neutrino" par E. Fermi) devait être électriquement neutre, avec une masse nulle ou quasi-nulle et dotée d'un spin 1/2. Ce ne fut que près de 30 ans après que les premiers (anti-)neutrinos électroniques ont été découverts par F. Reines et C. Cowan près de la centrale nucléaire de Savannah River, aux Etats-Unis.

Une série de découvertes marquantes suivirent après cette première découverte. Aujourd'hui, dans le modèle standard de la physique des particules, les neutrinos possèdent un nombre quantique, appelé "saveur", qui est conservé dans leurs interactions. Les neutrinos font partie des doublets de saveur de l'interaction faible, avec les leptons de la saveur correspondante, portée par les bosons W et Z. Alors que les leptons chargés peuvent également subir des interactions électromagnétiques, de par leur charge électrique, les neutrinos ne peuvent interagir que par l'interaction faible. Cette propriété, en plus de leur faible masse, rend très difficile leur détection expérimentale.

Pendant longtemps, les neutrinos étaient supposés avoir une masse nulle. La preuve que les neutrinos ont une masse non-nulle est venue en 1998, puis en 2001, quand les expériences Super-Kamiokande et SNO ont confirmé l'observation d'un phénomène appelé "oscillations de neutrinos". Ce phénomène implique que les états propres d'interaction (ou de saveur) des neutrinos ne sont pas équivalents à leur états propres de masse, ou les états propres de l'Hamiltonien de propagation. De ce fait, des neutrinos produits dans un état de saveur peuvent spontanément changer de saveur au cours de leur propagation. Les états propres de masse peuvent être exprimés comme une combinaison linéaire des états de saveur, reliés par une matrice de mélange unitaire. Cette matrice de mélange peut être paramétrée par trois angles de mélange, θ_{12}, θ_{13} et θ_{23}, et deux phases complexes - une phase qui détermine si la symétrie charge-parité (CP) est violée dans les oscillations de neutrinos, δ_{CP}, et deux phases dites "de Majorana", α_1 et α_2, qui ont des conséquences sur les observables physiques uniquement si les neutrinos sont des particules de Majorana, et non de Dirac (c'est à dire si les neutrinos sont leur propres anti-particules). La probabilité de transition entre deux états de saveur est régie par les termes de cette matrice de mélange, mais également par les différences des carrés des masses des neutrinos ($\Delta m_{ij}^2 = m_i^2 - m_j^2$) et par le rapport entre la distance de propagation des neutrinos et leur énergie (L/E).

Aujourd'hui, les expériences d'oscillations de neutrinos visent à mesurer les paramètres de cette matrice de mélange, ainsi que les différences entre les masses des neutrinos. Les trois angles de mélange sont connus avec différents degrés de précision, mais l'incertitude sur la valeur de la phase δ_{CP} et encore trop importante. Si cette dernière est différente de 0 ou π, nous observerons le premier exemple de violation de la symétrie CP dans le secteur leptonique. Ce fait permettrait de répondre à une des trois conditions énoncées par A. Sakharov pour expliquer l'origine de l'asymétrie entre la matière et l'antimatière dans l'Univers, un des mystères de la physique actuelle. Au-delà de la valeur

de la phase δ_{CP}, les valeurs précises des paramètres d'oscillations pourraient indiquer la présence de symétries intrinsèques gouvernant les oscillations des neutrinos. Il existe d'autres questions ouvertes dans la physique des neutrinos : nous ne connaissons toujours pas les masses absolues des neutrinos, et les limites actuelles montrent une valeur très faible pour ces quantités, qui nécessite des constantes de couplage au boson de Higgs anormalement basses. De nombreuses expériences de physique des particules et de cosmologie cherchent à répondre à ces questions, mais elles ne seront pas traitées en détail dans cette thèse.

Le sujet principal de ce document concerne la mesure des paramètres d'oscillation des neutrinos avec des expériences à longue distance, notamment l'expérience actuelle T2K et la future expérience Hyper-Kamiokande. Les Chapitres 1 et 2 représentent une introduction générale à la physique des neutrinos, en mettant l'accent sur les expériences d'oscillations de neutrinos issus d'accélérateurs. Le Chapitre 2 détaille le principe et les enjeux de l'expérience T2K.

Tokai-to-Kamioka (T2K) est une expérience à longue distance qui étudie les oscillations des neutrinos issus d'accélérateurs. Sur la côte est du Japon, à Tokai, au centre J-PARC (Japan Proton Accelerator Research Complex), un faisceau de neutrinos muoniques est produit en bombardant une cible de graphite avec des protons de 30 GeV. Les interactions des protons dans le graphite produisent des hadrons chargés qui se désintègrent en vol et produisent des neutrinos ou anti-neutrinos. Trois ensembles de cornes magnétiques sont utilisés pour séparer les hadrons selon leur charge, afin d'obtenir un faisceau de neutrinos ou d'anti-neutrinos. L'écrasante majorité des neutrinos dans le faisceau sont de saveur muonique, mais ce dernier a une contamination intrinsèque de neutrinos électroniques de l'ordre de 1%. Les neutrinos muoniques ainsi produits oscillent sur une distance de 295 km, jusqu'à atteindre le détecteur Super-Kamiokande (SK), près de la côte ouest du Japon. SK est un détecteur rempli d'eau pure qui sert de cible pour les interactions des neutrinos provenant de J-PARC. SK détecte des particules en utilisant l'effet Cherenkov.

Le but de l'expérience T2K est de mesurer des paramètres gouvernant les oscillations des neutrinos. La sensibilité de T2K aux paramètres d'oscillations vient à travers deux canaux. L'amplitude de la probabilité de disparition des neutrinos muoniques est régie par le terme $\sin^2\theta_{23}$, alors que la position du minimum de la probabilité de survie dépend de Δm^2_{32}. La probabilité d'apparition de neutrinos électronique est régie, au premier ordre, par le terme $\sin^2\theta_{13}$, mais les expériences d'oscillations de neutrinos venant des réacteurs nucléaires ont une bien meilleure sensibilité à ce paramètre. Par contre, une expérience à longue distance telle que T2K a une sensibilité particulière au paramètre δ_{CP} à travers la mesure de l'asymétrie entre les canaux d'apparition de neutrinos et anti-neutrinos électroniques. Pour maximiser les probabilités d'oscillation des neutrinos dans ces deux canaux, T2K emploie la méthode dite "hors-axe" - le faisceau produit à J-PARC est orienté à un angle de 2.5° par rapport à SK. Ce fait permet d'obtenir un flux concentré autour de 600 MeV, et également de réduire la contamination intrinsèque de saveur électronique dans le faisceau. T2K a aussi une faible sensibilité à la hiérarchie de masse qui peut changer le taux d'événements dans le canal d'apparition de $\sim$10%.

La composition du flux est mesurée précisément près du point de production à l'aide de deux détecteurs proches, appelés ND280 et INGRID. INGRID se trouve sur l'axe du faisceau et mesure sa position et sa stabilité. ND280 (pour *Near Detector at 280 m*) est quant à lui un détecteur hors-axe, au même angle par rapport au faisceau que SK. ND280 est un détecteur modulaire et complexe, agissant à la fois comme cible et trajectographe. En amont du faisceau, ND280 est actuellement doté d'un détecteur scintillant de pions neutres, appelé P∅D. Ce dernier est suivi par une structure alternant deux cibles de barres scintillantes (FGD, pour *Fine Grained Detectors*) et trois chambres à projections temporelle (TPC, pour *Time Projection Chambers*). Les interactions des neutrinos ont lieu principalement dans les FGD et les traces sont reconstruites dans les TPC. La première cible est constituée entièrement de plastique (donc de carbone et d'hydrogène, CH), tandis que la deuxième contient en plus des poches d'eau afin d'étudier également les interactions des neutrinos sur des noyaux d'oxygène. L'ensemble de ces modules (PØD, FGD et TPC) est entouré de calorimètres électromagnétiques (ECal) et le tout est placé à l'intérieur de l'aimant UA1, donné par le CERN. ND280 est ainsi un détecteur aimanté, contrairement à SK, et il peut donc séparer les traces des particules selon leurs charges électriques et donc discerner les interactions des neutrinos et des anti-neutrinos. Cette information est essentielle pour l'analyse d'oscillation. ND280 a des capacités excellentes à mesurer des particules chargées, à faible angle par rapport au faisceau, et allant dans la même direction que le faisceau.

Le taux d'évènements, au détecteur proche ainsi qu'à SK, est le résultat de la convolution du flux de neutrinos avec leur section efficace d'interaction avec la matière. Chaque détecteur a également une efficacité de détection. Ces trois effets sont souvent appelés des "nuisances", car ils ne contiennent pas les paramètres que l'on cherche à mesurer, mais influent sur le taux d'événements et peuvent fausser les résultats de l'expérience s'ils ne sont pas bien maîtrisés. Seul le taux d'événements à SK contient un terme lié à la probabilité d'oscillation des neutrinos d'une saveur à l'autre. Le rôle de ND280 est d'obtenir des contraintes sur les incertitudes systématiques liées au flux de neutrinos et aux interactions des neutrinos avec la matière.

Les Chapitres 3, 4 et 5 portent sur la mesure des paramètres d'oscillation avec l'expérience T2K. Le Chapitre 3 décrit la stratégie de l'analyse, les données et simulations utilisées, ainsi que le modèle d'erreurs systématiques et les améliorations récentes apportées à ce dernier. Le modèle d'erreur des systématiques du flux inclut un réajustement aux mesures de l'expérience NA61/SHINE. Les systématiques de détecteur sont établies à l'aide des échantillons de contrôle et exprimées comme des erreurs sur le nombre d'évènements dans des intervalles d'observables expérimentales. Le modèle d'erreur des systématiques de section efficace est probablement la partie la plus complexe dans la construction du modèle d'erreur. Des améliorations à ce modèle représentent une des contributions principales décrites dans ce manuscrit.

Autour du pic d'énergie de T2K, à 600 MeV, l'interaction dominante est celle dite quasi-élastique (CCQE, pour *charged current quasi-elastic*). Dans une telle interaction, un neutrino échange un boson W avec un nucléon et produit un lepton chargé et un nucléon dans l'état final. La détection du nucléon est souvent difficile. Cependant, comme il s'agit d'une interaction à deux corps, les propriétés du lepton chargé permettent, en principe, de reconstruire entièrement l'énergie du neutrino incident, en supposant que le nucléon initial est au repos. En réalité, les nucléons sont quasiment toujours liés dans des noyaux atomiques, et sont ainsi assujettis à une multitude d'effets nucléaires. On y compte notamment le mouvement de Fermi (le mouvement des nucléons dans le noyau), des corrélations à courte distance entre nucléons, ainsi que des interactions d'état final (FSI, *final state interactions,* en anglais). De plus, la distribution en impulsion du noyau à l'état fondamental n'est pas connue et plusieurs modèles peuvent être utilisés pour la décrire. Tout effet nucléaire induira un biais dans l'énergie reconstruite des neutrinos s'il n'est pas entièrement maîtrisé. C'est l'un des enjeux principaux pour les expériences d'oscillations de neutrinos.

Avant l'analyse présentée dans cette thèse, l'état fondamental des noyaux était décrit par un modèle simplifié, appelé "gaz de Fermi relativiste" (RFG ou *Relativistic Fermi Gas*, en anglais). Ce modèle décrit le potentiel nucléaire comme un puits d'énergie constant et ne tient pas compte de la structure complexe du noyau. Une amélioration importante apportée à l'analyse d'oscillations décrite dans ce document consiste en l'utilisation d'un modèle alternatif, beaucoup plus sophistiqué, pour décrire l'état fondamental du noyau - le modèle dit de Fonction Spectrale (SF, pour *Spectral Function*, en anglais). Ce modèle présente de nombreux avantages - il donne une description plus rigoureuse de la structure du noyau, en tenant compte, notamment, des couches nucléaires. De plus, ce dernier est ajusté de manière semi-empirique en utilisant des données des expériences de diffractions d'électrons. Enfin, l'utilisation de ce modèle est un premier pas vers une stratégie durable d'analyse car il sera adapté pour les futures analyses qui exploiteront également les hadrons des états finaux.

Une autre amélioration importante de l'analyse est décrite par l'exemple d'une nouvelle paramétrisation de la dépendance en énergie des interactions dites 2p2h (pour *two particles two holes*). Cette interaction est similaire à l'interaction CCQE, à l'exception du fait que le nucléon initial est corrélé avec un autre nucléon dans le noyau. Par conséquent, les particules produites dans les interactions 2p2h n'ont pas la même cinématique que les interactions CCQE, bien que leur état final soit très similaire. Il existe plusieurs modèles décrivant ce type d'interactions, mais avec des sections efficaces qui varient beaucoup en fonction de l'énergie du neutrino. Cette paramétrisation offre une liberté supplémentaire dans l'analyse, particulièrement importante dans l'extrapolation de la prédiction du détecteur proche à SK.

L'ajustement de la prédiction aux données du détecteur proche se fait à travers un algorithme qui maximise la vraisemblance (*maximum likelihood*, en anglais), en fonction de l'impulsion et de l'angle du muon produit dans les interactions des neutrinos. C'est un ajustement complexe, avec environ 700 paramètres systématiques pour 18 échantillons, et donc coûteux en termes de nécessités de calcul. Le fonctionnement de l'ajustement au détecteur proche et sa validation sont décrites dans le Chapitre 4.

Les résultats de l'analyse complète d'oscillations de T2K sont discutés en détail dans le Chapitre 5. L'ajustement au détecteur proche fait apparaître des corrélations entre les trois catégories d'erreurs systématiques, ce qui permet de les contraindre plus précisément. Pour cette analyse, les erreurs systématiques sur les échantillons CCQE de SK ont ainsi été réduites de l'ordre de $\sim 14\%$ à l'ordre de $\sim 4\%$ grâce au détecteur proche. De plus, grâce à l'utilisation du modèle SF, l'erreur dominante dans l'analyse précédente (sur l'énergie de liaison des nucléons dans le noyau) a été réduite à un niveau sous-dominant. Il est important de mentionner que l'analyse de T2K comporte une série d'études de robustesse. Ces études mettent le modèle d'erreurs systématiques à l'épreuve, en produisant des lots de données simulées suivant des modèles alternatifs. Si l'analyse est suffisamment robuste, elle aura la souplesse d'identifier les effets introduits par les modèles alternatifs. La chaîne entière de l'analyse est répétée pour chaque modèle alternatif, et l'impact quantitatif sur la sensibilité est estimé.

Les résultats obtenus avec les données de l'expérience T2K après toutes ces étapes confirment une indication de violation de la symétrie CP dans les oscillations de neutrinos, à 90% de degré de confiance.

Pour pouvoir prononcer un verdict à au moins 3σ sur la violation de la symétrie CP, T2K planifie une nouvelle campagne de prise de données en 2022, appelée T2K-II. Cette nouvelle étape consistera notamment en une mise à niveau du faisceau de J-PARC. Actuellement, ce dernier opère à une puissance de 515 kW - le but de la mise à niveau sera d'augmenter son intensité à 750 kW, puis à 1.3 MW. Cette intensité de faisceau permettra d'augmenter significativement la statistique de l'expérience, et à ce moment-là les erreurs systématiques deviendront le facteur limitant de l'analyse. Pour répondre à cet enjeu, l'expérience T2K envisage une mise à niveau de son détecteur proche, avec le projet ND280 Upgrade. Le but de cette mise à niveau est d'augmenter la masse des cibles, ainsi que d'améliorer les capacités de détection du ND280. La suite des améliorations permettra au détecteur proche d'identifier des particules à haut angle par rapport au faisceau de neutrinos, des protons de basse énergie (avec un seuil de 200 MeV, contre 400 MeV actuellement), et même identifier des neutrons et mesurer leur énergie en utilisant leur temps de vol. La mise à niveau consistera à remplacer le PØD, en amont du faisceau, par une cible à haute granularité composée de 2 millions de cubes scintillants, entourée de deux TPC horizontales utilisant la nouvelle technologie des MicroMégas résistives. Ces améliorations permettront au détecteur proche d'atteindre une couverture angulaire de 4π, comme celle de SK, et de sonder l'intégralité de l'état final des interactions de neutrinos.

Le Chapitre 6 présente en détail le projet de mise à niveau du ND280. Une attention particulière est portée sur les résultats des prises de données avec des faisceau de test (*test-beam*, en anglais) afin de valider et de caractériser les détecteurs à base de MicroMégas résistives. Le chapitre décrit également des études concernant les nouvelles observables physiques rendues accessibles grâce à cette mise à niveau. La possibilité de détecter des protons permet, notamment, d'exploiter des variables quantifiant le déséquilibre cinématique des interactions, ce qui permet de séparer différents effets nucléaires. De plus, en combinant ces variables avec la capacité du détecteur à identifier des neutrons, il est possible d'obtenir des échantillons dépourvus (ou presque dépourvus) d'effets nucléaires.

La mise à niveau de ND280 est un projet de longue haleine. En 2027, l'expérience de prochaine génération Hyper-Kamiokande (HK) commencera son activité. Cette dernière est le successeur naturel de l'expérience SK, consistera d'un détecteur environ 8 fois plus grand que SK, et sera utilisée comme détecteur lointain pour le programme d'oscillations des neutrinos issus d'accélérateur (Tokai to Hyper-Kamiokande, T2HK). Le détecteur ND280, après mise à niveau, sera utilisé comme détecteur proche pour HK, en plus d'un second détecteur à eau situé à distance intermédiaire. Le but du programme de neutrinos issus d'accélérateur de HK sera de déterminer à plus de 5σ, d'abord, si la violation de la symétrie CP a lieu dans les oscillations de neutrinos (en utilisant des neutrinos issus d'accélérateur, ainsi que des neutrinos atmosphériques), et ensuite d'effectuer des mesures de précision des paramètres d'oscillation. HK utilisera le faisceau de J-PARC, qui aura atteint 1.3 MW d'intensité. Ce fait, combiné à la masse importante de HK, permettra de récolter une quantité de données avec une incertitude statistique de l'ordre du pourcent. A ce stade, les incertitudes systématiques deviendront le facteur limitant pour des mesures de précision. Le Chapitre 7 décrit l'impact des systématiques de section efficace sur la sensibilité à la violation de la symétrie CP, ainsi que la relation entre l'incertitude sur l'échelle en énergie du détecteur et les perspectives de l'expérience concernant les mesures de précision.

Le Chapitre 8 présente une conclusion générale du manuscrit, en analysant le lien entre les différentes parties.

Contents

List of Figures

List of Tables

Chapter 1

Introduction

Neutrinos are the second most abundant particles in the universe, but remain extremely elusive. The neutrino was initially proposed as a “desperate measure” [11] to a puzzle particle physicists (or nuclear physicists, as they were referred to at the time) were striving to answer - the continuous spectrum of the β decay. Almost a century after it was initially postulated, the neutrino holds a distinct place in the particle physics landscape, both within and beyond the Standard Model. Despite their weakly interacting nature, neutrinos have been detected on numerous instances, pushing the boundaries of both theoretical and experimental frameworks.

This chapter aims to provide an overview of the history and understanding of neutrino physics which will be most relevant for the following chapters, with a particular focus on the experiments involved in neutrino detection. As such, Section 1.1 provides a historical overview of the neutrino from when it was postulated. Section 1.2 presents a brief description of how the neutrino fits (and doesn’t fit) in the Standard Model. Section 1.3 describes the discovery of neutrino oscillations, one of the most striking observations of physics beyond the Standard Model, and Section 1.4 introduces the formalism used to describe neutrino oscillations. Section 1.5 presents a certain type of neutrino experiments - long baseline accelerator experiments - as this will be the main focus of this thesis, and describes their principle. Finally, Section 1.6 gives an overview of the current world knowledge about neutrino oscillations, based on recent results.

1.1 History of neutrino physics

1.1.1 The β decay spectrum problem

The history of the neutrino has its origins at the beginning of the 20th century. In 1914, James Chadwick performed a measurement of the energy spectrum of electrons coming from the β decays. At the time, the electron and the proton were the only two known elementary particles. In this picture, a β decay (i.e. a radioactive decay in which electrons are emitted) occurs according to the following reaction:

$$_{\mathrm{Z}}\mathrm{X} \rightarrow_{\mathrm{Z+1}} \mathrm{Y} + e^- \tag{1.1}$$

meaning that an atom of the element X with atomic number Z decays into an atom of a new element Y and emits an electron, e^-. To conserve the electric charge, the new element has an atomic number of Z+1. According to Eq. (1.1), this is a two-body process. Therefore, the energy of the emitted electrons , E_e, can be calculated exactly, using energy and momentum conservation considerations, as

$$E_e = \frac{m_X^2 - m_Y^2 + m_e^2}{2m_X} \tag{1.2}$$

in which m_X, m_Y and m_e are the masses of the atoms X and Y and of the electron, respectively. The expectation was thus that the β decay spectrum would be centered, up to the experimental resolution, around a well defined, discrete energy.

What Chadwick found, instead, was that the β decay spectrum was continuous [12], with an end-point at the energy expected from Eq. (1.2), and his findings were further confirmed by others [13]. The shape of the β spectrum, shown in Fig. 1.1, is not at all in agreement with the prediction of the two-body decay in Eq. (1.1).

This finding was very puzzling for physicists at the time, as one of its possible implications was that energy conservation was violated. In 1930, Wolfgang Pauli proposed a solution to explain the shape of the spectrum, which respected energy conservation. In an open letter [11] addressed to Lise Meitner and Hans Geiger, and more broadly to the attendees of the nuclear physics conference in Tübingen, Pauli proposed that the shape of the spectrum could be caused by a third particle, unaccounted for in Eq. (1.1). Pauli termed this particle the “neutron”, stemming from the fact that it had to be electrically neutral. He also predicted that the “neutron” had a spin of 1/2, was very light (possibly massless), and as a result would be impossible to detect.

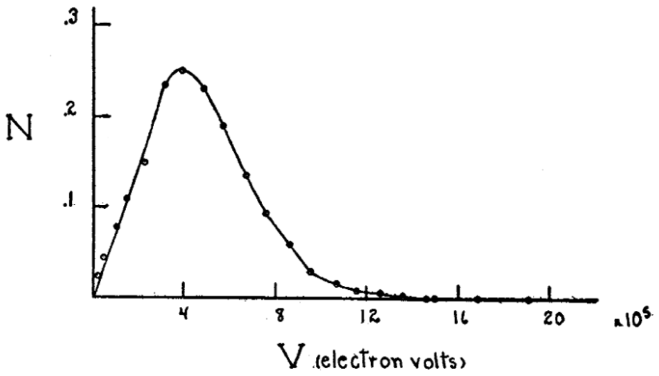

Figure 1.1: Spectrum of β decay, from [13].

In 1932, Chadwick discovered what is known today as the neutron [14] - a massive particle (whose mass is similar to that of the proton), electrically neutral, and which makes up part of the composition of the atomic nucleus. Enrico Fermi picked up Pauli’s proposition and developed a theory [15] of the new particle proposed by Pauli, which he instead named the “neutrino” - an Italian diminutive for the “neutron”, since the latter had just been discovered.

As a result, the continuous β spectrum was reconsidered under the three body approach, in which Eq. (1.1) became:

$${}_{Z}\mathrm{X} \rightarrow_{Z+1} \mathrm{Y} + e^- + \nu \tag{1.3}$$

where ν is the neutrino. The challenge at this point became the experimental discovery of the neutrino.

1.1.2 The discovery of the neutrino

The neutrino was an elusive particle for experimentalists for a long time. A giant leap in the field came with the advent of nuclear reactors, which, if Fermi's theory was correct, produced large fluxes of neutrinos, unattainable in small laboratories. According to Fermi's theory for β decay, the inverse process to the one shown in Eq. (1.3), termed "Inverse Beta Decay" (IBD) is also possible, and consists in the following reaction:

$$\bar{\nu} + p \rightarrow e^{+} + n \tag{1.4}$$

where p and n are a proton and a neutron, respectively, e^{+} is a positron. The neutrino appears in Eq. (1.4) as $\bar{\nu}$, because at the time it was already known that fermions existed in particle-anti-particle pairs, and the neutrino in Eq. (1.4) would have to be the anti-particle of that in Eq. (1.3), and there was no reason to assume that ν and $\bar{\nu}$ were the same particle.

In 1956, F. Reines and C. Cowan published the results which amounted to the discovery of the neutrino[1] [16, 17, 18]. In order to detect this elusive particle, Cowan and Reines placed two water tanks, deep underground, close to one of the Savannah River Plant reactors in the United States. The water tanks also contained cadmium chloride ($\mathrm{CdCl_2}$) and were sandwiched between three liquid scintillating detectors to detect the particles. In order to detect the process in Eq. (1.4), Reines and Cowan looked for the coincidence of two signals:

$$e^{+} + e^{-} \rightarrow 2\gamma \tag{1.5}$$

$$n +^{108}\mathrm{Cd} \rightarrow^{109}\mathrm{Cd}^{*} \rightarrow^{109}\mathrm{Cd} + \gamma \tag{1.6}$$

where Eq. (1.5) shows the annihilation of the positron produced in Eq. (1.4), resulting in the emission of two characteristic 0.511 MeV annihilation photons, and Eq. (1.6) shows the capture of the neutron produced in Eq. (1.4) by a Cadmium nucleus, which becomes excited and emits de-excitation photons. The signal for the process is thus the observation of two coincidence photons from the electron-positron pair annihilation, followed by the detection of photons emitted by the Cd nucleus, at a typical delay[2] of 5 μs.

Reines and Cowan observed about 3 such events per hour (one such signal is shown in Fig. 1.2a, from [17]), which was in agreement with the predicted cross-section for Eq. (1.4) of 6.4×10^{-44} cm^2, with a signal to background ratio of 20:1 [17]. For the discovery of the neutrino, Reines was awarded the Nobel Prize in physics in 1995 (Cowan had recently passed away).

Since this discovery, the neutrino physics landscape has been completed with the discoveries of several species of neutrinos and determination of their properties.

1.1.3 Discovery of other neutrino species

Ever since the discovery of the neutrino by Reines and Cowan, experimental progress in the field of neutrino physics was rapid.

In 1962, Leon Lederman, Melvin Schwartz and Jack Steinberger produced the first neutrino beam and used it to discover the muon neutrino (ν_μ) [19]. In an experiment at the Brookhaven National Laboratory (BNL) Alternating Gradient Synchrotron (AGS), they produced a neutrino beam by directing a proton beam onto a beryllium target. As a result, pions were produced and decayed in

---

[1] More precisely, what is now known as the electron antineutrino.

[2] This delay is due to the time the neutron diffuses in the target before being captured by a Cd nucleus.

flight, producing muons and neutrinos: $\pi^{\pm} \rightarrow \mu^{\pm} + \nu/\bar{\nu}$. The muons produced in the decay were stopped by a thick iron shield, such that the resulting beam was made almost entirely of neutrinos. The neutrinos then interacted in a 10 ton aluminum spark chamber through IBD. Since pion decays mainly produce muons (a very small fraction decays into electrons), this setup allowed to test if the neutrinos in the beam were of a different species than those observed by Reines and Cowan. If the species (or the flavor) of the neutrino is coupled with the leptons produced in the same decay, Lederman et al. expected to see muons as a result of the IBD in the spark chamber, whereas if there were only one type of neutrino, they expected to see equal amounts of muons and electrons. They observed 29 muon events (one such event is shown in Fig. 1.2b) and 6 electron events, thus confirming that there is indeed a second neutrino species, the muon neutrino.

Since neutrino flavors were coupled to the lepton flavors (ν_e for e and ν_μ for μ), the discovery of the τ lepton at the SLAC e^+e^- accelerator between 1975-1977 [20] led to a search for a third neutrino species. The theory of flavor symmetry was well developed at that time, and this implied that a third type of neutrino, the ν_τ should also exist. τ leptons are the heaviest leptons known to date, and require large amounts of energy to be produced. The τ neutrino was finally discovered by the DONUT experiment at the Fermilab Tevatron [21], using a beam composed of ν_τ coming primarily from the decay of τ leptons, themselves coming from the decay of D_S mesons produced when 800 GeV protons hit a tungsten beam dump. A nuclear emulsion was used to identify τ leptons coming from ν_τ scatterings - τ leptons leave a characteristic kinked track, signaling their decays. Four such events were identified, which was consistent with the theoretical prediction (one of the four events is shown in Fig. 1.2c).

Since all leptons in the standard model seem to have a corresponding neutrino, the next obvious question to ask is whether there are more than three lepton generations. A partial answer to this question was given by a combined fit from four experiments at the CERN LEP collider in 2006 [22]. The Z boson can decay into charged particles (which are easier to detect experimentally) and "invisible" particles at accelerators (such as neutrinos, which need a very large mass to interact). The width of the Z resonance (i.e. the inverse of its lifetime) thus has "visible" and "invisible" contributions from different channels. By measuring the total Z boson decay width and subtracting the contributions to the width from "visible" channels, the "invisible" width can be obtained. It is assumed that the invisible width comes from $Z \rightarrow \nu\bar{\nu}$, i.e. decays into neutrino-antineutrino pairs, and that each neutrino species contributes equally to this width. Since each individual $Z \rightarrow \nu\bar{\nu}$ width is calculable, the number of neutrino species contributing to this process can be measured. The high precision LEP measurements obtained that the invisible Z boson width is compatible with 3 neutrino species, illustrated in Fig. 1.2d. This does not mean that there are no other possible neutrino species, but rather that there are only three species that can couple to the Z boson or that can be produced by its mass. Other types of neutrinos (heavy or sterile neutrinos) are not yet ruled out.

1.2 Neutrinos in the Standard Model

The Standard Model (SM) (a review of which can be found in [23]) is a comprehensive model describing the interactions of elementary particles through three fundamental forces: the electromagnetic, strong and weak forces. It is based on the quantum theory of fields (QFT) and, to date, has been experimentally verified with great precision.

In the SM, elementary particles are divided into fermions, which have non-integer 1/2 spin, and

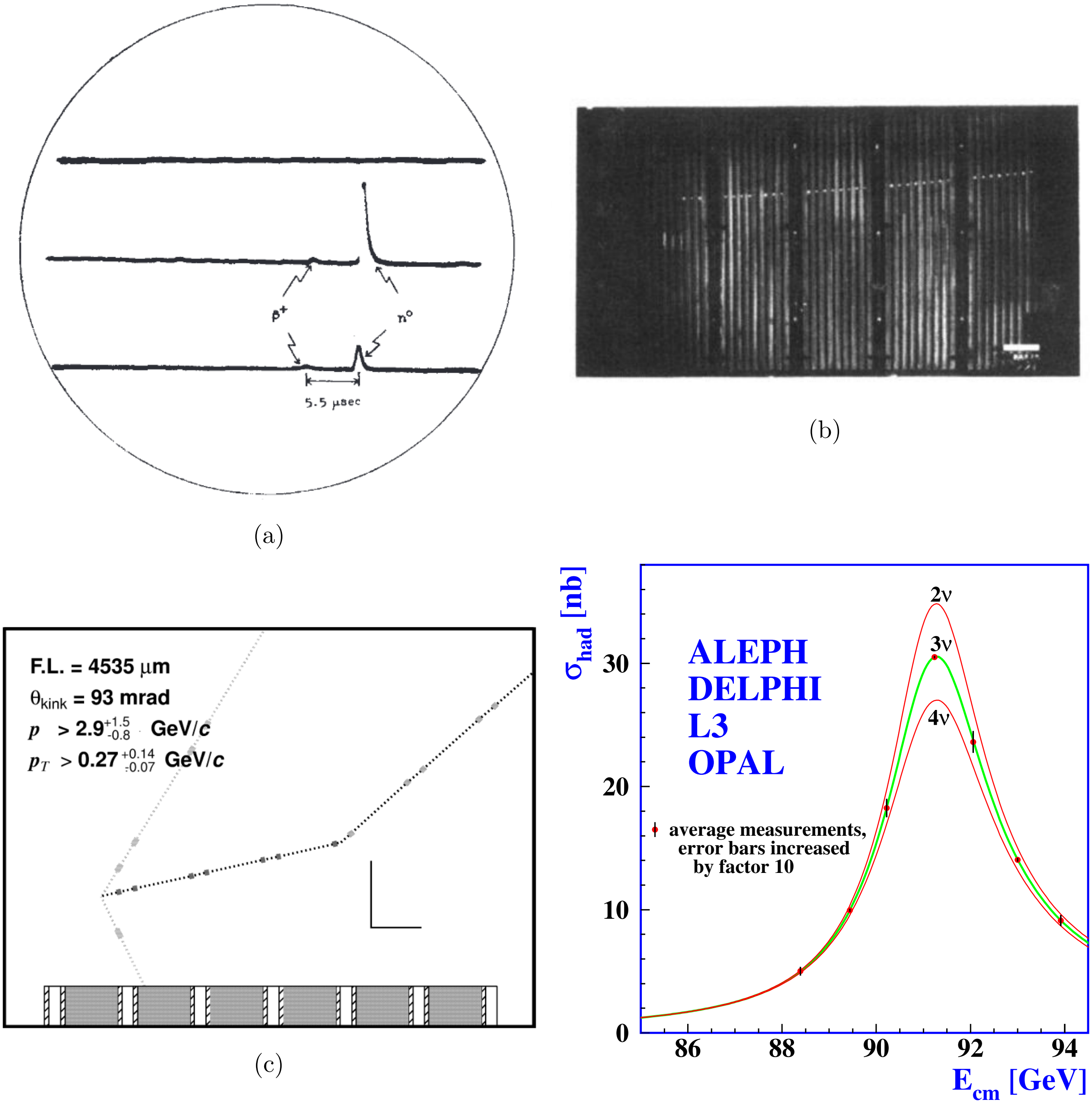

(a)

(b)

(c)

(d)

Figure 1.2: Illustrations of the discoveries of different neutrino species. (a) Coincidence signals from the experiment of Cowan and Reines [17]. (b) Example of a muon neutrino event in the spark chamber used in [19]. (c) One of the four ν_τ events recorded in the emulsion by the DONUT experiment [21]. (d) Combined result from the ALEPH, DELPHI, L3 and OPAL experiments at CERN, showing the hadron production cross-section around the Z resonance and comparing the result to the prediction for 2, 3 and 4 neutrino families [22].

bosons, which have an integer spin. Fermions obey the Pauli exclusion principle, whereas bosons, also known as “force carriers”, mediate the interactions between the different particles. The underlying philosophy behind the SM is that in nature there are symmetries, which are described by symmetry groups, forming an underlying algebra which interactions obey.

The experimental discovery of three species, or “generations” of leptons and their associated neutrinos is accommodated in the SM through what are known as the “weak interaction doublets”. This means that neutrinos and leptons always come in pairs and have the same quantum number, called flavor, which can be e, μ or τ. Neutrinos are neutral particles (as Pauli postulated in 1930), and thus cannot interact via the electromagnetic force (or, equivalently, do not couple to photons). They do not have a color charge, and thus do not interact via the strong force (i.e. do not couple to gluons). The only remaining interaction which they can undergo in the SM is the weak interaction, which is mediated by the $W^{\pm}$ and Z bosons. The latter have a very large mass compared to the null masses of photons and gluons, and this is at the origin of the “weak” term in their name. Such interactions happen at very short ranges due to the large mass of the $W^{\pm}$ and Z bosons, and for this reason neutrinos are notoriously difficult (but not impossible) to detect.

Experimental observations have made it possible to determine the properties of neutrinos in the SM. One particularly interesting property is that neutrinos are always “left-handed” whereas anti-neutrinos are always “right-handed”, a conclusion reached through empirical observations [24]. This conclusion was reached by measuring the helicity of neutrinos - the helicity is the projection of a particle’s spin onto its momentum. Left-(right-)handed particles have spins in the opposite (same) direction of their momentum, or left (right) helicity. This is in contrast to their corresponding leptons, which can have both types of helicities. The helicity of a particle is the same as its chirality if a particle is massless - for massive particles, the chirality and the helicity are no longer equal.

In the SM, there is no explicit requirement for neutrinos to have masses. As will be described in Section 1.3, there is indirect experimental evidence that neutrinos do, in fact, have non-zero masses. One way to accommodate neutrino masses in the SM is by adding right-handed neutrinos and left-handed anti-neutrinos to the SM lagrangian. The problem with this approach is that in order to explain the very small limits for neutrino masses obtained experimentally (latest results by the KATRIN experiment suggest that the absolute neutrino mass scale is <1 eV [25]), the coupling constant to the Higgs field would have an inexplicably low value. Another way to include neutrino masses in the SM is through an additional mass term, called the “Majorana” mass term (after Ettore Majorana [26]), which does not distinguish between neutrinos and anti-neutrinos. This does not violate the SM in its current form, but would imply that neutrinos are their own anti-particles (or, equivalently, that there are no exclusively left-handed neutrinos and exclusively right-handed anti-neutrinos, but rather both left-handed and right-handed neutrinos, as a single particle category). One way to verify this possibility experimentally is by searching for neutrino-less double β decay ($0\nu\beta\beta$), shown in Fig. 1.3, one of the rarest processes in nature (if it exists). In addition, even tighter limits can be put on the neutrino mass scale by cosmological observations: the free streaming neutrinos after the Big Bang affect the mass clustering in the universe and can be observed through the observation of Cosmic Microwave Background (CMB) lensing, large scale structures (LSS) and other cosmological effects. The current upper limit on the sum of the neutrino masses is ~100 meV [27].

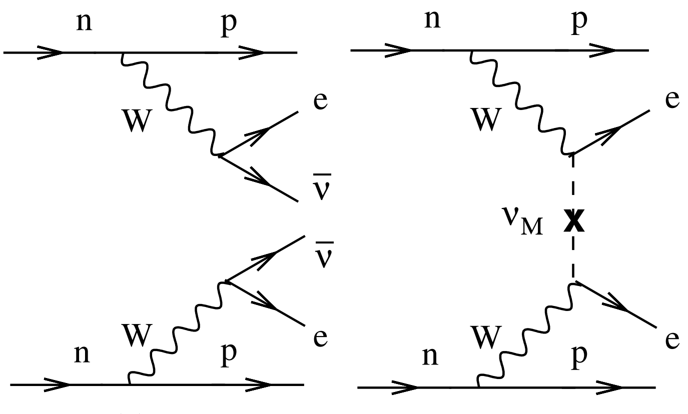

(a) $2\nu\beta\beta$ (b) $0\nu\beta\beta$

Figure 1.3: Feynman diagrams of double β decays, for different assumptions on the nature of the neutrino. (a) shows a 2-neutrino double β decay, in which one neutrino and one anti-neutrino are emitted in the final state. (b) shows the neutrino-less double β decay, in which there is only one type of Majorana neutrino, shown as ν_M. Figure from [28].

1.3 Neutrino Oscillations

1.3.1 The solar neutrino problem

Since neutrinos are weakly interacting neutral particles, they have a very large penetrating power, and thus can travel long path almost unaffected and carry information through large distances. This makes them a good candidate to observe cosmological phenomena. Many neutrinos are produced by nuclear reactions in stars or in the explosion of Supernovae. Unlike photons, which scatter frequently along their way, neutrinos reach the Earth often intact.

In 1968, R. Davis et al. published a paper detailing their measurement of the neutrino flux from nuclear reactions in the sun. They aimed to detect neutrinos produced in the β decay of ^{8}B according to $^8_5\mathrm{B} \rightarrow^8_4 \mathrm{Be}+\mathrm{e}^++\nu_\mathrm{e}$, and compare the flux to the one predicted by Bahcall et al. [29]. They used the inverse beta decay reaction of neutrinos on Cl atoms to identify the neutrino flux, with an experiment located in the Homestake mine in South Dakota. Davis et al. found [30] that the measured neutrino spectrum was two to three times smaller than the prediction following from on Bahcall's model. The initial guess was that either the prediction was flawed or that something was unaccounted for in the experiment. However, Bahcall's predictions were confirmed by helioseismological observations, and in the 1990s several other experiments reproduced the findings of Davis et al. - the GALLEX [31], SAGE [32] and Kamiokande [33] experiments performed model-dependent (with respect to the neutirno flux expectation) measurements of the neutrino flux from the sun, and in 2002 the SNO collaboration published the first model-independent measurement of the spectrum [34].

The solar neutrino problem observed by Davis et al. had a possible explanation even at the time. Bruno Pontecorvo had developed a theory of lepton number violation (violating individual lepton numbers, but conserving the total lepton number) [35, 36], which predicted that neutrinos can change their flavor, similarly to quarks. His theory was finally confirmed by the aforementioned SNO experiment, which measured, on the one hand, the ν_e flux from the sun, confirming the results of Davis et al., and, on the other hand, the total neutrino flux, through flavor independent neutral current reactions, which confirmed the Standard Solar Model predictions ([34]). These results were thus direct evidence that part of the ν_e produced in the Sun changed their flavor into ν_μ and ν_τ.

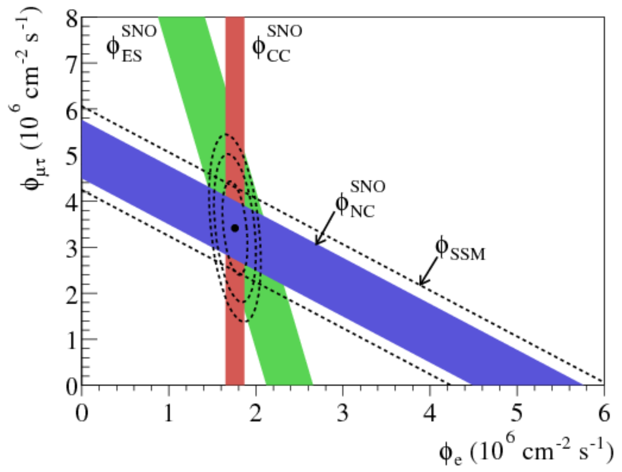

Figure 1.4: Solar neutrino flux in the three detection channels used in [34] - CC for charged current neutrino-nucleus interactions (sensitive to electron neutrino flux), NC for neutral current interactions (sensitive to the total neutrino flux) and ES for elastic scatters off electrons (sensitive to all neutrino flavors, but with an enhanced sensitivity to electron neutrinos). The dotted lines show the prediction of the Standard Solar Model. Figure from [34].

This flavor changing phenomenon is what is known as neutrino oscillations.
It is worth noting that SNO provided the answer to the solar neutrino puzzle in 2001. As will be described in the next section, the first evidence of neutrino oscillations actually came from atmospheric neutrinos measured by Super-Kamiokande in 1998.

1.3.2 Atmospheric neutrinos

In the 1980s, a second anomaly of neutrino fluxes was discovered, this time in neutrinos produced in the atmosphere of the Earth by cosmic rays. Cosmic rays in the atmosphere produce hadronic showers, made up of a majority of pions. The latter can decay in flight, producing muons and neutrinos:

$$\pi^\pm \rightarrow \mu^\pm + (\nu/\bar{\nu}) \tag{1.7}$$

$$\mu^\pm \rightarrow e^\pm + (\nu_e/\bar{\nu}_e) + (\nu_\mu/\bar{\nu}_\mu). \tag{1.8}$$

The expectation is thus that the observed flux should show twice as many muon neutrinos compared electron neutrinos. Several experiments targeting high-energy neutrino fluxes did, indeed, see this ([37, 38]). However, the IMB [39], Kamiokande [40] and Super-Kamiokande [41] experiments reported seeing equal amounts of muon and electron neutrinos.
Originally, the Kamiokande and Super-Kamiokande experiments were designed to measure proton decay. The experimental technology involved in these experiments is the detection of particles through the Cherenkov radiation they emit[3]. Since proton decay is a very rare process, backgrounds coming from unstable isotopes in the water and from cosmic rays need to be well constrained and characterized. In order to study the atmospheric neutrino flux, Super-Kamiokande uses the zenith angle with respect to the detector as a proxy for the distance travelled by neutrinos, as shown in

---

[3] Super-Kamiokande is one of the detectors of the T2K experiment, which is the subject of this thesis. A more detailed explanation of the Super-Kamiokande detector will be given in Section 2.3.

Fig. 1.5a. Broadly speaking, at Super-Kamiokande two types of neutrinos can be distinguished: down-going neutrinos, which are produced in the atmosphere above the detector, and up-going neutrinos, which are produced at large zenith angles. The main difference between the two types of neutrinos is in the distance they travel between their production point and the detector - down-going neutrinos travel distances of 10-500 km, whereas up-going neutrinos can cross distances of the order of 10^4 km, which is to say they have very different baselines. When measuring the ratio between the number of ν_μ and ν_e, Super-Kamiokande found that is was significantly different from the expected value of 2. In addition, the suppression was only seen for muon neutrinos, and not electron neutrinos, and this phenomenon seemed to have a dependence on the ratio between the baseline L of the neutrino and its energy, E_ν.

A possible explanation to this phenomenon could have been that some neutrinos interact in the Earth's crust. However, if that were the case, a similar suppression should have been visible for electron neutrinos. The results were also confronted with the theory of neutrino oscillations proposed by Ziro Maki, Masami Nakagawa and Shoichi Sakata [42], in 1962, expanding on Pontecorvo's initial theory of $\nu \rightleftarrows \bar{\nu}$ oscillations, but instead extending it to flavor oscillations. The Super-Kamiokande data were in agreement with this scenario, and provided the first evidence, in 1998, for neutrino oscillations. For this result, Takaaki Kajita of the Super-Kamiokande Collaboration was awarded the 2015 Nobel Prize in physics, along with Arthur B. McDonald of the SNO Collaboration, for the discovery of solar neutrino oscillations.

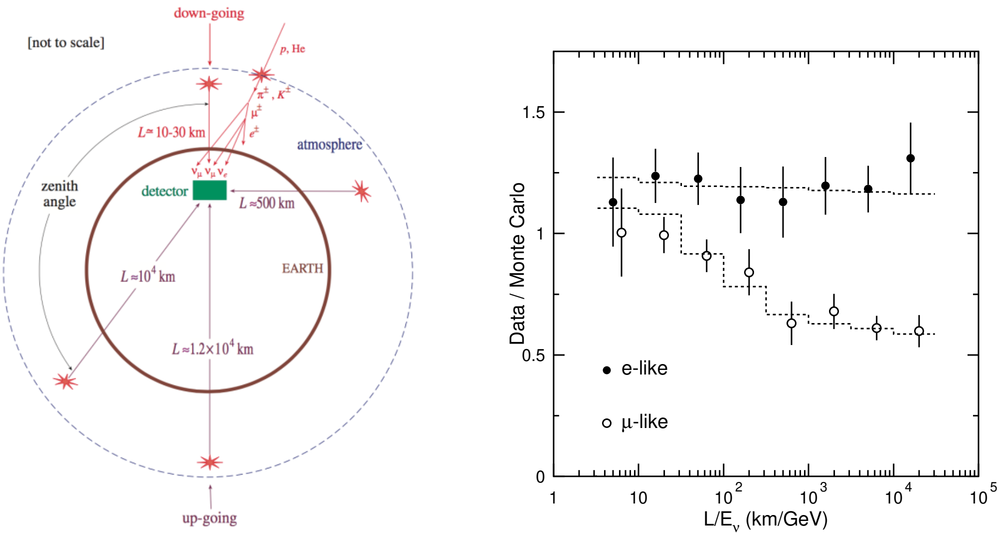

(a)

(b)

Figure 1.5: Illustration of Super-Kamiokande atmospheric neutrino detection technique (a) and ratio of data to Monte-Carlo prediction assuming no neutrino oscillations, for ν_μ and ν_e atmospheric neutrino events seen by Super-Kamiokande (b). Figure from [41].

1.3.3 Reactor neutrino experiments

After the discovery of solar and atmospheric neutrino oscillations, the KamLAND experiment measured the electron antineutrino flux from 55 Japanese nuclear power plants, at an average distance of 180 km from the detector [43, 44]. They observed a disappearance of electron anti-neutrinos which had a dependence on the neutrino energy, and which was also consistent with the prediction from the theory of neutrino oscillations (Fig. 1.6).

It is worth noting that the KamLAND experiment was a somewhat unusual reactor neutrino experiment, in the sense that its average baseline was much longer than that of more recent reactor experiments, such as Double CHOOZ [45], Daya Bay [46] and RENO [47] (which have baselines of a few km at most). More recent reactor experiments have focused on precisely measuring the value of θ_{13}, using the same IBD detection channel but with improved detection techniques.

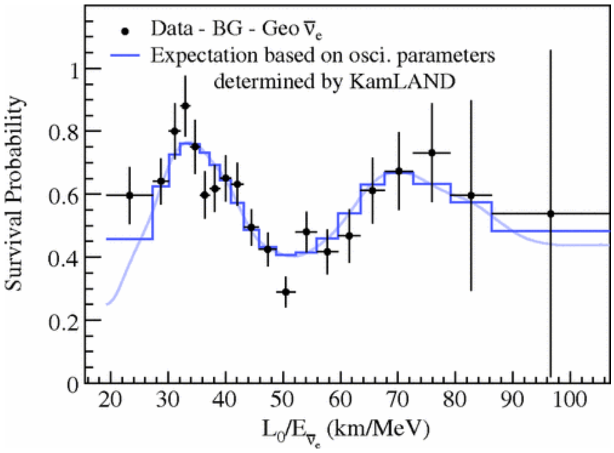

Figure 1.6: Ratio of the background and geoneutrino-subtracted $\bar{\nu}_e$ spectrum to the expectation for no-oscillation as a function of $L_0/E_{\bar{\nu}_e}$. L_0 is the effective baseline taken as 180 km. Figure from [44].

Today, the evidence is overwhelming and it is widely accepted that neutrino oscillations do, indeed, occur. The following section will provide a brief overview of the theory of neutrino oscillations. The focus of neutrino oscillation experiment nowadays is to test the validity of this theoretical framework, determine the remaining oscillation parameters, and move towards precision measurements of neutrino oscillation parameters.

1.4 Neutrino Oscillation Theory

The observation of neutrino oscillations has a profound implication, which is not included in the Standard Model. Namely, neutrino oscillations can occur only if neutrinos have mass, which was thought not to be the case until recently. The theory most widely used to describe neutrino oscillations is known as the Pontecorvo-Maki-Nakagawa-Sakata (PMNS) paradigm, owing its name to the people who have devised it.

1.4.1 Neutrino oscillations in vacuum

As weakly interacting particles, neutrinos can couple to the $W^{\pm}$ and the Z bosons. Due to the doublet structure of the weak interaction, neutrinos possess a quantum number, called flavor (or lepton flavor), which is the same as that of the other lepton in their doublet[4]:

$$\begin{pmatrix}\nu_e\\ e^-\end{pmatrix}\ \begin{pmatrix}\nu_\mu\\ \mu^-\end{pmatrix}\ \begin{pmatrix}\nu_\tau\\ \tau^-\end{pmatrix}\ + h.c. \tag{1.9}$$

Neutrinos can thus be described by *flavor eigenstates*, i.e. the eigenstates with respect to the weak interaction (based on the flavor symmetry of the weak interaction)- let us denote $|\nu_\alpha\rangle$ the α flavor eigenstate of a neutrino ($\alpha \in e, \mu, \tau$). The flavor eigenstates form a complete set ($\langle\nu_\alpha|\nu_\beta\rangle = \delta_{\alpha\beta}$), and each flavor eigenstate can be expressed as a superposition of eigenstates of another complete set, such as the mass eigenstates. The mass eigenstates are the eigenstates of the interaction Hamiltonian $\mathcal{H}$, and we will denote them as $|\nu_i\rangle$, assuming three neutrino states. The superposition can thus be written as

$$|\nu_\alpha\rangle = \sum_i U^*_{\alpha i}\,|\nu_i\rangle\,, \tag{1.10}$$

where U denotes the leptonic mixing matrix, called the PMNS matrix. U is a unitary matrix ($U^\dagger U = \mathbb{1}$), and it relates the mass eigenstates to the flavor eigenstates. For a 3-flavor picture, U is given by:

$$U = \begin{pmatrix} U_{e1} & U_{e2} & U_{e3}\\ U_{\mu 1} & U_{\mu 2} & U_{\mu 3}\\ U_{\tau 1} & U_{\tau 2} & U_{\tau 3}\end{pmatrix}. \tag{1.11}$$

Eq. (1.10) can be inverted and gives

$$|\nu_i\rangle = \sum_\alpha U_{\alpha i}\,|\nu_\alpha\rangle\,. \tag{1.12}$$

The time evolution of each mass eigenstate $|\nu_i(t)\rangle$ can be obtained by applying the time-dependent Schrödinger equation (using $c = \hbar = 1$ from this point until the end of the chapter) to Eq. (1.12):

$$i\frac{d}{dt}\,|\nu_i\rangle = \mathcal{H}\,|\nu_i(t)\rangle = E_i\,|\nu_i(t)\rangle\,, \tag{1.13}$$

where E_i is the particle energy, defined as $E_i = \sqrt{p_i^2 + m_i^2}$. The solution to Eq. (1.13) can be written in the form of plane waves with a time-dependent complex phase:

$$|\nu_i(t)\rangle = e^{-iE_i t}\,|\nu_i\rangle\,. \tag{1.14}$$

Combining Eq. (1.14) with Eq. (1.10), we can get the time evolution of flavor states:

$$|\nu_\alpha(t)\rangle = \sum_i U^*_{\alpha i} e^{-iE_i t}\,|\nu_i\rangle \tag{1.15}$$

and by inserting Eq. (1.12) into Eq. (1.15) the time evolution of each flavor state can be obtained as a function of the initial flavor states:

$$|\nu_\alpha(t)\rangle = \sum_\beta \sum_i U_{\beta i} U^*_{\alpha i} e^{-iE_i t}\,|\nu_\beta\rangle\,. \tag{1.16}$$

---

[4] In this chapter, *h.c.* stands for “hermitian conjugate”.

What Eq. (1.16) shows is that if the U matrix is not diagonal (i.e. the flavor states are different from the mass eigenstates), then a neutrino produced initially via a weak interaction with a flavor α can be detected via a weak interaction at some later point in time in a different flavor β. As a reminder, the neutrino production and detection always occurs via a weak interaction, and is thus sensitive to the flavor eigenstate of the neutrino (via, for instance, the corresponding lepton emitted in a charged current interaction) and not to its mass eigenstates. We can thus write the probability of detecting a neutrino of flavor β assuming that a neutrino of flavor α was produced as:

$$P_{\nu_\alpha \to \nu_\beta} = |\mathcal{A}_{\nu_\alpha \to \nu_\beta}|^2 = |\langle \nu_\beta | \nu_\alpha \rangle|^2 = \sum_{ij} U^*_{\alpha i} U_{\beta i} U_{\beta j} U^*_{\alpha j} e^{-i(E_i - E_j)t}. \tag{1.17}$$

The probability $P_{\nu_\alpha \to \nu_\beta}$ is also known as the *transition probability* or *oscillation probability.* We can make some approximations to Eq. (1.17), based on the fact that neutrinos are highly relativistic (i.e. $E_i \simeq p_i$). The neutrino energy can be approximated as $E_i \simeq E + m_i^2/2E$, where E is neutrino energy, assumed the same for all neutrinos[5]. Furthermore, the elapsed time between production and detection can be written in terms of the travelled distance (or baseline) L as $t \simeq L$. With these considerations in mind, Eq. (1.17) becomes

$$P_{\nu_\alpha \to \nu_\beta} = \sum_{ij} U^*_{\alpha i} U_{\beta i} U_{\beta j} U^*_{\alpha j} e^{-i\frac{\Delta m^2_{ij}}{2E}L}. \tag{1.18}$$

In Eq. (1.18), $\Delta m^2_{ij} = m_i^2 - m_j^2$ and represents the squared mass difference between the i and j neutrino masses. This means that the oscillation probability only depends on the difference between the mass squares, and not on the individual neutrino masses. Eq. (1.18) can also be expressed as a function of the real and imaginary components of the matrix product:

$$\begin{aligned} P_{\nu_\alpha \to \nu_\beta} = \delta_{\alpha\beta} &- 4 \sum_{i>j} \mathfrak{Re} \left(U^*_{\alpha i} U_{\beta i} U_{\beta j} U^*_{\alpha j} \right) \sin^2 \left(\frac{\Delta m^2_{ij} L}{4E} \right) \\ &+ 2 \sum_{i>j} \mathfrak{Im} \left(U^*_{\alpha i} U_{\beta i} U_{\beta j} U^*_{\alpha j} \right) \sin \left(\frac{\Delta m^2_{ij} L}{2E} \right). \end{aligned} \tag{1.19}$$

It is useful to make a few remarks at this point, based on Eq. (1.19).

- The oscillation probability becomes null if neutrinos have the same mass, and in particular if that mass is zero. Observing neutrino oscillations is only possible if neutrinos have non-zero mass.

- The argument of the sine functions depends on the difference of the mass squares, not on the individual neutrino masses. As a result, by observing neutrino oscillations, one is sensitive to the size of the mass splittings.

- If $\alpha \neq \beta$, a new neutrino flavor is said to "appear", while for $\alpha = \beta$, the initial neutrino flavor is said to "disappear". The probabilities $P_{\nu_\alpha \to \nu_\beta}$ and $P_{\nu_\alpha \to \nu_\alpha}$ are known as the "appearance probability" and "survival" probability, respectively[6].

---

[5] This is a bit of an arbitrary approximation - a more correct treatment does not require this approximation, but also passes through a more lengthy derivation. An example can be found in [48], but the final result is the same as the one derived in this section.

[6] The "disappearance" probability is one minus the survival probability.

- Since the matrix U is unitary, the sum of $P_{\nu_\alpha \to \nu_\beta}$ over all β flavors yields unity. This means that the total neutrino flux is conserved, but the relative flavor composition changes in time.
- The same probability can be written for anti-neutrinos, by applying the charge conjugation (C) and parity (P) operators to Eq. (1.16):

$$\begin{aligned} P_{\bar{\nu}_\alpha \to \bar{\nu}_\beta} &= \delta_{\alpha\beta} - 4\sum_{i>j} \mathfrak{Re}\left(U^*_{\alpha i} U_{\beta i} U_{\beta j} U^*_{\alpha j}\right) \sin^2\left(\frac{\Delta m^2_{ij} L}{4E}\right) \\ &- 2\sum_{i>j} \mathfrak{Im}\left(U^*_{\alpha i} U_{\beta i} U_{\beta j} U^*_{\alpha j}\right) \sin\left(\frac{\Delta m^2_{ij} L}{2E}\right). \end{aligned} \tag{1.20}$$

  The only difference between Eq. (1.19) and Eq. (1.20) is the sign of the last term. As a result, if the matrix U is complex, then $P_{\nu_\alpha \to \nu_\beta} \neq P_{\bar{\nu}_\alpha \to \bar{\nu}_\beta}$, which means that neutrino oscillations violate CP symmetry.

The matrix U can be parametrized as a rotation matrix. For a two-flavor case, the U matrix can be parametrized with a single free parameter, θ, known as the mixing angle:

$$U_{2-flav.} = \begin{pmatrix} \cos\theta & \sin\theta \\ -\sin\theta & \cos\theta \end{pmatrix}. \tag{1.21}$$

In the two flavor picture, the oscillation probability becomes

$$P_{\nu_\alpha \to \nu_\beta} = \sin^2 2\theta \sin^2\left(\frac{1.27\Delta m^2_{ij} L}{E}\right), \tag{1.22}$$

where the 1.27 factor comes from reintroducing the values of c and $\hbar$ such that L is expressed in km and E in GeV.

It has been shown in the previous paragraphs that three neutrino flavors, corresponding to three lepton generations, have been experimentally discovered. It is common to write the PMNS matrix under the following form:

$$U = \begin{pmatrix} 1 & 0 & 0 \\ 0 & c_{23} & s_{23} \\ 0 & -s_{23} & c_{23} \end{pmatrix} \begin{pmatrix} c_{13} & 0 & s_{13}e^{-i\delta_{\mathrm{CP}}} \\ 0 & 1 & 0 \\ -s_{13}e^{i\delta_{\mathrm{CP}}} & 0 & c_{13} \end{pmatrix} \begin{pmatrix} c_{12} & s_{12} & 0 \\ -s_{12} & c_{12} & 0 \\ 0 & 0 & 1 \end{pmatrix} \begin{pmatrix} e^{i\alpha_1/2} & 0 & 0 \\ 0 & e^{i\alpha_2/2} & 0 \\ 0 & 0 & 1 \end{pmatrix}, \tag{1.23}$$

where $c_{ij} \equiv \cos\theta_{\mathrm{ij}}$ and $s_{ij} \equiv \sin\theta_{\mathrm{ij}}$. The matrix is parametrized by three real mixing angles, θ_{12}, θ_{23} and θ_{13} and three phases appearing in complex terms, δ_{CP}, α_1 and α_2. The decomposition of the U matrix in Eq. (1.23) is useful as it illustrates how the different mixing angles and phases can be measured by different types of experiments. As such, the first matrix, containing (2,3) terms, is known as the "atmospheric" sector, because the θ_{23} angle regulates most of the atmospheric neutrino oscillations. The third matrix, containing (1,2) terms, is known as the "solar" sector, because the θ_{12} terms govern mostly solar neutrino oscillations.

The second term is known as the "cross-mixing" matrix and contains the first CP violating phase δ_{CP} and what is commonly referred to as the "reactor angle" θ_{13} since reactor experiments have the largest sensitivity to it. θ_{13} is actually the smallest of the three mixing angles, with the Daya Bay experiment providing the first 5σ evidence that it is not zero [46] and with T2K providing 7.3σ confirmation of the same fact [49]. If $\delta_{\mathrm{CP}} \neq 0, \pi$, then this would imply that CP symmetry is

violated in neutrino oscillations, the first evidence of CP violation in the lepton sector.
Finally, the fourth matrix in Eq. (1.23) is known as the “Majorana” matrix and only has physical consequences if neutrinos are Majorana particles (i.e. if neutrinos and antineutrinos are the same particles). The latter does not affect the oscillation probability, since the α_1 and α_2 terms cancel out when the U matrix is squared.

1.4.2 Matter effects

In the previous section, the mechanism of neutrino oscillations was explained assuming that neutrinos propagate in a vacuum between their production point and detection point. This is, of course, not the case in most neutrino experiments. For instance, solar neutrinos propagate through the sun, while atmospheric neutrinos (such as the up-going neutrinos in Fig. 1.5a) propagate through the Earth. Despite the weak nature of their interactions, neutrinos do interact with matter, and this will affect the final oscillation probability. This is known as the Mikheev-Smirnov-Wolfenstein (MSW) effect [50, 51].
In matter, neutrinos can interact via two channels leaving neutrinos in the final state[7]: an electron neutrino can scatter off an electron via the exchange of a $W^{\pm}$ boson, or a neutrino of any flavor can scatter off an electron, proton or neutron through a neutral current interaction (i.e. exchange of a Z boson) and produces a neutrino of the same flavor in the final state. These interactions are illustrated in Fig. 1.7.
Neutral current interactions do not affect the oscillation probability, since they do not discriminate based on the neutrino flavor. Charged current interactions, on the other hand, affect only electron neutrinos (and not neutrinos of other flavors, because stable matter is made up of electrons). This effect can be added in the oscillation probability derivation through an additional potential term in the interaction Hamiltonian, of the form

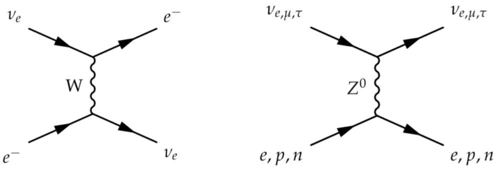

Figure 1.7: Tree-level Feynman diagrams of neutrino interactions with matter leaving neutrinos in the final state: charged current interaction (left) and neutral current interaction (right).

$$V_{CC} = \pm\sqrt{2}G_F n_e \tag{1.24}$$

in which G_F is the Fermi constant and n_e is the average electron density of the medium. The term in Eq. (1.24) has a positive sign for ν_e, and negative sign for $\bar{\nu}_e$.
The full treatment of matter effects in the three flavor neutrino case is lengthy and is well explained in many resources (e.g. [52]). The main impact of matter effects is that, since matter itself is formed of matter rather than anti-matter, the matter potential has a different sign for neutrinos and anti-neutrinos. This effect is different from CP violation, but if it is not accounted for, it can mimic CP

---

[7] Neutrinos can interact in many other ways with matter, as will be detailed in Section 2.4, but not all interactions produce neutrinos in the final state. Yet, in this section, we are examining interactions which affect the neutrino oscillation probability, so we only discuss the interactions which preserve a neutrino in the final state.

violation. Another important consequence of matter effects is that through matter effects we can acquire sensitivity to the sign of the mass splittings Δm^2_{ij}, and as a result, to the mass hierarchy. The impact of matter effects on the oscillation probability, depending on the sign of Δm^2 in a two-flavor neutrino oscillation framework, is illustrated in Fig. 1.8. At leading order, the oscillation probability depends on $\sin^2(\Delta m^2_{31}\, L/4E_\nu)$, which is not sensitive to the sign of Δm^2_{31}. Matter effects introduce an additional term in the probability which is proportional to $\sin(\Delta m^2_{31}\, L/4E_\nu)$, which in return can resolve the sign of the mass difference - the larger the amount of matter traversed by the neutrinos, the larger the term sensitive to the mass hierarchy. For this reason, experiments which have a large baseline and in which neutrinos travel through a significant amount of matter have the largest sensitivity to the mass hierarchy.

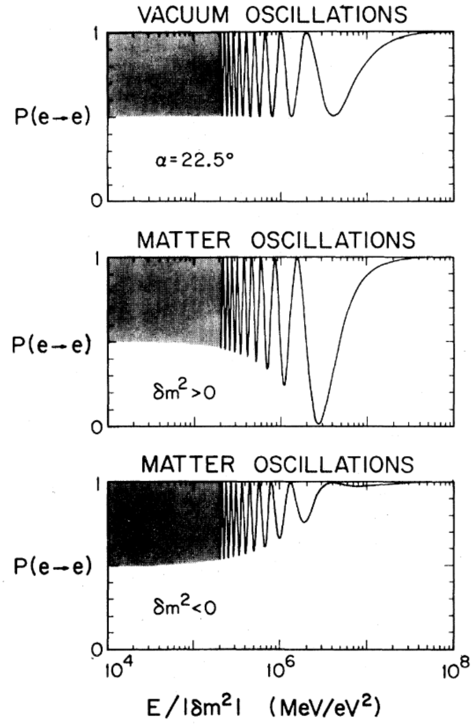

Figure 1.8: Comparison of vacuum and matter transition probability $P_{\nu_e\rightarrow\nu_e}$ for two neutrino flavors, assuming a mixing angle $\alpha = 22.5°$ at fixed baseline $L = 5000$km. Figure from [53].

1.5 Long baseline neutrino experiments

With the discovery of neutrino oscillations, one of the main goals of neutrino oscillation experiments is now the (increasingly more precise) measurement of oscillation parameters: the three mixing angles θ_{13}, θ_{23}, θ_{12}, two mass splittings Δm^2_{12} and Δm^2_{32}, and the CP-violating phase $\delta_{\rm CP}$. In addition, an important unanswered question concerns the neutrino mass hierarchy (MH, or mass ordering, MO). The oscillation probability is sensitive to the squared mass differences of the three neutrino masses, but the order of the latter is still unknown - for instance, is $m_3 > m_2 > m_1$ or is the ordering different? Fig. 1.9 shows the two possibilities. We can see that the ν_2 state (with mass m_2) has roughly similar contributions from ν_e, ν_μ and ν_τ. ν_1 and ν_3 are defined based on the dominating flavor contribution: ν_1 is dominated by ν_e and ν_3 is dominated by ν_τ. From solar neutrino experiments, which exploit the MSW effect in the Sun, the sign of the Δm^2_{21} term is known to be positive,

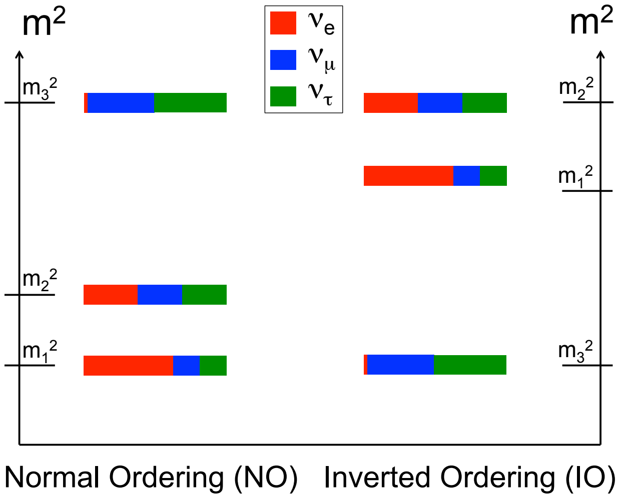

Figure 1.9: Illustration of the two mass hierarchies. For each hierarchy, the neutrino mass eigenstates are illustrated according to their composition in terms of flavor eigenstates, according to current measurements. Figure from [54].

meaning that $m_2 > m_1$. However, it is still not known whether the ν_τ enriched ν_3 is the heaviest, or the lightest mass eigenstate. As with solar neutrinos, the MSW effect can be used to resolve the mass hierarchy - if $m_3 > m_2$, the hierarchy is called “normal” (NH, called Normal because it reflects the ordering of charged leptons masses), whereas if $m_1 > m_3$, the hierarchy is called “inverted” (IH). The absolute scale of the neutrino masses is not measurable by neutrino oscillation experiments, but other types of experiments, such as KATRIN, which exploits the β decay spectrum of tritium, can achieve this and have made remarkable progress [25]. As previously mentioned, $0\nu\beta\beta$ experiments can also have sensitivity to the neutrino mass ordering if neutrinos are Majorana particles, and cosmological observations are also sensitive to the mass hierarchy, through the value of the sum of the neutrino masses.

As was shown in the previous section, the oscillation probability depends on the ratio of the baseline (the distance between production and detection points) and the neutrino energy, L/E. In some cases, this ratio is fixed by nature - this is the case for solar and atmospheric neutrino experiments. In the latter, neutrinos over a wide range of energies are produced. For solar neutrinos, the distance to the Sun is fixed, while for atmospheric neutrinos, the detector is located on a fixed place on the Earth, but neutrinos produced in the entire atmosphere reach it. In other cases, neutrino experiments have the choice to vary L/E to achieve an optimal sensitivity to some category of oscillation parameters. This is the case for reactor and accelerator neutrino experiment. Depending on the distance from the neutrino source, the latter experiments can further be categorized into short- or long-baseline experiments. The focus of this thesis will be on the T2K and Hyper-Kamiokande experiments, which are both long-baseline neutrino oscillation experiments using neutrino beams from an accelerator source. For this reason, this section will focus on the principle of long-baseline neutrino experiments, the oscillation parameters they can measure, and their challenges.

Long baseline neutrino oscillation experiments, as their name indicates, observe neutrino oscillations which occur over a long distance, which can be of the order of 100 km to 1000 km. The strategy of long-baseline neutrino experiments is thus to produce a well-controlled neutrino beam with an energy tuned to maximize the oscillation probability.

The first generation of neutrino experiments began in 1999 with the K2K experiment [55], which aimed to confirm the atmospheric neutrino disappearance found by Super-Kamiokande, but using a well-controlled muon neutrino beam as the neutrino source. This was the first neutrino oscillation experiment in which both the neutrino source and the detector were under experimental control. Following a similar goal, the MINOS [56] experiment ran from 2005 to 2012, searching for ν_μ disappearance with the NuMI beamline [57] at Fermilab. The goal of the first generation long-baseline neutrino oscillation experiments was to confirm and measure neutrino oscillations by searching for neutrino disappearance.

The second generation of neutrino oscillation experiments initially focused on detecting neutrino appearance, through the $\nu_\mu \rightarrow \nu_e$ channel. The T2K experiment (which will be described in detail in Chapter 2) was the first experiment to provide evidence [58] of this phenomenon, which it then measured with more than 7σ significance [49]. Initially, the θ_{13} angle was not known, and so the appearance probability was unknown. It turned out that the latter actually had a high value, making ν_e appearance quite likely. With this discovery (and a precise measurement of θ_{13} from the Daya Bay experiment [46]), the focus of T2K and other second generation long-baseline experiments shifted towards measuring and comparing the rate of ν_e and $\bar{\nu}_e$ appearance, which, as will be described in this section, offers sensitivity to the amount of CP violation in the lepton sector.

Current long-baseline neutrino oscillation experiments, such as T2K and NOνA [59], measure both the disappearance, $\nu_\mu \rightarrow \nu_\mu$, and the appearance $\nu_\mu \rightarrow \nu_e$ channels. Each channel is sensitive to certain oscillation parameters, and to illustrate this we can look at the example of the T2K experiment, shown in Fig. 1.10. If we consider the ν_μ disappearance, or survival probability

$$\begin{aligned} P(\nu_\mu \rightarrow \nu_\mu) &\simeq 1 - 4c_{13}^2 s_{23}^2 [1 - c_{13}^2 s_{23}^2] \sin^2(\Delta m_{32}^2 \, L/4E_\nu) \\ &\simeq 1 - \sin^2 2\theta_{23} \sin^2(\Delta m_{32}^2 \, L/4E_\nu), \qquad \text{(for } c_{13} \simeq 1\text{)}, \end{aligned} \tag{1.25}$$

where $s_{ij} = \sin\theta_{ij}$, $c_{ij} = \cos\theta_{ij}$, we can see that the amplitude of the disappearance dip in Fig. 1.10(left) is driven by $\sin^2\theta_{23}$, whereas the position of the dip is determined by Δm_{32}^2. The latter are commonly referred to as the "disappearance parameters".

In the appearance channel, $\nu_\mu \rightarrow \nu_e$, the oscillation probability formula, including matter effects, is

$$\begin{aligned} P(\nu_\mu \rightarrow \nu_e) = {} & 4c_{13}^2 s_{13}^2 s_{23}^2 \cdot \sin^2 \Delta_{31} \\ & + 8c_{13}^2 s_{12} s_{13} s_{23} (c_{12} c_{23} \cos\delta_{\rm CP} - s_{12} s_{13} s_{23}) \cdot \cos\Delta_{32} \cdot \sin\Delta_{31} \cdot \sin\Delta_{21} \\ & - 8c_{13}^2 c_{12} c_{23} s_{12} s_{13} s_{23} \sin\delta_{\rm CP} \cdot \sin\Delta_{32} \cdot \sin\Delta_{31} \cdot \sin\Delta_{21} \\ & + 4s_{12}^2 c_{13}^2 (c_{12}^2 c_{23}^2 + s_{12}^2 s_{23}^2 s_{13}^2 - 2c_{12} c_{23} s_{12} s_{23} s_{13} \cos\delta_{\rm CP}) \cdot \sin^2\Delta_{21} \\ & - 8c_{13}^2 s_{13}^2 s_{23}^2 \cdot \frac{aL}{4E_\nu}(1 - 2s_{13}^2) \cdot \cos\Delta_{32} \cdot \sin\Delta_{31} \\ & + 8c_{13}^2 s_{13}^2 s_{23}^2 \frac{a}{\Delta m_{31}^2}(1 - 2s_{13}^2) \cdot \sin^2\Delta_{31}, \end{aligned} \tag{1.26}$$

where $\Delta_{ij} = \Delta m_{ij}^2 \, L/4E_\nu$, and $a = 2\sqrt{2} G_F n_e E_\nu = 7.56 \times 10^{-5}[\text{eV}^2] \times \rho[\text{g/cm}^3] \times E_\nu[\text{GeV}]$. The corresponding formula for $\bar{\nu}_\mu \rightarrow \bar{\nu}_e$ can be obtained by replacing $\delta_{\rm CP}$ with -$\delta_{\rm CP}$ and a with $-a$, as outlined in the previous section. From Fig. 1.10(right), we can see that in this channel there will be an appearance "peak", centered around the same energy at which the ν_μ disappearance is maximal. The amplitude of the peak is driven by $\sin^2\theta_{13}$, from Eq. (1.26). We can further see that the peak shape and position is slightly sensitive to the presence of matter effects (leading to a small dependence on the mass hierarchy). At the T2K baseline of 295 km, the dependence on the MH is weak (~10%), but larger baseline experiments such as NOνA ($L \sim 800$ km) have a much larger

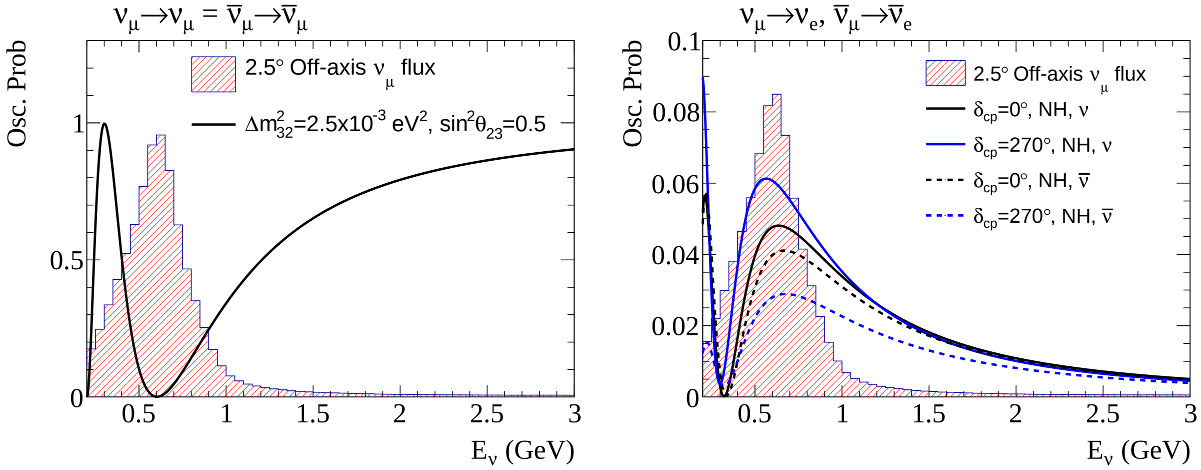

(a) (b)

Figure 1.10: Oscillation probabilities for two channels as a function of neutrino energy, for oscillation parameters specified in the legends. (a) ν_μ disappearance. (b) ν_e appearance. The T2K ν_μ flux with an arbitrary normalization is shown in the shaded red region.

sensitivity to the MH.

It is particularly important to note the dependence of Eq. (1.26) on the CP violating phase δ_{CP}. The terms proportional to $\cos\delta_{\mathrm{CP}}$ are only sensitive to the absolute value of δ_{CP}, and are called CP-even terms. Those proportional to $\sin\delta_{\mathrm{CP}}$ are sensitive to its sign, and are thus called CP-odd terms. If CP violation occurs in neutrino oscillations, i.e. if $\delta_{\mathrm{CP}} \neq 0, \pi$, and, if, in addition, $\delta_{\mathrm{CP}} \sim \pi/2$, the CP-even term in Eq. (1.26) becomes small, and the CP-odd term has opposite effects on ν_e and $\bar{\nu}_e$ appearance probability.

In order to actually measure the oscillation parameters, neutrino oscillation experiments first measure the event rate of reconstructed ν_μ/ν_e events as a function of some observable (most often the reconstructed neutrino energy, E_ν). The spectrum for the appearance and disappearance channels is then compared to Monte-Carlo simulations, in which oscillation parameters are varied until they are in agreement with the data. It is important to note that no single type of neutrino oscillation experiment is sensitive to all oscillation parameters at once (and not with the same precision), but the oscillation probability depends on all parameters at once. For this reason, neutrino experiments complement each other. Solar neutrino experiments are most sensitive to the solar parameters - θ_{12} and Δm^2_{21}, whereas reactor experiments are most sensitive to θ_{13}. The constraints obtained from other neutrino experiments are often used by long-baseline experiments to further improve the measurements on $\sin^2\theta_{23}$, Δm^2_{32} and δ_{CP}. The predicted neutrino event rate depends on the initial neutrino flux (how many ν_μ were created), the neutrino interaction cross-section with the detector (how probable it is that a neutrino will interact), the detector efficiency (how well the detector will be able to reconstruct the event signaling the neutrino) and, finally, on the oscillation probability (how many of the initial ν_μ survived, or how many ν_e appeared). Since neutrinos interact weakly, the precision on the event rate today is mainly limited by statistical errors. However, effects related to the flux, neutrino interaction cross-sections and the detector efficiency are sources of systematic errors. The impact of these systematic errors is one of the main topics discussed in this thesis.

The neutrino oscillations physics community is now working towards the development of the next generation of long-baseline experiments, the most prominent examples of which are the DUNE

		Normal Ordering (best fit)		Inverted Ordering ($\Delta\chi^2 = 2.7$)	
		bfp $\pm 1\sigma$	3σ range	bfp $\pm 1\sigma$	3σ range
without SK atmospheric data	$\sin^2\theta_{12}$	$0.304^{+0.013}_{-0.012}$	$0.269 \to 0.343$	$0.304^{+0.013}_{-0.012}$	$0.269 \to 0.343$
	$\theta_{12}/^\circ$	$33.44^{+0.78}_{-0.75}$	$31.27 \to 35.86$	$33.45^{+0.78}_{-0.75}$	$31.27 \to 35.87$
	$\sin^2\theta_{23}$	$0.570^{+0.018}_{-0.024}$	$0.407 \to 0.618$	$0.575^{+0.017}_{-0.021}$	$0.411 \to 0.621$
	$\theta_{23}/^\circ$	$49.0^{+1.1}_{-1.4}$	$39.6 \to 51.8$	$49.3^{+1.0}_{-1.2}$	$39.9 \to 52.0$
	$\sin^2\theta_{13}$	$0.02221^{+0.00068}_{-0.00062}$	$0.02034 \to 0.02430$	$0.02240^{+0.00062}_{-0.00062}$	$0.02053 \to 0.02436$
	$\theta_{13}/^\circ$	$8.57^{+0.13}_{-0.12}$	$8.20 \to 8.97$	$8.61^{+0.12}_{-0.12}$	$8.24 \to 8.98$
	$\delta_{\mathrm{CP}}/^\circ$	195^{+51}_{-25}	$107 \to 403$	286^{+27}_{-32}	$192 \to 360$
	$\frac{\Delta m^2_{21}}{10^{-5}\ \mathrm{eV}^2/c^4}$	$7.42^{+0.21}_{-0.20}$	$6.82 \to 8.04$	$7.42^{+0.21}_{-0.20}$	$6.82 \to 8.04$
	$\frac{\Delta m^2_{3l}}{10^{-3}\ \mathrm{eV}^2/c^4}$	$+2.514^{+0.028}_{-0.027}$	$+2.431 \to +2.598$	$-2.497^{+0.028}_{-0.028}$	$-2.583 \to -2.412$
		Normal Ordering (best fit)		Inverted Ordering ($\Delta\chi^2 = 7.1$)	
		bfp $\pm 1\sigma$	3σ range	bfp $\pm 1\sigma$	3σ range
with SK atmospheric data	$\sin^2\theta_{12}$	$0.304^{+0.012}_{-0.012}$	$0.269 \to 0.343$	$0.304^{+0.013}_{-0.012}$	$0.269 \to 0.343$
	$\theta_{12}/^\circ$	$33.44^{+0.77}_{-0.74}$	$31.27 \to 35.86$	$33.45^{+0.78}_{-0.75}$	$31.27 \to 35.87$
	$\sin^2\theta_{23}$	$0.573^{+0.016}_{-0.020}$	$0.415 \to 0.616$	$0.575^{+0.016}_{-0.019}$	$0.419 \to 0.617$
	$\theta_{23}/^\circ$	$49.2^{+0.9}_{-1.2}$	$40.1 \to 51.7$	$49.3^{+0.9}_{-1.1}$	$40.3 \to 51.8$
	$\sin^2\theta_{13}$	$0.02219^{+0.00062}_{-0.00063}$	$0.02032 \to 0.02410$	$0.02238^{+0.00063}_{-0.00062}$	$0.02052 \to 0.02428$
	$\theta_{13}/^\circ$	$8.57^{+0.12}_{-0.12}$	$8.20 \to 8.93$	$8.60^{+0.12}_{-0.12}$	$8.24 \to 8.96$
	$\delta_{\mathrm{CP}}/^\circ$	197^{+27}_{-24}	$120 \to 369$	282^{+26}_{-30}	$193 \to 352$
	$\frac{\Delta m^2_{21}}{10^{-5}\ \mathrm{eV}^2/c^4}$	$7.42^{+0.21}_{-0.20}$	$6.82 \to 8.04$	$7.42^{+0.21}_{-0.20}$	$6.82 \to 8.04$
	$\frac{\Delta m^2_{3l}}{10^{-3}\ \mathrm{eV}^2/c^4}$	$+2.517^{+0.026}_{-0.028}$	$+2.435 \to +2.598$	$-2.498^{+0.028}_{-0.028}$	$-2.581 \to -2.414$

Table 1.1: Three-flavor oscillation parameters from the fit to global data from [9]. $\Delta m^2_{3l} \equiv \Delta m^2_{32} > 0$ for NO and $\Delta m^2_{3l} \equiv \Delta m^2_{31} < 0$ for IO. “bfp” stands for “best fit point”.

[60] and Hyper-Kamiokande [10](described in detail in Chapter 7) experiments. Both of these experiments have rich physics programs, beyond long-baseline neutrino oscillations. In terms of the latter, however, the focus of next generation neutrino oscillation experiments will be to perform precision measurements of the oscillation parameters and to rule on whether CP violation occurs in neutrino oscillations and establish the Mass Ordering.

1.6 Current knowledge of neutrino oscillations

Since the discovery of neutrino oscillations, most of the parameters involved in this process have been measured, with different degrees of accuracy. Table 1.1 gives an overview of the global neutrino oscillation parameter data as a result of a global fit, described in [9].

In general, the solar and reactor parameters are determined with good precision, and are used in

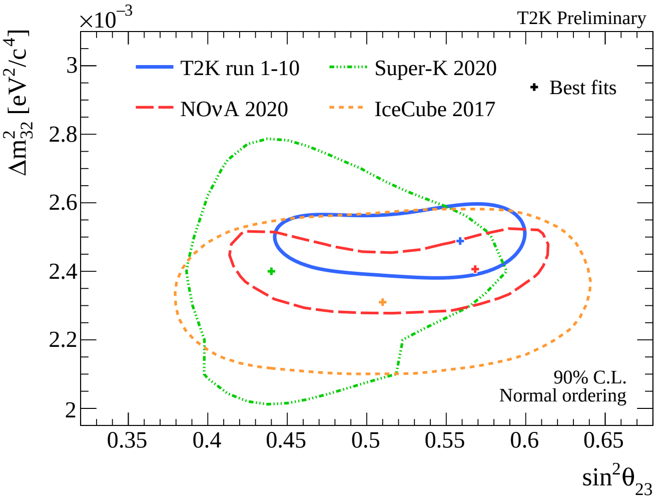

Figure 1.11: Comparison of 90% confidence levels for $\sin^2\theta_{23}$-Δm^2_{32} from different experiments: T2K [1], NOνA [2], Super-Kamiokande [3] and IceCube [4]. Note that at the time of writing, the T2K, NOνA and Super-Kamiokande results are still preliminary. Figure from the T2K Collaboration.

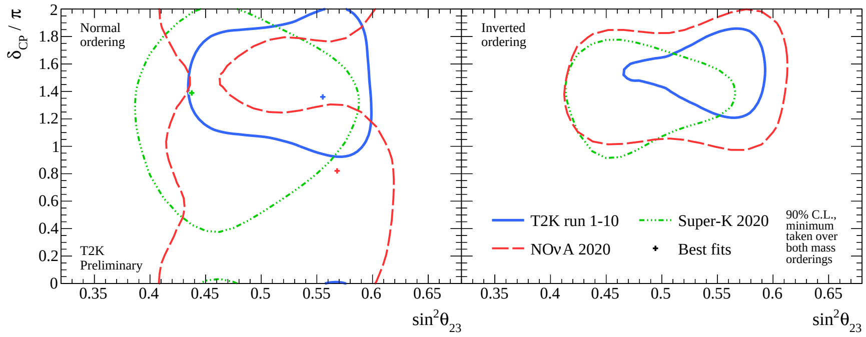

Figure 1.12: Comparison of 1σ confidence limits from T2K, NOνA and Super-Kamiokande, assuming normal ordering (left) and inverted ordering (right). Note that these results are preliminary. Figure produced by the T2K collaboration.

long-baseline neutrino oscillation experiments to provide constraints on the oscillation parameters. The atmospheric, or disappearance, parameters Δm^2_{32} and $\sin^2\theta_{23}$ are highly correlated, and thus are often presented as 2D contours. The current world picture for these parameters is shown in Fig. 1.11. δ_{CP} is the parameter with the largest uncertainty. T2K was the first experiment to provide hints of CP violation in the lepton sector [61], by excluding CP conserving values of 0 and π at the 95% confidence level. In June 2020, T2K presented its most recent results [1], to which the work presented in this thesis has contributed notably as presented in Chapter 3, Chapter 4 and Chapter 5. A preliminary comparison of the T2K, NOνA [2] and Super-Kamiokande [3] results for the δ_{CP} and $\sin^2\theta_{23}$ 1σ confidence levels can be seen in Fig. 1.12. There is some tension between the T2K and NOνA results - T2K data seem to have a small preference for maximal CP violation, which is disfavored by NOνA. In the inverted ordering picture, all three experiments seem to be in agreement concerning the value of δ_{CP}, but favor different octants of $\sin^2\theta_{23}$.

Chapter 2

The T2K Experiment

The T2K experiment is a long-baseline neutrino oscillation experiment located in Japan [62]. The main original goal of the experiment was the observation of electron neutrino appearance in a muon neutrino beam. This goal was achieved in 2013, when T2K reported an excess of electron neutrino events compared to the background prediction of 7.3 σ [49].
Ever since, the T2K experiment has developed a rich physics program, whose main goals today are:

- Search for CP-violation in neutrino oscillations.
- Performing neutrino interaction cross-section measurements.
- Searches for exotic neutrino physics signals, such as sterile neutrinos.

This chapter describes the functioning of the T2K experiment. In the T2K experiment, a muon neutrino beam is produced at the Japan Proton Research Accelerator Complex (J-PARC), located in Tokai, on the east coast of Japan. The composition of the beam is measured with a set of near detectors at a distance of 280 m from the beam production point, when the effect of oscillations is negligible. The beam crosses the earth for a distance of approximately 295 km, until it reaches the Super-Kamiokande (SK) detector. After this distance, the composition of the neutrino beam changes as a result of neutrino oscillations, and the resulting spectrum is measured at SK. An overview of the experiment is shown in Fig. 2.1. By comparing the neutrino spectrum composition between the near and far detectors, T2K can measure oscillation parameters.

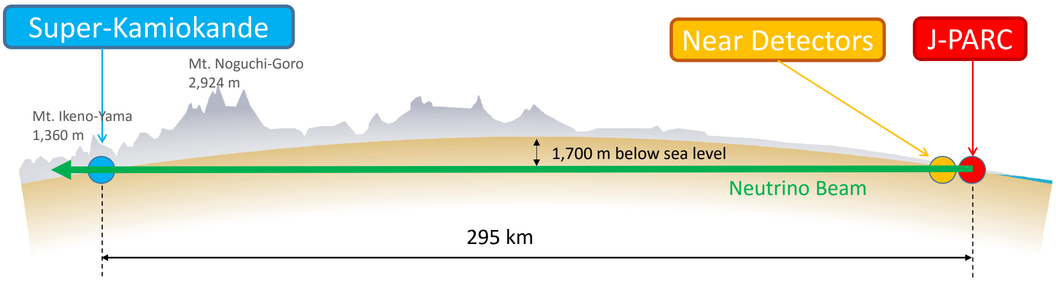

Figure 2.1: Schematic view of the T2K experiment.

The neutrino energy used in the T2K experiment is tuned, based on its 295 km baseline, to probe the first oscillation maximum. From the neutrino oscillation probability in Eq. (1.22), we can see that the term depending on the oscillation baseline and the neutrino energy is

$$\sin^2\left(\frac{\Delta \mathrm{m}_{32}^2 \mathrm{L}}{4\mathrm{E}_\nu}\right) \tag{2.1}$$

or, by computing the constant terms such that the baseline L is expressed in km, the neutrino energy E_ν is expressed in GeV and the Δm_{32}^2 term is expressed in eV^2/c^4:

$$\sin^2\left(1.27\frac{\Delta \mathrm{m}_{32}^2 \mathrm{L}}{\mathrm{E}_\nu}\right). \tag{2.2}$$

The maximum probability for muon neutrino disappearance and electron neutrino appearance occurs when Eq. (2.2) is equal to 1, or, equivalently, for a neutrino energy of $E_\nu = \left(2 \times 1.27 \times \Delta m_{32}^2 \times L\right)/\pi$. For $\Delta m_{32}^2 \sim 2.5 \times 10^{-3}\mathrm{eV}^2/c^4$ (based on the size of K2K results in [63]) and a baseline of 295 km, the term in Eq. (2.2) is maximal for a neutrino energy of ∼0.6 GeV. The neutrino energies used in the T2K experiment are thus tuned to be peaked around this energy to maximize both the ν_e appearance probability and the ν_μ disappearance probability.

2.1 The T2K Beam

2.1.1 The Beamline

The J-PARC beamline [64] accelerates protons which are used for the T2K experiment, but also for muon and neutron beamlines for the Materials and Life Sciences Facility.

T2K uses a proton beam to produce hadrons which decay into neutrinos. The proton beam used for T2K is obtained with the help of three accelerators: a 181 MeV LINAC, a 3 GeV rapid-cycle synchrotron (RCS) and a 30 GeV Main Ring synchrotron (MR). The three accelerators, as well as the T2K beamline, are shown in Fig. 2.2a.

First, a H^- beam is accelerated in the LINAC, and is then converted into a H^+ beam by charge stripping foils when injected into the RCS. Each RCS cycle contains two bunches. 5% of these bunches are supplied to the MR, with the rest being used for the Materials and Life Science Facility. Four groups of two bunches are fed at a time to the MR, filling eight of its nine buckets. Finally, for the neutrino beamline, all eight bunches are extracted by a set of five kicker magnets in a single turn (fast extraction). This is known as a “spill”, and takes 5 μs. There are $\sim 3\times 10^{14}$ protons per spill.

The neutrino beamline is composed of two sections: the primary and the secondary beamline. An overview of the neutrino beamline is shown in Fig. 2.2b.

In the primary beamline, the proton beam is bent and directed towards Kamioka. In the preparation section, the beam is tuned with 11 normal conducting magnets so that the beam can be accepted by the arc section. In the arc section, the beam is bent with a series of superconducting magnets to point towards Kamioka. Finally, the beam is focused and directed onto the target with a series of 10 normal conducting magnets. A well-tuned beam is essential for a stable neutrino beam production, so the beam intensity, profile and loss is monitored along the entire primary beamline with dedicated systems [62].

The secondary beamline consists of three sections: the target station, the decay volume, and the

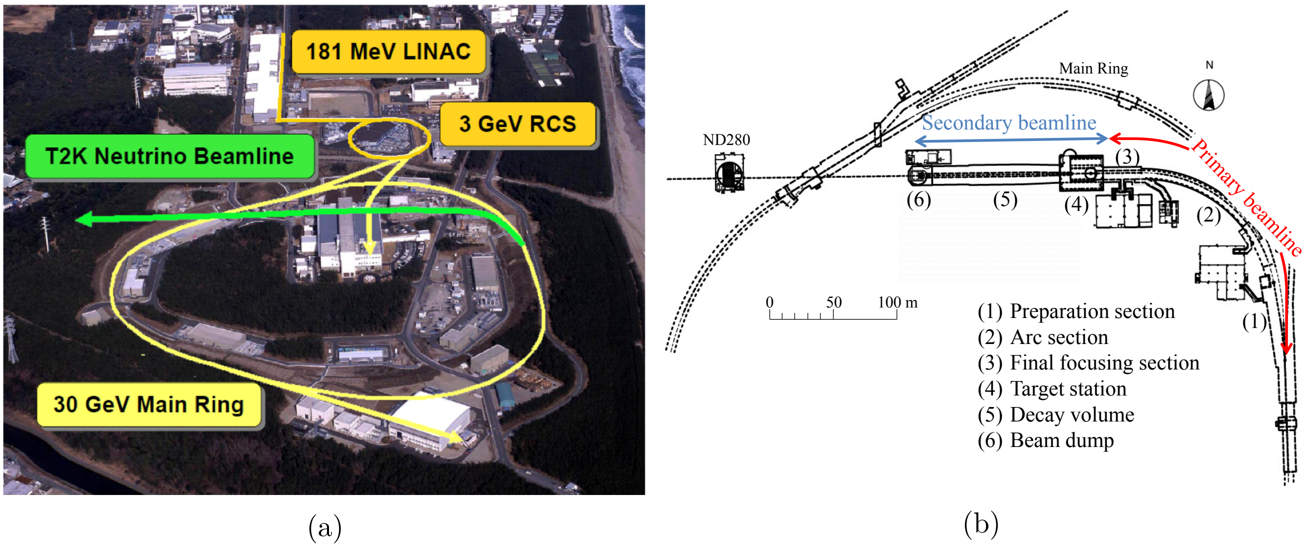

Figure 2.2: Overview of J-PARC proton accelerator complex and neutrino beamline. (a) Bird's eye view of J-PARC proton accelerator facility. (b) Overview of the neutrino beamline, with labeled components.

beam dump. An overview of the secondary beamline is shown in Fig. 2.3.

The proton beam impinges onto a 1.9 interaction length (91.4 cm long), 2.6 cm diameter and 1.8 g/cm^3 graphite rod. As a result, secondary mesons are produced (pions and kaons, mostly), which are focused by a set of three magnetic horns [65]. The target is located inside the first horn. The role of the magnetic horns is to focus the secondary particles produced in the proton interactions according to their sign, allowing them to then decay into a beam which will be enriched primarily in muon neutrinos or anti-neutrinos. The horns are operated with a 250 kA pulsed current, producing a 1.7 T magnetic field, which increases the total flux at Super-K by a factor of 17 [66]. Depending on whether the horns are operated with a positive current (+250 kA) or negative current (-250 kA), the operation mode is referred to as "Forward" or "Reverse" Horn Current mode, respectively (FHC and RHC for short). Operating in FHC mode produces a ν_μ beam, while operating in RHC mode produces a $\bar{\nu}_\mu$ beam.

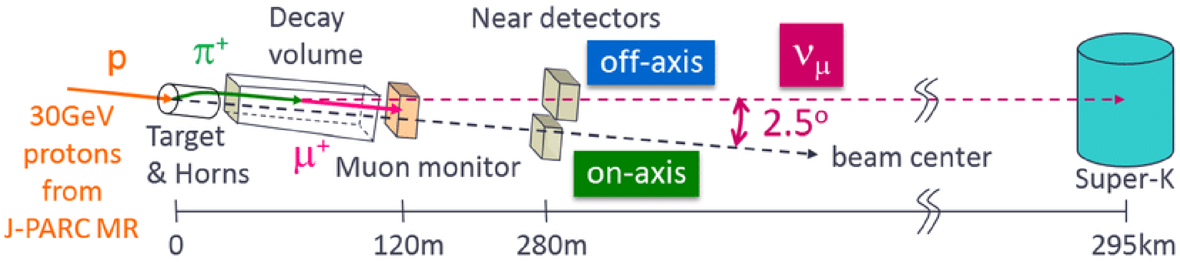

Figure 2.3: Overview of the secondary beamline, and the final neutrino beam.

The focused mesons then enter a 96 m long decay volume, in which the mesons decay to form the neutrino beam, and other leptons and hadrons. The main channels for meson decays, along with their branching ratios, are summarized in Table 2.1. The hadrons and leptons produced in these interactions encounter a beam dump at the end of the decay volume. The beam dump's core is

Particle	Decay Products	Branching Fraction (%)
π^+	$\rightarrow \mu^+\nu_\mu$	99.9877
	$\rightarrow e^+\nu_e$	1.23×10^{-4}
K$^+$	$\rightarrow \mu^+\nu_\mu$	63.55
	$\rightarrow \pi^0\mu^+\nu_\mu$	3.353
	$\rightarrow \pi^0 e^+\nu_e$	5.07
K^0_L	$\rightarrow \pi^-\mu^+\nu_\mu$	27.04
	$\rightarrow \pi^- e^+\nu_e$	40.55
μ^+	$\rightarrow e^+\bar{\nu}_\mu\nu_e$	100

Table 2.1: Neutrino-producing decay modes for FHC operation. Decay modes for $\bar{\nu}_\mu$ and $\bar{\nu}_e$ are omitted in this table. The π^-, K$^-$ and μ^- modes are charge conjugates of the π^+, K$^+$ and μ^+ modes, respectively. Taken from [66].

made of 75 tons of graphite (1.7 g/cm^3), and is 3.174 m long, 1.94 m wide and 4.69 m high. It is hosted in a cooling structure. The only particles that are not stopped by the beam dump are high-energy muons ($\sim$5 GeV/c). These muons are measured with a muon monitor, the MUMON detector. The role of the muon monitor is to infer the neutrino beam intensity and direction. It does so by measuring high energy muons which pass the beam dump, exploiting the fact that muons are mostly produced in two-body pion decays, so the muon direction is a direct probe of the neutrino beam direction. The muon monitor measures the neutrino beam direction with a precision better than 0.25 mrad, which corresponds to a 3 cm precision of the muon profile center. It is also required to monitor the stability of the neutrino beam intensity with a precision better than 3%. These measurements are used to inform the beam simulation group.

The amount of data collected by T2K is measured in units of “protons on target”, or POT. The history of POT data taking since the beginning of the T2K experiment is shown in Fig. 2.4. As of 2020, a stable beam power of 515 kW was reached. A total of 3.60×10^{21} POT have been delivered, with 1.97×10^{21} POT in FHC mode and 1.63×10^{21} POT in RHC mode.

2.1.2 The Off-Axis Angle

As previously explained, the T2K baseline of 295 km, along with the energy range of the neutrino beam, is tuned to the first oscillation maximum, which occurs at 0.6 GeV in the neutrino energy spectrum. The ν_μ beam contains a non-negligible amount of ν_e particles. The latter are the same particles that constitute the signal sample at SK for ν_e appearance as a result of oscillations. It is therefore important to a) precisely know the amount of this background b) reduce it as much as possible.

To respond to these requirements, T2K employs the “off-axis” technique, which consists in purposely directing the neutrino beam 2.5° away from the J-PARC-Super-Kamiokande axis. T2K was the first neutrino oscillation experiment to employ this technique.

The reasoning behind this technique is related to the kinematics of pion decays. The great majority of the ν_μ beam composition comes from two-body $\pi^+ \rightarrow \mu^+\nu_\mu$ decays. For a pion decaying along

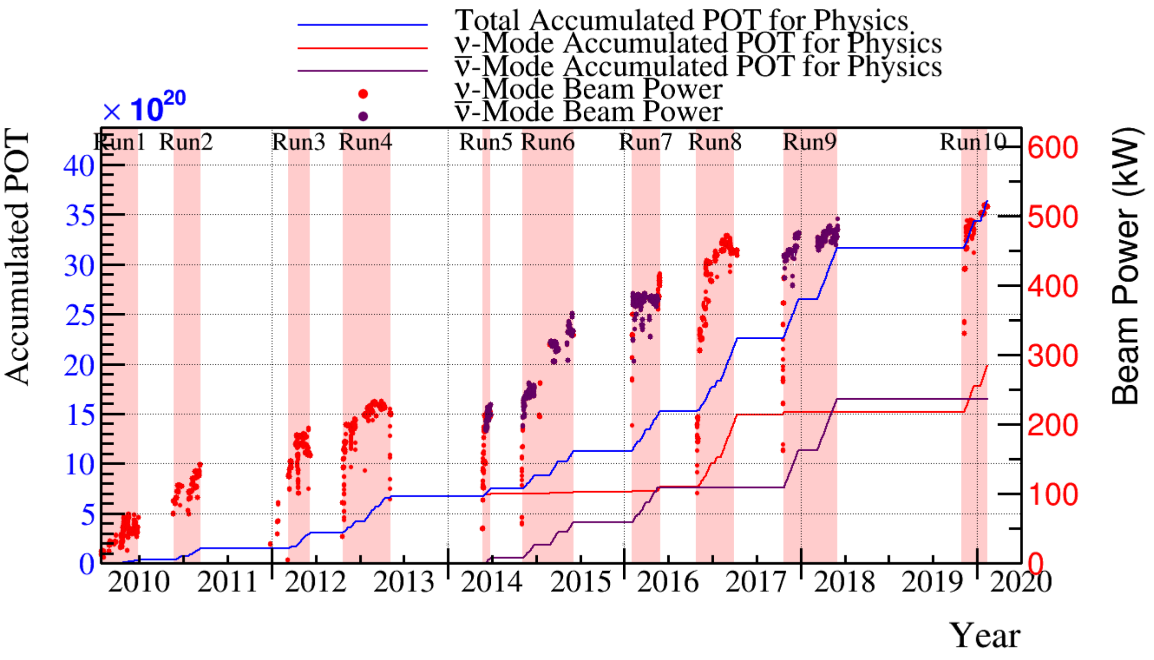

Figure 2.4: Delivered number of POT and beam power as a function of time.

the decay tunnel axis, the energy of the neutrino produced in the decay, E_ν, can be written as

$$E_\nu = \frac{m_\pi^2 - m_\mu^2}{2\left(E_\pi - p_\pi \cos\theta\right)} \tag{2.3}$$

where m_π and m_μ are the pion and muon masses, p_π is the pion momentum, and $\cos\theta$ is the direction of the neutrino with respect to the pion (for a pion along the tunnel axis, this is also the angle of the neutrino in the lab frame). Using the fact that

$$p_\pi = \sqrt{E_\pi^2 - m_\pi^2} \tag{2.4}$$

we can compute the derivative of the neutrino energy in Eq. (2.3) with respect to the pion energy E_π at constant θ:

$$\begin{aligned}
\left.\frac{dE_\nu}{dE_\pi}\right|_{\theta=\text{const.}} &= \left.\frac{dE_\nu}{d\left(E_\pi - p_\pi \cos\theta\right)}\right|_{\theta=\text{const.}} \left.\frac{d\left(E_\pi - p_\pi \cos\theta\right)}{dE_\pi}\right|_{\theta=\text{const.}} \\
\left.\frac{dE_\nu}{d\left(E_\pi - p_\pi \cos\theta\right)}\right|_{\theta=\text{const.}} &= \frac{m_\mu^2 - m_\pi^2}{2\left(E_\pi - p_\pi \cos\theta\right)^2} \\
\left.\frac{d\left(E_\pi - p_\pi \cos\theta\right)}{dE_\pi}\right|_{\theta=\text{const.}} &= 1 - \frac{E_\pi \cos\theta}{\sqrt{E_\pi^2 - m_\pi^2}} = 1 - \frac{E_\pi \cos\theta}{p_\pi} \\
\left.\frac{dE_\nu}{dE_\pi}\right|_{\theta=\text{const.}} &= \frac{m_\mu^2 - m_\pi^2}{2\left(E_\pi - p_\pi \cos\theta\right)^2}\left(1 - \frac{E_\pi \cos\theta}{p_\pi}\right).
\end{aligned} \tag{2.5}$$

The derivative vanishes for a certain pion energy E'_π such that

$$\begin{aligned} \left.\frac{dE_\nu}{dE_\pi}\right|_{\theta=\text{const.}} &= \frac{m_\mu^2 - m_\pi^2}{2\,(E'_\pi - p'_\pi \cos\theta)^2}\left(1 - \frac{E'_\pi \cos\theta}{p'_\pi}\right) = 0 \\ E'_\pi &= \frac{p'_\pi}{\cos\theta} \end{aligned} \tag{2.6}$$

and the neutrino energy reaches a maximum value $E_\nu^{\max}$ for a pion energy $E'_\pi = p'_\pi/\cos\theta$, corresponding to

$$E_\nu^{\max} = \frac{m_\pi^2 - m_\mu^2}{2E'_\pi \sin^2\theta}. \tag{2.7}$$

This implies that the energies of all neutrinos produced in the pion decay will be below $E_\nu^{\max}$. The effect is illustrated[1] in Fig. 2.5a. As a result, selecting an appropriate angle has the effect of peaking the flux around a chosen maximum energy. Since for T2K the appearance maximum occurs at 0.6 GeV, an off-axis angle of 2.5° was chosen. The impact on the T2K flux is shown in Fig. 2.5b.

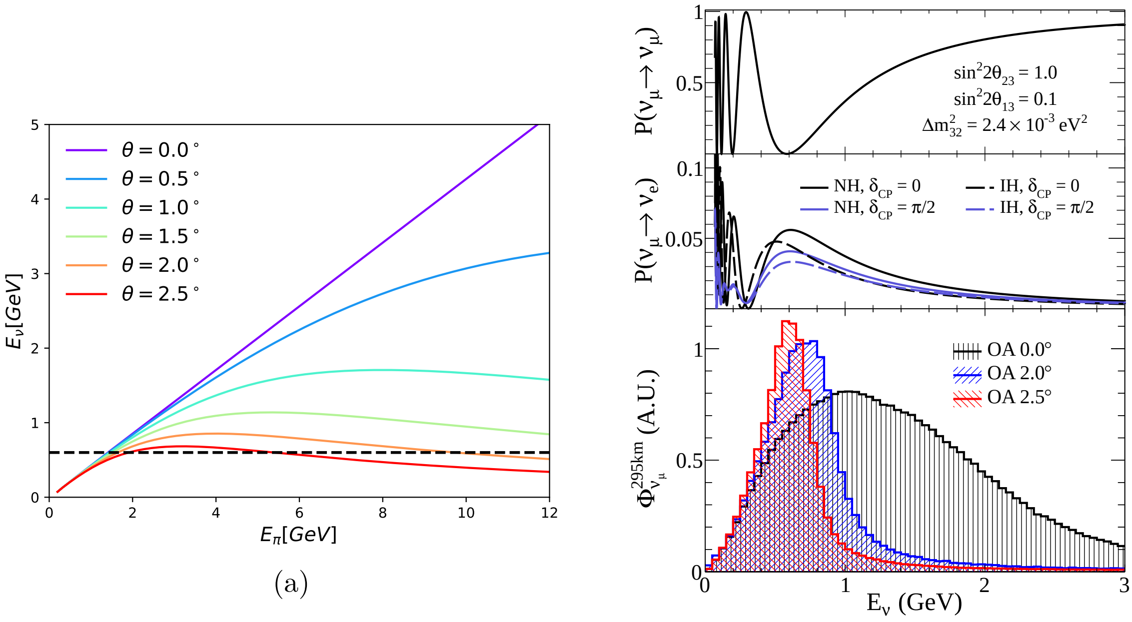

(a) (b)

Figure 2.5: Off-axis angles at T2K. (a) Neutrino energy as a function of pion energy for different angles. The black dashed line marks 600 MeV on the E_ν scale. (b) Oscillation probabilities (top) and T2K flux (bottom) as a function of neutrino energy, for different off-axis angles. Note that the fluxes have an arbitrary normalization, and in reality a higher off-axis angle suppresses the event rate with respect to the on-axis case.

The off-axis angle strategy is optimal for three main reasons:

- Such a position peaks the muon neutrino flux at energies around 600 MeV.

---

[1] Note that in Fig. 2.5a the maximum neutrino energy is not *exactly* 0.6 GeV, due to the fact that the approximate treatment described here only considers neutrinos coming from pions.

- This value of off-axis angle greatly reduces the spread of the spectrum, which is useful because the spectrum is focused not only at the oscillation maximum, but also in the region dominated by quasi-elastic interactions (described in Section 2.4.2), where the energy reconstruction using lepton information only is more precise.
- This angle reduces this intrinsic ν_e contamination in the beam, which is a source of background for the ν_e interaction signal events coming from oscillated ν_μ particles. The reason behind this reduction is that the ν_e contamination comes as a result of three-body decays, whereas the off-axis angle technique favors the results of two-body decays.

2.1.3 Flux composition and simulation

The precise measurement of event rates at both the near and far detector relies heavily on a good knowledge of the incoming neutrino/antineutrino flux.

There are three stages in the development of the T2K flux prediction. First, a Monte Carlo simulation of the proton interactions in the graphite target is generated using the FLUKA v.2011.2c.6 [67] package, which simulates the hadronic production chains inside the target, as well as re-interactions inside the target. Second, the outgoing secondary particles (mainly pions and kaons), are tracked using the T2K JNUBEAM software package throughout their propagation to ND280 and SK. JNUBEAM is a GEANT3-based [68] Monte Carlo simulation, used for propagating the particles exiting the target volume through the magnetic field generated by the horns described in Section 2.1.1. In addition, JNUBEAM also simulates re-interactions outside of the target volume using the GCALOR 1.05/04 [69] package. The choice of using FLUKA, rather than GCALOR, to simulate interactions inside the target volume was based on its better agreement with NA61/SHINE hadron production data. Finally, the simulated flux is tuned using hadron production data obtained at the dedicated NA61/SHINE [70] experiment at CERN.

The flux composition is illustrated in Fig. 2.6. As expected, the flux is largely dominated by ν_μ ($\bar{\nu}_\mu$) in FHC (RHC) mode.

However, non-negligible sources of background are present.

- In neutrino mode, the largest background is formed by $\bar{\nu}_\mu$ events - this is the wrong-sign background which could not be reduced by the magnetic horn selection. The ν_e and $\bar{\nu}_e$ components make up for less than 1% in the near detector flux in the peak of the distribution.
- In antineutrino mode, the wrong-sign contamination (i.e. ν in $\bar{\nu}$ beam) is larger, especially at higher energies. While some of this contamination comes from particles which were not properly focused with the magnetic horns, the main difference is due to the higher production multiplicities of positive, rather than negative, parent particles [71].

As SK is located far away from the neutrino beam production point, the predicted unoscillated flux at SK is significantly smaller than at the near detectors.

2.2 The Near Detector Complex

Before measuring the oscillated spectrum at the Super-Kamiokande detector, T2K uses a set of detectors to measure the spectrum before oscillations. Two detectors are used for this: INGRID

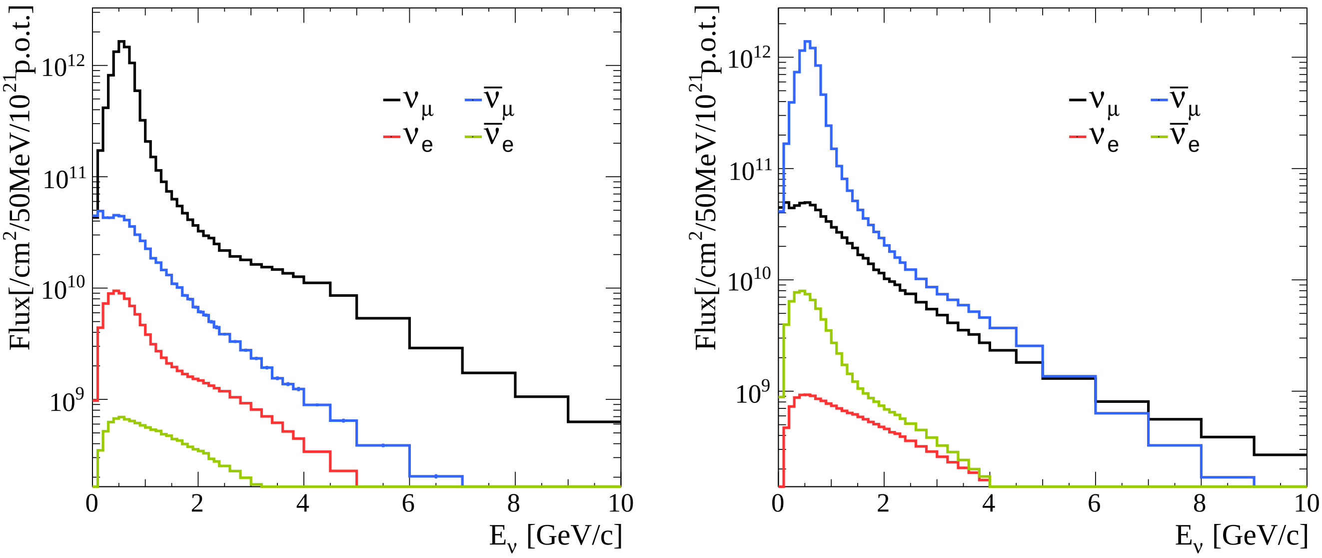

(a) Near Detector, Neutrino Mode

(b) Near Detector, Antineutrino Mode

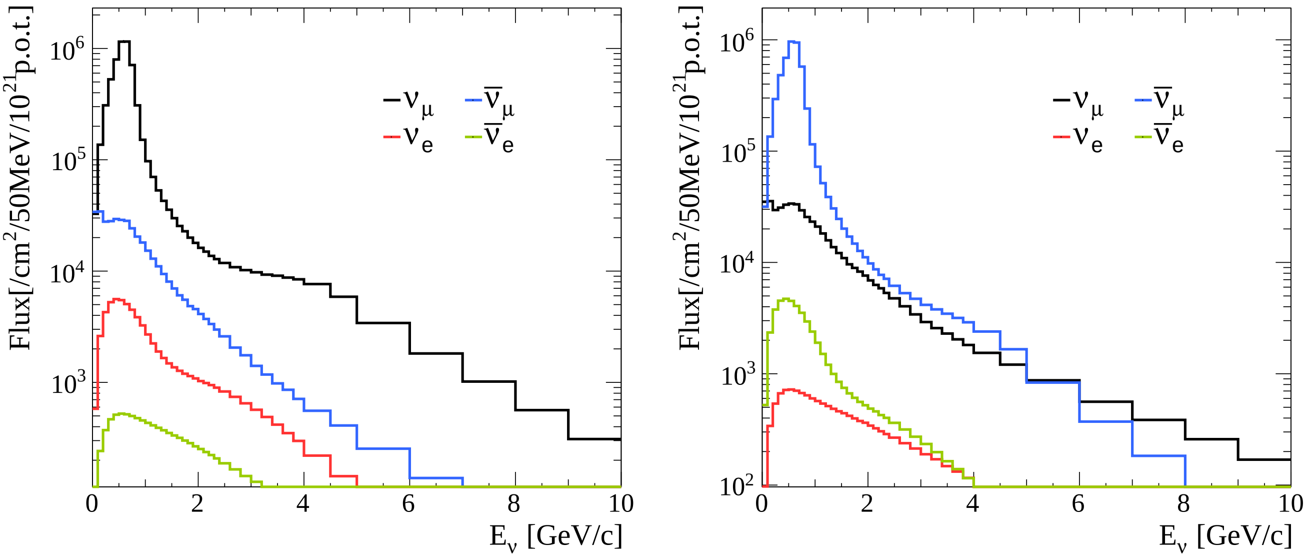

(c) Far Detector, Neutrino Mode

(d) Far Detector, Antineutrino Mode

Figure 2.6: Unoscillated T2K flux prediction and composition.

and ND280. They are both located in a pit 280 m away from the neutrino beam production point, and each serves a specific purpose. An overview of the two near detectors and their relative location in the pit is shown in Fig. 2.7

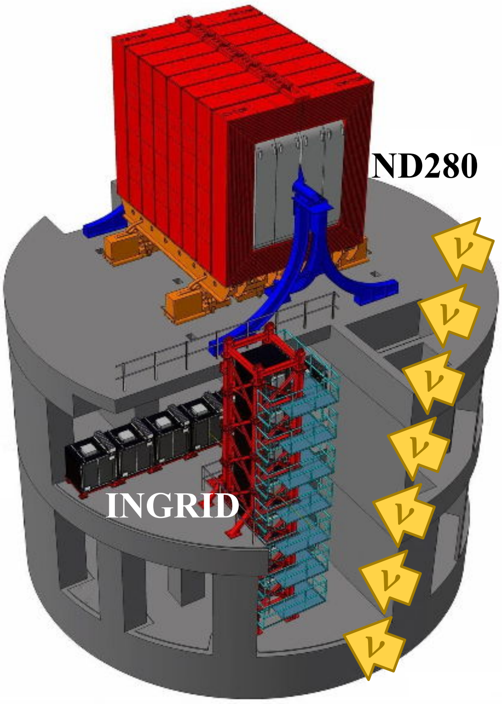

Figure 2.7: Location of INGRID and ND280 in the near detector pit. The neutrino flux is shown with yellow arrows.

2.2.1 The On-Axis Detector: INGRID

The Interactive Neutrino GRID (INGRID) is a neutrino detector centered on the neutrino beam axis. Its main purpose is to precisely monitor the beam position and intensity. A schematic representation of INGRID is shown in Fig. 2.8a. INGRID consists of 14 modules arranged in a cross shape (7 in each direction) perpendicularly to the neutrino beam. The beam center, at 0°, crosses the two central overlapping modules. Each module (Fig. 2.8b) is made up of 9 iron planes, sandwiched between 11 plastic scintillating planes. Each scintillating plane consists of two sub-planes of optically-isolated scintillating rods instrumented with wavelength shifting fibers (WLS), which read out the scintillation light. The two scintillating bars are arranged horizontally and vertically, respectively. Each module is surrounded by an extra set of veto scintillating planes, whose role is to reject interactions occurring outside of a module.

The INGRID detector samples a 10 m×10 m section of the neutrino beam[2]. The high density of the iron target planes makes it possible to collect enough neutrino interaction data in order to be able to monitor the beam position on a spill-by-spill basis.

INGRID is capable of monitoring the beam direction with a 0.2 mrad resolution, or a spatial resolution of 5 cm. A precise knowledge of the beam position and direction are essential in order to correctly predict the off-axis angle at the off-axis detector, ND280. INGRID data is in excellent

---

[2] The spatial spread at 280 m of the neutrino beam is of 5 m.

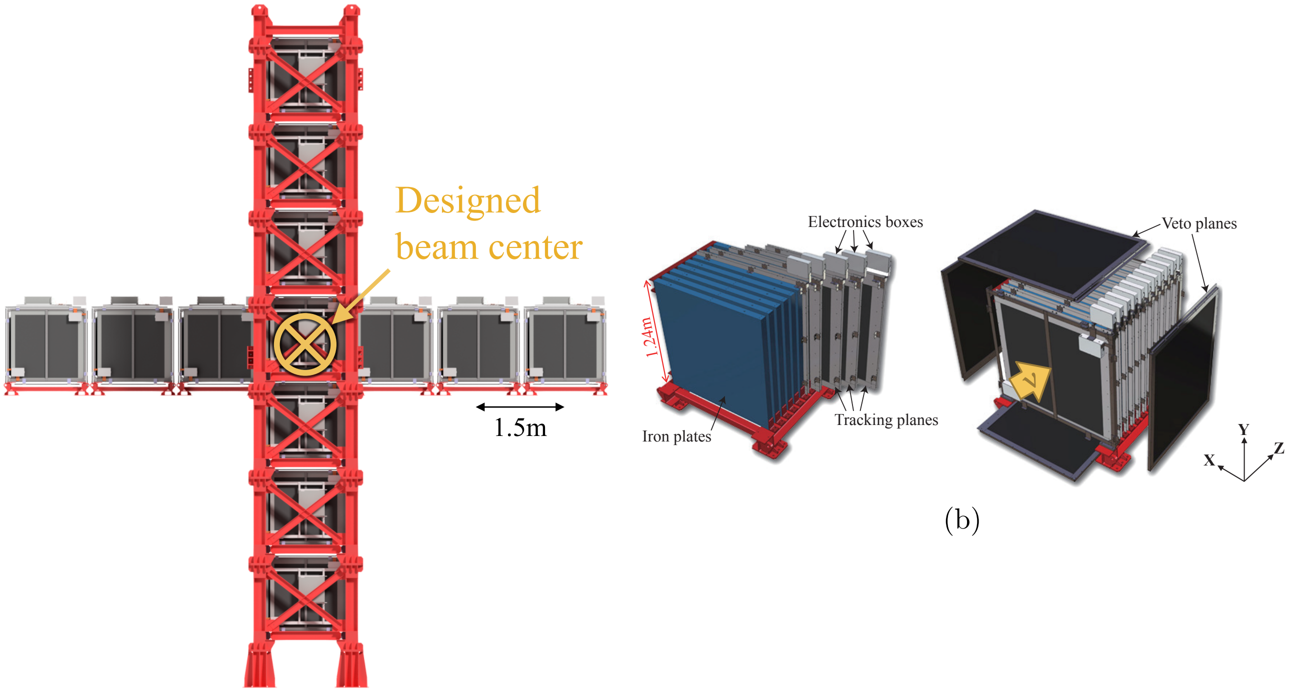

(a)

(b)

Figure 2.8: Overview of the INGRID detector (a) and an INGRID iron module (b).

agreement with MUMON data (within 0.2 mrad), as can be seen in Fig. 2.9.

An additional module, with no iron plates, was placed between the horizontal and vertical INGRID axes. This fully scintillating module, called the "proton module", is used to detect recoil protons together with muons, which are produced in neutrino interactions. The goal of the module is to perform cross-section measurements on carbon targets (since the plastic scintillators are mostly made of carbon).

In addition to precisely monitoring the neutrino beam and event rate, INGRID has been used in a number of neutrino cross-section measurements [72, 73].

2.2.2 The Off-Axis Detector: ND280

The ND280 detector is an off-axis (2.5°) complex set of sub-detectors which satisfies several physics goals for the T2K experiment. Its main purpose is to precisely measure the off-axis ν_μ flux, in order to predict the flux at the far detector. In addition, it is a magnetized detector, and as such it measures the wrong sign background in the flux, which is not possible at the far detector, Super-K. The ND280 detector must also measure the intrinsic ν_e component of the beam, in order to constrain this irreducible background for the ν_e appearance channels. Finally, it is able to precisely reconstruct the exclusive final states of $\nu_\mu/\bar{\nu}_\mu$ interactions, and as a result its data is used as one of the main inputs in the oscillation analysis in order to constrain the neutrino flux and interaction systematic effects.

A schematic view of the ND280 detector is shown in Fig. 2.10. The detector consists of a tracker comprised of three types of sub-detectors: a sandwiched structure of fine-grained scintillating targets (FGDs) and gaseous time projection chambers (TPCs), with a π^0 detector (P0D) in the upstream

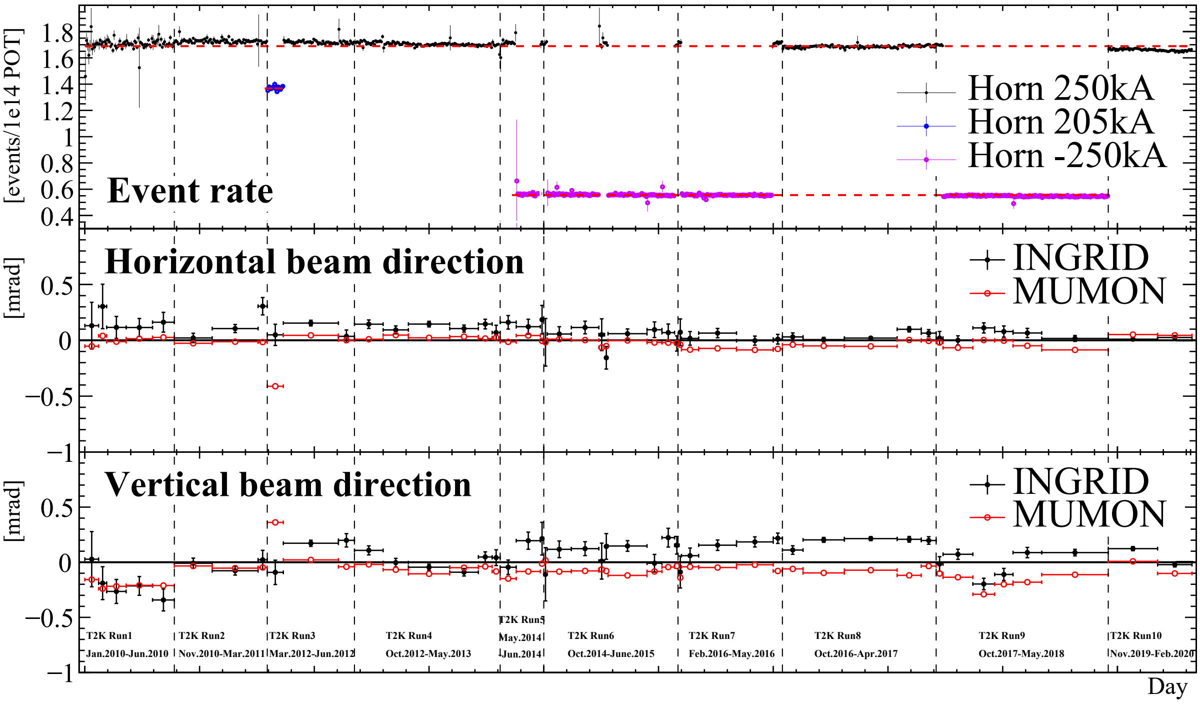

Figure 2.9: Beam position and event rate as a function of time, as measured by INGRID and MUMON.

part of the tracker. The tracker is surrounded by electromagnetic calorimeters (ECal), and placed inside a magnet yoke instrumented with scintillating detectors acting as a side-muon tracking device (SMRD).

The ECal which surrounds the ND280 tracker is a scintillator-based calorimeter, consisting of three components: the barrel ECal (surrounding the FGD+TPC section of the tracker), the downstream ECal (placed at the downstream end of the third TPC) and the P∅D ECal, surrounding the P∅D detector. As a result, the ECal ensemble offers near hermetic coverage of the ND280 tracker. The ECal is made of scintillating active material interleaved with lead absorber plates. Its function is to complement the tracker reconstruction process, by detecting photons, measuring their energy and direction, as well as by detecting charged particles and separating them by their shower patterns.

The ND280 tracker and the ECal is surrounded by the re-purposed UA1 magnet [62] from CERN, which was also used in the NOMAD experiment. The magnet provides a 0.2 T magnetic field, which makes it possible to identify particle charges based on their track curvature. The magnet consists of water-cooled aluminum coils which create a horizontally oriented dipole field, and a flux-return yoke. The dimensions of the inner volume of the magnet are of 7.0m×3.5m×3.6m, which limits the size of the P∅D +FGD+TPC tracker. The magnetic field created by the magnet is known with a precision of 2×10^{-4} T.

The magnet yoke is additionally instrumented with 440 horizontal and vertical scintillator modules [74] which are inserted in 1.7 cm air gaps between 4.8 cm thick steel plates which make up the UA1 magnet flux return yokes. The ensemble of these scintillator modules forms the Side Muon Range Detector (SMRD). The SMRD is used to veto tracks coming from interactions in the magnet and the surrounding cavity walls and to trigger on cosmic ray muons useful for calibration purposes.

In the upstream part of the tracker there is a dedicated π^0 detector, called the P∅D. It consists of tracking planes of scintillator bars, interleaved with lead or brass sheets. The purpose of the

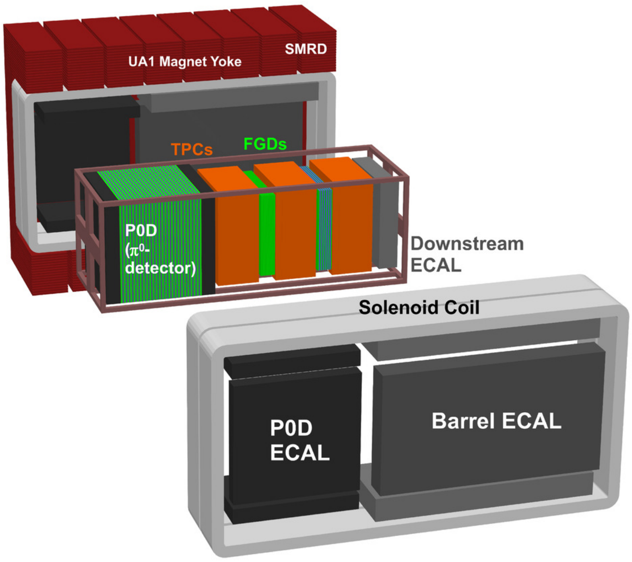

Figure 2.10: Exploded view of the ND280 detector.

PØD is to measure neutral current neutrino events on a water target, by measuring the produced π^0 particles. As such, the planes of scintillator bars are additionally interleaved with fillable water target bags, which enables water cross-section measurements by subtracting the cross-section on carbon obtained with the FGD1 target.

The FGD and TPCs constitute the main tracking devices used in the analyses presented in this thesis, and will be described in more detail in the following sections.

2.2.2.1 Fine Grained Detectors (FGDs)

T2K uses two fine-grained detectors (FGDs) [75] as the main target for neutrino interactions in the ND280 tracker. The FGDs are sandwiched between three TPCs and located in the tracker region of the detector. Each FGD has an active mass of 1.1 t, driven mainly by the required amount of statistics for neutrino oscillation and cross-section measurements.

The FGDs are located in the center of the tracker (FGD1) and more downstream along the tracker region (FGD2). Both FGD1 and FGD2 share the same detector technology. Both FGDs are made of 9.61 mm×9.61 mm×1864.3 mm bars of extruded polystyrene scintillator, which are oriented perpendicular to the beam in either the x or y direction (with z being the beam direction). Each scintillator bar is instrumented with a wavelength-shifting fiber (WLS) for optical readout of the scintillation light produced in neutrino interactions. FGD1 consists of 5760 scintillator bars, arranged into 30 layers of 192 bars each (called “XY modules”), with each layer oriented alternatingly in the x and y directions perpendicular to the neutrino beam. As a result, the light collected in two consecutive perpendicular bars makes it possible to determine the track position. FGD2 uses a similar detection technology, with an important additional feature - instead of having 15 plastic scintillator XY modules, FGD2 has 7 scintillator XY modules, and the 2.5 cm spaces between the modules are filled with water bags. As a result, FGD1 provides an entirely hydrocarbon-based target, whereas FGD2 is a hybrid water-hydrocarbon interaction target. The T2K near detector data is used in the oscillation analysis in order to constrain the data at the far detector. In order to minimize systematic errors related to neutrino interactions on different nuclear targets, the near de-

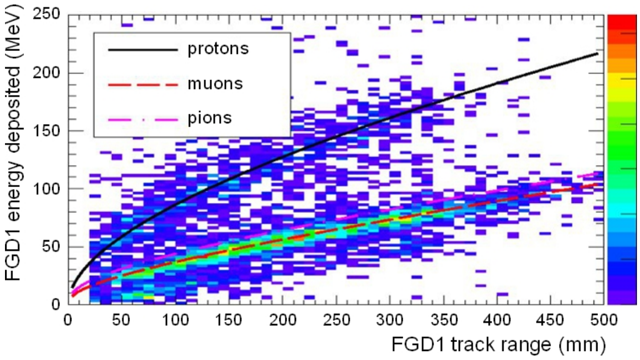

Figure 2.11: Total deposited energy in FGD1 as a function of the track range, compared to MC predictions (solid, dashed and dot-dashed lines). Figure taken from [75].

tector target needs to be close to that at the far detector (water, at Super-K). Carbon has an atomic number close enough to that of oxygen, and is widely used to fabricate scintillating detectors, so is represents a good compromise. The water layers in FGD2 make it possible to measure interactions occurring on water targets directly, thus reducing the systematic errors related to carbon/oxygen differences.

In addition to providing a target for neutrino interactions, the FGDs serve the purpose of tracking particles from their interaction vertex. Due to the small size of FGDs in the direction parallel to the beam (36.5 cm), particle tracks are most often reconstructed with the TPCs, which have better momentum resolution and particle identification (PID) capabilities. However, low momentum or high angle particles do not always escape the FGDs, and do not reach the TPCs. For such fully-contained tracks, the momentum cannot be measured using the track curvature, as done by the TPCs, since the tracks are too short to provide an accurate spatial resolution. Instead, this is done using the momentum-by-range method. The particle momentum is calculated by summing the energy deposits from its stopping point in the FGD[3] until the interaction vertex. In a similar way to the TPCs, the FGDs can identify the particle ID based on the deposited energy along its expected track range. The performance of FGDs in terms of PID is illustrated in Fig. 2.11: the FGDs are, in particular, capable of distinguishing protons from muons and pions. The FGD PID algorithm uses the total deposited energy and the length of the track, and infers the particle ID based on the MC expectations.

Additionally, particles in the TPC are traced back and matched to FGD tracks in order to determine the interaction vertex.

2.2.2.2 Time Projection Chambers (TPCs)

There are three T2K Time Projection Chambers (TPCs) [76], which alternate with the two FGDs and the P0D in the following order: P0D-TPC1-FGD1-TPC2-FGD2-TPC3. The TPCs are an essential component of the ND280 tracker and serve three purposes.

- Track reconstruction - thanks to the magnetic field in the ND280 tracker, multi-particle events will produce tracks with different curvatures, determined by their charge and momenta. The TPCs have the capability to reconstruct the particle tracks in three dimensions, thus making it possible to distinguish the number of tracks and obtain high-purity neutrino interaction samples.

---

[3] Provided the particle indeed stops inside the FGD.

- Momentum measurements - thanks to the curvature of the track, particle momenta can be measured and used to reconstruct the unoscillated neutrino energy spectrum, prior to oscillations, which is an essential step in the oscillation analysis.

- Particle identification - by measuring the energy loss of charged particles as a function of their momenta, the TPCs are able to perform particle identification, which is particularly important for measuring the intrinsic ν_e contamination in the ν_μ beam, an irreducible source of background for neutrino oscillation analyses.

The general working principle of a TPC detector is as follows: a charged particle passes through the TPC chamber, which is filled with a gas in the case of T2K. Along its track, the particle ionizes the gas in the chamber, producing free electrons. The entire chamber is subjected to an electric field, and, as a result, the ionization electrons drift towards the anode, located at one end of the chamber. The anode usually has a read-out plane, which is used to image the track projection on the anode plane. In order to reconstruct the full, 3D track, an external trigger is used to mark the time when the track enter the chamber, and the time difference between the trigger and the moment when the charge is read out by the anode is used to reconstruct its position along the axis perpendicular to the anode plane. In addition, a magnetic field is applied to the chamber. This is done for two reasons - first, the magnetic field bends the charged particle tracks and makes it possible to measure their momentum and charge based on the track curvature; second, the magnetic field limits the diffusion of the drift electrons inside the chamber gas.

The T2K TPCs follow the general TPC operation principle described above, with one important improvement. Just before the anode, a micro-mesh is placed and an additional voltage is applied between the mesh and the anode. As a result, the electric signal is amplified near the anode, causing an electron avalanche to occur. This has the effect of amplifying the electric signal, for a precise anode readout. This principle is known as the MicroMegas technology [77], and T2K is the first full-scale experiment to use this technology. Fig. 2.12a summarizes the working principle of T2K TPCs, with a particular focus on the MicroMegas technology.

A schematic representation of a T2K TPC is shown in Fig. 2.12b. Each one of the three TPCs consists of an inner box, the field cage, contained inside an outer box. The space between the inner and outer boxes is filled with CO_2 gas, which is an electrical and chemical insulator. The inner box is filled with a Ar:CF_4:iC_4H_{10} (95:3:2) gas mixture, which was chosen for its high speed, low diffusion, and good performance with MicroMegas chambers [62].

The TPCs perform charge identification by looking at the energy loss per unit of distance in the TPC gas. Charged particles lose energy according to the Bethe-Bloch formula [79], which yields theoretical curves to which the TPC data can be compared. Fig. 2.13 shows that there is a clear separation between minimum ionizing particles (muons and pions) and electrons and protons. These curves are used to compute the likelihood that a track was produced by a specific particle, under four particle hypotheses: muons, electrons, pions and protons. The resolution on the dE/dx, the energy loss per unit distance, is of 7.8%±0.2% for minimum ionizing particles, better than the original 10% requirement [76]. The 10% requirement is driven by the need to separate electrons from muons with at least 4σ precision, and it can be seen in Fig. 2.13 that electrons lose about 40% more energy than muons, hence the requirement. The particle momentum is measured by looking at the curvature radius of tracks under the influence of the magnetic field, $\vec{B}$, created by the UA1 magnet. The magnetic field exerts a Lorentz force on charged particles entering the TPC, and it is

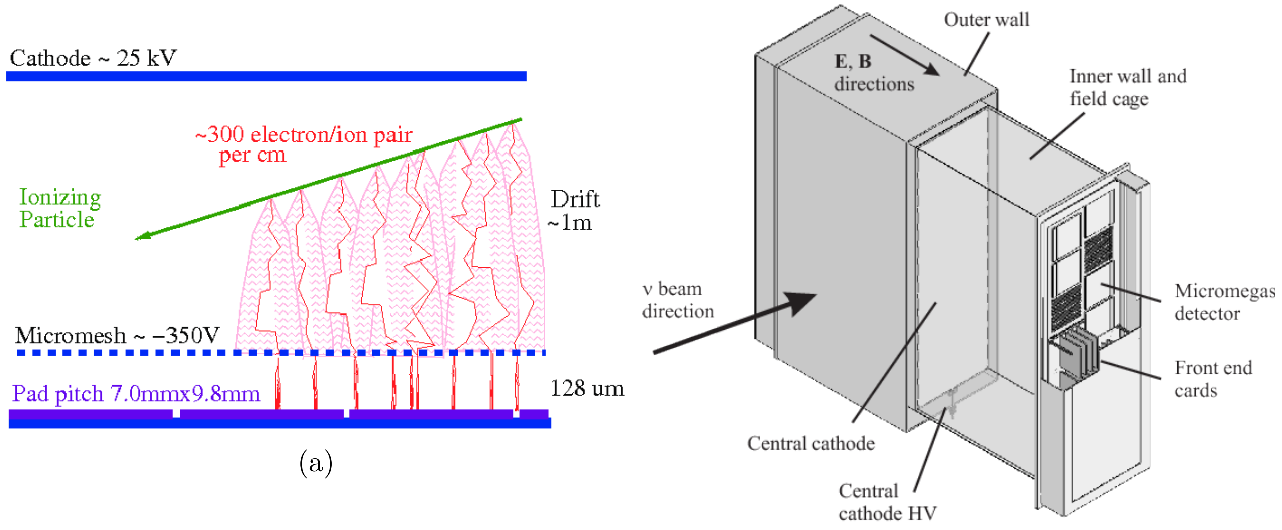

(a) (b)

Figure 2.12: (a) Illustration of T2K TPCs operation principle, along with MicroMegas technology, taken from [78]. (b) Schematic view of T2K TPC, with labeled components. Figure taken from [62]

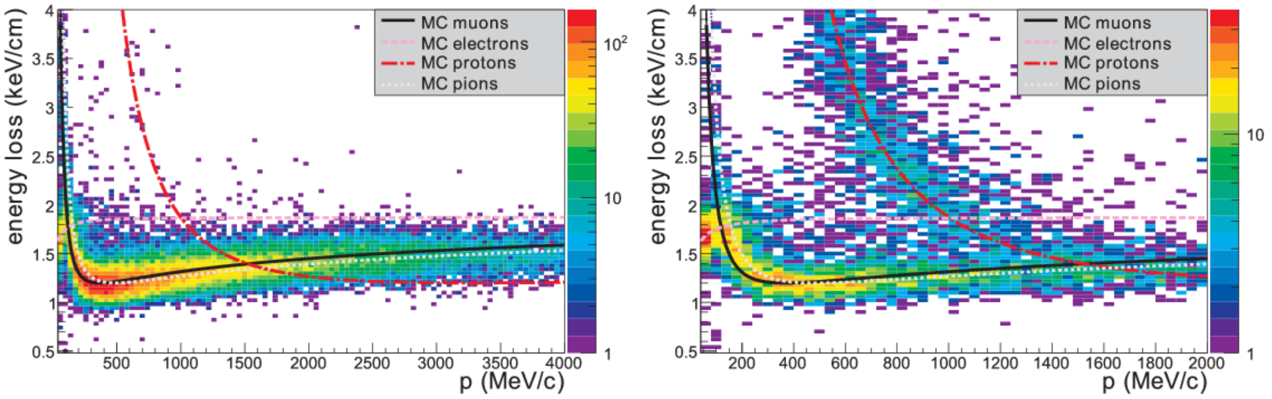

(a) (b)

Figure 2.13: Comparison of theoretical curves (solid, dashed and dot-dashed lines) to TPC data, for energy loss as a function of particle momentum. (a) negatively charged particles. (b) positively charged particles. Figures from [76].

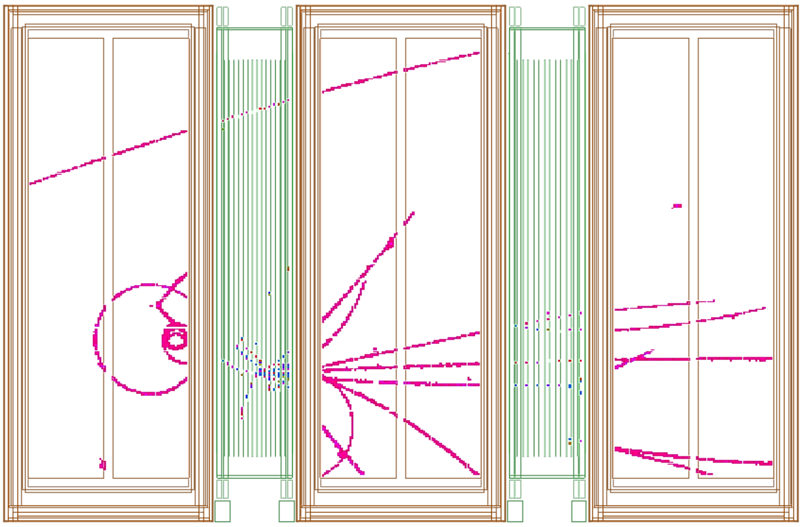

Figure 2.14: Example of an event recorded in the tracker section of the ND280 detector. One neutrino interacted upstream of the first TPC and produced a high momentum, single track. Another neutrino interacted in FGD1 in a highly inelastic way, producing multiple tracks in all three TPCs.

related to the track curvature by the relation

$$R = \frac{p_\perp}{zB} \tag{2.8}$$

in which R is the curvature radius of the track in meters, z is the charge of the particle in units of e, B is the magnetic field strength in Tesla, and $p_\perp$ is the transverse momentum of the particle in GeV/c (i.e. in the direction perpendicular to the magnetic field). The T2K TPCs have a transverse momentum resolution of 10% for particles with transverse momenta of 1 GeV/c, satisfying the requirements for the TPC momentum resolution performance.

The spatial resolution of the TPCs is between 0.6 mm and 0.7mm (depending on the drift distance) for straight tracks (i.e. tracks parallel to the MicroMegas pads) and degrades when the track angle increases. This is sufficient to achieve the momentum resolution required for the TPCs.

To illustrate the performance of the TPCs and FGDs in terms of track separation, Fig. 2.14 shows the tracks produced in a highly inelastic scatter in the FGD1. The TPCs are capable of resolving this complicated event topology, and the interaction vertex is clearly visible in the FGD. Note that most of the events used in the analysis do not usually have such a large number of tracks, as will be detailed in Section 2.4.

2.3 The Far Detector: Super-Kamiokande

The Super-Kamiokande (Super-K, SK) detector [80] serves as the far detector for the T2K experiment. It is located 295 km away from the neutrino production point at J-PARC, in the Kamioka mine, under Mt. Ikeno, in the Gifu prefecture of Japan. As a result, it has a rock overburden of 1000 m, corresponding to roughly 2700 meters-water-equivalent (m.w.e.), providing significant shielding from cosmic ray backgrounds. A sketch of the detector's location in the mine is presented in Fig. 2.15. SK is a water Cherenkov detector, meaning that is uses the Cherenkov radiation emitted by particles to reconstruct their momenta and directions. Simply put, the Cherenkov effect is

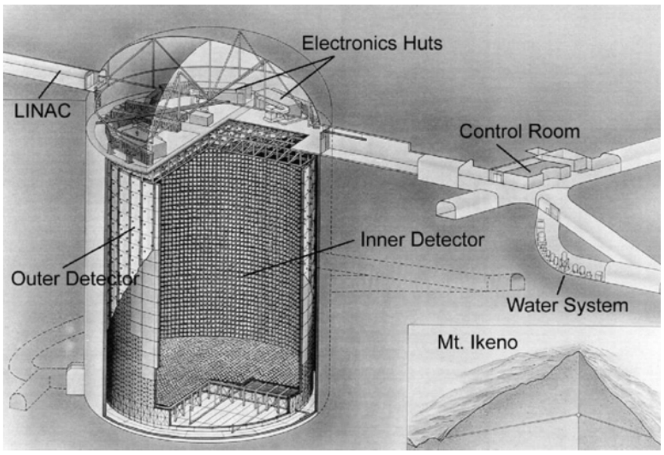

Figure 2.15: Schematic cross-section representation of the Super-Kamiokande detector and its location in the Kamioka mine. Figure from [81].

analogous to the supersonic effect for acoustic waves. When a particle travels faster than the speed of light in a dielectric medium (such as water), it emits Cherenkov radiation in the form of a light cone whose base is centered on the particle direction of propagation. The angle of the light cone, θ is related to the particle velocity v by

$$\cos\theta = \frac{c}{nv} \tag{2.9}$$

where c is the speed of light (in vacuum) and n is the refractive index of the medium.

To detect this type of light, SK consists of a stainless-steel tank, 39 m in diameter and 42 m tall, which is filled with 50 kton of ultra-pure water. The water serves both as an interaction target for neutrinos, as well as a medium for the propagation of the Cherenkov light. The detector consists of two regions: the inner detector (ID) and the outer detector (OD). The ID is lined with 11,146 inward-facing 20” photo-multiplier tubes (PMTs) and the OD has 1,885 8” outward-facing PMTs. SK has a 40% photo-coverage in the ID. The role of the ID PMTs is to capture the Cherenkov light emitted by particles inside the detector water, and thus gather signal events. The role of the OD is to provide a veto for particles originating outside of the detector, such as (rare) cosmic ray events, or products on interactions in the rock or detector material. To further shield the inner detector, a Tyvek and polyethylene layer is placed between the ID and the OD - its role is to both reflect light on the OD side, and to serve as an absorptive surface in the dead space between the ID and OD PMTs.

SK aims to identify neutrinos according to their flavor - i.e. electron or muon neutrinos, and it does so by looking at the products of neutrino interactions with the water in the ID. Neutrino interactions at T2K beam energies mostly occur through either charged or neutral currents (explained in more detail in Section 2.4). In charged current reactions, a ν_μ or ν_e exchanges a W boson with a nucleon in the target (neutron or proton), and the final state of the interaction is made of a lepton of the same flavor as the incoming neutrino (a muon for ν_μ, and electron for ν_e) and a nucleon. Cherenkov radiation can only be produced by charged particles, so neutrons cannot be identified using Cherenkov light[4] For charged particles to be able to emit Cherenkov radiation, their energy

---

[4] Neutrons can be detected through capture on nuclei such as Gadolinium. In such a process, the excited Gd nucleus after the neutron capture emits de-excitation photons. A distinctive signal of 4 de-excitation photons, which occurs at a precise time delay (depending on the Gd concentration) from when the lepton in an anti-neutrino

needs to be above a certain threshold, proportional to their mass. As a result, protons produced in neutrino interactions, which typically have energies of the order of a few hundreds of MeV, are well below their Cherenkov threshold of ∼1400 MeV, and thus cannot be detected by SK. As a result, only muons and electrons have a low enough Cherenkov threshold and are thus the main charged particles detected at SK. Charged particles can be produced in the final state of both charged and neutral current neutrino interactions, but in the case of neutral current interactions the neutrino flavor is uncorrelated with the final state particles and cannot thus be measured. As a result, in order to tag the neutrino flavor and thus observe neutrino oscillations, SK looks for charged-current interaction products. The leptons from these interaction are directly related to the neutrino flavor, and it is important to distinguish between Cherenkov rings coming from electrons and muons[5].
To distinguish between electrons and muons, SK looks at the “fuzziness” of the Cherenkov rings, two examples of which are shown in Fig. 2.16. Muons have a mass which is much larger than that of electrons (m_μ=105.6 MeV/c^2, m_e=0.511 MeV/c^2). Therefore, they are less likely to undergo scatters with the water in the tank, and as a result they produce clear, sharp Cherenkov rings (Fig. 2.16a). Electrons, on the other hand, undergo frequent scatters and produce electromagnetic showers, producing “fuzzy” rings (Fig. 2.16b), which are actually a superposition of the multiple rings generated in the scatters. From the timing information, it is possible to reconstruct the interaction vertex.

It should be noted that SK is not a magnetized detector, and as a result it cannot measure particle charge. An electron-like event, for example, may therefore come from either an electron, or a positron. For this reason, T2K relies heavily on information from the magnetized ND280 detector and J-PARC beam information, in order to estimate the size of wrong sign background.
In addition to serving as the far-detector for the T2K physics program, the Super-Kamiokande

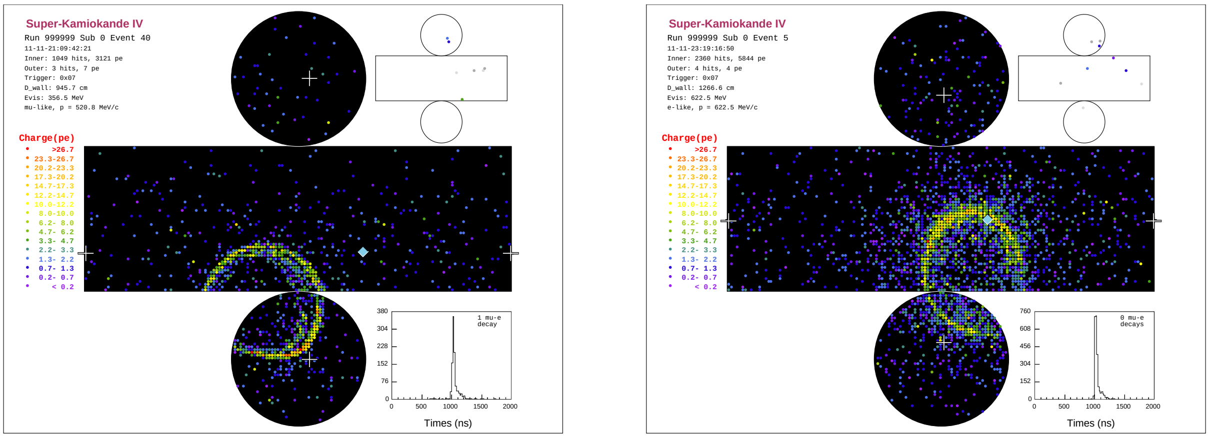

(a)

(b)

Figure 2.16: Examples of SK event displays for two types of rings. (a) Muon-like event. (b) Electron-like event. The squares represent PMT modules in the ID, the color of each square gives the amount of charge in units of photo-electrons (p.e.).

---

interaction with an initial state proton occurs, can be used to tag neutrons. For this reason, SK has begun loading its water with gadolinium salt. It is also possible to tag neutrons via capture on hydrogen, and this has been used in Super-Kamiokande Supernova Relic Neutrino searches (see e.g. [82]).

[5] A τ lepton has a very high Cherenkov threshold of 2.7 GeV, completely unattainable at T2K energies.

detector (and, by extension, the Super-Kamiokande collaboration), has a rich physics program of its own. It has notably built on the experience of its scientific predecessors, Kamiokande and IMB [39]. Super-K performs atmospheric neutrino oscillation measurements, solar neutrino flux measurements, as well as searches for proton decay and supernova neutrinos.

2.4 Neutrino interactions at T2K

In a neutrino oscillation experiment such as T2K, the oscillation parameters are measured by looking at the oscillated neutrino spectrum at the far detector. In practice, the spectrum is measured by detecting products of neutrino interactions with the nuclei forming the detector target (water at SK). The measured neutrino event rate will thus be the result of a convolution of the neutrino oscillation probability with the neutrino flux, which gives the number of available neutrinos, and the neutrino interaction cross-section, which shows how likely it is that a neutrino of a given energy will interact with the detector material. Apart from the SK detector resolution and mis-identification probability, the knowledge of the neutrino flux (i.e. the range of available neutrino energies and the rate of neutrinos produced) and the neutrino interaction cross-section (i.e. what the interaction probability is and how it changes as a function of neutrino energy) represent two of the largest sources of systematic uncertainty in the measurement of neutrino oscillation parameters [83]. In order to reduce these systematic errors, T2K uses its near detector, ND280, to measure the neutrino spectrum before oscillations. The near detector spectrum is then modified under the effect of expected oscillation probabilities, and is used to predict the spectrum at the far detector. The correct extrapolation between near and far detector relies heavily on a good understanding of the neutrino flux and neutrino interactions with matter. The flux model is built with the help of external hadron production data from the NA61/SHINE experiment (described in more detail in Section 3.3.1), whereas the neutrino interaction model relies on the current knowledge of neutrino interactions with matter.

Neutrino interactions are broadly categorized into charged-current (CC) interactions, mediated by the charged $W^{\pm}$ boson, or neutral current (NC) interactions, mediated by the neutral Z boson. Most neutrinos will interact with nuclei via CC interactions (as opposed to neutrino-lepton scatters via neutral or charged currents which are even rarer processes). The simplest type of interactions of neutrinos with nucleons (elastic scatters) are illustrated in Fig. 2.17, at the tree diagram level. In neutrino oscillation experiments, the goal is to identify the incoming neutrino flavor by its final state products. In Fig. 2.17a, it is clear that this can be done for CC interactions, whereas in NC interactions (Fig. 2.17b) there is no outgoing lepton which would allow us to identify the neutrino flavor. As such, CC interactions constitute the signal at SK, whereas NC interactions are a source of background for neutrino oscillation parameter measurements.

The Feynman diagrams in Fig. 2.17 are very simple, but in reality, nucleons are almost never isolated. They are bound in complex nuclei, and are thus prone to a plethora of "nuclear effects". These include, but are not limited to, the Fermi motion (i.e. the movement of nucleons inside the nucleus), correlations between the target nucleon and surrounding spectator nucleons, and the re-interaction of ejected hadrons within the nucleus. The types of interactions neutrinos can undergo with matter depend on the incoming neutrino energy, as shown in Fig. 2.18. Each type of interaction will be detailed in this section.

An important thing to note is that since the Cherenkov threshold for protons is very high, SK

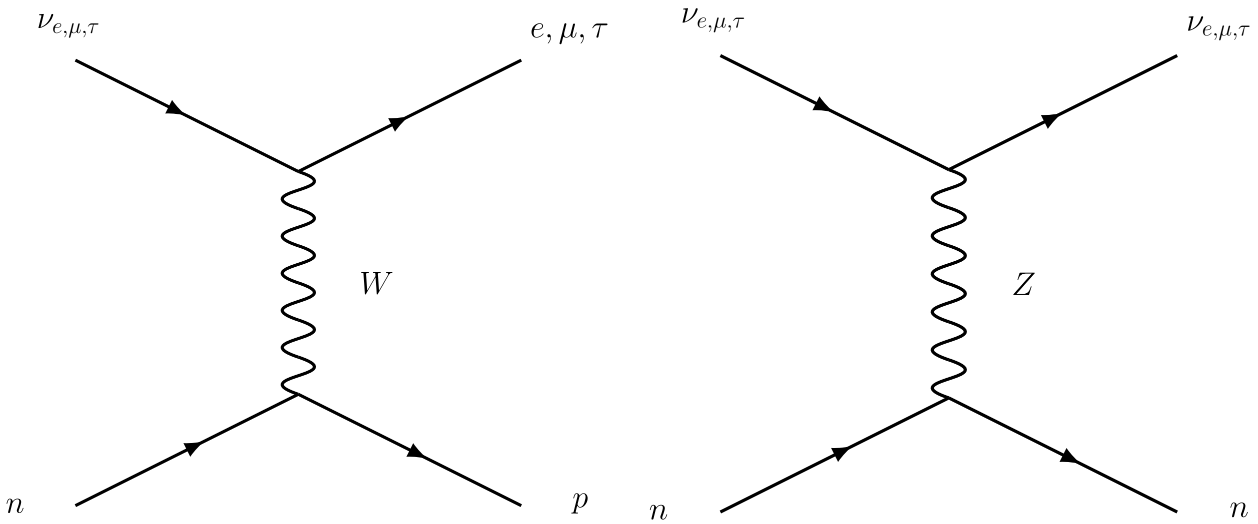

(a) (b)

Figure 2.17: Feynman diagrams for charged current (a) and neutral current (b) neutrino-nucleon (quasi-)elastic interactions.

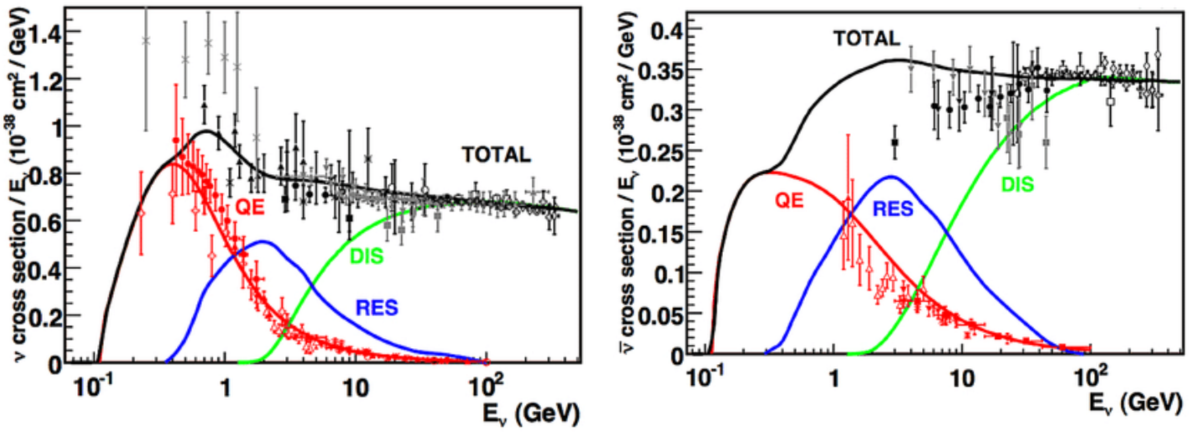

(a) (b)

Figure 2.18: Muon neutrino (a) and anti-neutrino (b) interaction cross-section as a function of neutrino energy. The data come from a number of sources, detailed in [84]. The solid lines show the prediction for the dominant types of charged-current interactions: quasi-elastic, CCQE (red), resonant pion production, RES (blue), deep inelastic scattering, DIS (green). Figure from [84].

cannot often detect final state protons in most of the neutrino interactions[6], and it cannot detect neutrons either. As a result, the neutrino energy spectrum is reconstructed using lepton kinematics alone. As shown in Fig. 2.18, the dominant type of interaction at T2K energies (peak at 600 MeV) is the charged-current quasi-elastic interaction (CCQE), which is the same as that shown in Fig. 2.17a, but bearing in mind that the initial state neutron is bound inside a nucleus and is thus not at rest. Since this is a two-body interaction, the neutrino energy E_{rec} can be reconstructed, assuming that the target nucleon is at rest and with some fixed removal energy, as

$$E_{rec} = \frac{m_p^2 - (m_n - E_b)^2 + m_l^2 + 2\,(m_n - E_b)\,E_l}{2\,(m_n - E_b - E_l + p_l \cos\theta_l)} \tag{2.10}$$

where m_p, m_n and m_l are the masses of the proton, neutron and lepton (muon or electron) involved in the interaction, p_l and E_l are the lepton momentum and energy, respectively, and E_b is the removal energy, or binding energy, i.e. the energy necessary to remove the bound nucleon from the nucleus[7]. It is worth noting here that any nuclear effect will introduce a bias in the reconstructed energy using Eq. (2.10).

Considering only lepton kinematics for the neutrino energy reconstruction is known as the "inclusive" approach. The downside of this method is that using lepton kinematics alone does not allow us to probe the full extent of nuclear effects, and therefore relies on inclusive model predictions. A more "exclusive" approach relies in measuring final state hadrons, for a more complete description of the final state of the interaction, and a more model independent type of analysis. There is ongoing work to expand the capabilities of the T2K near detector to achieve this type of analysis, some of which will be described in Chapter 6.

After an overview of the available nuclear ground state models, the following sections will briefly describe the most relevant interactions at T2K energies.

2.4.1 Nuclear ground state models

In order to provide predictions of the interaction cross-section as a function of muon kinematics, and in the absence of final state hadronic information, we rely on the availability of models which describe the initial state of the nucleon in the interaction. The motions of nucleons inside the nucleus, called Fermi motion, can be described using different assumptions, with equally different predictions on the nucleon kinematics.

The three most commonly used models to describe the initial nuclear ground state in neutrino interactions in the few-GeV regime are the Relativistic Fermi Gas (RFG), the Local Fermi Gas (LFG) (here discussed according to [85]) and the Spectral Function model by Benhar et al. [86]. Their predictions on the nucleon momenta in a carbon nucleus, obtained with the NuWro [87] event generator, are shown in Fig. 2.19.

The RFG model is the simplest of all nuclear models and has been widely used to model neutrino interactions, including by T2K, MINERνA and MiniBooNE. The nucleons inside the nucleus are treated as non-interacting fermions inside a nuclear potential, and the nucleons fill the available energy levels from the ground up. The highest-momentum level is known as the "Fermi energy",

---

[6] The Cherenkov threshold for a proton is of ~1.4 GeV.

[7] Note that all of these considerations can also be applied to anti-neutrinos. The main difference is that the anti-neutrino interacts with a proton and produces a neutron in the final state, and the final state leptons are the charge conjugates of those shown in Fig. 2.17a. Eq. (2.10) is then modified by swapping the neutron and proton masses.

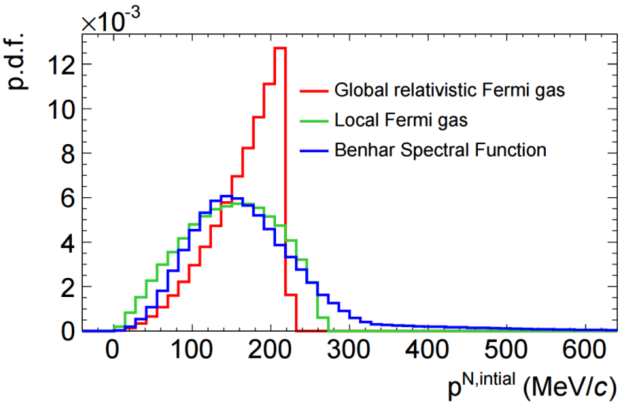

Figure 2.19: Comparison of initial state nucleon momentum prediction for the RFG, LFG and SF models. Adapted from [88].

or "Fermi momentum", and yields a sharp cut-off in the range of available energies, as can be seen in Fig. 2.19. The main shortcoming of this model is that it does not take into account interactions between fermions, and it also assumes that the nuclear density is flat inside the nucleus. This model has been used in all T2K oscillation analyses prior to the one described in this thesis.

LFG models account for local variations in nuclear density. In LFG models, the nuclear potential felt by a nucleon is assumed to vary as a function of the the radial position of the nucleon inside the nucleus. It can be seen as a continuum of RFG models, each with a different Fermi momentum determined by the local nuclear potential. As a result, in Fig. 2.19, the LFG model has a smoother prediction, but still does not address interactions between nucleons.

The most sophisticated of the three is the Spectral Function (SF) model, discussed here under the form presented by O. Benhar [86]. This model takes into account the shell structure of the nucleus, and is based on both electron-scattering data and theoretical calculations. A comparison of the nuclear ground state for the RFG and SF model is presented in Fig. 2.20. In the SF picture, the $1p_{1/2}$ and $1p_{3/2}$ nuclear shells are clearly visible as sharp lines at around 12 MeV and 18 MeV energy respectively, whereas the $1s_{1/2}$ shell is much broader, extending up to high energies.

2.4.2 Charged-current quasi-elastic process (CCQE)

The CCQE interaction is the dominant interaction channel at T2K energies, and the simplest to reconstruct. The Feynman diagram for such an interaction can be seen in Fig. 2.17a, but it is important to bear in mind that the initial state nucleon is in fact bound in a complex nucleus. The scatter of a neutrino off a single nucleon is also known as the one-particle-one-hole (1p1h) process, since a nucleon is struck from the nucleus and leaves a "hole". Since CCQE interactions are mediated by a W boson, the interaction occurs via vector and axial-vector currents. It is possible to parametrize the CCQE cross section using the Llewellyn-Smith approach [90]. The resulting cross section is a complex combination of terms accounting, on the one hand, for the individual nucleon taking part in the interaction via form factors pertaining to different currents, and, on the other hand, for the nuclear medium in which the interaction takes place, via a probability density of finding a nucleon with a certain momentum and binding energy. This type of parametrization gives access to experimental observables, which can be measured in a variety of experiments.

Electron-scattering experiments are of particular interest to the physics of neutrino nucleus interac-

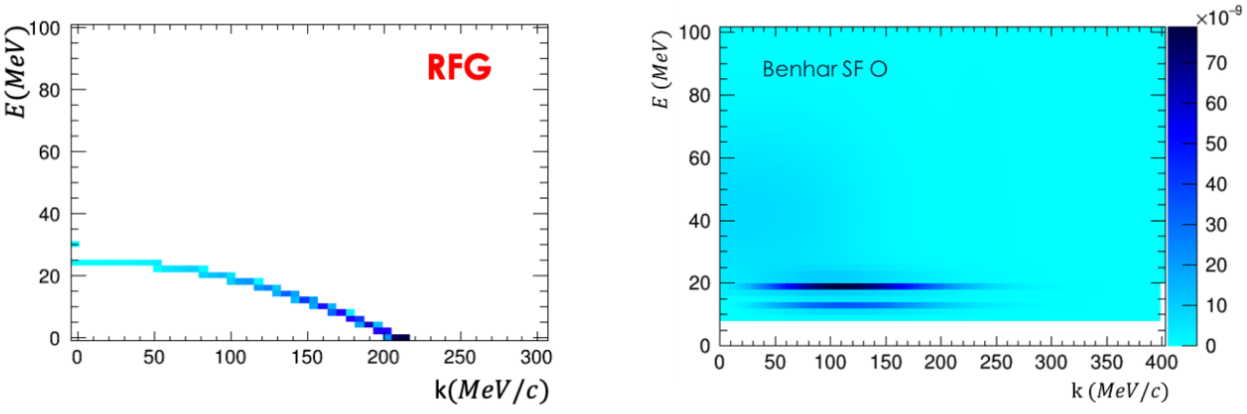

(a) (b)

Figure 2.20: Comparison of RFG (a) and SF (b) nuclear ground states for ^{16}O. k corresponds to the initial nucleon momentum while E is the nuclear removal energy used in the SF approach. Taken from [89].

tions. Since electrons and neutrinos are both leptons, they interact with nucleons in a similar way. The Feynman diagram of a quasi-elastic electron-nucleon scatter is the same as that presented in Fig. 2.17a, with an electron instead of the initial state neutrino, an electron in the final state, and mediated through a photon. The latter process thus takes place through a vector current, and, up to a scaling factor, it is identical to the vector part of the neutrino-nucleus cross-section. Measuring electron-nucleus scatters is thus of great interest, since, unlike neutrinos, electrons have a larger chance of interaction, thus providing enough statistics for accurate measurements. In addition, electron beams have a more narrow energy spectrum than neutrino beams. As a result, electron scattering experiments can be used to measure the vector part of neutrino-nucleon cross sections, and also to probe the structure of the nucleus (notably to extract the spectral function describing the nuclear ground state).

The axial part of the cross section depends on the the axial form factor[8] $F_A(Q^2)$:

$$F_A(Q^2) = \frac{F_A(0)}{\left(1 + Q^2 / \left(M_A^{QE}\right)^2\right)^2} \tag{2.11}$$

where Q^2 is the transferred four-momentum squared, $F_A(0)$ is the form factor at null transferred four-momentum, and M_A^{QE} is called the “nucleon axial mass”. The effect of this term on the cross-section is similar to that of an overall normalization (with some shape dependence). The value of M_A^{QE} had been determined by fits to bubble chamber data of neutrino scattering on deuterium and hydrogen targets (thus, light nuclei), and was thought to be close to 1.03 GeV/c^2 [92]. However, with the advent of heavy nuclei experiments, the value of M_A^{QE} gained a renewed interest from the neutrino physics community. This was due, in part, to the “MiniBooNE puzzle”. In the first measurement of the ν_μ CCQE cross-section, MiniBooNE [93] found a large discrepancy between the data and the cross-section predicted using the value of M_A^{QE} of 1.03 GeV/c^2 measured by bubble chamber experiments (Fig. 2.21). To correct for this discrepancy, the value of M_A^{QE} was inflated, in

---

[8] Eq. (2.11) assumes a dipole form factor. The dipole form factor has been known not to be in good agreement with data at large values of Q^2, and more sophisticated form factor models exist, such as the Z-expansion [91].

stark disagreement with the result of bubble chamber experiments.

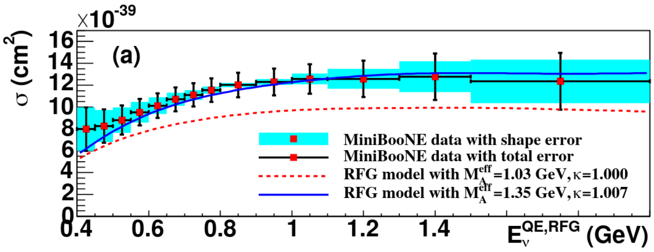

Figure 2.21: Flux-unfolded MiniBooNE ν_μ CCQE cross-section per nucleon as a function of neutrino energy. Predictions for different values of M_A^{QE} are compared. Adapted from [93].

2.4.2.1 Multi-nucleon (2p2h) interactions

There is increasing evidence that the MiniBooNE discrepancy is actually due to different processes, which have a similar signature to that of CCQE interactions. Recent models of neutrino-nucleus interactions include the possibility of neutrino scatters off correlated states states of two or more nucleons inside the nucleus. This is known as the n-particle-n-hole process (npnh), and the most common occurrence is for correlated states of two particles, i.e. the 2p2h process. Fig. 2.22 illustrates how one such model, by Nieves et al. [94], substantially improves the agreement with MiniBooNE data, while reducing the disagreement with the bubble chamber data value of M_A^{QE}.

There are multiple ways in which neutrinos can interact with two correlated nucleons, but they can all be broadly split into two categories: nucleon-nucleon correlations (NN) and meson exchange currents (MEC), in which a Δ resonance is formed. An interference between the two types of

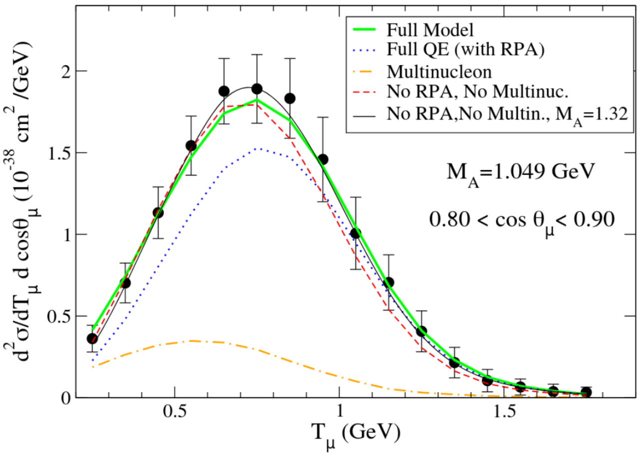

Figure 2.22: Flux-folded MiniBooNE data, compared to the model of Nieves et al. [5] (green). The different contributions to the model are shown separately: QE component with random phase approximation (RPA) corrections (blue dotted) and multi-nucleon contributions (orange dot-dashed). The predictions without multi-nucleon and RPA contributions are also shown for two values of M_A^{QE}: 1.049 GeV (red dashed) and 1.32 GeV (solid black). Except for the solid black line, all curves use M_A^{QE} =1.049 GeV. Figure from [5].

processes can also occur. Fig. 2.23 gives an overview of the different 2p2h channels. Multiple models have been proposed to describe 2p2h interactions [7, 94, 95, 96], with varying predictions on the relative amount of NN and MEC interactions. An overview of three 2p2h models is shown in Fig. 2.24, highlighting the large difference in cross-section predictions. Since 2p2h interactions have a similar final state as CCQE interactions, and given that in T2K the neutrino energy is reconstructed using lepton information only, incorrectly accounting for the presence of 2p2h interactions will produce a bias in the reconstructed neutrino energy spectrum. Indeed, this is shown in Fig. 2.25, and is a result of the fact that muon kinematics are altered with respect to the CCQE prediction.

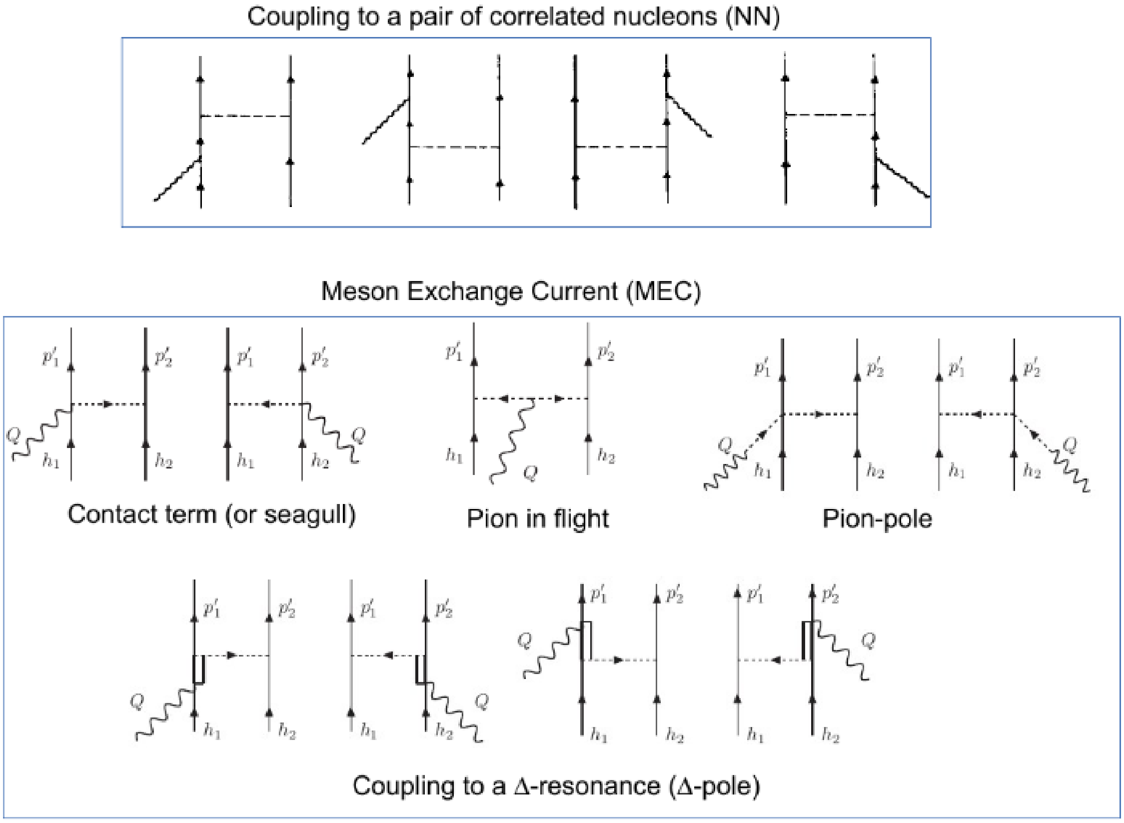

Figure 2.23: Feynman diagrams of NN and MEC interactions, adapted from [6] and [7]. Single lines represent nucleons, double lines represent the Δ resonances, dashed lines represent pions, and curly lines represent the W boson [89].

Our knowledge of multi-nucleon interactions is still limited, and no single model has been able to describe all of the available data. They are nevertheless a crucial part of a complete neutrino interaction model, and need to be accounted for.

2.4.3 Other interactions - CCRES, CCDIS and CCCoh

Neutrinos can interact with nucleons though other channels than CCQE and 2p2h interactions. The larger the available neutrino energy, the finer the nucleus structure is probed in the interaction. First the nucleus is probed in charged-current coherent interactions, which are essentially elastic for the nucleon. If the transferred energy to the nucleus is large enough to produce a resonance, then

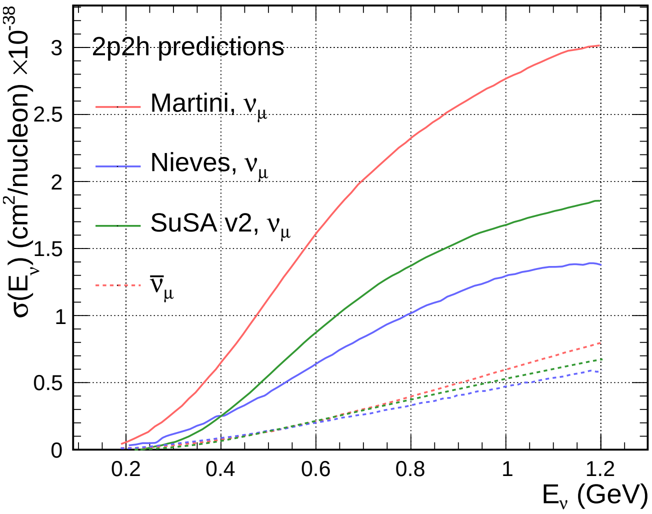

Figure 2.24: Comparison of 2p2h cross-section predictions as a function of true neutrino energy, from Nieves et al. [94], Martini et al. [95] and the SuSAv2 model [96].

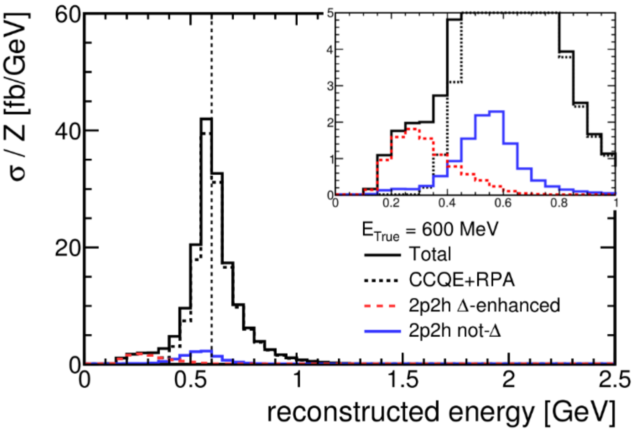

Figure 2.25: Reconstructed neutrino energy bias, for a true neutrino energy of 600 MeV. The contributions to the bias from NN ("2p2h not-Δ") and MEC ("2p2h Δ-enhanced") channels are shown in blue and red, respectively. Figure from [89].

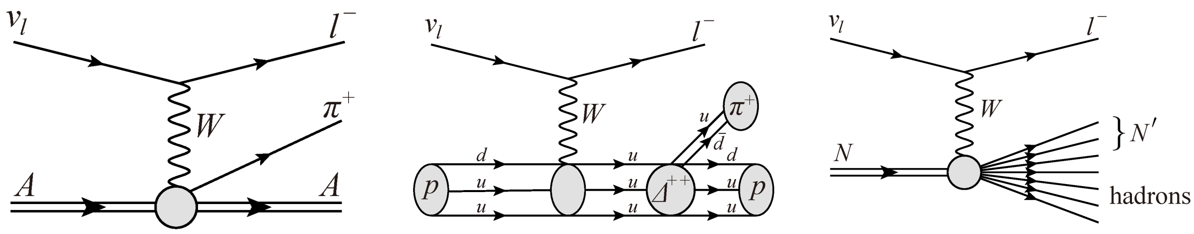

(a) CC-Coherent

(b) CC-Resonant

(c) CC-DIS

Figure 2.26: Feynman diagrams of non-CCQE charged current processes.

individual nucleons are probed through the production and subsequent decay of a Δ resonance, known as the charged-current resonant pion production channel (CCRES). Finally, when the neutrino energy is very large ($\mathcal{O}(10\text{ GeV})$) then the neutrino can resolve the quarks inside nucleons, in deeply inelastic processes (CCDIS).

These three processes are illustrated in Fig. 2.26. A coherent scatter happens when the neutrino scatters off the entire nucleus, without fragmenting it. Such a process can take place via neutral or charged currents. During such an interaction, a single pion is produced in the final state. These interactions are possible at low values of transferred four-momentum, and have small cross sections. As a result, they are rare at accelerator neutrino experiment energy levels. Such interactions are modelled with the Berger-Sehgal model [97].

When the center of mass energy in a neutrino-nucleus scatter is larger than the mass of a Δ baryon (1232 MeV/c^2), the interaction can produce a resonant state, as shown in Fig. 2.26b. Fig. 2.18 also shows that this is the dominant interaction mode in the 1.5-5 GeV range. The decay of the Δ baryon produces charged or neutral pions in the final state. Such interactions are modelled using the Rein-Sehgal model [98], which uses a similar formalism to the CCQE Llewellyn-Smith model [90], in particular in the use of nuclear form factors. There are two parameters describing the form factors, an axial mass, M_A^{RES}, similar to the M_A^{QE} axial mass for CCQE interactions, and C_5^A, which is the equivalent of $F_A(0)$ in Eq. (2.11). Unlike the CCQE form factor, the resonant pion production form factors cannot be easily determined from electron scattering experiments. It is important to note that the delta resonance is produced still inside the nuclear medium, and as a result the produced pion has a chance to be reabsorbed inside the nucleus. The observable final state topology of such an event is identical to that of a CCQE event, and it is therefore important to have a good understanding of resonant pion production processes.

Lepton kinematics in DIS processes are fully described with the Bjorken x and Bjorken y variables, which represent the fraction of the nucleon momentum carried by the quark involved in the interaction and the fraction of the neutrino energy transferred to the hadronic system, respectively. The interaction cross-section is calculated from ‘structure functions’, which in turn are calculated from ‘parton distribution functions’ (PDFs) which give the probability to find a quark of a given type with a given value of x inside the nucleon.

In addition, particles other than pions can be produced, such as kaons (K), etas (η) and gammas (γ).

2.4.4 Final State Interactions (FSI)

Final State Interactions (FSI) are subsequent interactions with the nuclear matter undergone by the particles produced in the final state of neutrino-nucleon interactions. At T2K energies, three types of final state particles are commonly produced: leptons (μ or e), nucleons (p or n), and pions (π). Each of these particles is prone to undergo FSI inside the complex structure of a ^{12}C or ^{16}O nucleus. At T2K energies, pion FSI is of particular importance, since the final state pion multiplicity is used to determine the samples used in the neutrino oscillation analysis. For example, a pion produced in a resonant decay should be reconstructed as a background event, not a signal CCQE event. However, if this pion undergoes absorption inside the nucleus (one probable outcome), the event will instead be reconstructed in a signal sample, and this will bias the reconstructed neutrino energy for CCQE samples which assume 2-body QE kinematics.

There are four main processes which pions can undergo inside the nucleus (illustrated in Fig. 2.27): absorption (ABS), in which the pion is absorbed inside the nuclear medium and does not escape the nucleus; charge exchange (CX or CEX), in which typically a charged pion scatters off a nucleon producing a neutral pion decaying into two photons; quasi-elastic scattering, in which the kinematics of the pion are modified (QE); and inelastic processes (INEL or Hadron Production), in which the original pion undergoes inelastic processes usually creating additional pions.

With the current detector configuration, which is able to detect pions with a relatively high efficiency, modeling pion FSI is one of the main priorities. However, as stated before, pions are not the only particles which can undergo FSI - protons and neutrons, in particular, are prone to such effects. The current proton momentum threshold in the ND280 detector is relatively high (400 MeV/c in proton momentum), but the upgrade of the ND280 detector (described in Chapter 6) will enable low momentum proton measurements at the T2K near detector. In preparation for this added capability, there is an ongoing effort to improve the description of proton FSI processes in neutrino event generators, as it will become an important source of systematic uncertainty when hadronic variables start being used in the T2K oscillation analysis.

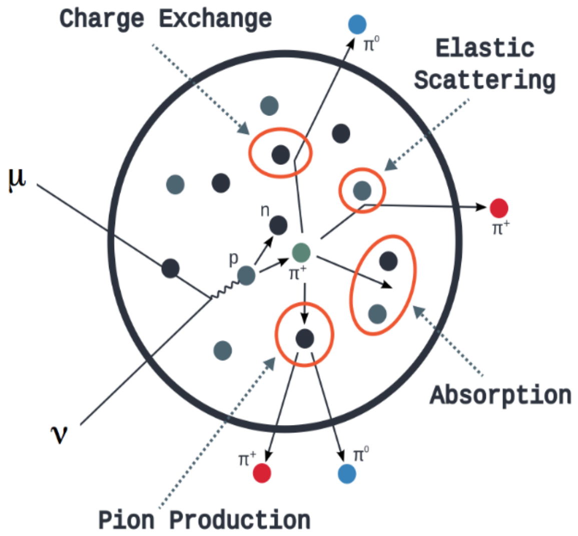

Figure 2.27: Schematic representation of different types of pion FSI. Taken from [99].

Chapter 3

The T2K Oscillation Analysis

One of the main goals of the T2K experiment is to measure the oscillation parameters $\sin^2\theta_{23}$, $\sin^2\theta_{13}$, Δm^2_{32} and δ_{CP}. This chapter describes the procedure and inputs used in the 2020 iteration of the T2K oscillation analysis (OA). This analysis has known many improvements since the previous one [61, 100] and was presented at the Neutrino 2020 conference as a T2K flagship analysis. The general structure of the different analysis strategies is described in Section 3.1. Section 3.2 describes the data used in the analysis, the Monte Carlo production, and the selection process applied to build the signal and background samples. Section 3.3 describes the systematic uncertainties, broken down into flux, cross-section and detector modelling uncertainties.

The oscillation analysis is a complex, multi-step process, and it is the result of extremely hard work from many people. In this chapter, my personal contribution is outlined in the near-detector implementation of a new nuclear ground state model and of dedicated systematic uncertainties regulating quasi-elastic and multi-nucleon neutrino interaction processes. The following chapter will describe in greater detail the near detector fit to data, for which I was one of the two analyzers for the near detector fit used in the 2020 results presented at the Neutrino 2020 conference[1].

3.1 Structure of the Oscillation Analysis

The T2K oscillation analysis extracts the neutrino oscillation parameters by performing a fit to the oscillated data at SK. In practice, this involves estimating the event rate at SK as a function of neutrino energy (after oscillation) and requires a good knowledge of the event rate at ND280 (before oscillation). The event rate at the near and far detectors can be written as a function of the true neutrino energy E_ν as:

$$N^{ND}_{\nu_\alpha}(E_\nu) = \Phi^{ND}_{\nu_\alpha}(E_\nu) \times \epsilon^{ND}(E_\nu) \times \sigma^{ND}_{\nu_\alpha}(E_\nu) \tag{3.1}$$

$$N^{FD}_{\nu_\beta}(E_\nu) = \Phi^{FD}_{\nu_\beta}(E_\nu) \times \epsilon^{FD}(E_\nu) \times \sigma^{FD}_{\nu_\beta}(E_\nu) \times P_{\nu_\alpha\to\nu_\beta}(E_\nu) \tag{3.2}$$

The ND and FD superscripts stand for Near Detector and Far Detector, respectively. Φ_{ν_α} represents the flux distribution of α-flavored (anti)neutrinos. $\epsilon(E_\nu)$ is the detector (ND280 or SK) efficiency to tag and reconstruct neutrino interactions at a given neutrino energy. σ_{ν_α} is a global cross-section function of all of the interactions ν_α particles can undergo. The α and β subscripts indicates generic neutrino flavors which can be detected at T2K (e, μ). The forms of Eq. (3.1) and Eq. (3.2) are identical up to the last term, $P_{\nu_\alpha\to\nu_\beta}(E_\nu)$, which gives the probability of oscillation from flavor α to flavor β as a function neutrino energy and at a given oscillation baseline.

Eq. (3.1) and Eq. (3.2) show that the event rate depends on three sources of effects in addition to the oscillation probability. The aforementioned flux, detector and cross-section terms are thus sources of systematic uncertainties which affect the outcome of the event rate measurement, and should be reduced or constrained as much as possible. T2K uses the data from the near detector to constrain these uncertainties at the far detector. The flux, detector and cross section uncertainties are parametrized by three sets of parameters, $\vec{b}, \vec{d}$ and $\vec{x}$, respectively, referred to as *nuisance parameters*, since they are not parameters of interest (unlike the set of oscillation parameters, hereby referred to as $\vec{o}$), but describe sources of systematic uncertainty on the final result. A detailed description of each set of nuisance parameters is provided in Section 3.3.

T2K performs the OA using three different fitting frameworks at the level of the far detector, called P-Theta, MaCh3 and VaLOR. P-Theta and VaLOR are semi-frequentist fitters, using gradient descent minimization (GDM) algorithms to find the best-fit points for the oscillation parameters, and then marginalize over nuisance parameters. The results are expressed in the form of frequentist confidence limits (C.L.) on the oscillation parameters. The main difference between P-Theta and VaLOR lies in the choice of the variable in the fit: VaLOR uses a two dimensional binning of the data in terms of E_{rec} (reconstructed neutrino energy) and θ (reconstructed outgoing lepton angle with respect to the incoming neutrino beam), whereas P-Theta has the possibility of using either a $p - \theta$ binning (lepton momentum and angle) or the aforementioned $E_{rec} - \theta$ binning. MaCh3 is a Bayesian fitting framework, which samples the parameter space using MCMC techniques and outputs posterior distributions for the parameters of interest. The oscillation parameter results are expressed as credible intervals (C.I.). At the far detector level, MaCh3 performs a one-dimensional fit of the data as a function of E_{rec}.

The three fitters have different ways of incorporating the near detector constraint in their frameworks: MaCh3 is in reality a simultaneous fit of near and far detector data, whereas P-Theta and VaLOR use the near detector constraints provided by a dedicated near detector fitting framework, called BANFF (standing for Beam And ND280 Flux extrapolation task Force). BANFF is a binned semi-frequentist fitting framework, and it uses a two dimensional binning in $p_\mu - cos\theta_\mu$ (i.e. reconstructed muon momentum and orientation with respect to the neutrino beam direction). Since MaCh3 performs a simultaneous ND-FD fit, it also fits the near detector data, and the choice of observable binning at the near detector is the same as in the case of BANFF. The features of each fitter framework are summarized in Table 3.1

	ND		FD		
	BANFF	MaCh3 (ND)	MaCh3 (FD)	P-Theta	VaLOR
Fit binning	2D $p_\mu - cos\theta_\mu$	2D $p_\mu - cos\theta_\mu$	1D E_{rec}	$p - \theta$ $E_{rec} - \theta$	2D $E_{rec} - \theta$
Stat. approach	Semi-freq.	Bayesian	Bayesian	Semi-freq.	Semi-freq.
Fit algorithm	GDM	MCMC	MCMC	GDM	GDM
	Treatment of ND		Joint ND-FD fit	BANFF	BANFF
	Treatment of syst. param.		Marginalization		
	Result		C.I.	C.L	C.L

Table 3.1: Summary of T2K fitting frameworks. The near detector systematic parameters which are not propagated as a constraint to the far detector fitters are marginalized over.

3.2 Selections and Monte-Carlo Production

3.2.1 Accumulated data

T2K has been taking data since 2010, in both neutrino- and antineutrino mode. The data are classified according to the period in which they were taken (*run periods* or simply *runs*). The oscillation analysis presented in this document uses ND280 data taken in runs 2 through 9, whereas runs 1 through 10 were used for the SK data.

Table 3.2 shows the accumulated data in units of 10^{19} POT accumulated at both ND280 and SK since the beginning of T2K data taking. Compared to the previous analysis [100], the SK data has increased by about 30%. The ND280 data was nearly doubled in neutrino mode, and nearly tripled in anti-neutrino mode.

Run	ND280 /10^{19} POT		SK /10^{19} POT	
	FHC	RHC	FHC	RHC
1	—	—	3.26	—
2	7.93	—	11.22	—
3	15.81	—	15.99	—
4	34.26	—	35.97	—
5	—	4.34	2.44	5.12
6	—	34.09	1.92	35.46
7	—	24.38	4.84	34.98
8	57.31	—	71.69	—
9	—	20.54	2.04	87.88
10	—	—	47.26	—
Total	115.31	83.35	196.63	163.44
Total×[100]	1.98	2.93	1.32	1.00
Combined Total	198.66		360.07	

Table 3.2: Collected data, expressed in units of 10^{19} POT at ND280 and SK, separated by beam magnetic horn polarity. The last row shows the ratio of the current amount of data with respect to what was used in the previous oscillation analysis [100].

3.2.2 Monte-Carlo Production

The neutrino interactions used in the T2K MC are simulated with the NEUT v5.4.0 [101] package. The same neutrino interactions generator is used for both ND280 and SK.

The initial nucleon momentum distribution inside the target nuclei (i.e. mostly ^{12}C and ^{16}O) is assumed to follow the Spectral Function (SF) model, developed by O. Benhar [86], for CCQE interactions. For all non-CCQE interactions, a relativistic Fermi Gas (RFG) [102] initial distribution of momenta is assumed. For multi-nucleon, or two-particle-two-hole (2p2h) interactions, the Nieves et al. [94] model is used. Resonant pion production interactions are modelled under the Rein-Sehgal model [98], and then tuned to form factor corrections obtained from K. Graczyk and J. Sobczyk [103]. Coherent pion production, on the other hand, assumes a Berger-Seghal [104] model. Deep inelastic scatters are modelled using different tools depending on the regime of the mass of the hadronic recoil system, W: at low W, interactions are modelled with the NEUT "multi-pi" mode, and apply corrections extracted from the Bodek-Yang model [105]; at high W, the PYTHIA 5.7 package [106] is used to model interactions. Final state interactions are modelled with NEUT intranuclear cascades. Further details about the NEUT 5.4.0 features used in the analysis presented in this thesis can be found in [107].

The generated events are then propagated using detector simulation packages: ND280 uses the GEANT4 [108] library, as well as a dedicated package, ElecSim [62], to model the electronics response; SK uses a custom package called SKDETSIM [81], based on GEANT3 [68].

3.2.3 ND280 Event Selections

For the purposes of the oscillation analysis[1], ND280 data and MC events are separated into 18 samples based on three features: the "right-sign" of the neutrinos with respect to the beam polarity at the time of data taking (i.e. whether the beam was mainly composed of ν_μ or $\bar{\nu}_\mu$, corresponding to an FHC or RHC configuration, respectively); the target in which the event took place (FGD1 or FGD2); and finally by event topology into one of three categories based on number of final state pions (no pions, one charged pion or any number of pions). The remaining 6 samples are control samples describing the ν_μ background in $\bar{\nu}_\mu$ beam mode (RHC ν_μ), and they are also broken down by interaction target and topology. The latter are referred to as "wrong-sign" selections, since they describe the contamination of a $\bar{\nu}_\mu$ beam by ν_μ events. The contamination in the opposite configuration (i.e. ν_μ contamination by $\bar{\nu}_\mu$) is much smaller and is thus not constrained at the near detector[2]. The latter samples are also of particular interest since SK is not a magnetized detector, and can thus not control this background on its own.

The selections defined above target charged-current (CC) events exclusively, and so their names will be prefaced by "CC". The selections are also referred to as "CC-Inclusive", since the particle kinematics are inferred by measuring charged leptons (muons or electrons) and pions, and without considering final state proton or neutron information. This choice was made in order to have correlated nuclear systematics between the near detector and SK, as the latter has a high Cherenkov threshold for protons and is therefor blind to final state hadrons. In addition, the current ND280 tracker also has a high proton detection threshold. The ND280 Upgrade project, described in Chapter 6, will introduce an extra scintillating target (SuperFGD) at the near-detector complex. The SuperFGD has a much lower proton detection threshold than current FGDs, and will make it possible to use hadron information in the analysis.

The three interaction topologies based on number of final state pions are aimed at defining data samples enriched in events coming from the dominant interaction types at T2K energies (Section 2.4). As such, a charged current event with a single muon and no pions in the final state defines the CC0π sample, enriched in charged-current quasi-elastic (CCQE) interactions; a CC event with a muon and a single final state pion falls into the CC1π sample, enriched in charged-current resonant (CCRes) events; and finally any other charged current event falls into the CCOther sample, enriched in charged-current deep inelastic scattering (CCDIS) events.

The idea behind these selections is not new to this analysis. However, in previous analyses (e.g. [61, 100]), only the FHC samples were split by topology, whereas RHC samples were categorized

---

[1] Other T2K analyses, in particular cross-section analyses, have more selections. They may notably be determined by the number of final state protons, photons, or other particles.

[2] This is due to the fact that $\bar{\nu}_\mu$ interactions have a much smaller cross-section than ν_μ interactions, and to the pion production kinematics in the beam target. More positively charged pions are produced, and therefore the ν_μ component in the $\bar{\nu}_\mu$ beam is larger than in the opposite configuration.

according to *track multiplicity*: $\bar{\nu}_\mu$ events with exactly one good quality positive muon track fell into the CC-1Track sample, and all other events made up the CC-NTrack sample. The analysis which will be described in this document is the first to use the same topology-based definition in both FHC and RHC. In addition, it is also the first analysis to apply these selections to "wrong-sign" samples. These two improvements contribute to a better control of background events, as well as a more direct correspondence of $\nu_\mu/\bar{\nu}_\mu$ systematic uncertainties.

All CC selections stem from a common selection process, where various cuts are applied sequentially in order to reduce background contamination. The process is described in detail in [107, 109], and is summarized below.

3.2.3.1 FHC ν_μ Selections

ν_μ CC samples are designed to select neutrino interactions originating in one of the FGDs and containing one negatively charged muon track in the following TPC. All negative tracks associated with the event are sorted according to their momenta and the highest-momentum negatively charged track is retained as a preliminary muon candidate. A set of selection criteria common to all ν_μ CC tracks are then applied:

- **Event Quality Cut:** The event is required to have occurred within the bunch time window of the neutrino beam. In addition, general ND280 data quality cuts are applied, ensuring that all sub-detectors and the magnet were operational and taking data at the time.

- **Total Multiplicity, Quality and Fiducial Volume (FV) Cuts:** The event must have at least one reconstructed track crossing the TPC right after the FGD target in which the interaction occurred. The event must have at least one reconstructed track in the considered FGD fiducial volume and at least one track with segments in the FGD and TPC. The starting point of the track (i.e. the vertex) must be inside the FGD FV. In addition, since short track reconstruction in the TPCs is less reliable, the track is required to have at least 18 clusters in the TPC.

- **Upstream Background Veto:** A veto is applied on events whose second-highest momentum track starts 150 mm upstream of the muon candidate track. The goal of this veto is to reject backward-going particles, as well as muons originating in other parts of ND280 (such as the P∅D) which undergo multiple scatters and are reconstructed as two distinct tracks.

- **Broken Track Cut:** It may happen that the reconstruction procedure breaks up a track into two parts: one which is fully contained in the FGD and one that crosses the last few layers of the FGD and then the TPC. The latter of the two parts may thus be identified as the main candidate, making the vertex reconstruction unreliable. To reject such tracks, the starting position of the muon candidate is required to start no further than 425 mm away from the FGD upstream edge if the associated event has at least one reconstructed FGD-only track.

- **Muon PID Cut:** Events having passed the above cuts are considered muon candidates. Particle identification techniques based on energy loss in the TPC (dE/dx) are applied to determine whether the candidate is indeed compatible with a muon. The measured dE/dx in the TPC is compared to expected energy depositions under the hypothesis that the particle is a muon, an electron or a proton.

Events which satisfy the above requirements are then split into three categories using pion identification criteria. The secondary tracks associated with the muon candidate event (and which are not the muon candidate itself) are retained and the following criteria are applied for each track:

- **Beam Spill and Bunch Match:** The retained track must have the same beam spill and bunch as the muon candidate.

- **Starting Position:** The track must originate in the same FGD FV used for the muon candidate selection and enter the following TPC (i.e. enter TPC2 and TPC3 for FGD1 and FGD2 origins respectively).

- **Pion PID Cut:** Depending on the PID technique used to identify pions, they can be categorized according to their "tag".
  Tracks which satisfy the same TPC event quality cuts as the muon candidate are identified using TPC information. Charged pions (π^+ and π^-) are identified using the same PID technique as the muon, and are referred to as "TPC" pions. The main difference is in the alternative hypotheses considered in the rejection process: for positive tracks, the π^+, e^+ (positron) and p (proton) hypotheses are considered; for negative tracks, π^- and e^- (electron) hypothesis are considered. The total number of charged pions associated with an event will thus be given by the number of tracks consistent with a charged pion hypothesis. Neutral pions, on the other hand, are identified by the positrons and electrons produced in their decay.
  For charged particles only, if the particle momentum is too low or its angle too high, thus not allowing it to enter the TPC, FGD information can be used to identify it. If the particle track is too short, and cannot be considered an independent track, the Michel tagging procedure is used, and the resulting particles are called "Michel-tagged" pions. The procedure consists in searching for a signal compatible with a delay of 2.19 μs in the FGD caused by the decay electron (Michel electron) produced in the pion decay. This signal is required to be outside the bunch time window. If the particle momentum is high enough for the track to be fully contained in the FGD and thus not enter the TPC, FGD PID criteria are used. Such a track must have the same time bunch as the muon candidate, start in and be fully contained in the FGD FV. This last type of pions are sometimes referred to as "FGD-iso" or "FGD-only" pions.

Other remaining particles in the event (e.g. pions, hadrons) are identified using TPC PID.
Once all final state pions have been identified, the three samples are defined as follows:

- **FHC ν_μ CC0π:** Events with no identified charged pions, electrons or positrons using TPC PID, and no Michel electrons or charged pions found in the FGD.

- **FHC ν_μ CC1π:** Events with exactly one reconstructed positively charged pion. This is equivalent to requiring either that the sum of the number of positive pions found in the TPC and the number of Michel electrons is one, or, if no Michel electrons are found, that the sum of positive pions found in the TPC and FGD is equal to one.

- **FHC ν_μ CCOther:** Events not belonging to the previous two samples, which pass the general selection criteria for the CC-Inclusive samples.

3.2.3.2 RHC $\bar{\nu}_\mu$ Selections

The main difference between the selection processes for ν_μ and $\bar{\nu}_\mu$ events lies in the charge of the highest momentum muon track. For $\bar{\nu}_\mu$ events, the same event quality and FV cuts are applied as in the case of ν_μ events, but the highest momentum track is chosen among *positive* tracks. The sample definition is thus (for events passing the latter cuts):

- **RHC ν_μ CC0π:** Events with no identified charged pions, electrons or positrons using TPC PID, and no Michel electrons or charged pions found in the FGD.
- **RHC ν_μ CC1π:** Events with exactly one reconstructed *negatively* charged pion. This is equivalent to requiring either that the sum of number of negative pions found in the TPC and the number of Michel electrons is one, or, if no Michel electrons are found, that the sum of negative pions found in the TPC and FGD is equal to one. All positive secondary tracks are rejected.
- **RHC ν_μ CCOther:** Events not belonging to the previous two samples, which pass the general selection criteria for the CC-Inclusive samples.

3.2.3.3 RHC ν_μ Selections

The criteria for RHC ν_μ selections are identical to those for FHC ν_μ selections, but applied to events from RHC runs. The main difference lies in the resulting purity and efficiency of RHC ν_μ selections, due to a larger right-sign background present in these samples. RHC ν_μ samples are nevertheless of prime importance in the oscillation analysis: as previously explained, since SK is not a magnetized detector, it cannot reject neutrino events in RHC. Yet, a good discrimination between ν_μ and $\bar{\nu}_\mu$ is of particular interest in the measurement of δ_{CP}.

Table 3.3 shows the purity and selection efficiencies for each of the aforementioned samples. There is no large difference between FGD1 and FGD2 samples. The signal samples (FHC ν_μ CC0π and RHC $\bar{\nu}_\mu$ CC0π) have a high purity (∼70%), and the largest detection efficiencies in their beam categories. The RHC ν_μ samples have a lower purity due to the wider neutrino spectrum, which makes multi-particle states more likely. The RHC $\bar{\nu}_\mu$ CC0π selections have larger selection efficiency, because they produce an invisible final state neutron. The FHC ν_μ CC0π counterpart produce a final state proton, which does leave a track in the FGDs but is poorly reconstructed and may be mistaken for a pion, another particle, or not enter any selection at all. The RHC $\bar{\nu}_\mu$ CCOther samples perform worst in terms of purity, because of wrong-sign events: such events have high energies and may produce multiple pions, some of which can be reconstructed as muons. A similar thing can happen for 1 GeV/c protons, whose energy loss in the TPCs is simular to that of a muon, which makes it hard to distinguish them.

3.2.3.4 ND280 Nominal Prediction

The near detector samples are binned two dimensionally in reconstructed muon momentum, p_μ, and reconstructed muon direction, $\cos\theta_\mu$. The binning has been chosen so as to have at least 20 raw MC events per bin, which corresponds to 1-2 data events[3]. The complete binning is presented below:

---

[3] Requiring 1-2 data events per bin is a choice motivated by the way the data statistical error is calculated, using a Poisson error.

Beam	Topology	Target	Purity [%]	Efficiency [%]
FHC ν_μ CC	0π	FGD1	71	48
		FGD2	68	48
	1π	FGD1	52	29
		FGD2	51	24
	Other	FGD1	71	30
		FGD2	71	30
RHC $\bar{\nu}_\mu$ CC	0π	FGD1	75	70
		FGD2	73	69
	1π	FGD1	45	19
		FGD2	41	17
	Other	FGD1	26	27
		FGD2	26	24
RHC ν_μ CC	0π	FGD1	56	60
		FGD2	53	60
	1π	FGD1	44	30
		FGD2	45	26
	Other	FGD1	68	27
		FGD2	70	27

Table 3.3: Purity and selection efficiency for the ND280 samples. The values are approximated to the nearest integer.

- **FHC ν_μ CC0π:**
  p_μ (MeV/c): 0, 200, 300, 400, 450, 500, 550, 600, 650, 700, 750, 800, 850, 900, 950, 1000, 1050, 1100, 1200, 1300, 1400, 1500, 1600, 1700, 1800, 2000, 2500, 3000, 5000, 30000 - 29 bins.
  cosθ_μ: -1, 0.5, 0.6, 0.7, 0.76, 0.78, 0.8, 0.83, 0.85, 0.88, 0.89, 0.9, 0.91, 0.92, 0.925, 0.93, 0.935, 0.94, 0.945, 0.95, 0.955, 0.96, 0.965, 0.97, 0.975, 0.98, 0.985, 0.99, 0.995, 1 - 29 bins.

- **FHC ν_μ CC1π:**
  p_μ (MeV/c): 0, 300, 350, 400, 500, 600, 650, 700, 750, 800, 900, 1000, 1100, 1200, 1500, 2000, 3000, 5000, 30000 - 18 bins.
  cosθ_μ: -1, 0.6, 0.7, 0.8, 0.85, 0.88, 0.9, 0.92, 0.93, 0.94, 0.95, 0.96, 0.97, 0.98, 0.99, 0.995, 1 - 16 bins.

- **FHC ν_μ CCOther:**
  p_μ (MeV/c): 0, 300, 400, 500, 600, 650, 700, 750, 800, 900, 1000, 1100, 1250, 1500, 1750, 2000, 3000, 5000, 30000 - 18 bins.
  cosθ_μ: -1, 0.6, 0.7, 0.76, 0.8, 0.85, 0.88, 0.89, 0.9, 0.91, 0.92, 0.93, 0.94, 0.95, 0.96, 0.97, 0.98, 0.99, 0.995, 1 - 19 bins.

- **RHC $\bar{\nu}_\mu$ CC0π:**
  p_μ (MeV/c): 0, 300, 400, 500, 550, 600, 650, 700, 750, 800, 900, 1000, 1100, 1200, 1500, 2000, 4000, 30000 - 17 bins.
  cosθ_μ: -1, 0.6, 0.7, 0.8, 0.85, 0.9, 0.92, 0.93, 0.94, 0.95, 0.96, 0.965, 0.97, 0.975, 0.98, 0.985, 0.99, 0.995, 1 - 18 bins.

- **RHC $\bar{\nu}_\mu$ CC1π:**
  p_μ **(MeV/c):** 0, 500, 700, 900, 1300, 2500, 30000 - 6 bins.
  cosθ_μ: -1, 0.7, 0.8, 0.9, 0.94, 0.96, 0.98, 0.99, 1 - 8 bins.

- **RHC $\bar{\nu}_\mu$ CCOther:** p_μ **(MeV/c):** 0, 600, 800, 1000, 1250, 1500, 2000, 4000, 30000 - 8 bins.
  cosθ_μ: -1, 0.7, 0.8, 0.85, 0.9, 0.93, 0.95, 0.97, 0.98, 0.99, 1 - 10 bins.

- **RHC ν_μ CC0π:**
  p_μ **(MeV/c):** 0, 300, 500, 700, 800, 900, 1250, 1500, 2000, 4000, 30000 - 10 bins.
  cosθ_μ: -1, 0.7, 0.8, 0.85, 0.88, 0.9, 0.92, 0.94, 0.96, 0.97, 0.98, 0.99, 1 - 12 bins.

- **RHC ν_μ CC1π:**
  p_μ **(MeV/c):** 0, 600, 800, 1500, 30000 - 4 bins.
  cosθ_μ: -1, 0.7, 0.8, 0.86, 0.9, 0.94, 0.96, 0.97, 0.98, 0.99, 1 - 10 bins.

- **RHC ν_μ CCOther:**
  p_μ **(MeV/c):** 0, 600, 1000, 1250, 2000, 4000, 30000 - 6 bins.
  cosθ_μ: -1, 0.7, 0.8, 0.86, 0.9, 0.93, 0.95, 0.97, 0.99, 1 - 9 bins.

The same binning is used for FGD1 and FGD2 samples, yielding a total of 4238 bins. The two near detector fitters, BANFF and MaCh3, use identical binning[4]. The nominal MC distributions, projected in p_μ and broken down by interaction types, compared with the data[5], are presented in Fig. 3.1, Fig. 3.2 and Fig. 3.3. The corresponding distributions projected in cosθ_μ are presented in Fig. 3.4, Fig. 3.5 and Fig. 3.6. The 1D distributions are very useful to illustrate at a glance the MC composition and give a general idea of the data-MC agreement. However, it is important to bear in mind that the near detector fit is a two-dimensional fit, in p_μ and cosθ_μ.

The nominal distributions have the following characteristics:

- **CC0π samples:** in FHC ν_μ samples, the MC underestimates the data by 10-20% in the bulk of the p_μ distribution, in both FGD1 and FGD2.
  For RHC $\bar{\nu}_\mu$ samples, the size of the discrepancy in p_μ is significantly smaller. This is also the case for RHC ν_μ samples. In cosθ_μ, a 10% discrepancy can be seen at forward angles.

- **CC1π samples:** for FHC ν_μ and RHC ν_μ samples, the MC overestimates the data by about 5-10% in the high-momentum, forward angle regions. The updates to the neutrino interaction model for this analysis are expected to improve substantially the data-MC agreement after the fit.

- **CCOther samples:** the MC underestimates the data across all such samples. These samples are designed to control background processes, such as deep inelastic scatters. In addition, these samples also contain events with final states containing etas and kaons, on which little

---

[4] In reality, BANFF and MaCh3 use the same binning only when using ROOT TH2D objects. In this analysis, the MaCh3 framework has an added functionality, allowing it to use TH2Poly objects to bin the data. TH2Poly objects have the possibility to define non-uniform bins, and make the choice of binning more flexible to the shape of the spectrum. In particular, the peak region at forward angles and mid-range momentum can be binned with better precision. For future analysis, there is an ongoing effort to introduce this functionality to the BANFF framework as well

[5] The data-MC distributions presented in this section have two additional sets of weights applied: one to tune the spectrum according to neutrino interaction models considerations (described in Section 3.3.2), and one to account for ND280 detector systematics (Section 3.3.3).

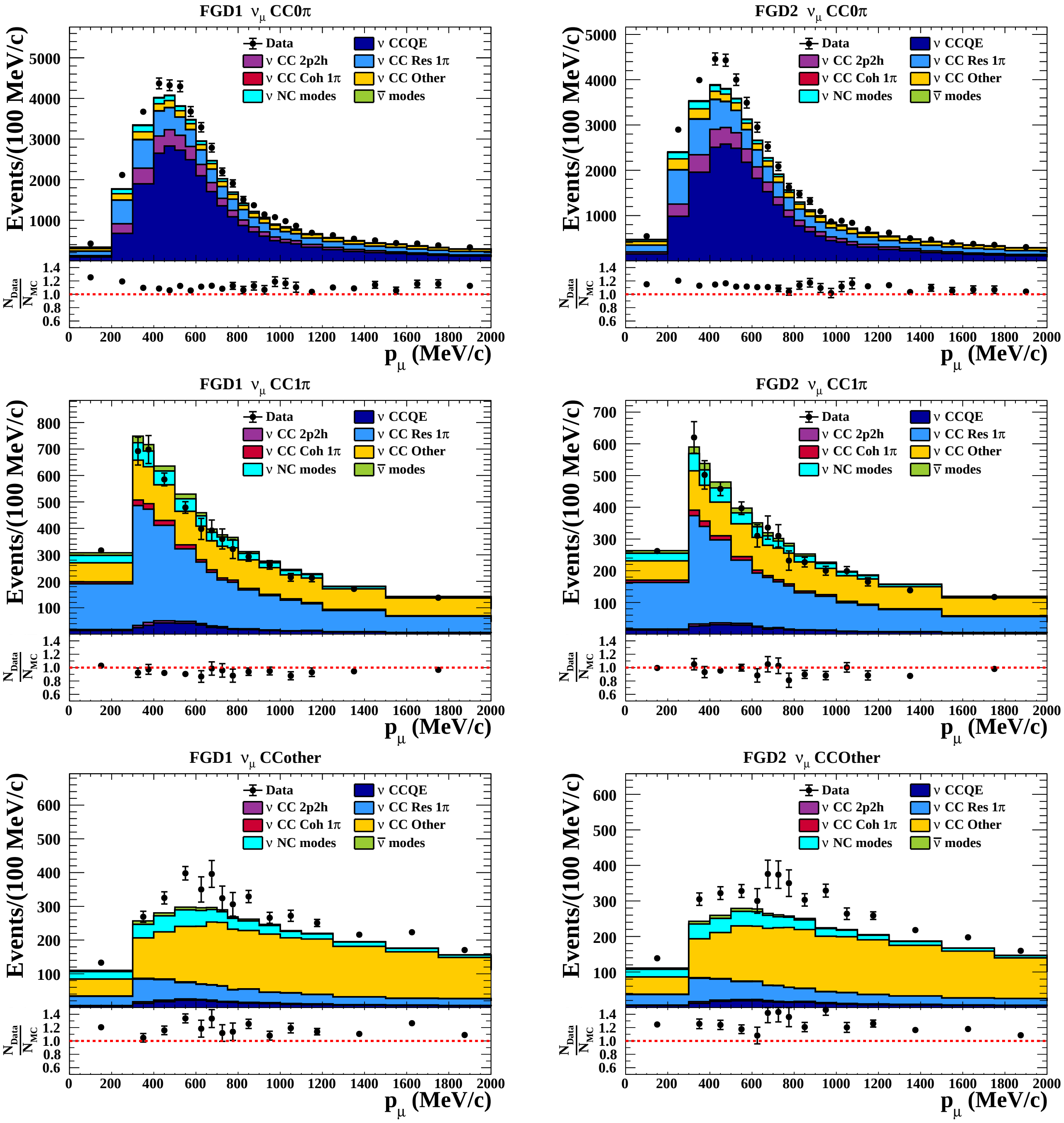

Figure 3.1: Nominal data-MC comparisons for FHC ν_μ samples.

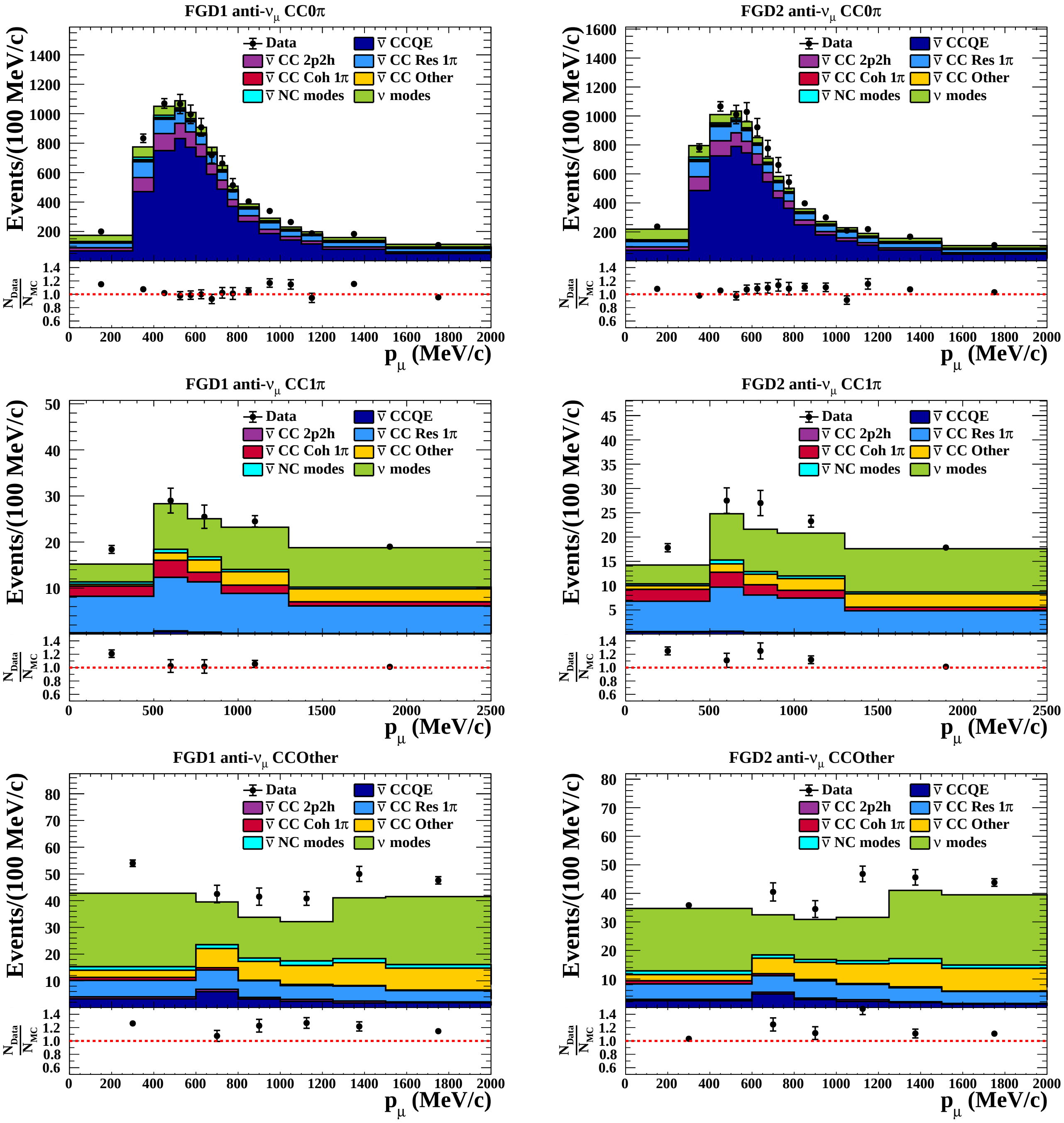

Figure 3.2: Nominal data-MC comparisons for RHC $\bar{\nu}_\mu$ samples.

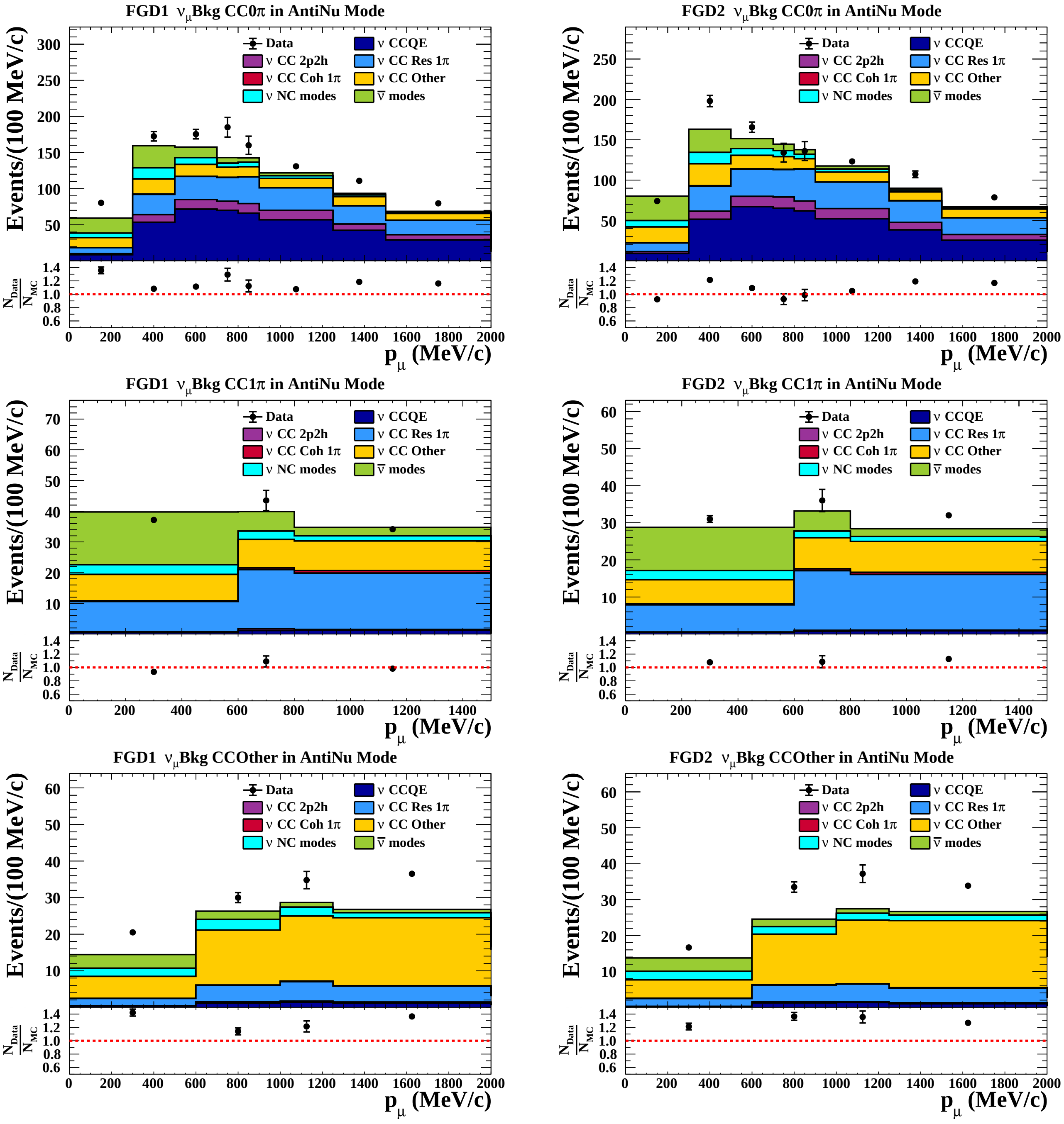

FGD1 ν_μBkg CC0π in AntiNu Mode

FGD2 ν_μBkg CC0π in AntiNu Mode

FGD1 ν_μBkg CC1π in AntiNu Mode

FGD2 ν_μBkg CC1π in AntiNu Mode

FGD1 ν_μBkg CCOther in AntiNu Mode

FGD2 ν_μBkg CCOther in AntiNu Mode

Figure 3.3: Nominal data-MC comparisons for RHC ν_μ samples.

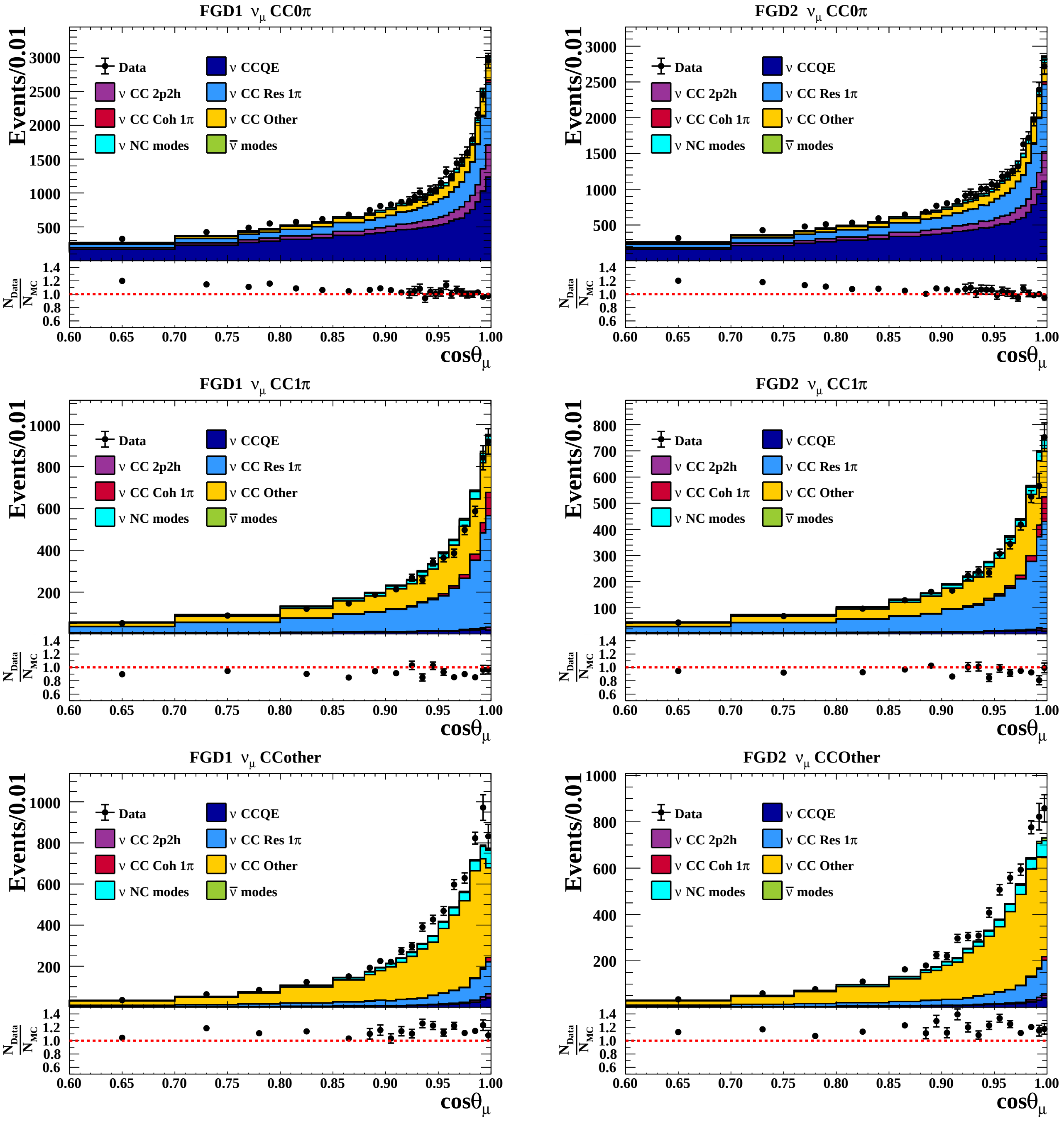

Figure 3.4: Nominal data-MC comparisons for FHC ν_μ samples.

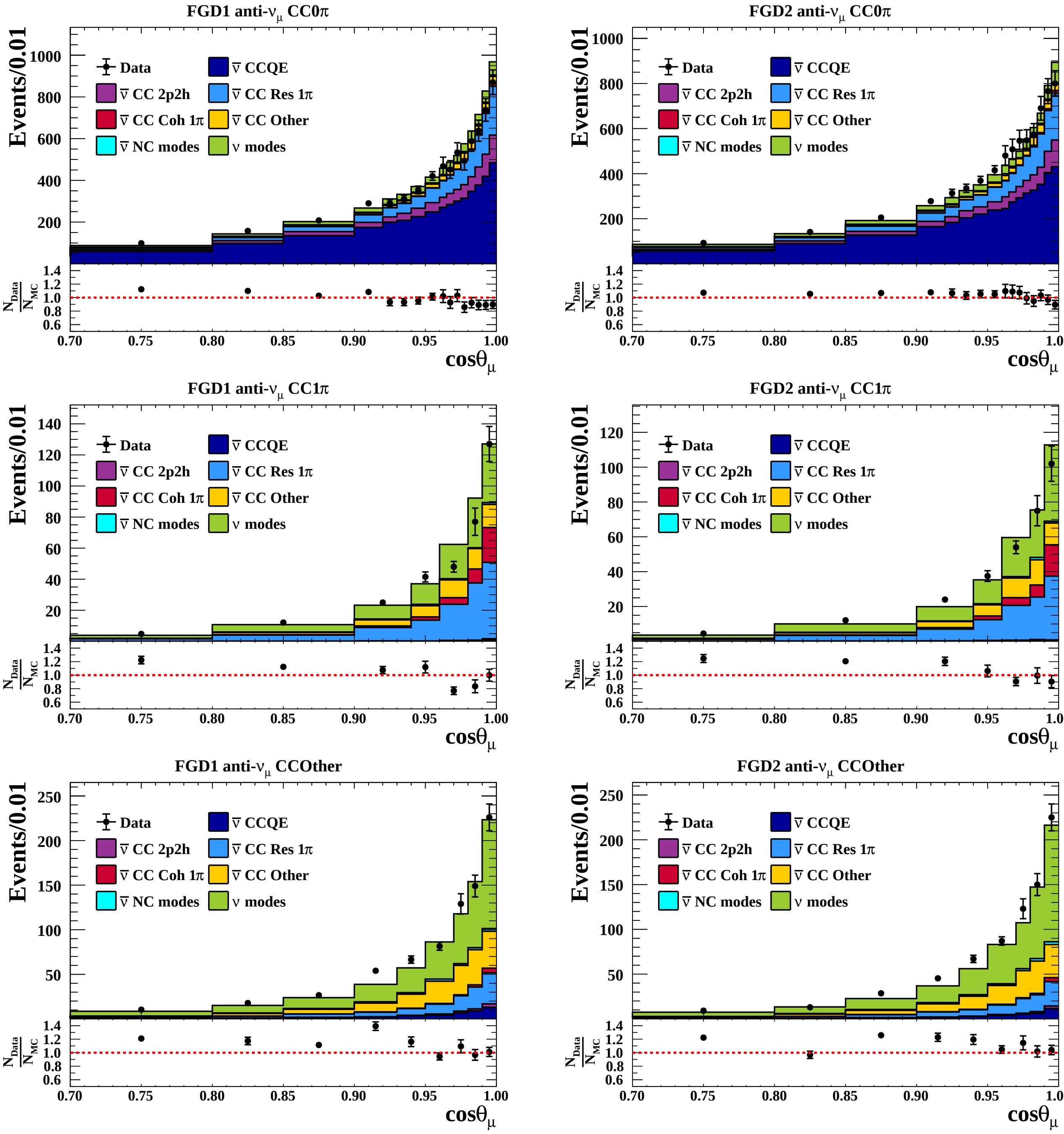

Figure 3.5: Nominal data-MC comparisons for RHC $\bar{\nu}_\mu$ samples.

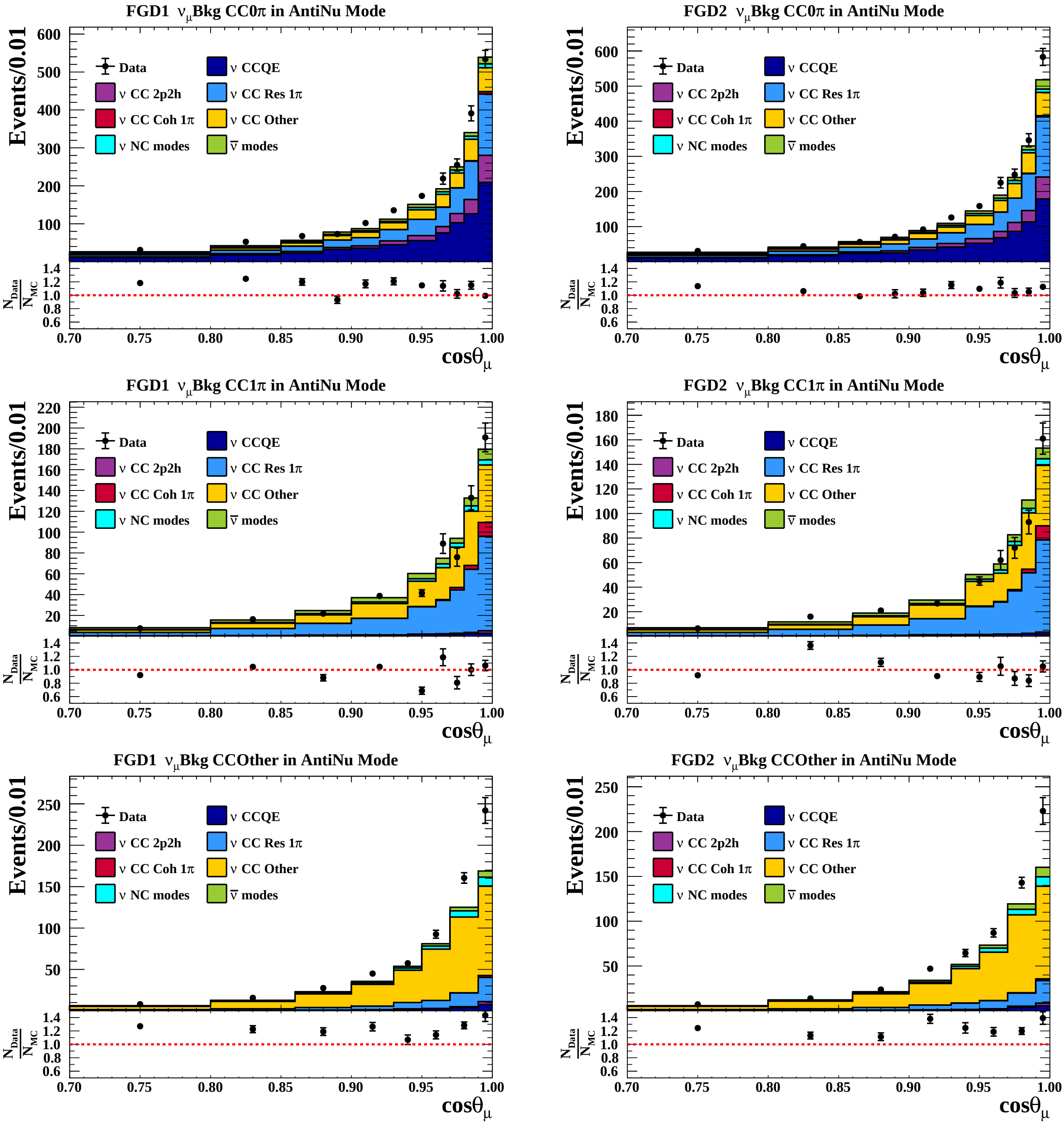

Figure 3.6: Nominal data-MC comparisons for RHC ν_μ samples.

information is available, and the events in these samples span a wide range of the p_μ-cosθ_μ phase space.

3.2.4 SK Event Selections

For the purposes of the OA, SK data are split into samples based on the reconstructed lepton flavor (μ-like or e-like), the magnetic horn polarity of the J-PARC beam, and the number of primary Cherenkov rings[6]. They are designed to target two types of interactions:

- **CCQE:** Samples which have a single lepton ring (1R) which is μ-like or e-like - FHC 1Rμ, RHC 1Rμ, FHC 1Re and RHC 1Re.
- **Resonant pion production (CC1π^+):** Sample with a single e-like ring (1Re) and with a delayed e-like ring from the Michel electron stemming from a muon decay (1de), itself stemming from the decay of the π^+ product of the resonant process. This sample is called FHC 1Re1de.

Currently, there is only one sample for SK CC1π^+ events, but there is ongoing work to develop more pion-targeted samples for future analyses.
Detailed information about the selections can be found in [110], [111], and is summarized below.

Since SK is a multi-purpose detector which studies neutrinos from different sources, it is first necessary to make sure that the events selected for T2K oscillation analyses are indeed produced by the J-PARC beam. This is done by selecting events which occur in the same time window as beam bunches.
The SK event selection also follows a series of quality cuts. All selections apply the Fully Contained Fiducial Volume (FCFV) cuts. These cuts aim to select neutrino events which can be accurately reconstructed, as well as reject cosmic background events and external events. The fully contained (FC) cut requires that there be no hit cluster in the outer detector (OD) with 16 or more hit PMTs. The fiducial volume (FV) cut states that events must occur inside the SK fiducial volume by limiting the space in which the reconstructed vertex can occur in the following way:

- for e-like candidates: the reconstructed vertices are required to be at least 80 cm from the detector wall and the distance from the vertex to the detector wall in the momentum direction must be larger than 170 cm.
- for μ-like candidates: the reconstructed vertices are required to be at least 50 cm from the detector wall and the distance from the vertex to the detector wall in the momentum direction must be larger than 250 cm.

Events that occur close to the wall are more difficult to reconstruct and are more likely to have originated outside the inner detector (ID). All single ring samples require that the number of rings found by the ring-counting algorithm be equal to one. 1Rμ samples require the following additional cuts:

- **PID cut:** The ring pattern must be compatible with the hypothesis of a muon.
- **Momentum cut:** The reconstructed momentum of the muon must be greater than 200 MeV/c.

---

[6] For a reminder of the SK detector description and particle detection techniques, see Section 2.3.

- **Decay electron cut:** The number of identified decay electron rings must be less than or equal to one.

CCQE 1Re samples require the following additional cuts:

- **PID cut:** The ring pattern must be compatible with the hypothesis of an electron.
- **Visible energy cut:** The visible energy E_{vis} of the event (defined as the sum of energy from all rings identified in the event, assuming the rings to be electron-like during energy reconstruction), must be greater than 100 MeV. This cut ensures the rejection of neutral-current events and Michel electrons produced by invisible muon events, while CCQE events are unlikely to occur at such low energies.
- **Decay electron cut:** The event must have no decay electron rings.
- **Reconstructed energy cut:** Because SK is located off-axis with respect to the J-PARC neutrino beam, which in return peaks the spectrum sharply around ~600 MeV, e-like events with high reconstructed neutrino energies are more likely to have actually originated from the $\nu_e/\bar{\nu}_e$ intrinsic beam contamination rather than $\nu_\mu/\bar{\nu}_\mu$ events which have oscillated into $\nu_e/\bar{\nu}_e$. They can be rejected by requiring that the reconstructed neutrino energy under the CCQE (Eq. (2.10)) hypothesis be less than 1.25 GeV.
- **π^0 rejection cut:** A large source of neutral current (NC) background comes from π^0 particles. A π^0 decays into two photons, which can undergo conversion into an e^+e^- pair, which in turn produce two electron-like rings. The likelihood of an event is evaluated under both the electron-like hypothesis and the π^0 hypothesis. The difference between the log-likelihoods under a π^0 hypothesis and an electron hypothesis is plotted against the invariant di-photon mass $m_{\gamma\gamma}$ from the photon conversion. Since π^0 events and signal events populate distinct regions in this space, a selection cut can be defined. Events more compatible with a π^0 under this picture are thus rejected and the π^0 background is reduced by a factor of 9[7].

Finally, the 1Re1de sample applies the following specific cuts:

- **PID cut:** The ring pattern must be compatible with the hypothesis of an electron.
- **Visible energy cut:** As in the case of 1Re samples, the visible energy E_{vis} must be above 100 MeV.
- **Decay electron cut:** The number of decay electrons must be *equal to one.*
- **Reconstructed energy cut:** The 1Re1de sample no longer targets CCQE interactions, but rather CC1π^+ interactions. The neutrino energy ($E_{rec}^{\nu_e CC\Delta}$) is thus reconstructed under the pion production hypothesis via the decay of a Δ^{++}:

$$E_{rec}^{\nu_e CC\Delta} = \frac{2m_n E_e + m_{\Delta^{++}}^2 - m_n^2 - m_e^2}{2\left(m_n - E_e + p_e \cos\theta_\mathrm{e}\right)} \tag{3.3}$$

  where m_n is the neutron mass, E_e and p_e are the electron energy and momentum, respectively, $m_{\Delta^{++}}$ is the mass of the Δ^{++} and $\cos\theta_\mathrm{e}$ is the electron direction with respect to the incoming neutrino direction. The reconstructed neutrino energy with this hypothesis is therefore also required to be less than 1.25 GeV.

---

[7] More details about the π^0 rejection procedure can be found in [112].

- π^0 **rejection cut:** The same π^0 rejection cut applied to 1Re samples is also applied to 1Re1de sample.

The SK data and MC, before applying the near detector fit constraint, are shown in Fig. 3.7. The MC prediction is also broken down by the main interaction modes. The total predicted MC event rates, with and without applying oscillations according to parameters in Table 4.1, are compared to the data event rates in Table 3.4. From the latter, the effect of oscillations can be clearly seen.

The SK binning varies between the three far detector fitters. Details about each analysis can be found in [113], [114], [115].

Sample	Predicted		Data
	unoscillated	oscillated	
FHC 1Rμ	1409.18	327.96	318
RHC 1Rμ	432.31	133.00	137
FHC 1Re	19.24	84.56	94
RHC 1Re	6.43	15.71	16
FHC 1Re1de	3.23	10.53	14

Table 3.4: Predicted MC event rates at SK, with and without applying the effect of neutrino oscillations, compared to the number of events in the data.

3.3 Systematic Uncertainties for the Oscillation Analysis

T2K uses a set of external inputs to constrain the flux and cross-section models before the oscillation analysis. These inputs are complementary to measurements performed by the T2K beam and cross-section working groups.

3.3.1 Neutrino Flux Model

Previously, the flux tuning was obtained using a thin (2 cm) graphite target [116]. Despite already substantially reducing the errors coming from hadron production models, the thin target data does not account for re-interactions which occur in the full length of the T2K target (90 cm) or for the particle kinematics which are influenced by the full-size target (e.g. different exiting angles according to production point). The analysis described in this work is the first T2K oscillation analysis to include a flux tuning obtained with NA61/SHINE data using a T2K replica-size target [117]. Fig. 3.8 shows a schematic view of the difference between the thin target and the T2K replica targets used to obtain the flux tuning.

The flux uncertainty model is parametrized as a function of neutrino (or antineutrino) energy, using a fractional flux covariance matrix presented in Fig. 3.11. The flux parameters used in the oscillation analysis correspond directly to bins in true neutrino/antineutrino energy. The full documentation of the flux tuning using the NA61 replica-target data can be found in [118].

Flux parameters are indexed by their bin numbers, and are defined according to the following features:

- Magnetic horn polarity - The beam is produced in either Forward Horn Current (FHC) or Reverse Horn Current (RHC). This setting defines what will be considered the “right sign” of the beam - a ν_μ or $\bar{\nu}_\mu$ beam is produced in FHC or RHC mode, respectively.

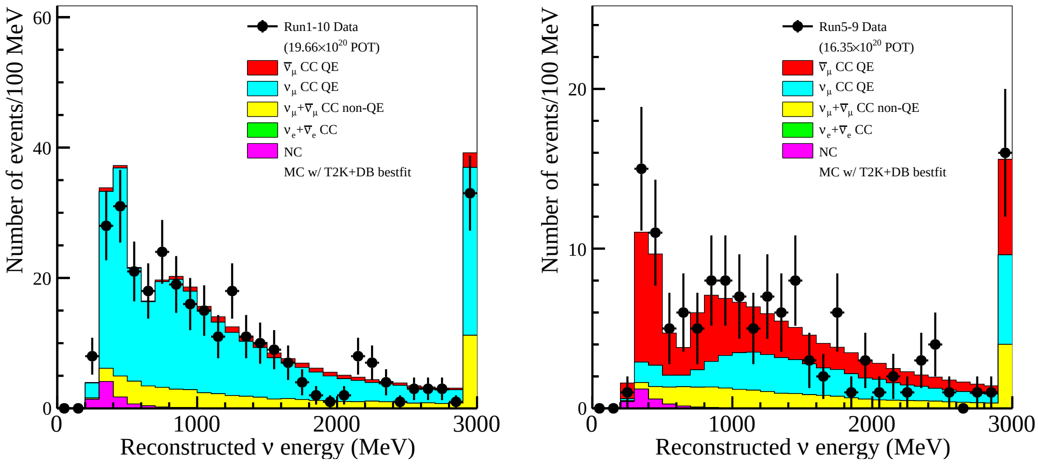

(a) FHC 1Rμ (b) RHC 1Rμ

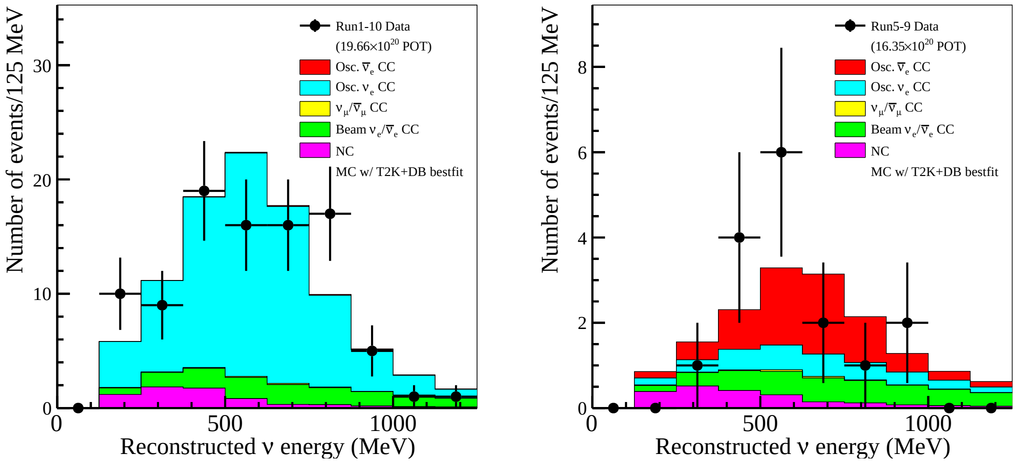

(c) FHC 1Re (d) RHC 1Re

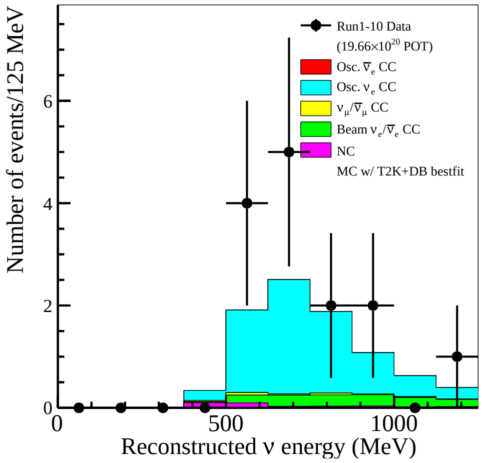

(e) FHC 1Re1de

Figure 3.7: Data-MC comparisons for SK selections as a function of reconstructed energy, before applying the near-detector tuning.

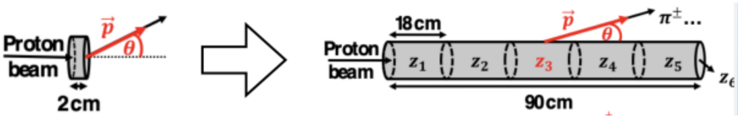

Figure 3.8: Comparison of thin target (left) and full-size T2K replica target (right) used by NA61/SHINE to obtain T2K flux tunings.

- Neutrino flavor component - Although the beam is designed to be enriched in muon flavored (anti)neutrinos, (anti)neutrinos of other flavors are also present in its composition. The beam composition is therefore broken down into ν_μ, $\bar{\nu}_\mu$, ν_e and $\bar{\nu}_e$ components.

- Detector - The flux prediction is different at ND280 and at SK. ND280 is relatively close, for instance, to the production point, and its shape and size has to be taken into consideration when predicting event rates. SK, on the other hand, is far enough from the beam target to justify considering it point-like.

The different contributions to the flux uncertainty obtained with the replica target tuning are presented in Fig. 3.9 and Fig. 3.10. They are also compared to the previously used thin-target tuning, highlighting how the errors have been reduced with the new tuning.

The largest contribution to the uncertainty comes from "hadron interactions", a term which encompasses three types of effects: the uncertainty on the production cross-section for various hadron species; the uncertainty on the multiplicity of final state hadrons exiting the target; and the uncertainty on the hadron interaction length[8]. These uncertainties are significantly reduced (by ~50%) with respect to the previous thin-target uncertainties, mainly due to the fact that NA61 replica-target data is used to constrain the multiplicities of exiting pions. When using thin-target data, the uncertainty on exiting pion yields was included as additional uncertainties in the total hadron interaction uncertainty. The reduction of such uncertainties is particularly striking at energies around the T2K flux peak (~0.6 GeV), where they are reduced from the level of 10% to the level of 4%.

The second dominant source of systematic uncertainty comes from the proton beam profile and the measurement of the off-axis angle between the beam and the direction of the T2K detectors used in the oscillation analysis (ND280 and SK). Overall this contribution is small, except around the energy peak.

Lastly, there are minor uncertainties associated with the magnetic current passing through the horns used to focus the neutrino beam.

Overall, the replica-target flux uncertainties are below those obtained with the thin target. However, it is interesting to note that for the FHC $\bar{\nu}_e$ and the RHC ν_e flux, the replica-target tune actually increases the uncertainties. There are a number of interactions that are not constrained by NA61 measurements, mainly due to lack of data. These interactions are part of the hadron interaction uncertainties. Some of these interactions come from neutral kaons, which in previous flux tunes were accidentally left out of the analysis due to a GEANT3-FLUKA particle ID convention. It is thus not the replica-target tune itself which increases the uncertainty on these interactions, but rather correctly accounting for the presence of neutral kaon interactions [118].

---

[8] Which itself has two contributing terms: the uncertainty on the distance travelled by a hadron inside the target before interacting with a nucleus, and the uncertainty on the distance travelled by the hadron after the interaction *before* exiting the target.

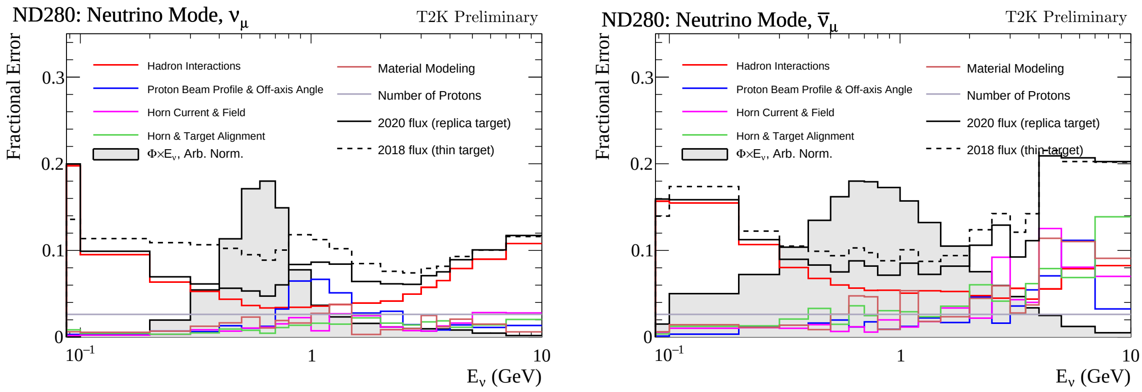

(a) ND280 FHC ν_μ (b) ND280 FHC $\bar{\nu}_\mu$

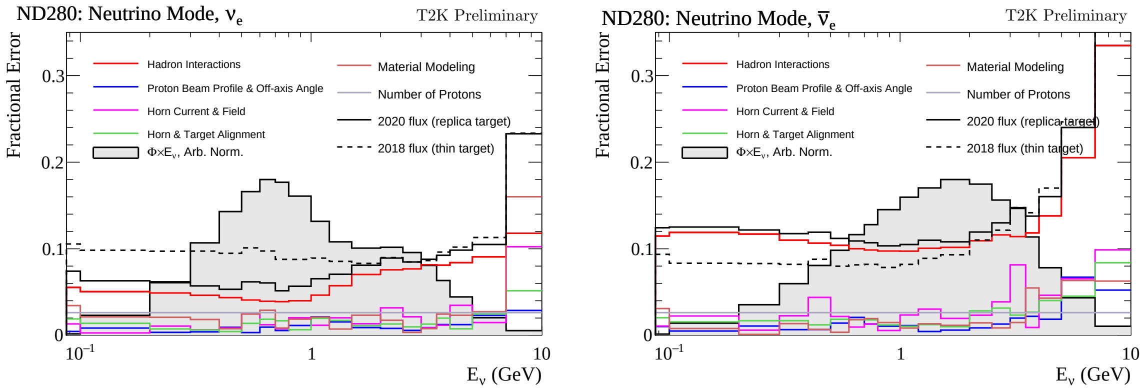

(c) ND280 FHC ν_e (d) ND280 FHC $\bar{\nu}_e$

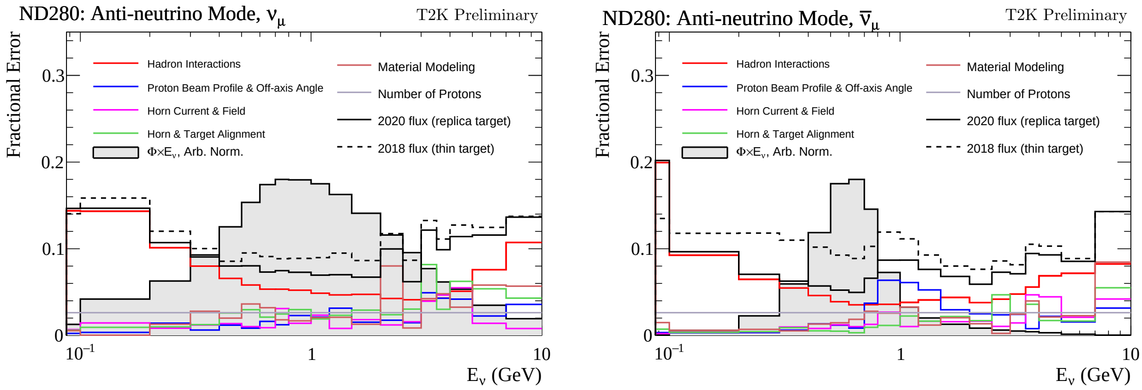

(e) ND280 RHC ν_μ (f) ND280 RHC $\bar{\nu}_\mu$

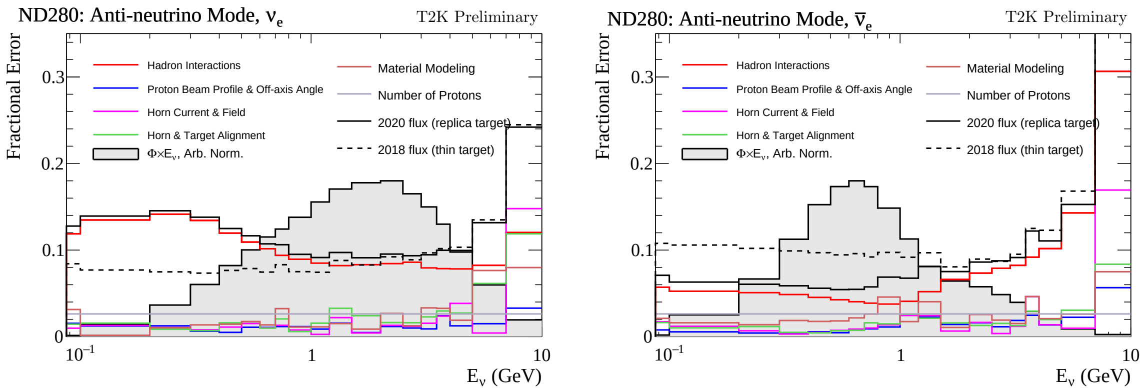

(g) ND280 RHC ν_e (h) ND280 RHC $\bar{\nu}_e$

Figure 3.9: Total flux uncertainty as a function of true neutrino energy at ND280. The full flux binning is used.

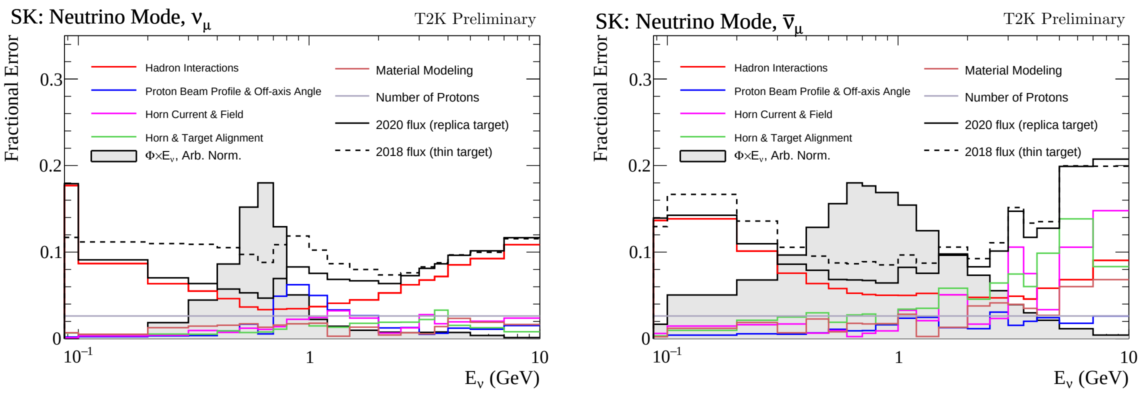

(a) SK FHC ν_μ (b) SK FHC $\bar{\nu}_\mu$

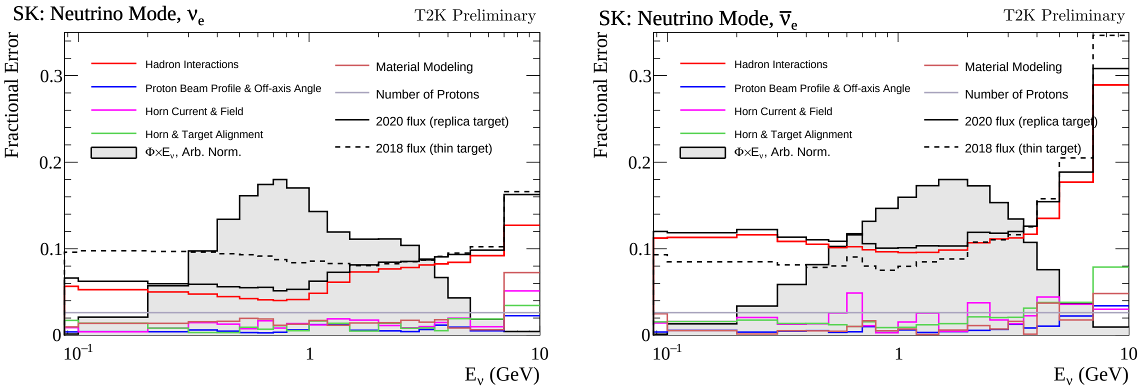

(c) SK FHC ν_e (d) SK FHC $\bar{\nu}_e$

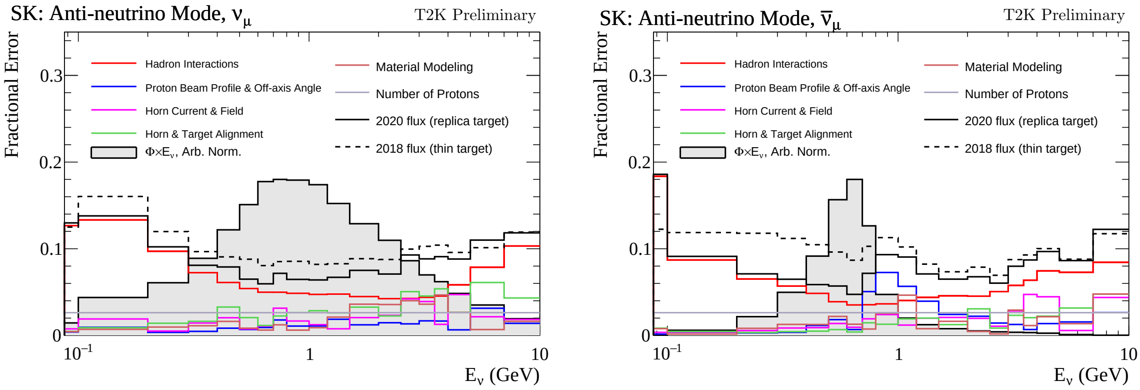

(e) SK RHC ν_μ (f) SK RHC $\bar{\nu}_\mu$

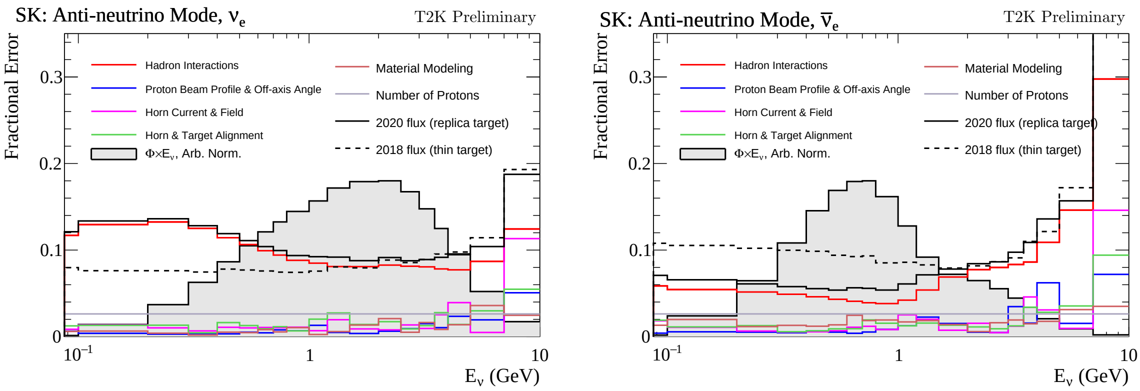

(g) SK RHC ν_e (h) SK RHC $\bar{\nu}_e$

Figure 3.10: Total flux uncertainty as a function of true neutrino energy at SK. The full flux binning is used.

The true neutrino energy binning used in the OA flux uncertainty parametrization has been optimized so as to pass on as much information as possible without introducing too many nuisance parameters. The binning is thus finer around the oscillation maximum (∼600 MeV) and coarser in regions with fewer events. The following binning has been used in this analysis:

- FHC ν_μ: 0, 0.4, 0.5, 0.6, 0.7, 1, 1.5, 2.5, 3.5, 5.0, 7.0, 30.0 [GeV] - 11 bins;
- FHC $\bar{\nu}_\mu$: 0, 0.7, 1.0, 1.5, 2.5, 30.0 [GeV] - 5 bins;
- FHC ν_e: 0, 0.5, 0.7, 0.8, 1.5, 2.5, 4.0, 30.0 [GeV] - 7 bins;
- FHC $\bar{\nu}_e$: 0, 2.5, 30.0 [GeV] - 2 bins;
- RHC ν_μ: 0, 0.7, 1.0, 1.5, 2.5, 30.0 [GeV] - 5 bins;
- RHC $\bar{\nu}_\mu$: 0, 0.4, 0.5, 0.6, 0.7, 1.0, 1.5, 2.5, 3.5, 5.0, 7.0, 30.0 [GeV] - 11 bins;
- RHC ν_e: 0, 2.5, 30.0 [GeV] - 2 bins;
- RHC $\bar{\nu}_e$: 0, 0.5, 0.7, 0.8, 1.5, 2.5, 4.0, 30.0 [GeV] - 7 bins.

The same binning was used for both ND280 and SK flux parameters, giving a total of 100 flux parameters.

It is important to note that despite the fact that different parameters are used for the two detectors, as well as for the different beam compositions, the flux parameters are positively correlated, as can be seen in Fig. 3.11. This makes it possible to constrain the ν_e or $\bar{\nu}_e$ flux at SK, for instance, despite the fact that no dedicated ν_e or $\bar{\nu}_e$ selections are used at ND280.

The flux parameters are normalization parameters, meaning that their value is a multiplicative factor used to scale events whose true (anti)neutrino energy is inside the corresponding bin. Their priors follow Gaussian distributions centered on the nominal value, with a width corresponding to the normalized error which has been extracted from the flux covariance matrix.

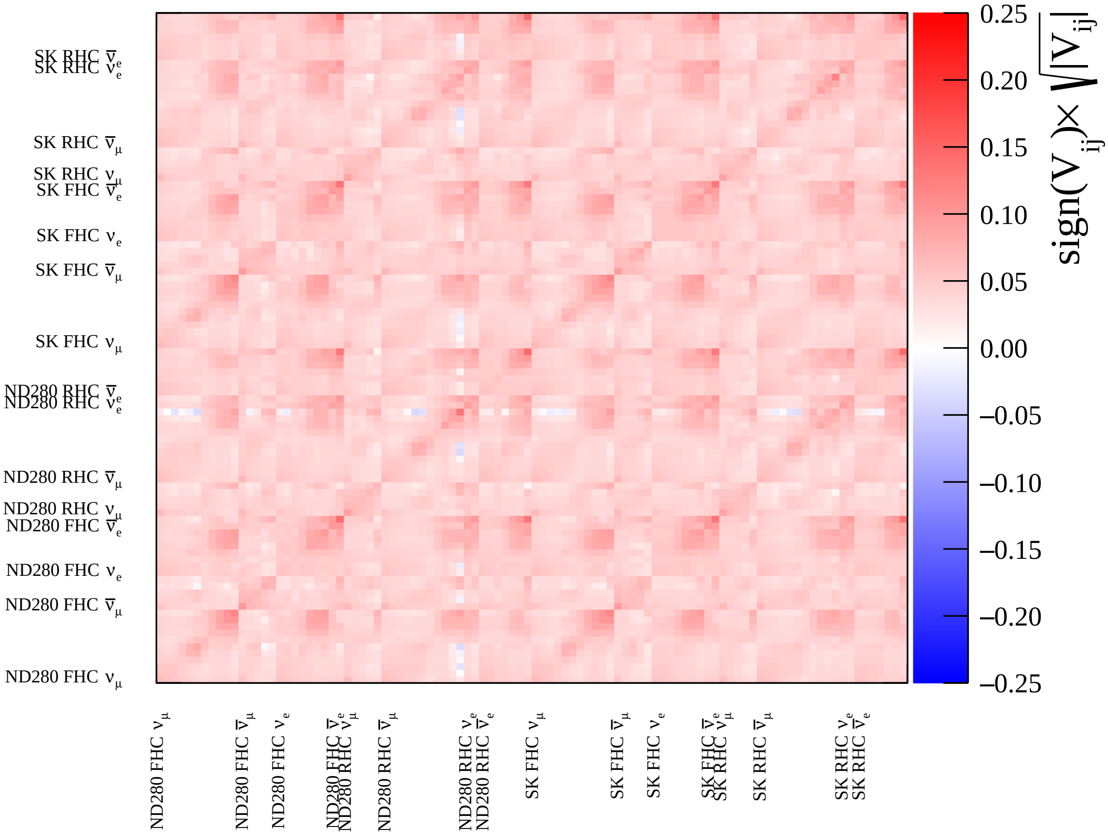

Figure 3.11: Reduced flux covariance matrix. V_{ij} represents the squared uncertainty for each parameter. Each entry corresponds directly to the flux uncertainty used for each flux parameter in the OA. The labels denote the beginning of each flux uncertainty contribution, and the binning corresponds to the reduced binning used in the OA described in the text.

3.3.2 Neutrino Cross-section Model

The cross-section uncertainty model is elaborated in close collaboration with the T2K Neutrino Interactions Working Group (NIWG). The NIWG gives recommendations on the baseline models used in the analysis, as well as a parametrization of the systematic uncertainties which affect each model. The latter are tuned to measurements performed by external dedicated neutrino cross-section experiments, such as MINERνA and MiniBooNE, ANL and BNL, as well as internal ND280 cross-section measurements.

As described in Section 2.4, at T2K energies the dominant interaction types are CCQE, followed by CCRES and CCDIS. There are also contributions which come from NC events or the wrong sign background. As such, cross-section parameters are designed in order to target each type of interaction.

There are two main types of cross-section parameters: shape and normalization parameters. Normalization parameters are one-time weights which affect all events defined by a certain interaction type. They are not sensitive to an event's kinematic features and apply the same weight to all

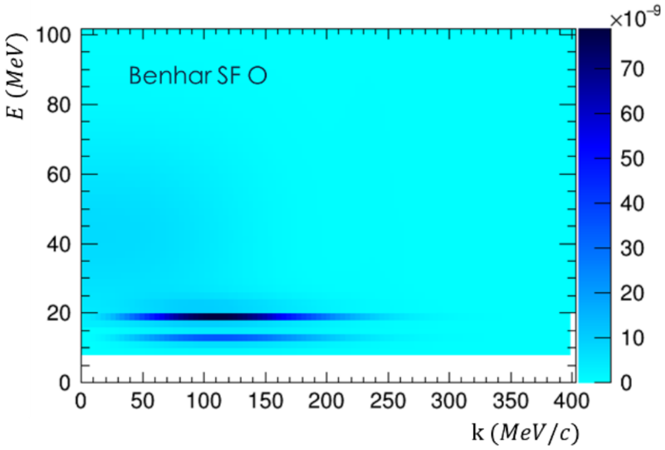

Figure 3.12: Nuclear ground state from the SF model. 'k' corresponds to the initial nucleon momentum and 'E' is the nuclear removal energy used in the SF approach. Two nuclear shells are clearly visible.

events across the neutrino energy spectrum. Unlike normalization parameters, shape parameters are sensitive to individual event kinematics. They are parametrized as response functions giving the weight that should be applied to an event as a function of the parameter value.

The cross-section model is designed by the Neutrino Interactions Working Group (NIWG), who give recommendations which are updated at each iteration of the oscillation analysis. Extensive information about the cross-section model used in this analysis can be found in [119], and will be summarized shortly in the following sections, grouped by the types of interactions they target.

3.3.2.1 CC0π parameters

The CC0π samples are designed to be enriched in CCQE interactions, which are the main source of signal. Since these samples are based on the final state topology, other channels giving the same observable final state will also populate these samples. The main sources of background for CC0π samples come from multinucleon (2p2h) interactions, as well as pion absorption processes.

The nuclear ground state model (Section 2.4.1) for CCQE interactions is the Benhar Spectral Function (SF) model [86], shown in Fig. 3.12. This is the first analysis to use the Benhar SF as a baseline model and marks an important step towards using exclusive neutrino interaction data. Although this particular analysis still only uses outgoing lepton information, the upgrade of the ND280 (Chapter 6) will allow us to also measure nucleons, and thus perform reliable *exclusive* measurements. SF agrees best with electron scattering data ($ee'p$) (see [120]), which is a reliable probe for exclusive measurements. On top of being more theoretically grounded (by taking into account the nuclear shell structure, for instance), the SF model will provide a base on which systematics addressing the nucleon in neutrino scatters will be developed. Such work is already under way for cross-section measurements at T2K, and is being extended to future oscillation analyses.

There are thirteen systematic parameters which control CCQE interactions:

- **M_A^{QE}:** This shape parameter corresponds to the axial mass in the dipole form factor parametrization in the Llewellyn-Smith model [90], and has been introduced in Section 2.4.2. For historical reasons, the default M_A^{QE} value in NEUT is 1.21 GeV. This parameter has been present in all T2K analyses, and it is an effective parameter. This means that it does not correspond directly to a variation of the axial mass, but rather replicates its effect on the event rate. As such, in past analyses it used to be a free parameter, due to the large uncertainty surrounding the axial mass value, as well as the fact that it was used as an effective dial to reabsorb nuclear effects. In this analysis, M_A^{QE} is still an effective dial, but it is far less polluted by other nuclear effects thanks to a more general Q^2-dependent parametrization (described later in this section). In the analysis described in this thesis, the value of the M_A^{QE} parameter was changed from the default NEUT value used in the MC generation (1.21 GeV)[9] to a value of 1.026 GeV. The latter value was obtained from bubble chamber data from neutrino scattering bubble-chamber experiments [92]. Unlike in previous analyses, where the M_A^{QE} parameter was left completely free in the fit, this analysis applies a tight Gaussian prior on M_A^{QE}, corresponding to a 3% error. The choice to constrain this parameter in this analysis is complementary to the introduction of a Q^2 dependent freedom in the model (described in the next item). The Q^2 freedom, M_A^{QE} and CC0π flux parameters all have similar effects on the spectra, albeit coming from different sources. A tight prior was placed on M_A^{QE} in an effort to decouple these effects[10].

- **Q^2 dependent freedom:** Two sets of *ad-hoc* parameters have been implemented in the cross-section model, with different motivations.
  At low values of transferred four-momentum Q^2, a discrepancy has been seen for the SF model in both T2K [121] and MINERνA [122] data. Most models implemented in neutrino interaction generators (both the currently used SF model, as well as relativistic Fermi gas models, such as RFG and LFG) are built on the impulse approximation (IA). The latter assumes that in a neutrino-nucleus scatter, the nucleus can be considered as a collection of independent nucleons and therefore only one nucleon takes part in the interaction [123]. The validity of this approximation is determined by the amount of transferred three-momentum of the interaction, $|\mathbf{q}|$. For $|\mathbf{q}| \gtrsim 400$ MeV/c, the IA works well, but below such values $|\mathbf{q}|$, this approximation begins to break down. The low-Q^2 region where data-MC discrepancies are observed corresponds directly to $|\mathbf{q}| \lesssim 400$ MeV/c. In Fermi-gas models, this discrepancy has been adressed by including Random Phase Approximation (RPA) corrections. For the SF model, RPA corrections are not included in the generator, and the previously used RFG RPA corrections are not applicable. This was the motivation for including a set of five *ad-hoc* normalization parameters to the [0,0.25] GeV^2 Q^2 region, corresponding directly to five 0.05 GeV^2 bins. These parameters are left completely free in the near detector fit, and are expected to show a suppression of events in this region (i.e. they would translate to a sub-unitary weight applied to CCQE events in these bins).
  On the other hand, the bubble chamber data which constrain M_A^{QE} were obtained at low-Q^2, and the data at higher Q^2 values is sparse. The dipole parametrization for M_A^{QE} is an approximation, and there are several, more modern, form factor parametrizations which deviate significantly from the dipole model at high values of Q^2. Two examples are the 3-component [124] and the Z-expansion [91] form factor models. Since other nuclear effects are partially uncorrelated from the effect of M_A^{QE} via the introduction of the low-Q^2 parameters, M_A^{QE} may absorb nuclear effects from the high-Q^2 region of the spectrum, where its value is not well constrained. For this reason, three more *ad-hoc* Q^2 parameters were added, covering

---

[9] In previous analyses, M_A^{QE} was a free parameter in the fit, so its initial value had little importance since the constraint on it was entirely driven by the data.

[10] There is an exception to this rule: hydrogen targets, i.e. unbound protons, are by definition free of nuclear effects. For neutrino interactions on hydrogen, the value of M_A^{QE} is *fixed* at 1.026 GeV^2 and no error is applied.

the rest of the $Q^2 > 0.25\text{GeV}^2$ in the following bins: [0.25, 0.50, 1.00, 10.00] GeV^2. Unlike the low-Q^2 parameters, the high-Q^2 parameters have a prior uncertainty with a Gaussian distribution. These uncertainties were estimated based on different predictions of the Q^2 shape in the dipole axial form factor parametrization and the Z-expansion parametrization. Since this parametrization effectively bins the Q^2 spectrum in eight bins, the names of the Q^2 parameters (also referred to as dials or modifications) are indexed by their respective bin number, in ascending order, starting from 0.

- **Removal energy (E_b):** The removal energy, or binding energy, E_b, is the energy required to remove a single nucleon from its bound state inside a nucleus. In simpler models such as RFG, the removal energy has a single value for all nucleons and only depends on the type of nucleus (for T2K targets, ^{12}C or ^{16}O). In the previous T2K oscillation analysis, the removal energy was the largest source of systematic uncertainty [61] and was not an actual parameter allowed to vary in the fit. Its effect was gauged in a heuristic way by performing a simulated data fit in which the MC was modified to reflect a 9 MeV variation around the nominal 27 MeV for the carbon removal energy.
  Unlike RFG, the SF model accounts for the shell structure of the nucleus, and therefore does not have a single fixed removal energy value. Along with the implementation of the SF model for this analysis, four dedicated parameters were designed to reflect the effect of shifts in removal energy according to the neutrino type (ν_μ or $\bar{\nu}_\mu$) and the target nucleus (^{12}C or ^{16}O): $E^C_{b,\nu}$, $E^C_{b,\bar{\nu}}$, $E^O_{b,\nu}$ and $E^O_{b,\bar{\nu}}$.
  Directly implementing a reweighting procedure for the effect of the removal energy using NEUT is a difficult task, as the effect of the removal energy on near detector kinematics (p_μ and cosθ_μ) may introduce or remove regions of phase-space near the kinematic limits. To mitigate such cases, the effect of the removal energy is instead applied in the following way:

  1. A large number of CCQE events are generated with NEUT for different values of E_b and over a range of neutrino energies E_ν. It should be noted that "different values of E_b", in the SF paradigm, is shorthand for applying different offsets to the SF nuclear removal energy (ΔE_b), and taking into account the effect this has on the initial nucleon momentum (see Fig. 3.12). An offset in the removal energy therefore shifts the entire two-dimensional SF distribution, and still accounts for the nuclear shell structure. This process is done for all four neutrino species (ν_μ, $\bar{\nu}_\mu$, ν_e, $\bar{\nu}_e$).
  2. From each of the generated samples, the cross-section distribution as a function of lepton momentum p_l, the lepton angle cosθ_l and E_ν is drawn - $\sigma(E_\nu, p_l, \cos\theta_\mathrm{l}, \Delta\mathrm{E_b})$.
  3. The cross-section distribution is profiled over the lepton momenta, yielding the $\bar{p}_l(E_\nu, \cos\theta_\mathrm{l}, \Delta\mathrm{E_b})$ distribution which gives the predicted change in final state lepton momentum for a shift in E_b.
  4. The obtained $\bar{p}_l(E_\nu, \cos\theta_\mathrm{l}, \Delta\mathrm{E_b})$ can then be used to subtract the prediction for the nominal SF to obtain a distribution of momentum shifts Δp_l for a given E_b shift, ΔE_b: $\Delta p_l(E_\nu, \cos\theta_\mathrm{l}, \Delta\mathrm{E_b})$.
  5. This process is done at some discrete E_b shifts, referred to as 'knots'. The shift in lepton momentum at any given E_b shift is calculated by interpolating between the knot values.

  This process is done separately for neutrino events on ^{12}C and ^{16}O.
  In addition to defining this parametrization, the NIWG has estimated a set of conservative

uncertainties to cover variations not yet addressed in the model. The latter come from three sources:

- **Peak resolution:** The positions of E_b peaks for nuclear shells are determined from electron-scattering data, and therefore have an associated resolution. The value of the peak resolution is between 2 MeV and 6 MeV [125], and has been set in this analysis to the largest value (6 MeV).
- **Proton/neutron ground states:** Electron scattering data used to constrain the SF model is obtained with electrons scattering off *protons*, and is used for anti-neutrino CCQE interactions. The conjugate process of neutrinos scattering off neutrons cannot be constrained precisely by electron scattering experiments, as neutrons detection is famously difficult and unreliable. In the current NEUT implementation, protons and neutrons off which (anti)neutrinos scatter are assumed to be the same. This is known not to be true and it is known that proton and neutron ground states differ in their removal energy by around 1 MeV to 4 MeV depending on the shell and target [126]. A conservative uncertainty to account for this difference of 4 MeV was therefore chosen by the NIWG.
- **^{12}C/^{16}O differences:** The shifts introduced by the E_b parameters should not differ too much for ^{12}C and ^{16}O. The uncertainty on ^{12}C/^{16}O differences has been estimated at 3 MeV.

These three sources of uncertainty were combined in order to extract first-order correlations between the E_b parameters. The parameters applying to neutrino events have an assumed 100% anti-correlation with the parameters for anti-neutrino events within the 4 MeV uncertainty; ^{12}C parameters are anti-correlated in the same way to ^{16}O parameters, assuming a 3 MeV uncertainty; and finally the total resolution uncertainty of 6 MeV is 100% correlated across all four parameters. Combining these three effects we obtain the following covariance (left) and correlation (right) matrices:

$$\begin{array}{c} \\ E^O_{b,\nu} \\ E^O_{b,\bar{\nu}} \\ E^C_{b,\nu} \\ E^C_{b,\bar{\nu}} \end{array}
\begin{array}{c} \begin{array}{cccc} E^O_{b,\nu} & E^O_{b,\bar{\nu}} & E^C_{b,\nu} & E^C_{b,\bar{\nu}} \end{array} \\ \begin{pmatrix} 36 & 28 & 31.5 & 23.5 \\ 28 & 36 & 23.5 & 31.5 \\ 31.5 & 23.5 & 36 & 28 \\ 23.5 & 31.5 & 28 & 36 \end{pmatrix} \end{array} \mathrm{MeV}^2
\qquad
\begin{array}{c} \\ E^O_{b,\nu} \\ E^O_{b,\bar{\nu}} \\ E^C_{b,\nu} \\ E^C_{b,\bar{\nu}} \end{array}
\begin{array}{c} \begin{array}{cccc} E^O_{b,\nu} & E^O_{b,\bar{\nu}} & E^C_{b,\nu} & E^C_{b,\bar{\nu}} \end{array} \\ \begin{pmatrix} 1. & 0.778 & 0.875 & 0.653 \\ 0.778 & 1. & 0.653 & 0.875 \\ 0.875 & 0.653 & 1. & 0.778 \\ 0.653 & 0.875 & 0.778 & 1. \end{pmatrix} \end{array}$$

The diagonal elements of the covariance matrix correspond to the square of the total 6 MeV uncertainty, and off-diagonal elements contain the remaining effects described above.

Two-particle-two-hole (2p2h) interactions (Section 2.4.2.1) are constrained by the following parameters:

- **2p2h normalization parameters:** As their name indicates, these parameters regulate the total normalization of 2p2h events. In the case of interactions on carbon, there are two separate parameters, for neutrino and antineutrino events. The latter are completely uncorrelated, and do not have a prior uncertainty. Events on oxygen (i.e. in FGD2) are regulated by a third normalization parameter which scales the 2p2h normalization on carbon for events on oxygen. This is an important parameter because it constrains the overall 2p2h normalization at SK. It

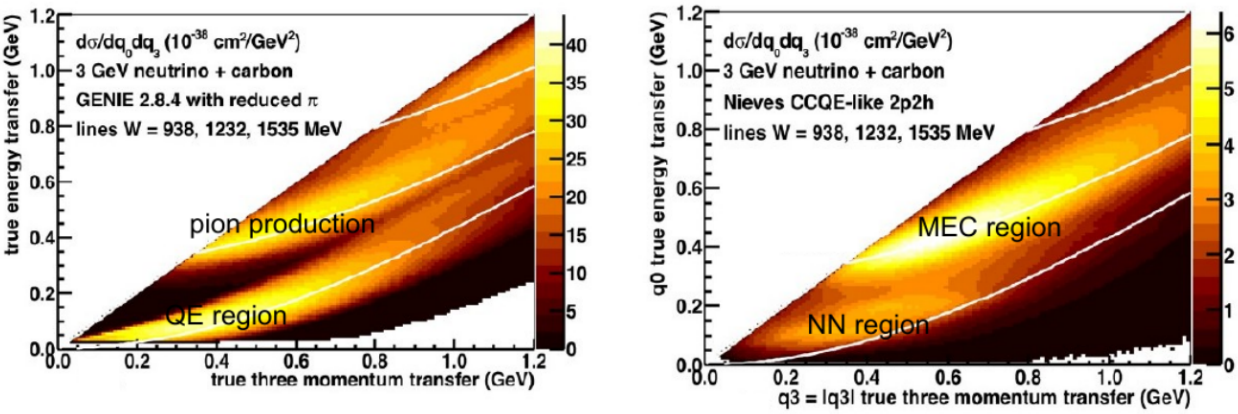

(a) (b)

Figure 3.13: The two sources of 2p2h interactions overlap with the QE-region (for NN interactions) and with the pion production region (for MEC interactions). (a) GENIE 2.8.4 prediction in the $q_0 - q_3$ phase space (see text). (b) 2p2h contributions to the total cross-section.

has been assigned a 20% uncertainty, extracted from fits to electron scattering data [89, 127], and it is fully correlated for neutrino and antineutrino events.

- **2p2h shape parameters:** 2p2h interactions are often treated as a single process, but in reality such channels have (at least) three contributions, as presented in Section 2.4.2.1. Meson exchange currents (MEC) are dominated by the pion-less decay of a Δ resonance, while nucleon-nucleon (NN) correlations affect the final state kinematics. There may also be interference between these processes. Fig. 3.13 shows that in the nominal Nieves et al. model [94], these two contributions populate separate regions in the transferred energy-transferred 3-momentum phase space ($q_0 - q_3$ space, where $Q = (q_0, q_3) = P_\nu - P_\mu$, the difference between the neutrino and muon 4-momenta). However, different models include different predictions about the relative strength and shape of these processes. Electron scattering data could in principle be used to tune 2p2h-models, but the electron-to-neutrino extrapolation is not straightforward. For this reason, two dedicated shape parameters have been introduced in the fit: 2p2h shape C and 2p2h shape O. The latter are different for interactions on carbon and oxygen. At their extreme values, they shift the entire 2p2h population to the Δ-like region (i.e. MEC region) or not-Δ-like region (i.e. NN region) in the q_0, q_3 phase space. The interval between these two values is spanned continuously by the parameters, and at its nominal value it reproduces the Nieves et al. prediction (i.e. a mix of Δ-like and not-Δ-like events). These two shape parameters affect individual events, apply identically to neutrino and antineutrino events (i.e. are fully correlated), and the 2p2h shape O parameter has a 30% correlation with the 2p2h shape C parameter. They are allowed to vary uniformly between the two extreme values (i.e. fully Δ-like or fully not-Δ-like).

- **2p2h energy dependence parameters:** This a new set of parameters, implemented for the first time in the analysis described in this thesis. The presence of 2p2h processes has been established in electron-scattering, ND280 and MINERνA data [120, 122, 128], but no single model is entirely capable of describing them. The available predictions differ greatly across the neutrino energy spectrum. A first step in trying to account for this variation is

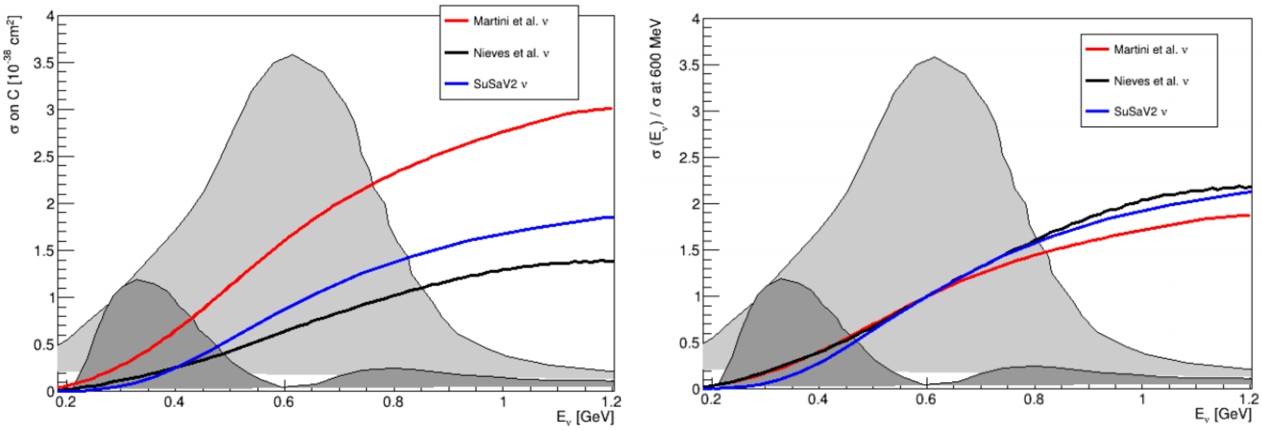

(a) (b)

Figure 3.14: Model predictions overlaid on top of the oscillated (dark grey) and unoscillated (light grey) spectrum at SK. (a) Cross-section as a function of true neutrino energy for three different 2p2h models, detailed in the text. (b) Equivalent of previous plot on the left, but where each model prediction was normalized to its value at 600 MeV in true neutrino energy.

to assign the difference between a range of models as an additional uncertainty on the 2p2h cross-section. Fig. 3.14 shows the predictions as a function of true neutrino energy for three available models: the Nieves et al. model [94], the Martini et al. model [95] and the SuSAv2 model [7, 96, 129, 130]. An arbitrary point was chosen (here, 600 MeV, corresponding to the oscillation maximum at T2K), and each model prediction was re-normalized to its cross-section at 600 MeV.

The final uncertainty parametrization is built in the following way. At each energy, the difference between the highest and the lowest renormalized predictions is calculated and stored in a function r:

$$r(E_\nu) = \frac{\sigma_R^{max}(E_\nu)}{\sigma_R^{min}(E_\nu)}. \tag{3.4}$$

A different ratio is obtained for neutrino $r_\nu(E_\nu)$ and antineutrino $r_{\bar{\nu}}(E_{\bar{\nu}})$. The final 2p2h cross-section is then parametrized by:

$$\begin{aligned}
\sigma_\nu(E_\nu) &= \sigma_\nu^{MC}(E_\nu) * N_\nu * [1 + (1 - a_l)/r_\nu(E_\nu)]\ ;\ E_\nu < 600 MeV && (3.5)\\
\sigma_\nu(E_\nu) &= \sigma_\nu^{MC}(E_\nu) * N_\nu * [1 + (1 - a_h)/r_\nu(E_\nu)]\ ;\ E_\nu > 600 MeV && (3.6)\\
\sigma_{\bar{\nu}}(E_{\bar{\nu}}) &= \sigma_{\bar{\nu}}^{MC}(E_{\bar{\nu}}) * N_{\bar{\nu}} * [1 + (1 - b_l)/r_{\bar{\nu}}(E_{\bar{\nu}})]\ ;\ E_{\bar{\nu}} < 600 MeV && (3.7)\\
\sigma_{\bar{\nu}}(E_{\bar{\nu}}) &= \sigma_{\bar{\nu}}^{MC}(E_{\bar{\nu}}) * N_{\bar{\nu}} * [1 + (1 - b_h) \times r_{\bar{\nu}}(E_{\bar{\nu}})]\ ;\ E_{\bar{\nu}} > 600 MeV && (3.8)
\end{aligned}$$

where $\sigma_\nu^{MC}(E_\nu)$ corresponds to the simulated cross-section, N_ν corresponds to the the overall normalization of the 2p2h cross-section (described in a previous bullet point) and a_l, a_h (b_l, b_h) are the parameters allowed to vary during the fit to regulate the uncertainty on the energy dependence of the cross-section, at low and high energy, respectively.

It was noted that, curiously, the nominal Nieves model used in the T2K MC generation is almost always the highest re-normalized model, except at high anti-neutrino energies ($E_{\bar{\nu}}$>600 MeV). The parameters are allowed to span the entire band formed by the re-normalized models, and they are fully uncorrelated and left free in the fit. It was found that the near detector data did not have enough sensitivity to constrain these parameters, so as a consequence they are only applied in the far detector fits.

More details about the normalization parameters can be found in [131]. The shape parameters are described in great detail in [89], and the energy dependence parameters are documented in [119].

3.3.2.2 CC1π parameters

While the main source of signal for oscillation parameter measurements is made up by CCQE-like samples (single-ring samples at SK and CC0π samples at ND280), events which contain pions (and in particular low-momentum pions) in the final state are significantly present in the single ring samples. The 1Re1de sample at SK was designed specifically in order to control this background. Events containing final state pions were thus promoted from background events to actual signal events.

The main pion-producing channels have been described in Section 2.4 in greater detail. As a reminder, the dominant channel at T2K energies is the charged-current resonant pion production (CCRES), followed by multi-pion interactions (CCMultiPi) and charged-current coherent pion production (CCCoh). The NIWG has recommended the following parameters to decribe these interactions:

- **M_A^{RES}:** As in the case of QE interactions, M_A^{RES} is an effective shape parameter regulating the effect of the axial mass in the Rein-Sehgal model [98]. The nominal value of the axial mass in resonant pion production processes in NEUT 5.4.0 is set to 0.95 GeV, and this is the value used in the MC event generation. However, the NIWG has found from looking at ANL and BNL data that this value was too low. A tune was therefore applied to the nominal MC events, corresponding to a value of M_A^{RES} =1.07 GeV. A prior Gaussian uncertainty of 0.15 GeV was also applied, with no prior correlations to other parameters.

- **C_5^A:** This shape parameter describes the normalization of the axial form factor C_5^A (0) at $Q^2 = 0$ in the Graczyk-Sobczyk [103] parametrization. As for M_A^{RES}, it was found that the NEUT nominal value suggesting a slight enhancement of this factor (1.01) was too high compared to ANL and BNL data. While the latter value was kept in the event generation, the NIWG recommended applying an additional tuning, bringing the value of this parameter to 0.95 (i.e. a suppression). This parameter has a prior Gaussian uncertainty of 0.15 and no other prior correlations.

- **Isospin 1/2 ($I_{1/2}$) background:** Other processes (in particular non-resonant channels) can also lead to pion production and constitute a source of background for resonant pion production events. The main source is non-resonant isospin 1/2 pion production, in which the initial nucleon is excited but does not produce a resonance, and then emits a final state pion. This shape parameter gives the relative size of the isospin 1/2 non-resonant background compared to the size of resonant isospin 3/2 interactions. Nominally, the NEUT value for this parameter is 1.3, and was used in the MC generation. As for the previous two parameters, the NIWG recommended applying a tuning extracted from ANL and BNL bubble chamber fits bringing it to a value of 0.96. It has a Gaussian prior uncertainty of 0.4 and no prior correlations. This dial applies to single pion production anti-neutrino events that produce a final state low momentum negative pion with a pion momentum above 200 MeV and to all single pion production neutrino events that produce a final state.

- **Isospin 1/2 ($I_{1/2}$) background for low momentum pions:** The previous dial was tuned to exclusive neutrino-mode data sets. Since reliable anti-neutrino date sets are not available, an extra *ad-hoc* dial was introduced for anti-neutrino, single pion production events that produce a final state low momentum negative pion. These events have a high chance of being reconstructed at SK as 0π events and introduce a bias in the reconstructed neutrino energy. As this is an effective freedom on top of an outdated, simplistic model, it is not clear that this freedom should influence the near detector fit or that any near detector constraint should be trusted as predictive for the far detector analysis. The NIWG thus recommended that this extra freedom only be used at the far detector, uncorrelated to the three standard resonant pion production parameters. The uncertainty for this parameter is 100% with a Gaussian prior and a lower bound of 0. This is motivated mostly by the desire to stabilise the parameter in the FD fit, where no data-constraint is expected.

- **CC Coherent (CC-Coh) parameters:** At low values of transferred momentum, the neutrino interacts with the entire nucleus, rather than with individual nucleons or quarks. This is referred to as a 'coherent' scatter and dominates the low-energy/momentum part of the spectrum. These interactions are modelled with the Berger-Sehgal model [97] and two normalization parameters control their strength. There is one parameter for ^{12}C events and one for ^{16}O events. These two parameters have a 30% prior Gaussian uncertainty extracted from MINERνA data [132], and are fully correlated in the prior.

3.3.2.3 CCDIS parameters

Deep inelastic scattering (DIS) corresponds to the interaction of a neutrino with a quark inside a nucleon through a $W^{\pm}$(CC) or Z^0(NC) boson. The nucleon is typically broken as a result, and the fragmentation of the quarks produces a number of hadrons. In the MC generation process, DIS processes are modelled in two ways within the NEUT 5.4.0 generator. The invariant mass of the hadronic system W determines two regimes where separate models are applied:

- for $W < 2\text{GeV}/c^2$, a custom-made NEUT "Multi-π" model is used.
- for $W > 2\text{GeV}/c^2$, the PYTHIA [106] generator is used.

The following parameters regulate the uncertainty model for multi-pi and DIS interactions.

- **CC Bodek-Yang DIS and CC Bodek-Yang Multi-π:** DIS interactions in NEUT are modelled according to old PDFs (GRV98 [133]), with a set of corrections from Bodek and Yang (BY) [105] to better describe the effect at low Q^2, where the perturbative QCD models used in the PDFs begin to break down. As given by the authors, these corrections do not contain any correlations, and it is thus difficult to estimate the effect of possible correlations on their errors. A simplistic parametrization was applied to account for this possibility: the difference between the GRV98 PDFs with and without BY corrections was taken and used to construct two shape uncertainty parameters (called CC Bodek-Yang DIS and CC Bodek-Yang Multi-π). The difference between the GRV98 PDFs with and without BY corrections is taken as the 1σ error on these parameters, and in order to be conservative they are allowed to vary between the basic GRV98 predictions and GRV98+twice the BY corrections (so enhancing the low Q^2 corrections). The two parameters apply separately to DIS events (i.e. those generated with PYTHIA) and Multi-π events (i.e. generated with the NEUT custom model).

- **Multi-π AGKY parameter:** In the Multi-π NEUT model, the number of hadrons produced in the interaction is randomly generated using a multiplicity model which gives the probability to have a given number of hadrons produced as a function of W. A change in the multiplicity model will affect the number of events with two or more pions and therefore the Multi-π cross-section. The AGKY multiplicity model [134] was implemented in NEUT, and used to build a shape uncertainty giving the effect of the AGKY model compared to the custom NEUT model. This dial is applied to Multi-π events, and is parametrized in an analogous way to the CC BY parameters.

- **CC Multi-π normalizations:** In addition to the shape parameters, two normalization parameters regulate the strength of CC Multi-π interactions, one for ν events and one for $\bar{\nu}$ events. The size of the uncertainty (3.5% for ν and 6.5% for $\bar{\nu}$) is extracted from the difference between the Particle Data Group (PDG) world-average CC-inclusive cross section [135] and the NEUT CC-inclusive cross section.

- **Other DIS (CC Misc.) parameters:** The previous general-purpose CCOther uncertainties are now only applied to events not falling in the DIS and Multi-π categories (generally, events with particles such as η, K, γ). For the purposes of this analysis, these events are referred to as CC Miscellaneous (CC Misc.). The shape parameter regulating the uncertainty on these events is simply parametrized as a 40% uncertainty (the size of the uncertainty on these models at E_ν =1 GeV) scaled to the neutrino energy (thus increasing at lower energies) in the following way, where σ is the uncertainty and E_ν is neutrino energy.

  $$\sigma(E_\nu) = \frac{0.4}{E_\nu} \tag{3.9}$$

  It is parametrized as an error envelope of size $2\times\sigma$ around the nominal prediction, and it has a Gaussian of 1σ size prior applied.

The parameters described above are new in the oscillation analysis, and more information can be found in [119]. The previous, general purpose dial is described in [89].

3.3.2.4 Coulomb Correction Uncertainty

The Coulomb correction (often referred to as CC, not to be confused with 'Charged Current' CC) is the change in the momentum of the outgoing lepton in a neutrino scatter due to the charge of the remnant nucleus. The size of this effect can be gauged with electron/positron scattering data (e.g. [136]) and is parametrized in the following way:

$$|V_C| = \frac{(1.27 \pm 0.10)(\mathrm{MeV\ fm})}{< r^2 >^{1/2} = 2.47\ \mathrm{fm}} Z. \tag{3.10}$$

where $|V_C|$ is the Coulomb potential and r and Z are the radius and charge, respectively, of the nucleus.

A complete treatment of the Coulomb correction would be to include the effect of the Coulomb potential in the cross-section calculation (through a lepton plane wave distorted by the electrostatic potential, for instance). In the absence of this framework, a Coulomb correction is applied *a posteriori* on the outgoing lepton momentum, according to Eq. (3.10). It should be noted that in the nucleus charge Z will be different for neutrino $(Z+1)$ and antineutrino $(Z-1)$ interactions. Table 3.5 gives the size of the corrections applied to events on ^{12}C and ^{16}O.

Target	μ^-	μ^+
Carbon	-3.6 MeV	+2.6 MeV
Oxygen	-4.3 MeV	+3.3 MeV

Table 3.5: Momentum shifts to be applied to the outgoing leptons in neutrino scattering. The values are computed by applying Eq.3.10.

The effect of Coulomb corrections on electron vs. positron scattering data is a normalization difference of 1.04, with a 3% uncertainty. This uncertainty has been included in the oscillation analysis (i.e. applied to neutrino scattering) via two normalization parameters, CC Norm. ν and CC Norm. $\bar{\nu}$, with an uncertainty of 2% and 1% respectively, and which are fully correlated. This ensures that the total CC normalization uncertainty matches the 3% from electron scattering data. These normalization parameters only apply to events whose true neutrino energy is between 300 MeV and 600 MeV. The reason for this range is that there is an energy dependence of the uncertainty: very energetic leptons will be weakly affected by the electrostatic potential, and the correction should approach unity.

An extensive discussion of these parameters and the motivation of Coulomb corrections can be found in [119].

3.3.2.5 ν_e/ν_μ and $\bar{\nu}_e/\bar{\nu}_\mu$ differences

ND280 only uses ν_μ and $\bar{\nu}_\mu$ events to constrain cross-section systematic parameters. However, SK also has e-like samples, containing ν_e and $\bar{\nu}_e$ events. It is therefore necessary to scale the effect of parameters obtained from ν_μ and $\bar{\nu}_\mu$ measurements to ν_e and $\bar{\nu}_e$ events.

Two main sources of difference are considered in this analysis.

- **Secondary class currents:** Due to the mass difference between the outgoing lepton (e in ν_e interactions and μ in ν_μ interactions), the interaction phase space is different. While these mass effects are included in the simulations, they are also convoluted with nucleon form factors and with nuclear response functions which in turn have large and not well known uncertainties. A particular difference is seen in a group of form factors, called secondary class currents (SCC) due to their second order effect.

- **Radiative corrections:** A full computation of the cross-section would contain a multitude of radiative corrections, such as the emission of real photons both from leptons and hadrons, lepton-hadron exchange of virtual photons and photon loops in the lepton leg of the Feynman diagram. This is not available yet, and so far only leading-order corrections are included. However, these contributions depend on the lepton mass as well, and are actually larger for electrons compared to muons.

These effects have been included in an approximate way via two normalization parameters, ν_e/ν_μ and $\bar{\nu}_e/\bar{\nu}_\mu$. They have a 2% uncertainty, uncorrelated between neutrino and antineutrino, stemming from SCC and partially radiative corrections, and an additional 2% uncertainty, fully anti-correlated between neutrino and antineutrino, stemming from radiative corrections. The two parameters have the following covariance matrix:

$$V_{\nu_e,\bar{\nu_e}} = V_{SCC} + V_{rad.corr.} = \begin{pmatrix} 2 \times 0.02^2 & -0.02^2 \\ -0.02^2 & 2 \times 0.02^2 \end{pmatrix}$$

3.3.2.6 Neutral current interactions

Neutral current (NC) interactions are a source of background. The majority of NC events are filtered out at the selection stage. However, at SK, NC events producing a photon (NC1γ) and coherent NC events producing a neutral pion (NC1π^0) constitute an important source of background. The photon from the NC1γ interaction, as well as the photons from the π^0 decay from NC1π^0 interactions, can undergo conversion into an electron-positron pair (e^-e^+) which may be mis-identified as an electron-like ring in the 1Re and 1Re1de samples (which should be enriched in CCQE and CCRES events). It is therefore important to control these processes at both the ND and the FD. The size of NC contributions is controlled by a set of four parameters[11].

- **NC Coherent normalization:** Similarly to its CC-Coherent counterpart, the NC coherent interaction probes the nucleus rather than its finer structure. In such interactions, a forward-going π^0 is emitted from the exchanged $W^\pm$ boson. This interaction is modelled with the same Berger-Seghal [98] model used for CC coherent interactions. A normalization parameter is used to control this process, with a 30% Gaussian uncertainty, and has no prior correlations.

- **NC1γ normalization:** This process involves the emission of a photon during a non-resonant NC neutrino scatter. A study by Wang *et al.* [137] showed that the NEUT NC1γ cross section was roughly half of the cross section calculated from a model by Alvarez-Ruso as a function of the photon energy or the neutrino energy. There is no control sample at ND280 for such processes and the limited external data cannot provide a constraint yet. It was therefore decided to enhance the NEUT NC1γ prediction by a factor of 2, and apply a conservative 100% Gaussian uncertainty on this parameter.

- **NC Other normalization:** The other possible sources of NC background events are lumped together in the 'NC Other' category. The latter includes elastic, Multi-π and DIS NC events. These events are regulated by two normalization parameters, one applied at the ND and one at the FD. A 30% Gaussian uncertainty around the nominal NEUT prediction was applied to each of these parameters, and the ND constraints on the 'NCOther Near' parameter are not propagated to the far detector (it is instead used in the marginalization), which has its own dedicated 'NCOther Far' parameter.

3.3.2.7 Final State Interactions

As explained in Section 2.4.4, final state interactions (FSI) alter the observed final state particles, and can introduce a bias in the neutrino energy reconstruction. NEUT models FSI via intra-nuclear cascade models [138]. A pion produced in a neutrino-nucleon interaction is propagated in steps through the nucleus, and at each step the probability of one of the processes mentioned in the previous paragraph is evaluated. This is done until the pion either is absorbed, or exits the nucleus. Quasi-elastic, single charge exchange and absorption interaction probabilities for low momentum

---

[11] Elastic NC events are unlikely to be reconstructed in any SK sample, as they do not produce final state leptons.

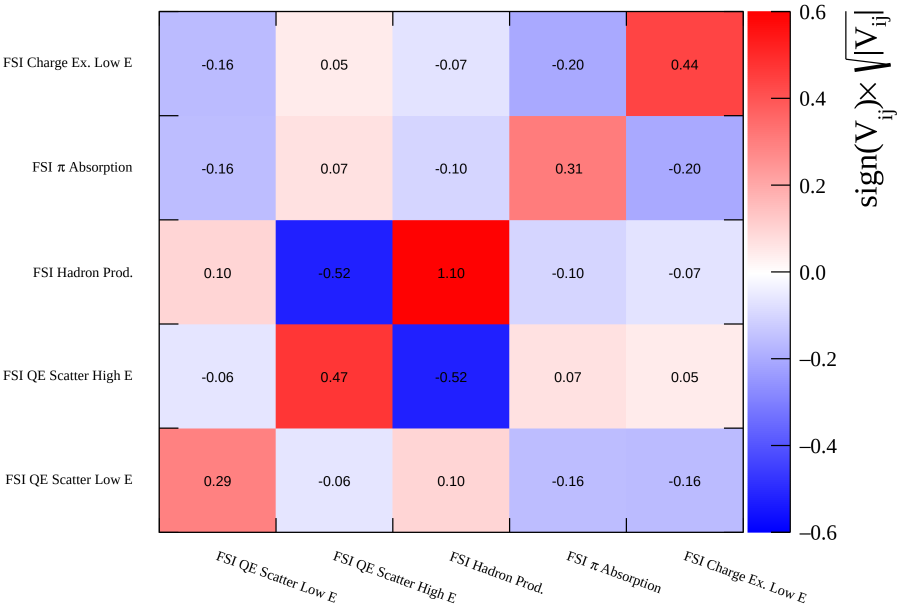

Figure 3.15: Fractional covariance matrix used to constrain near detector FSI parameters. These constraints are applied in the ND fit, which then passes on tighter constraints to the FD fitters.

pions are determined based on the Salcedo *et al.* model [139], while for high momentum pions the interaction probabilities are calculated from $\pi^{\pm}$ scattering off free proton and deuteron cross section data compiled by the PDG [140]. For this analysis, an improved fitting procedure was used (for details see [141]) and also uses recent DUET data [142].

Up until this analysis, dedicated FSI parameters were implemented only at the near detector. The effect of FSI at SK was modelled through the SK detector covariance matrix, which contained the effect of varying NEUT FSI parameters. This approach did not allow for the ND constraint on FSI parameters to be applied at SK. The analysis described in this thesis is the first in which corresponding FSI parameters are implemented and used in FD fits, with a 100% correlation to the ND FSI parameters.

Five shape parameters are used in this analysis. Their uncertainties and correlations obtained via the methods described above are presented in Fig. 3.15.

3.3.2.8 Summary of cross-section uncertainty model

The uncertainties described above are summarized in Table 3.6 and the final correlation matrix used as an input to the near detector fit is presented in Fig. 3.16. As a reminder, like the flux parameters, the cross-section parameters are first constrained at the near detector. As a result of the ND fit, we obtain a correlation matrix, which introduces, in particular, correlations between flux and cross-section parameters, and correlations between cross-section parameters assigned to different interaction types. The resulting ND fit correlation matrix used as input to subsequent SK analyses is presented in Chapter 5.

Parameter	Nom. (Gen.)	Uncertainty	Prior	Type	ND/SK
M_A^{QE}	1.03 (1.21) GeV	0.06 GeV	Gaus.	Shape	ND, SK
Q^2 norm. 0.00-0.05 GeV^2 (0)	1.00	1.00	Flat	Norm.	ND, SK
Q^2 norm. 0.05-0.10 GeV^2 (1)	1.00	1.00	Flat	Norm.	ND, SK
Q^2 norm. 0.10-0.15 GeV^2 (2)	1.00	1.00	Flat	Norm.	ND, SK
Q^2 norm. 0.15-0.20 GeV^2 (3)	1.00	1.00	Flat	Norm.	ND, SK
Q^2 norm. 0.20-0.25 GeV^2 (4)	1.00	1.00	Flat	Norm.	ND, SK
Q^2 norm. 0.25-0.50 GeV^2 (5)	1.00	0.11	Gaus.	Norm.	ND, SK
Q^2 norm. 0.50-1.00 GeV^2 (6)	1.00	0.18	Gaus.	Norm.	ND, SK
Q^2 norm. 1.00-10.0 GeV^2 (7)	1.00	0.40	Gaus.	Norm.	ND, SK
$E_{b,\nu}^{C}$	2 (0) MeV	6 MeV	Gaus.	Mom. shift	ND
$E_{b,\bar{\nu}}^{C}$	0 (0) MeV	6 MeV	Gaus.	Mom. shift	ND
$E_{b,\nu}^{O}$	4 (0) MeV	6 MeV	Gaus.	Mom. shift	ND, SK
$E_{b,\bar{\nu}}^{O}$	0 (0) MeV	6 MeV	Gaus.	Mom. shift	ND, SK
2p2h norm. ν	1.0	1.0	Flat	Norm.	ND, SK
2p2h norm. $\bar{\nu}$	1.0	1.0	Flat	Norm.	ND, SK
2p2h norm. C to O	1.0	0.2	Gaus.	Norm.	ND
2p2h shape C	0.0	1.0	Gaus.	Shape	ND
2p2h shape O	0.0	1.0	Gaus.	Shape	ND, SK
2p2h E. dep. low-E_ν	1	1	Flat	Shape	SK
2p2h E. dep. high-E_ν	1	1	Flat	Shape	SK
2p2h E. dep. low-$E_{\bar{\nu}}$	1	1	Flat	Shape	SK
2p2h E. dep. high-$E_{\bar{\nu}}$	1	1	Flat	Shape	SK
M_A^{RES}	1.07 (0.95) GeV	0.15 GeV	Gaus.	Shape	ND, SK
C_5^A	0.96 (1.01)	0.15	Gaus.	Shape	ND, SK
$I_{1/2}$	0.96 (1.3)	0.4	Gaus.	Shape	ND, SK
$I_{1/2}$ low. p_π	0.96 (1.3)	1.3	Gaus.	Shape	SK
CC norm. ν	1.00	0.02	Gaus.	Norm.	ND, SK
CC norm. $\bar{\nu}$	1.00	0.01	Gaus.	Norm.	ND, SK
ν_e/ν_μ	1.000	0.028	Gaus.	Norm.	ND, SK
$\bar{\nu}_e/\bar{\nu}_\mu$	1.000	0.028	Gaus.	Norm.	ND, SK
CC BY DIS	0	1	Gaus.	Shape	ND, SK
CC BY Multi-Pi	0	1	Gaus.	Shape	ND, SK
CC AGKY Multi-Pi	0	1	Gaus.	Shape	ND, SK
CC Misc.	1	1	Gaus.	Norm.	ND, SK
CC DIS Multi-Pi Norm. ν	1.000	0.035	Gaus.	Norm.	ND, SK
CC DIS Multi-Pi Norm. $\bar{\nu}$	1.000	0.035	Gaus.	Norm.	ND, SK
CC Coh. C	1.0	0.3	Gaus.	Norm.	ND
CC Coh. O	1.0	0.3	Gaus.	Norm.	ND, SK
NC Coh.	1.0	0.3	Gaus.	Norm.	ND, SK
NC 1γ	1	1	Gaus.	Norm.	SK
NC Other Near	1	0.3	Gaus.	Norm.	ND
NC Other Far	1	0.3	Gaus.	Norm.	SK
π-FSI QE	1.069	0.313	Gaus.	Shape	ND, SK
π-FSI QE High	1.824	0.859	Gaus.	Shape	ND, SK
π-FSI Hadron Prod.	1.002	1.101	Gaus.	Shape	ND, SK
π-FSI Absorption	1.404	0.432	Gaus.	Shape	ND, SK
π-FSI Charge Exchange	0.697	0.305	Gaus.	Shape	ND, SK

Table 3.6: Summary of cross-section systematic parameters. The second column gives the nominal value used to tune the prediction, and the value used in the MC generation is given in parentheses. The “Prior” column indicates the type of prior applied - gaussian or flat. The last column indicates whether the parameter is varied in the near detector fit, the far detector fit, or both. It should be noted that for parameters which are varied at both the ND and SK, the error during the SK fit is not the one given in the table, but rather the one obtained as a result of ND fit. Most parameters are either shape or normalization parameters, with the exception of the binding energy parameters, which act as a momentum shift.

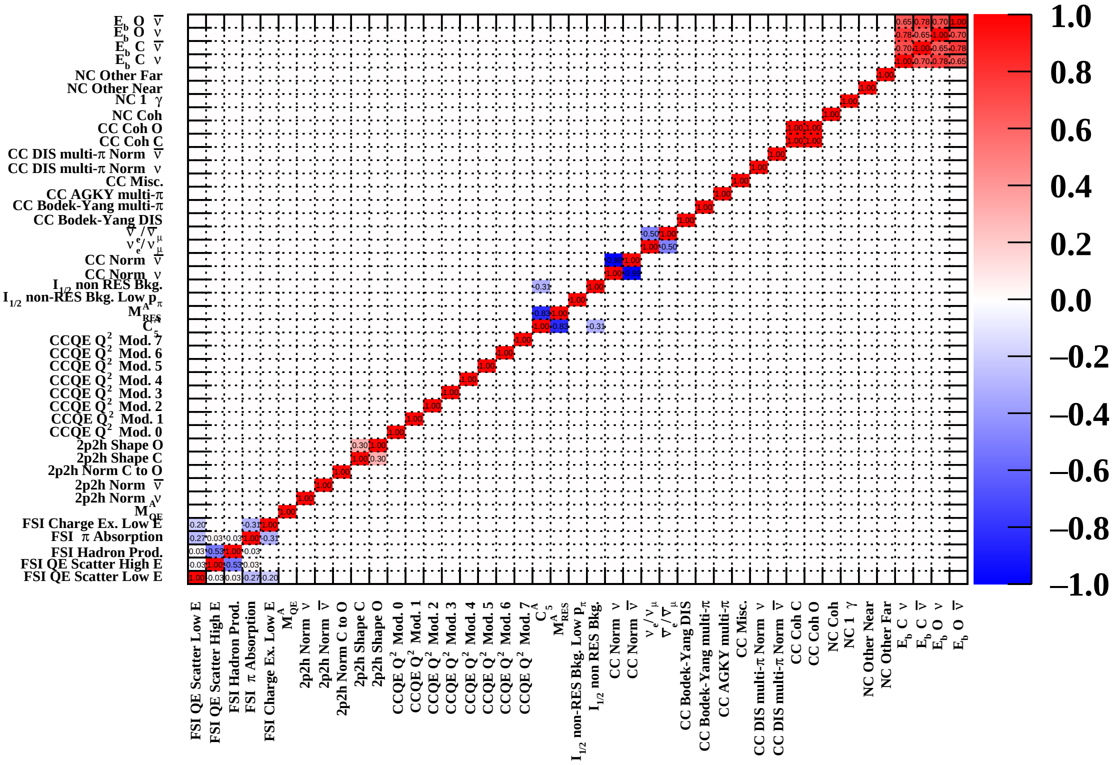

Figure 3.16: Correlation matrix for cross-section parameters used as an input to the near detector fit. This is a correlation matrix, not a covariance matrix, so the values show the correlation strength, rather than the absolute error. This choice was made for readability, as the cross-section parameters have very different ranges for their errors.

3.3.3 Detector parameters

The detector parameters implementation and parametrization is quite different between the near and the far detector. The two detector complexes have different structures, particle identification techniques and flux exposures, so each one needs a different parametrization.

3.3.3.1 ND280 Detector Systematics

There are three categories of near detector systematics, with corresponding propagation procedures.

- **Observable-variation systematics:** The systematics in this category affect the physical observables measured at ND280. As the samples used in the oscillation analysis are binned according to observable particle kinematics (currently, in reconstructed muon momentum, p_μ, and muon direction, $\cos\theta_\mu$), the effect of detector systematics on these observables may change the sample, by migrating events between bins or between samples. There are dedicated observable-variation systematics for each type of sub-detector used in the reconstruction process. The TPC momentum scale and the TPC momentum resolution control the accuracy of the measurement of a particle's momentum if it passes through a TPC. The TPC PID systematic describes the ability to discriminate between particle identities - this is especially important as the samples used in the oscillation analysis are split according to number of final state pions, and the selection process relies on an accurate identification of a muon candidate. The TPC magnetic and electric field distortion systematic stems from the fact that both of these fields are not entirely uniform and may impact track reconstruction. There are also two FGD observable-variation systematics: the FGD PID, similar to the TPC PID, and the FGD1-FGD2 time-of-flight, which assesses the precision of FGD time-of-flight information to discriminate between forward- and backward-going tracks.
  Each observable-variation systematic is applied in a different way depending on whether it is probed against truth information or data. The methods of applying each systematic are described extensively in [109].

- **Efficiency systematics:** The systematics in this class are based on studies comparing data and MC predictions in well known control samples. They assume that the ratio between the efficiencies in data and MC used in the analysis is the same as the ratio between the efficiencies of data and MC for control samples. They do not affect the event observables, but modify the relative weight of an event within a sample.

- **Normalization systematics:** These uncertainties affect the total event normalization. For example, an error is associated with the mass of an FGD module: if the true mass is larger than the measured one, the event rate should increase.

More information can be found in [109].
Ideally, the simultaneous effect of the near detector systematic errors would be evaluated on an event-by-event basis during the near detector fit. In reality, this process is computationally expensive and bin migration of events may give rise to discontinuities in the likelihood computation[12]. A compromise can be reached by parametrizing the effect of near detector uncertainties in the form of bin-content normalizations in the fit space. In order to obtain these normalizations, the detector

---

[12] This is in principle only a problem for the BANFF fit, where discontinuities in the likelihood surface will cause convergence problems. In the MCMC based fitter MaCh3, event migration between bins is not a problem.

systematics are varied in 500 toy experiments in a dedicated framework. The variations induced on the nominal MC prediction are then used to extract the size of the systematic effect on each bin used in the fit. The process of varying the detector systematics also produces a covariance matrix, introducing sizable correlations between samples and adjacent bins. There are 574 such parameters, called *observable-normalization parameters* (sometimes referred to as *obsnorm* parameters). Since the number of kinematic bins used in the fit is very large (4238 bins), the binning for detector parameter systematics is coarser to reduce computation time. This is justified choice, since the bin reduction was chosen based on adjacent bins with similar responses to detector systematics variations. The following binning was used to index observable normalization parameters:

- **FHC ν_μ CC0π:**
  p_μ **(MeV/c):** 0, 300, 1000, 1250, 1500, 2000, 3000, 5000, 30000 - 8 bins.
  cosθ_μ: -1.0, 0.6, 0.8, 0.85, 0.9, 0.92, 0.98, 0.99, 1.0 - 8 bins.
- **FHC ν_μ CC1π:**
  p_μ **(MeV/c):** 0, 300, 400, 700, 800, 1000, 1500, 2000, 5000, 30000 - 9 bins.
  cosθ_μ: -1.0, 0.6, 0.8, 0.9, 0.92, 0.94, 0.96, 0.98, 0.99, 1.0 - 9 bins.
- **FHC ν_μ CCOther:**
  p_μ **(MeV/c):** 0, 300, 400, 700, 800, 900, 1250, 2000, 3000, 5000, 30000 - 10 bins.
  cosθ_μ: -1.0, 0.6, 0.8, 0.85, 0.9, 0.92, 0.96, 0.98, 0.99, 1.0 - 9 bins.
- **RHC $\bar{\nu}_\mu$ CC0π:**
  p_μ **(MeV/c):** 0, 300, 2000, 4000, 30000 - 4 bins.
  cosθ_μ: -1, 0.6, 0.8, 0.9, 0.96, 1 - 5 bins.
- **RHC $\bar{\nu}_\mu$ CC1π:**
  p_μ **(MeV/c):** 0, 500, 30000 - 2 bins.
  cosθ_μ: -1, 0.7, 1 - 2 bins.
- **RHC $\bar{\nu}_\mu$ CCOther:**
  p_μ **(MeV/c):** 0, 600, 800, 30000 - 3 bins.
  cosθ_μ: -1, 0.7, 0.95, 0.97, 1 - 4 bins.
- **RHC ν_μ CC0π:**
  p_μ **(MeV/c):** 0, 300, 1500, 30000 - 3 bins.
  cosθ_μ: -1, 0.7, 1 - 2 bins.
- **RHC ν_μ CC1π:**
  p_μ **(MeV/c):** 0, 600, 800, 30000 - 3 bins.
  cosθ_μ: -1, 0.7, 1 - 2 bins.
- **RHC ν_μ CCOther:**
  p_μ **(MeV/c):** 0, 600, 30000 - 2 bins.
  cosθ_μ: -1, 0.7, 1 - 2 bins.

The 574 ND280 detector parameters are indexed as a function of p_μ bins, and then listing the following cosθ_μ bins. For example, the first eight parameters correspond to the 8 cosθ_μ bins associated with the [0,300] MeV/c p_μ bin, the next eight parameters are the cosθ_μ bins corresponding

to the [300, 1000] MeV/c p_μ bin, and so on.
The near detector covariance matrix used in this analysis is presented in Fig. 3.17.

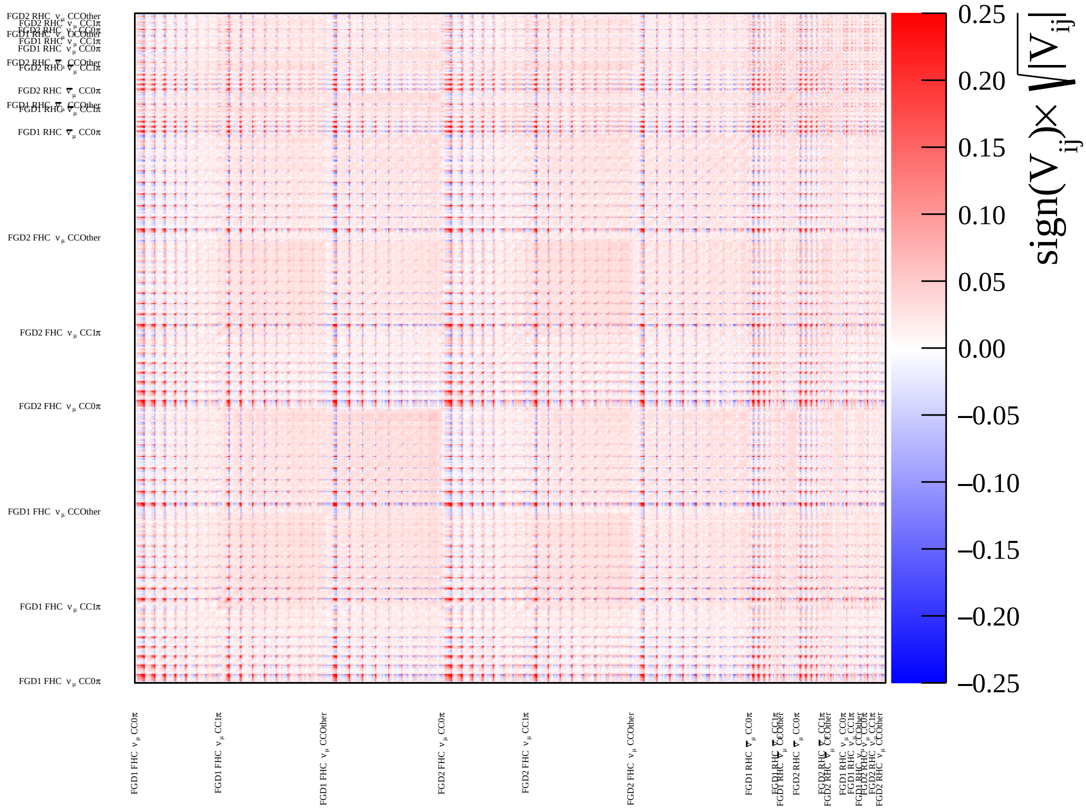

Figure 3.17: Fractional detector covariance matrix used to constrain near detector systematic variations. Each label corresponds to the first p_μ bin in a category, and the way the bins are indexed is explained in the text.

3.3.3.2 SK Detector Systematics

The SK covariance matrix is provided by the T2K-SK group, and is documented in detail in [143, 144, 145]. The fundamental sources of detector systematic uncertainties are those which affect the light signal collection by the PMTs - the water transparency and the PMT timing resolution and gain. Similarly to the ND280 detector systematics, SK systematics are estimated based on the cuts applied to construct the samples used in the analysis. Three types of control samples are used to estimate detector systematic uncertainties: cosmic-ray muons stopping in the detector, atmospheric neutrino samples of all of the relevant species, and a hybrid π^0 sample. The detector systematic parameters are then varied in the same way as the ND280 systematics via MC toy experiments.
The resulting variations are used to extract a covariance matrix, similar to the near detector covariance matrix. This means that the diagonal elements give the size of the uncertainty, and are applied as bin-content normalizations during the fit. This covariance matrix can either be indexed

by bins in reconstructed neutrino energy or reconstructed lepton momentum. The reason for this separation is that different analyses use different observables during the fit - MaCh3 and VaLOR use a reconstructed energy binning, whereas p-theta nominally uses a reconstructed lepton momentum and angle binning (although it has the possibility to use a reconstructed neutrino energy and lepton angle binning).
The SK covariance matrix used in this analysis consists of 45 parameters:

- **FHC 1Re**: 12 parameters - 3 for oscillated ν_e and $\bar{\nu}_e$ CC events, 3 for beam ν_μ and $\bar{\nu}_\mu$ CC events, 3 for beam ν_e and $\bar{\nu}_e$ CC events, and 3 for NC events.
- **FHC 1Rμ**: 6 parameters - 3 for beam ν_μ and $\bar{\nu}_\mu$ CCQE events, one for ν_μ and $\bar{\nu}_\mu$ CCnQE (non quasi-elastic) events, one for beam ν_e and $\bar{\nu}_e$ CC events and one for NC events.
- **RHC 1Re**: 12 parameters - 3 for oscillated ν_e and $\bar{\nu}_e$ CC events, 3 for beam ν_μ and $\bar{\nu}_\mu$ CC events, 3 for beam ν_e and $\bar{\nu}_e$ CC events, and 3 for NC events.
- **RHC 1Rμ**: 6 parameters - 3 for beam ν_μ and $\bar{\nu}_\mu$ CCQE events, one for ν_μ and $\bar{\nu}_\mu$ CCnQE (non quasi-elastic) events, one for beam ν_e and $\bar{\nu}_e$ CC events and one for NC events.
- **FHC 1Re1de**: 8 parameters - 2 for oscillated ν_e and $\bar{\nu}_e$ CC events, 2 for beam ν_μ and $\bar{\nu}_\mu$ CC events, 2 for beam ν_e and $\bar{\nu}_e$ CC events and 2 for NC events.
- **SK energy scale uncertainty**: This is the last SK detector uncertainty and the only one which is not applied as a bin-content normalization. The SK energy scale error describes the discrepancy between the true and reconstructed energy scale itself and is estimated with cosmic ray muons and LINAC electrons control samples. Its value is fixed at 2.4% for all neutrino energies, and quantifies the uncertainty on the detector energy calibration.

The final covariance matrix actually has two more contributions. In addition to the detector parameter uncertainties, it contains the uncertainty on hadron secondary interactions (SI) in the detector and the nucleus involved in the interaction, as well as uncertainties related to photo-nuclear reactions (PN), in which photons are absorbed by surrounding nuclei. These two effects are evaluated separately and produce two extra covariance matrices. It is worth mentioning that in previous analyses, there was a third contribution describing the effect of final state interactions (FSI). In this analysis, for the first time, the same FSI cross-section parameters used in the near-detector fit are used in far-detector fits, and are directly constrained by the near detector. Hence, the FSI contribution is no longer included in the detector covariance matrix.
The resulting purely detector, SI and PN matrices are then combined to form the general SK detector covariance matrix, whose fractional version is presented in Fig. 3.18.

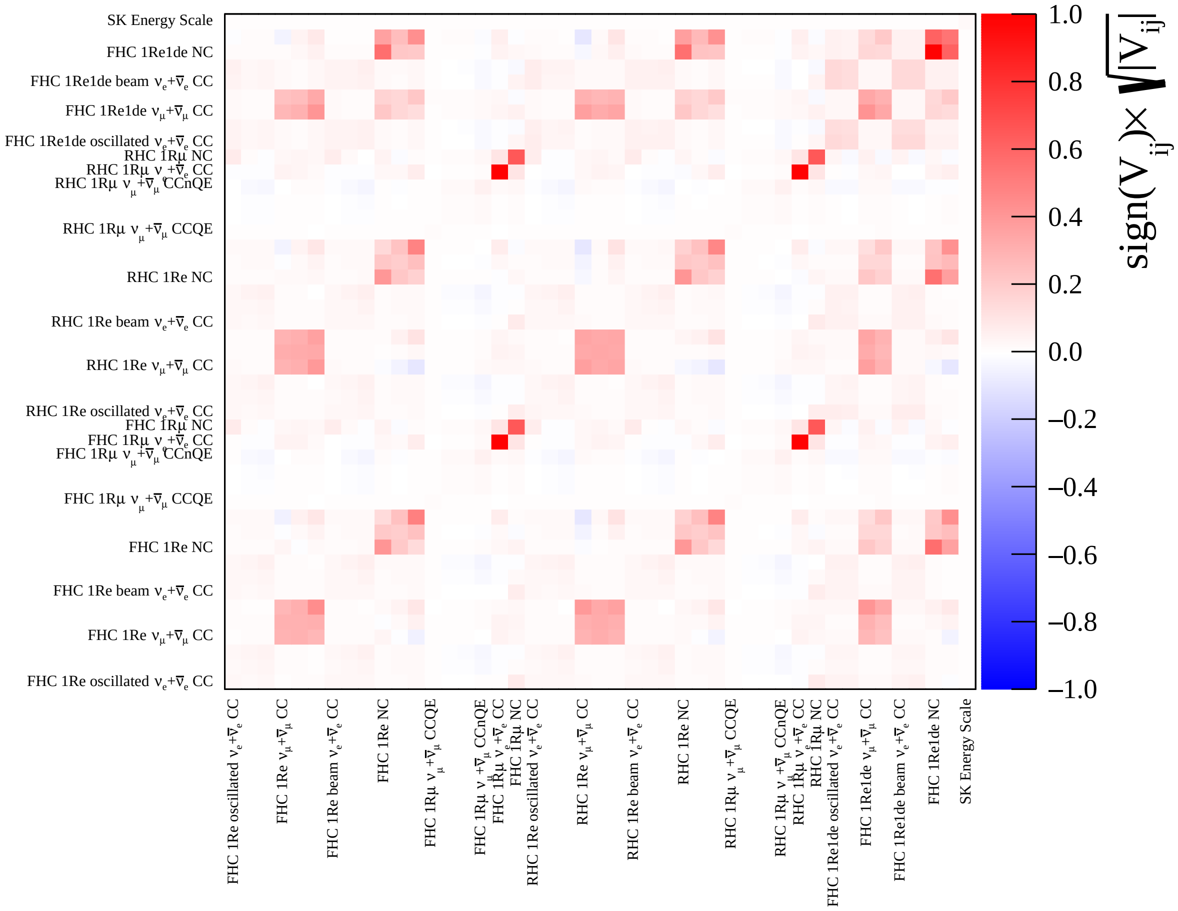

Figure 3.18: Fractional detector covariance matrix (including SI and PN uncertainties) used in the far detector fits. Note: for illustrative purposes, the elements of this covariance matrix are indexed according to reconstructed neutrino energy bins. There is an equivalent version indexed by lepton momentum bins. The bin labels indicate the first bin in a category (full description in the text).

Chapter 4

The Near Detector Fit: Framework and Validation

The BANFF fit (**B**eam **A**nd **N**D280 **F**lux extrapolation task **F**orce) is a semi-frequentist fit to near detector data. The data are binned in 2D distributions in reconstructed muon momentum (p_μ) and reconstructed muon orientation with respect to the neutrino beam axis ($\cos\theta_\mu$). The BANFF fit aims to provide constraints on flux and cross-section systematic parameters in the context of the T2K oscillation analysis. This chapter describes the statistical framework used during the BANFF fit, and presents the results of validation studies to ensure the proper operation of the framework. The following chapter will present the results obtained after the fit to ND280 data collected through 2020.

I was one of two analyzers responsible for performing the BANFF fit for the 2020 oscillation analysis [1].

4.1 Statistical Framework

The BANFF fit searches for an optimal set of parameters describing how systematic uncertainties change the predictions on the event rate, given the data. During the fit, a global likelihood is maximized with using the MINUIT package in ROOT. It uses the MIGRAD gradient descent minimization algorithm.

The near detector likelihood has several contributions:

- For each bin, the number of events is distributed according to a Poisson distribution:

$$P(N_i^{obs}|N_i^{pred}) = \frac{(N_i^{pred})^{N_i^{obs}} e^{-N_i^{pred}}}{N_i^{obs}!}. \tag{4.1}$$

  $P(N_i^{obs}|N_i^{pred})$ is the probability to observe N_i^{obs} events in the i-th bin and N_i^{pred} is the predicted number of events in the i-th bin. The product of these terms over all of the analysis bins is the statistical contribution to the likelihood, $\mathcal{L}_{Stat.}$

- Multivariate gaussian penalty terms for the different sources of systematic uncertainties:

$$\pi(\vec{s}) = (2\pi)^{n_s/2}|V_s|^{1/2}e^{-\frac{1}{2}\Delta\vec{s}(V_s)^{-1}\Delta\vec{s}^T}. \tag{4.2}$$

> $\vec{s}$ is the vector of systematic parameters ($\vec{s} \in \{\vec{b}, \vec{x}, \vec{d}\}$, where $\vec{b}, \vec{x}, \vec{d}$ correspond to the flux, cross-section and detector parameters, respectively), n_s is the size of the vector (i.e. the number of systematic parameters of a given category), $\Delta\vec{s}$ is the vector giving the difference between a considered set of systematic parameter values and the nominal value of the systematic parameters (and $\Delta\vec{s}^T$ its transposed vector), and V_s is the covariance matrix for a given set of systematic parameters.

The maximized quantity is the likelihood ratio between the likelihood at a given point in the systematic parameter space, for N_i^{pred} events in bin i, and the likelihood of the nominal model (i.e. for the nominal value of the systematic parameters and at the number of observed data events, N_i^{obs}, in bin i):

$$\mathcal{L}_{ND280} = \frac{\pi(\vec{b})\pi(\vec{x})\pi(\vec{d}) \prod_{i=1}^{N_{bins}} \left((N_i^{pred})^{N_i^{obs}} e^{-N_i^{pred}} / N_i^{obs}!\right)}{\pi(\vec{b}_{nom})\pi(\vec{x}_{nom})\pi(\vec{d}_{nom}) \prod_{i=1}^{N_{bins}} \left((N_i^{obs})^{N_i^{obs}} e^{-N_i^{obs}} / N_i^{obs}!\right)}, \tag{4.3}$$

where $\pi(\vec{b}_{nom})$, $\pi(\vec{x}_{nom})$ and $\pi(\vec{d}_{nom})$ are the gaussian penalty terms evaluated at their nominal values, and N_{bins} is the total number of bins.
In practice, it is easier to *minimize* the negative logarithm of $\mathcal{L}_{ND280}$:

$$\begin{aligned}
-2\log\mathcal{L}_{ND280} =& 2\sum_{i=0}^{N_{bins}} \left(N_i^{pred}(\vec{b}, \vec{x}, \vec{d}) - N_i^{obs} + N_i^{obs} \log \frac{N_i^{obs}}{N_i^{pred}(\vec{b}, \vec{x}, \vec{d})}\right) \\
&+ \sum_{i=0}^{N_b}\sum_{j=0}^{N_b} \Delta\vec{b}_i \left(V_b^{-1}\right)_{ij} \Delta\vec{b}_j^T \\
&+ \sum_{i=0}^{N_x}\sum_{j=0}^{N_x} \Delta\vec{x}_i \left(V_x^{-1}\right)_{ij} \Delta\vec{x}_j^T \\
&+ \sum_{i=0}^{N_d}\sum_{j=0}^{N_d} \Delta\vec{d}_i \left(V_d^{-1}\right)_{ij} \Delta\vec{d}_j^T \\
&\equiv \Delta\chi^2_{ND280}
\end{aligned} \tag{4.4}$$

where N_{bins}, N_b, N_x and N_d are the numbers of bins, flux parameters, cross-section parameters and detector parameters, respectively.
It is worth noting that for sufficient statistics, Eq. (4.4) resembles a χ^2 distribution, and will therefore be referred to as $\Delta\chi^2_{ND280}$.
During the fit, the $\Delta\chi^2_{ND280}$ is minimized as a function of the systematic parameters. The nominal values of the systematic parameters are referred to as their “pre-fit” values, whereas the set of parameter minimizing $\Delta\chi^2_{ND280}$ as a result of the fit are called “post-fit” values (or parameters). The post-fit values are accompanied by a set of post-fit uncertainties. Before the fit, no prior correlations are assumed to exist between flux, cross-section and detector parameters. After the fit, due to the fact that these three sets of parameters are varied simultaneously, correlations will arise between the three categories. These are obtained via the post-fit covariance matrix, which is the inverse of the Hessian matrix, containing the second derivatives of the parameters at their minimized values. The latter is obtained using the MINUIT HESSE algorithm.

4.2 Validating the Fitter

Before fitting the ND280 data, it is important to check that the fitter is working correctly. There are a number of procedures for doing this, detailed below. Only illustrative results will be shown in this thesis, but the complete set of validations can be found in [146].

It should be noted that the validations were performed with a slightly modified cross-section error model than the one presented in the previous data-MC pre-fit comparison. Based on T2K and MINERνA data [121, 122], a low-Q^2 suppression was needed and initially applied as a tuning of the nominal model. This tuning was used to perform the validations and simulated data studies, but was not applied in the data fit. The low-Q^2 parameters are left free during the data fit, letting the ND data, which has enough statistical power, constrain them. This was done to avoid "over-fitting", as the initial tunings were based on T2K data as well [119].

4.2.1 Asimov Fits

An Asimov fit is a fit in which the data are replaced with the nominal MC prediction. The results of such a fit give two pieces of information: first, they allow to check that the fitting framework can recover the well known nominal model predictions; second, this is the equivalent of a maximum-sensitivity fit, since the "data" is the nominal MC and by definition it matches the nominal prediction perfectly. Due to the correlations which arise during the fit between the different categories of parameters, the overall errors on the systematic parameters are reduced. The expected result of an Asimov fit is therefore to see the post-fit values of the systematic parameters at their nominal value, and gauge the extent to which the errors can be reduced.

Fig. 4.1 presents a selected set of parameters to illustrate the results of the Asimov fit. As expected, the Asimov fit successfully recovers the pre-fit values of all of the parameters. In addition, a significant reduction of errors can be seen across all parameter categories. In particular, flux parameters at both ND280 and SK are constrained to the level of 5%, whereas their prior errors are of the order of 8-10%. It should be noted that some cross-section parameters are fixed during the BANFF fit. This is the case for the low-momentum pion $I_{1/2}$ non-resonant background, NC1γ and NC Other Far. These parameters are not varied in the BANFF fit, but are instead adjusted in the far detector fit, because the ND fit does not have enough statistical power to constrain them.

4.2.1.1 Correlations

Fig. 4.2 shows the evolution of parameter correlations[1] before (left) and after (right) the Asimov fit. Anti-correlations appear between the flux, detector, and cross-section parameters.

Fig. 4.3 shows a zoom on the correlations between flux and cross-section parameters. Since the flux parameters have a normalization-like effect, they anti-correlate strongly with normalization-like cross-section parameters. This is the case for the Q^2 normalization parameters and for CC0π and CC1π normalization parameters. Finally, Fig. 4.4 shows a zoom on the cross-section parameter correlations. Relatively strong correlations appear between the all of the Q^2 parameters, due to the fact that several Q^2 parameters can affect the same p_μ-cosθ_μ bin. The high Q^2 parameters anti-correlate with M_A^{QE}, as they affect the same high-Q^2 region of the spectrum. In general, there are strong correlations between parameters which affect events with similar topologies - i.e. between

---

[1] In this thesis, "correlation" is used as a generic term which can signify both positive or negative correlation (anti-correlation).

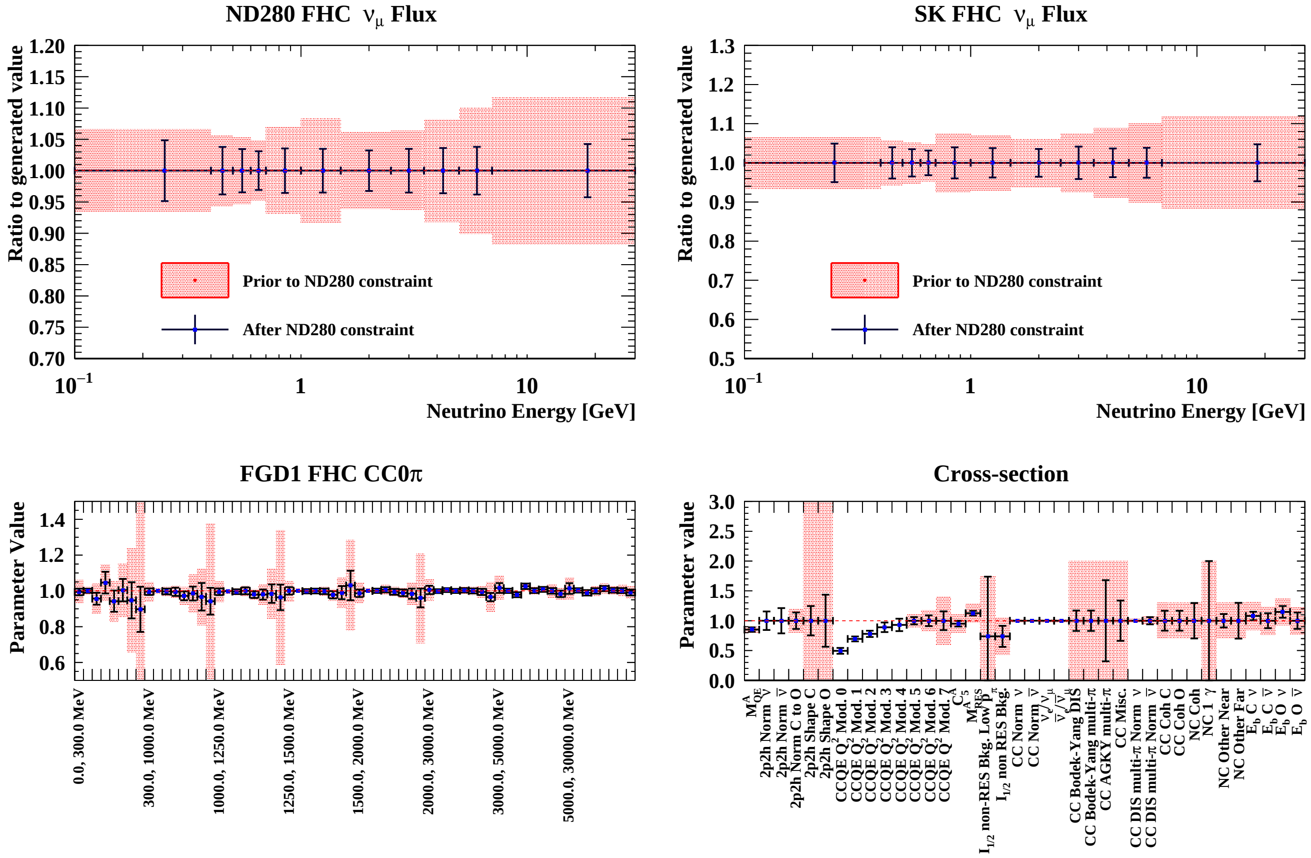
ND280 FHC ν_μ Flux

SK FHC ν_μ Flux

FGD1 FHC CC0π

Cross-section

Figure 4.1: Selected sets of parameters, before (shaded red) and after (blue points with black error bars) the BANFF Asimov fit. All parameters and prior uncertainties are normalized to their generated MC value. The near detector tuning for detector and cross-section parameters can be seen in cases where the pre-fit value deviates from the generated value of 1. Note that the prior uncertainties are shown only for parameters which have a prior Gaussian penalty term. As such, some cross-section parameters which are left completely free during the fit do not have a prior uncertainty.

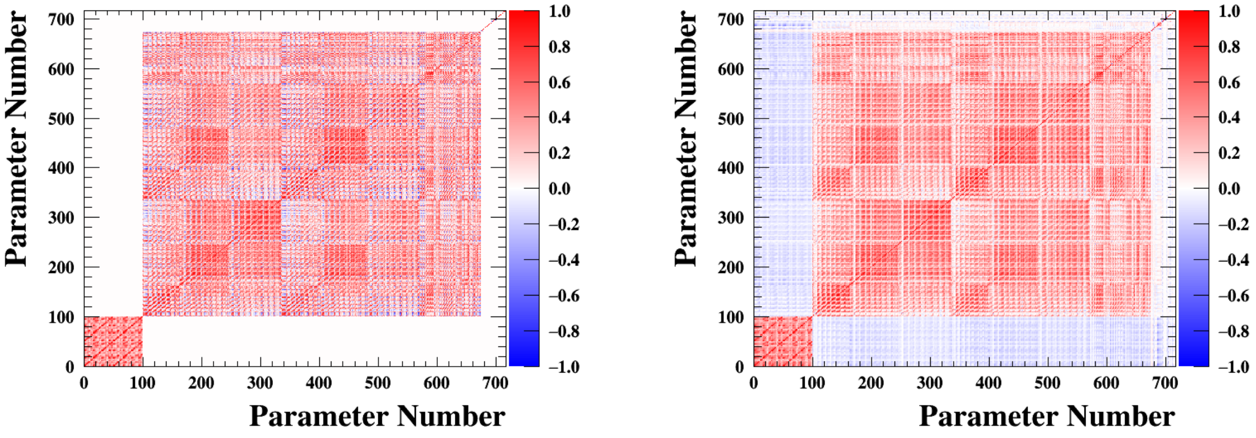

(a) Pre-fit (b) Post-fit

Figure 4.2: Comparison of pre-fit and post-fit correlation matrices from the Asimov fit. The parameter numbers correspond to the following systematic categories: flux parameters, from 0 to 99; detector parameters from 100 to 673; and cross-section parameters from 674 to 716.

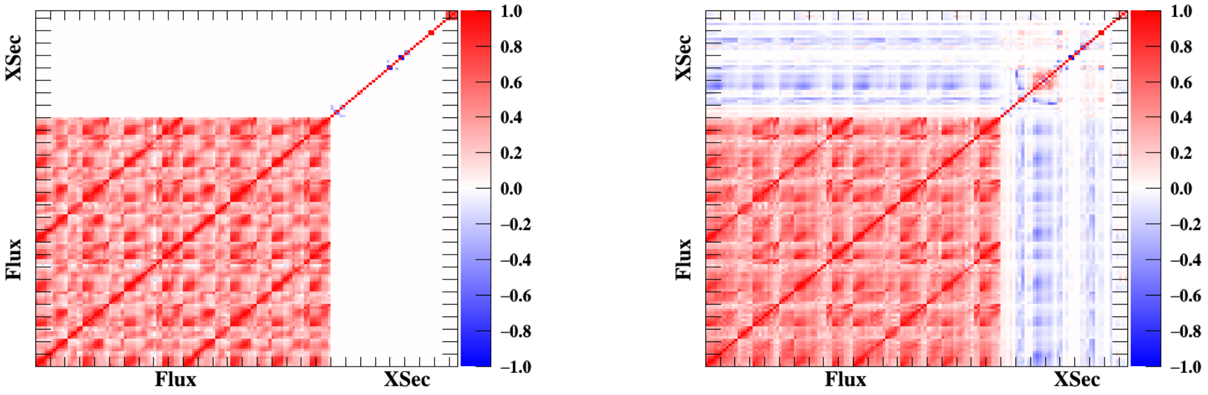

(a) Pre-fit (b) Post-fit

Figure 4.3: Comparison of pre-fit and post-fit correlation matrices from the Asimov fit, for flux and cross-section parameters.

M_A^{QE} and the Q^2 parameters, which affect CCQE events, and the 2p2h parameters, which affect 2p2h events, but often get reconstructed in the CC0π samples. There are also slight correlations between CCQE parameters and some CC1π parameters, for the same reasons: due to pion absorption or poor reconstruction, some CC1π events end up in the CC0π samples. The presence of correlations between different parameter categories is a double-edged sword in the analysis. On the one hand, the presence of correlations makes it possible to reduce the errors on the post-fit parameters and thus constrain the SK spectrum more precisely. On the other hand, the amount of correlations is directly dependent on the models used to parametrize the uncertainties. Furthermore, the higher the correlation between two parameters, the harder it becomes to distinguish their individual effects. This is the case especially for CCQE parameters and the flux parameters, which are all strongly correlated. As a result, mis-modelled cross-section effects might end up being picked up by the flux parameters and introduce a bias in the oscillation parameter measurements. The size of this effect will be investigated and quantified in Section 5.4.

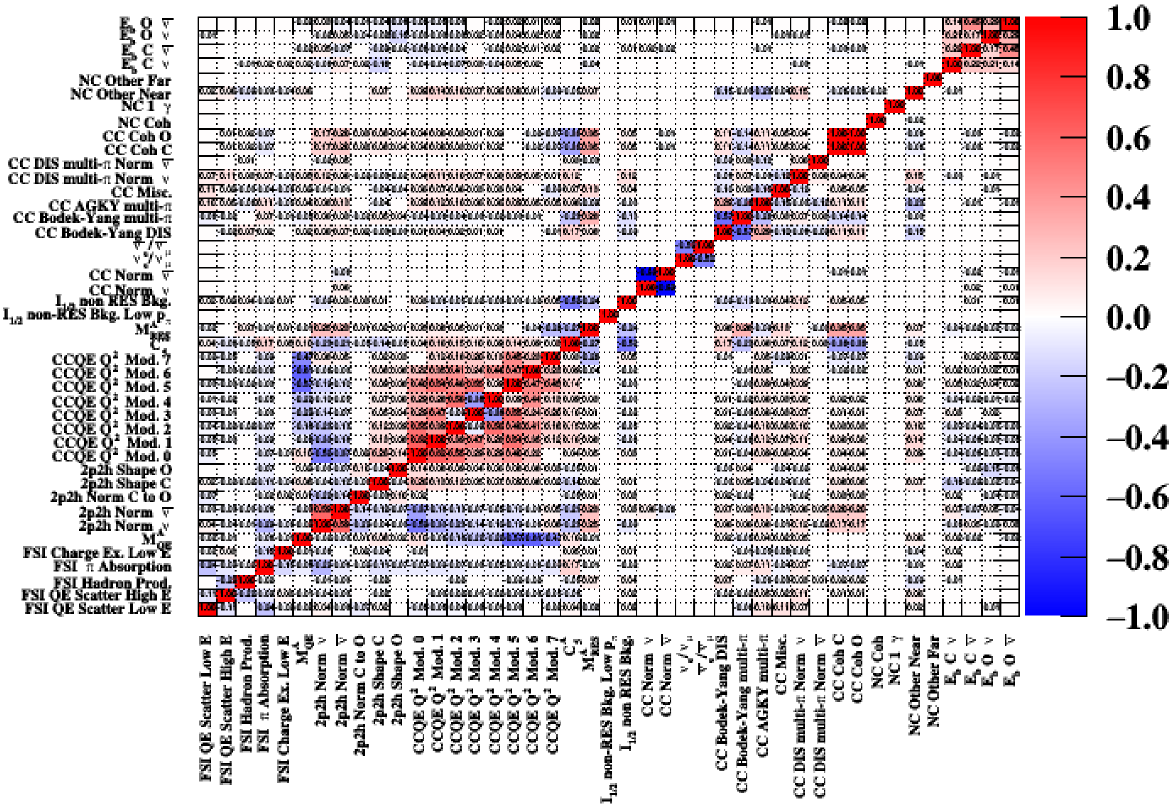

Figure 4.4: Post-fit correlation matrix for cross-section parameters after the Asimov fit.

4.2.2 Likelihood Scans

The BANFF fit is sensitive to the smoothness of the likelihood surface in the parameter space. Discontinuities can cause minimization issues. It is therefore important to look at the behavior of

the likelihood as a function of the variation for each systematic parameter.
For this purpose, we perform *likelihood scans*, in which the contributions to the $\Delta\chi^2$ in Eq. (4.4) are calculated as a function of individual parameter variations.
In addition to checking for discontinuities in the likelihood, these checks allow us to gauge which effects constrain the parameters. Let us take the example of flux parameters: as shown in Fig. 3.9, the error on the flux parameters varies across the neutrino energy spectrum. The high and low energy regions of the spectrum have limited statistics and are not able to constrain their corresponding flux parameters on their own. Fig. 4.5a illustrates this: the parameter affecting the low energy region events, with 0.0 GeV$< E_\nu <$ 0.4 GeV, has a negligible contribution from the Poissonian term of the likelihood (referred to as the "sample" contribution), and thus is dominated by the flux penalty contribution. Towards the peak of the spectrum, the increase in statistics allows for a larger sample constraint, and therefore a reduction of the penalty contribution (seen here on the example of the parameter affecting events with 0.7 GeV$< E_\nu <$ 1.0 GeV).
Conversely, a parameter impacting phase space regions with high statistics will be mostly constrained by the sample itself. This is the case of the M_A^{QE} parameter, whose scan is shown in Fig. 4.5b. It is, of course, preferable to influence the fit as little as possible and let the data drive the constraint on the parameters. However, due to the large number of parameters in the BANFF fit and to the correlations which arise during the fit, some degree of physically motivated prior constraint is necessary in order to prevent degeneracies in the minimization process.

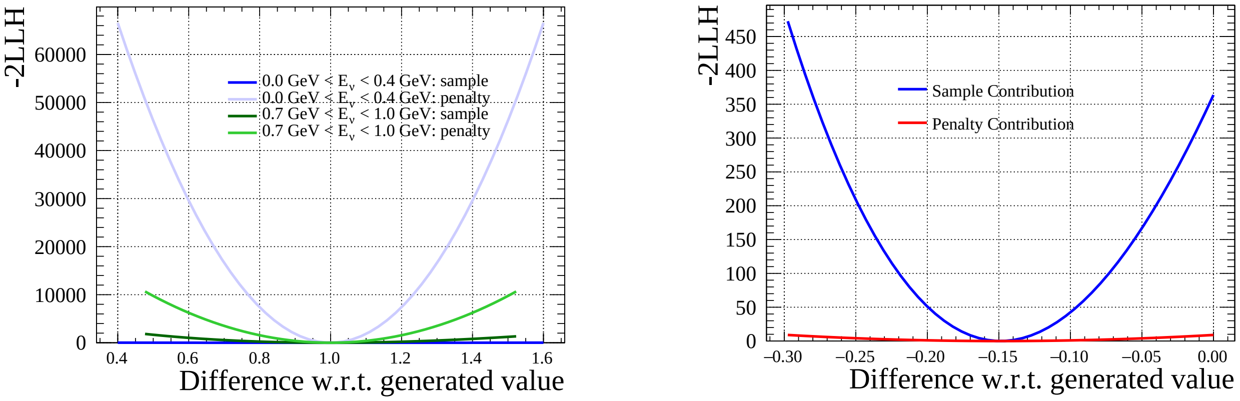

(a) FHC ν_μ flux

(b) M_A^{QE}

Figure 4.5: The sample and penalty contributions for different systematic parameters. (a) Two FHC ν_μ flux parameters; the energies they apply to are given in the legend. (b) The M_A^{QE} effective cross-section parameter.

The BANFF fit assumes that the errors of all of the parameters used in the fit have a gaussian distribution around their central value, which is why the penalty terms are all gaussian. For a gaussian parameter, the contribution to the $\Delta\chi^2$ is quadratic, reflecting the fact that the change in event rate in the samples is symmetric with respect to changes around the maximum likelihood value. Assuming that all of the parameters are gaussian is an approximation, and while it is good enough for the vast majority of the parameters, it is certainly not true for all. Fig. 4.6 shows two examples of such parameters. In the case of FSI parameters (Fig. 4.6a), the sample contribution is far from quadratic. This is due to the intrinsic mechanism of FSI reweighting. Similarly, Fig. 4.6b shows an example of a slight non-gaussianity in the 2p2h normalization applied to neutrino events.

The likelihood scan is performed on an Asimov set, and thus also allows to make sure that the minimum log-likelihood value is indeed the one which was used to generate the spectrum[2].

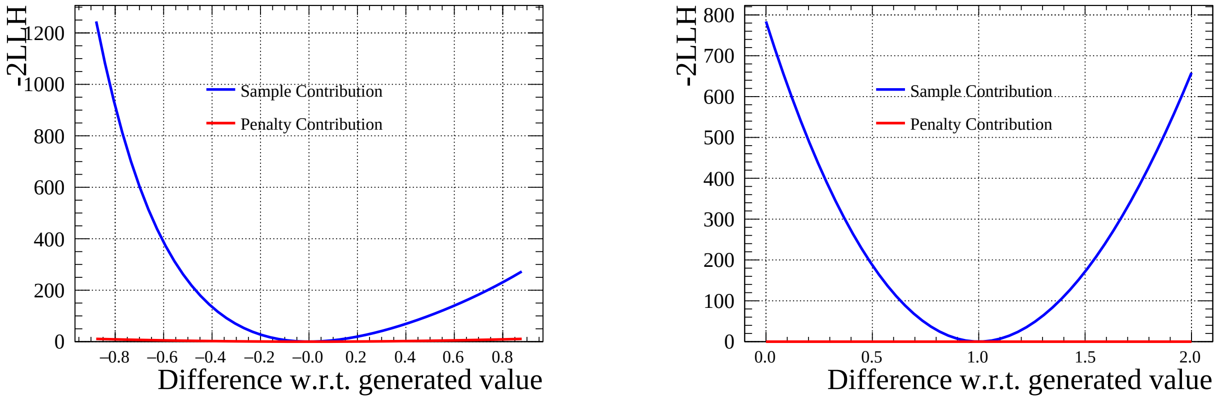

(a) QE FSI parameter

(b) 2p2h ν normalization

Figure 4.6: Examples of non-gaussian systematic parameters.

It is worth noting that during a likelihood scan each parameter is varied individually. This is therefore not a good way to extract the constraint on each parameter, as no correlations have been taken into account. The Asimov fit, on the other hand, does this job and should be used to gauge the expected sensitivity, as it varies all of the parameters at the same time.

4.2.3 Bias studies

It is possible that the error model used in the BANFF fit may introduce biases in the systematic parameters or that the post-fit errors might be over- or underestimated. In order to check the robustness of the fitter to such effects, a bias test can be performed by looking at the *pulls* in the parameters for a large number of toy experiments. In order to create these toy experiments, the entire parameter space is sampled according to the pre-fit correlations and errors, yielding *throws*. Each throw consists of a set of values for the systematic parameters selected according to their prior errors and correlations. As such, more probable regions of the parameter space will have a higher chance of being reflected in the throws[3]. The exception to this is the detector parameters: they are not thrown from the effective matrix shown in Fig. 3.17, but rather from the original detector uncertainties. This is done in order to reflect the non-gaussian behavior of detector parameters.
Each set of thrown parameters is then used to reweight the nominal MC, and a Poissonian fluctuation is applied to each bin in order to simulate statistical fluctuations of the data.

---

[2] Note that the value used to generate the Asimov spectrum may be different from the "generated value", which is the one used to create the MC. Some parameters, such as M_A^{QE}, have an extra tuning applied on top of the MC prediction, which explains why the M_A^{QE} scan in Fig. 4.5b does not have its minimum at 1. Also, due to implementation reasons, some parameters have their nominal value at 0, while others have it at 1. In Fig. 4.5 and Fig. 4.6, all of the parameters do indeed recover the minimum log-likelihood value at their nominal value, despite having different defintions of the "nominal".

[3] Unconstrained parameters, such as most of the CC0π parameters, are not varied in this process, since by definition they do not have a prior gaussian uncertainty from which to perform the throws.

This process is repeated a large number of times[4], and each simulated data set is used to perform an Asimov fit with the thrown systematic parameters as the new priors. For each fit, the pulls are defined as

$$pull = \frac{p_{fit} - p_{prior}}{\sigma_{fit}} \tag{4.5}$$

where p_{prior} and p_{fit} are the systematic parameter values before and after the Asimov fit, respectively, and σ_{fit} is the error on the parameter after the Asimov fit.

For each parameter, the distribution of the pulls is fit with a gaussian function, and its mean and width are used to diagnose the robustness of the fitter. According to Eq. (4.5), for an ideal Asimov fit the mean of the pulls should be 0. Given that the parameters are thrown according to gaussian priors, the distribution of the pulls should have a standard deviation (width) of 1. A deviation of the mean from 0 indicates the presence of a bias. If the width is below 1, the errors are overestimated in the nominal error model, whereas a width larger than 1 indicates that the errors are underestimated.

Fig. 4.7 shows the results of the bias study for different categories of systematic parameters. The flux and detector parameters are globally unbiased, with the exception of high-energy RHC $\bar{\nu}_\mu$ flux parameters and high p_μ-high cosθ_μ detector parameters. This is due to the non-gaussianity of detector parameters: although the effect of detector parameters is applied during the BANFF fit via normalization parameters affecting kinematic bins, in reality the fundamental detector parameters do not have a gaussian behavior. For both flux and detector parameters, the widths are well-centered around one, indicating an optimal error coverage.

Cross-section parameters are also generally unbiased, with the exception of the 2p2h shape parameter for ^{12}C, the high-Q^2 parameters (Q^2 normalization bins 5, 6 and 7), M_A^{RES}, C_5^A and the $I_{1/2}$ background, and the carbon binding energy shifts. The 2p2h shape parameter for ^{12}C has the particular feature of having a physical boundary contained inside the error envelope, so a precise pull cannot be estimated for it.

Some degree of bias is intrinsic to the error model. The effect of the biases presented above on the far detector fitters was tested by shifting the prior of the Asimov post-fit prediction for biased parameters by the amount of the bias. On near detector samples, applying this correction has a 1.3% effect across all samples, with the largest individual change occuring in the RHC $\bar{\nu}_\mu$ CC1π event rates (2.7%). The modified near-detector predictions were passed on to the P-Theta fitting group for comparison to the nominal Asimov results. Fig. 4.8 shows the appearance and disappearance in the oscillation parameter space extracted in the far detector fit using in an Asimov fit. The Asimov fit assumes the oscillation parameter values in Table 4.1. The effect of the near detector bias is negligible.

4.3 Effect on Far Detector Sensitivity

The impact of the Asimov near detector constraint is also used to gauge the far detector sensitivity to oscillation parameters. Fig. 4.9 illustrates the expected sensitivity to the disappearance (Fig. 4.9a) and appearance parameters (Fig. 4.9b) obtained as a result of an Asimov fit to the SK MC with the constraint from the BANFF Asimov fit [115]. These results also include the PDG2019 constraint

---

[4] In this analysis, 1000 fits were performed, of which 753 converged successfully. The fits which did not converge were ones in which very extreme regions of the parameter space were sampled (e.g. some parameters at their physical limit).

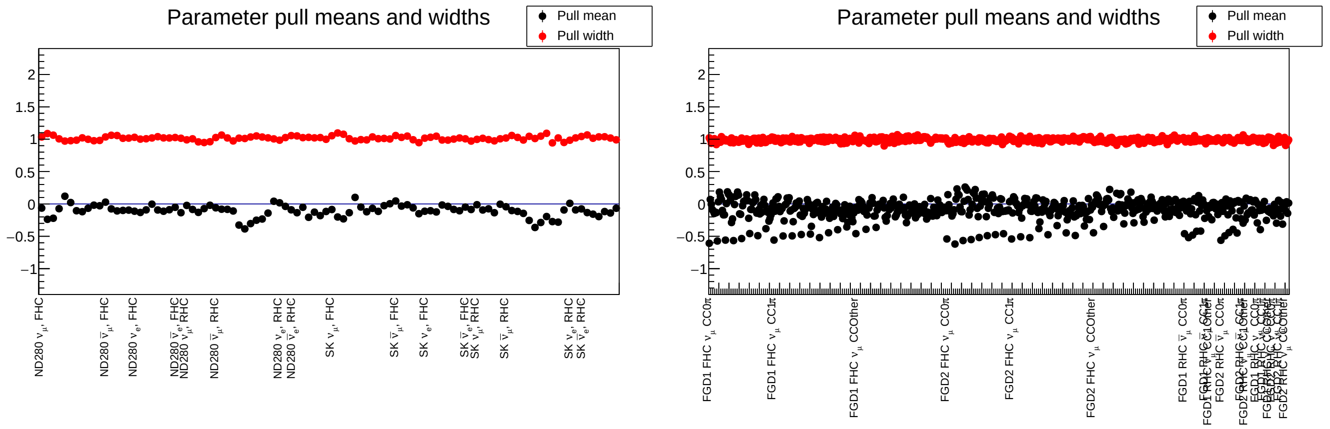

(a) Flux parameters (b) Detector parameters

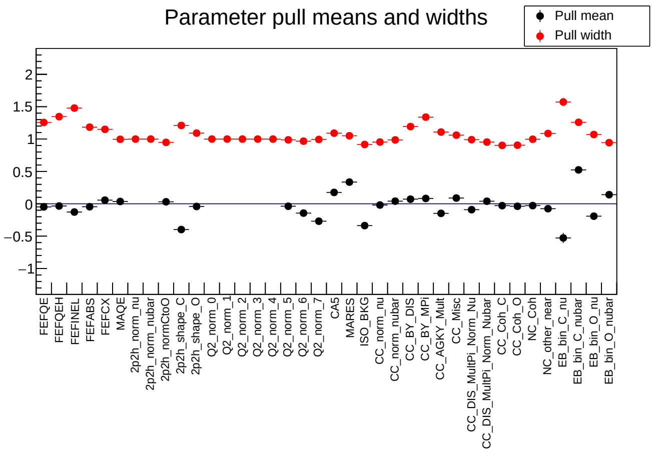

(c) Cross-section parameters

Figure 4.7: Mean and widths of pulls distributions for flux (a), detector (b) and cross-section (c) parameters.

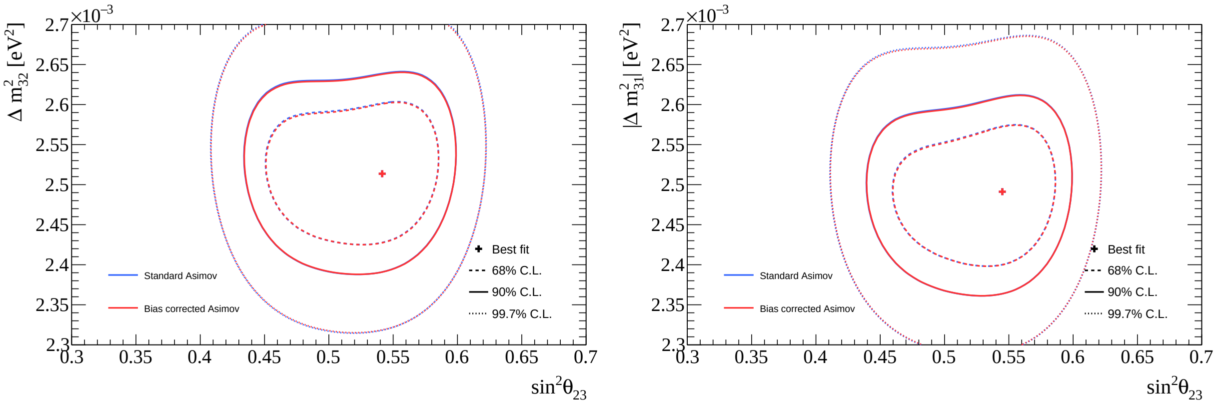

(a) Disappearance contours, NH (b) Disappearance contours, IH

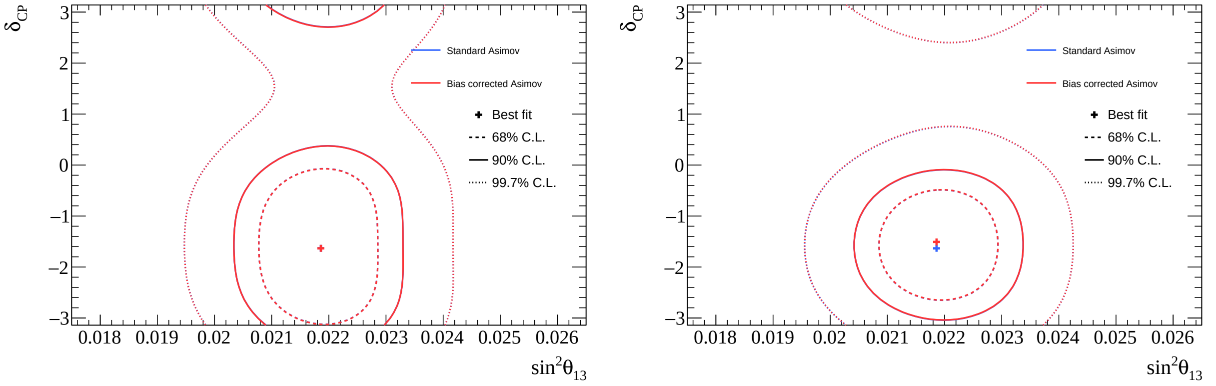

(c) Appearance contours, NH (d) Appearance contours, IH

Figure 4.8: Comparison of bias-corrected Asimov fit results to the nominal Asimov results.

on the $\sin^2\theta_{13}$ parameter [147]. The oscillation parameter values used in the Asimov fit are given in Table 4.1.

Parameter	Value
δ_{CP}	-1.601
$\sin^2\theta_{23}$	0.528
$\sin^2\theta_{13}$	0.0218
$\sin^2\theta_{12}$	0.307
Δm^2_{32}	$2.509\times10^{-3}\mathrm{eV}^2$
Δm^2_{21}	$7.53\times10^{-5}\mathrm{eV}^2$
Earth Matter Density	2.6 g/cm^3
Mass Hierarchy	Normal

Table 4.1: Oscillation parameter values assumed in the Asimov fit [115].

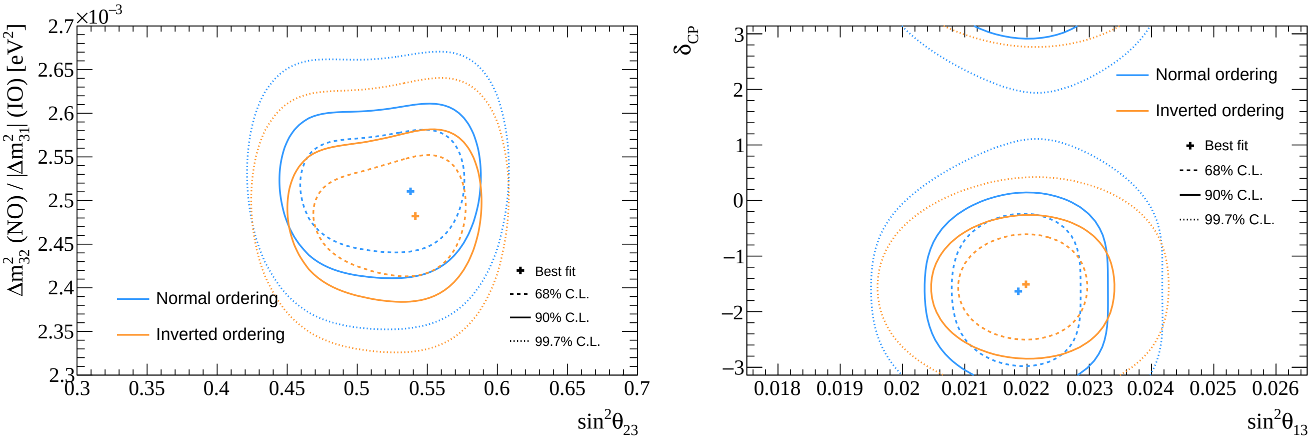

(a) Disappearance parameters.

(b) Appearance parameters.

Figure 4.9: Results of the far detector Asimov fit, including the reactor constraint on $\sin^2\theta_{13}$.

It is interesting to compare the evolution of the Asimov sensitivity since the previous oscillation analysis [100]. In order to illustrate the effect of incremental changes, let us denote the 2018 OA result as data set A. The following changes have occurred since the last OA:

- **B -** The cross-section model (and implicitly the near detector error model) has been significantly improved since the last analysis (described in Section 3.3.2). Data set B is defined as the 2018 OA data set (A) plus the cross-section model improvements for the 2020 OA and the new BANFF constraint, which reflects the addition of new the near detector data (“2020xsec+BANFF”): B=A+xsec2020+BANFF.

- **C -** The 2019 update of the PDG constraint for $\sin^2\theta_{13}$ (RC, for reactor constraint): C=B+PDG2019 RC

- **E -** The addition of SK run 10 data: E=C+run10. This last change corresponds to the nominal model used in this analysis.

Fig. 4.10 illustrates the evolution of the sensitivity to δ_{CP} as a function of the incremental changes presented above. It is important to note that the sensitivity to δ_{CP} depends on the ν_e and $\bar{\nu}_e$ event rates. As such, data set B provides a sizable increase in sensitivity, thanks to the error reduction from the BANFF fit. This sensitivity is tempered by the application of the PDG 2019 constraint, which slightly modifies the $\nu_e/\bar{\nu}_e$ appearance event rate. Finally, the largest leap in sensitivity is acquired via the addition of run 10 data at SK[5].

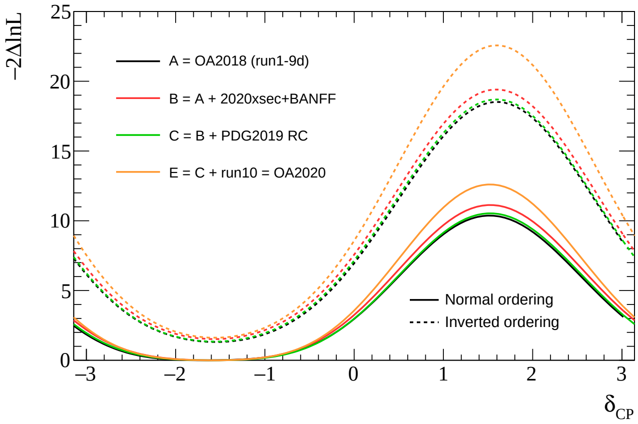

Figure 4.10: Evolution of δ_{CP} Asimov sensitivity from the previous analysis (data set A) to the analysis described in this thesis (data set E). The intermediate steps are described in the text. Contours for normal (solid lines) and inverted (dashed lines) are compared.

---

[5] Note that this is an Asimov fit - the addition of run 10 data corresponds to scaling the additional run 10 MC production to the data POT.

Chapter 5

Results of the T2K Oscillation Analysis, with a focus on the Near Detector fit

The validations discussed in the previous chapter allow us to perform the near detector fit to the ND280 data confidently. Section 5.1 details the results obtained as after the BANFF fit to the near detector data using T2K run 2-9 ND280 data. Section 5.2 assesses the compatibility of the near detector fit with the data. Section 5.3 shows the effect of the near detector fit on the far detector data. A detailed account of robustness studies of the oscillation analysis framework under alternative models and tunes is presented in Section 5.4. Finally, the global oscillation parameter results, including SK run 1-10 data, are discussed in Section 5.5.
In addition to being responsible for the near detector fit to data, I was also in charge of performing the simulated data set fits described in Section 5.4 with the near detector fitting framework. I was also involved in the implementation and design of these simulated data sets, which aim to probe the robustness of the neutrino interaction error model used in this analysis using alternative models or tunes.

5.1 Near Detector Fit Results

Table 5.1 shows the event rate before and after the BANFF fit, together with the unnormalized contribution to the minimized quantity $\Delta\chi^2$.

The pre-fit distributions were shown in Section 3.2.3. Fig. 5.1, Fig. 5.2 and Fig. 5.3 show the event rate predictions as a function of p_μ after the BANFF fit, and Fig. 5.4, Fig. 5.5 and Fig. 5.6 the corresponding distributions as a function of $\cos\theta_\mu$. Comparing the pre- and post-fit distribution, a substantial improvement in the data-MC agreement can be seen.

Beam	Topology	Target	Data	Prefit	Postfit	$\Delta\chi^2$	Bins
FHC ν_μ CC	0π	FGD1	33443	30598.50	33387.70	872.76	841
		FGD2	33156	30018.40	33150.90	859.75	
	1π	FGD1	7713	8388.91	7930.96	295.05	288
		FGD2	6281	6741.44	6423.44	313.87	
	Other	FGD1	8026	7056.15	7946.17	422.12	342
		FGD2	7700	6477.68	7313.67	396.02	
RHC $\bar{\nu}_\mu$ CC	CC 0π	FGD1	8388	8163.65	8430.25	378.51	306
		FGD2	8334	7865.32	8184.52	375.38	
	1π	FGD1	698	694.87	681.54	58.77	48
		FGD2	650	625.33	636.19	55.61	
	Other	FGD1	1472	1297.49	1469.29	90.65	80
		FGD2	1335	1185.51	1377.96	118.67	
RHC ν_μ CC	0π	FGD1	3594	3192.26	3580.46	133.87	120
		FGD2	3433	3154.03	3528.39	135.88	
	1π	FGD1	1111	1160.69	1154.22	62.29	40
		FGD2	926	931.49	920.74	57.70	
	Other	FGD1	1344	1075.91	1290.46	58.66	54
		FGD2	1245	1002.77	1196.24	51.39	

Table 5.1: Event rates for each of the ND280 selections for data and the prediction before the BANFF fit, and after the BANFF fit to data.

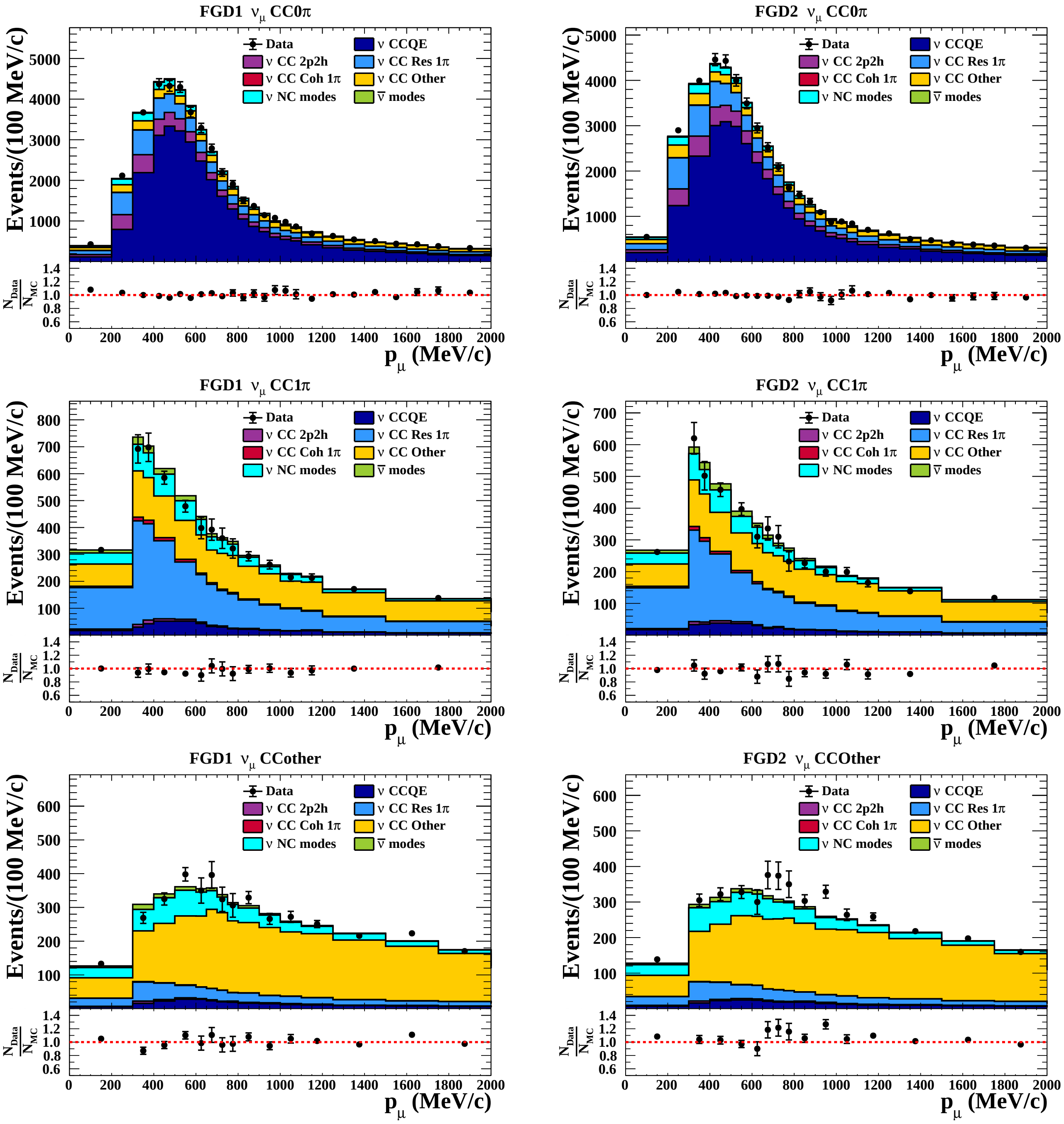

Figure 5.1: Data-MC comparisons for FHC ν_μ samples after the BANFF fit, projected as a function of p_μ.

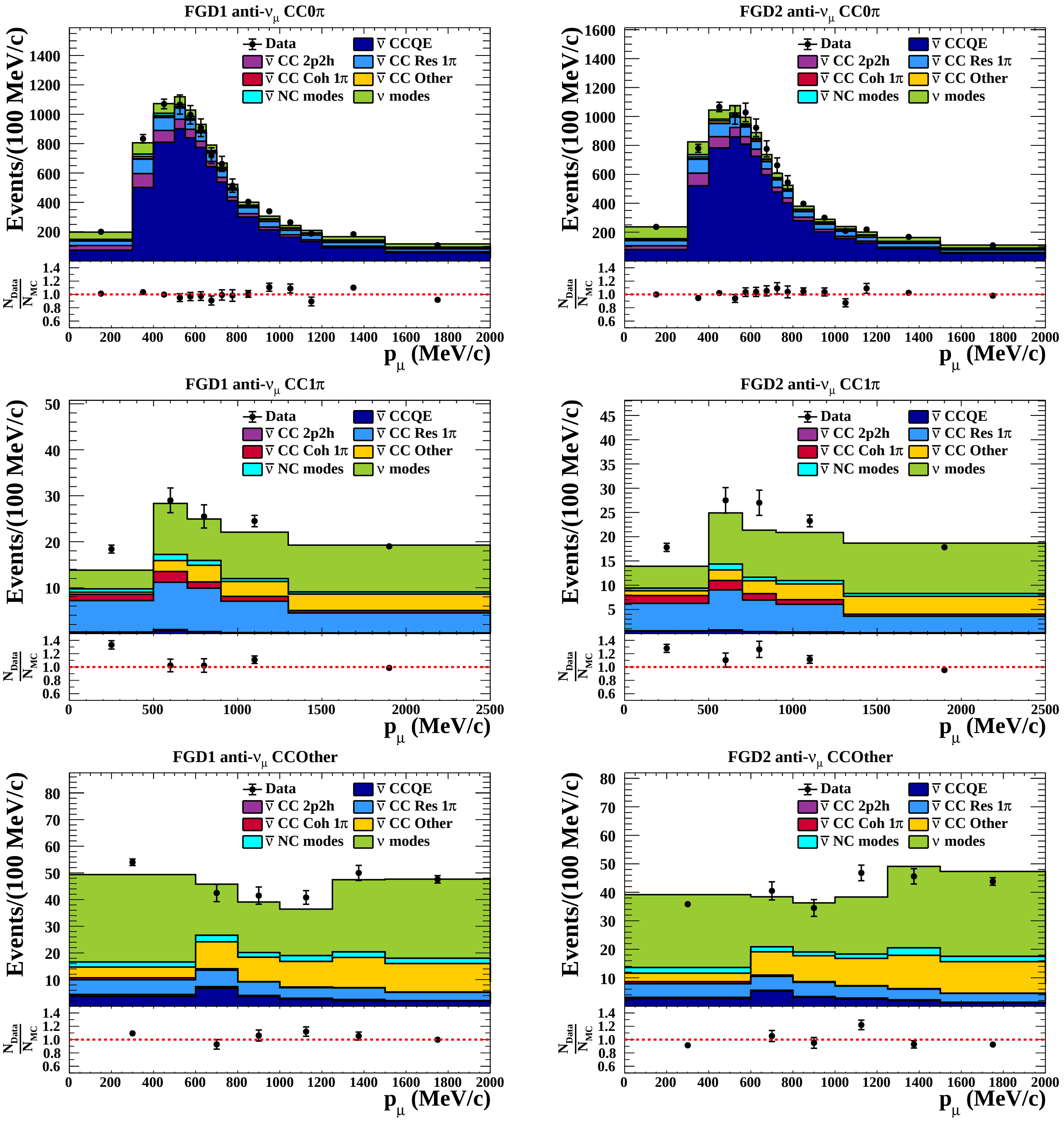

Figure 5.2: Data-MC comparisons for RHC $\bar{\nu}_\mu$ samples after the BANFF fit, projected as a function of p_μ.

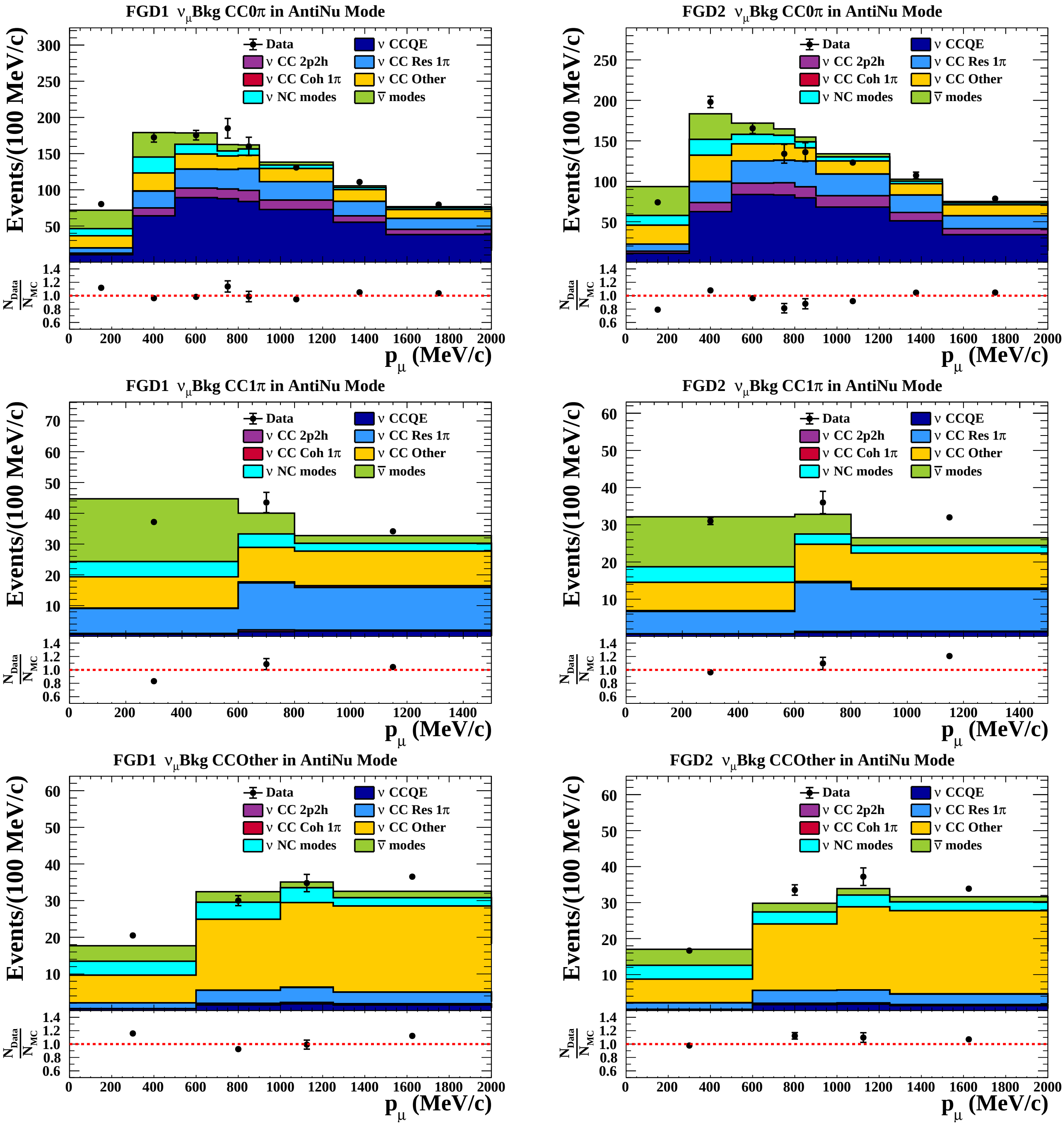

Figure 5.3: Data-MC comparisons for RHC ν_μ samples after the BANFF fit, projected as a function of p_μ.

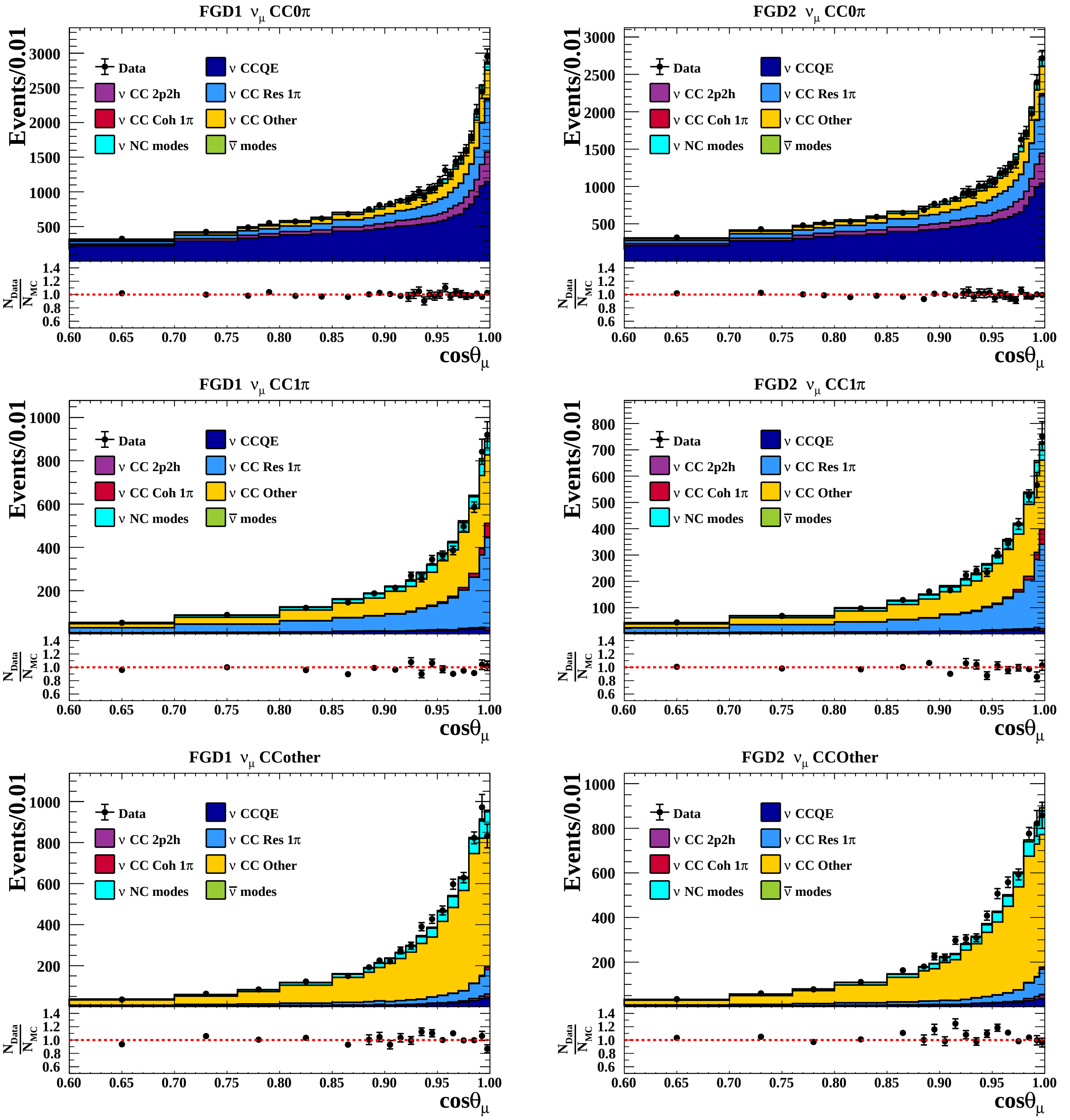

Figure 5.4: Data-MC comparisons for FHC ν_μ samples after the BANFF fit, projected as a function of cosθ_μ.

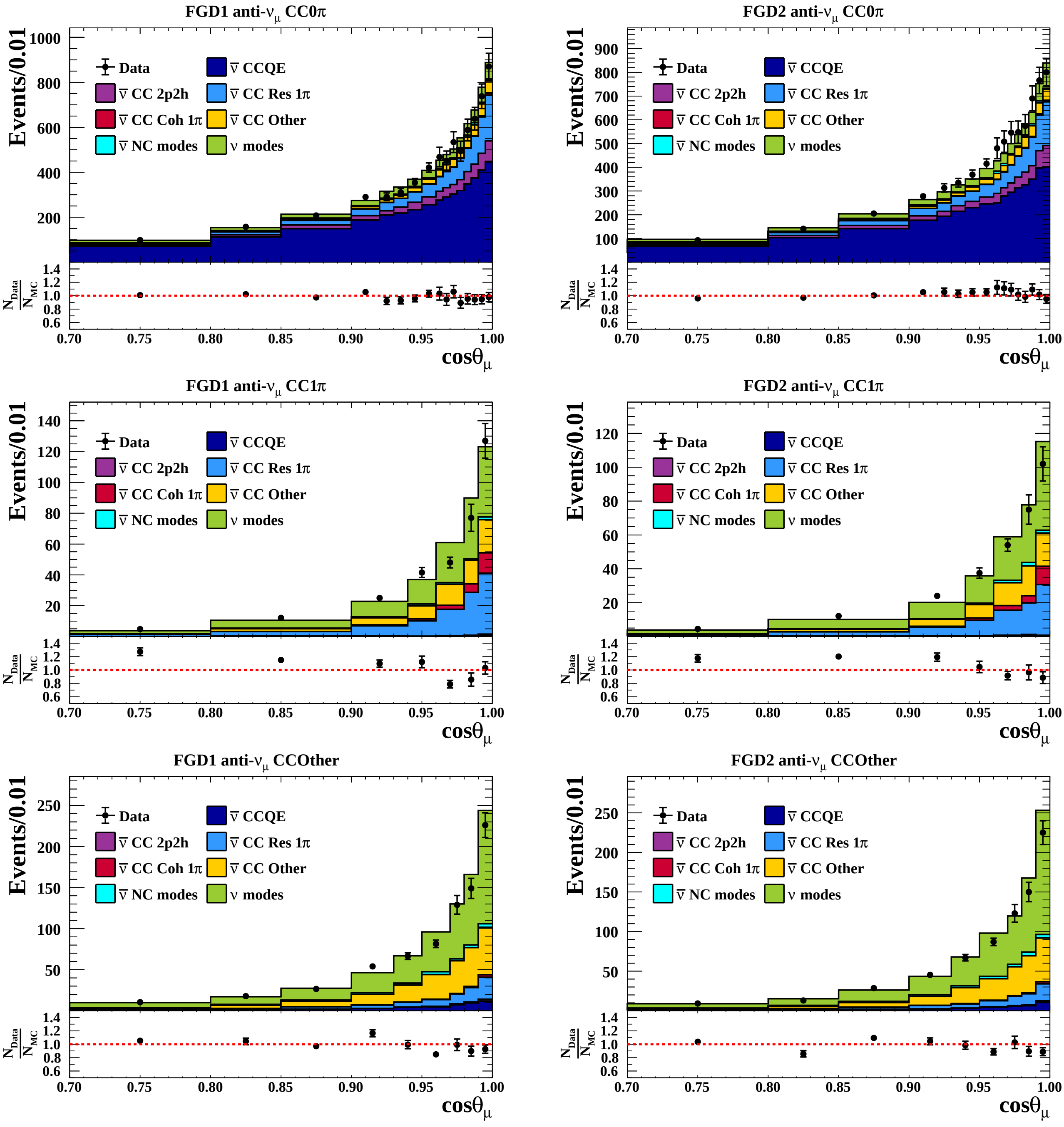

Figure 5.5: Data-MC comparisons for RHC $\bar{\nu}_\mu$ samples after the BANFF fit, projected as a function of $\cos\theta_\mu$.

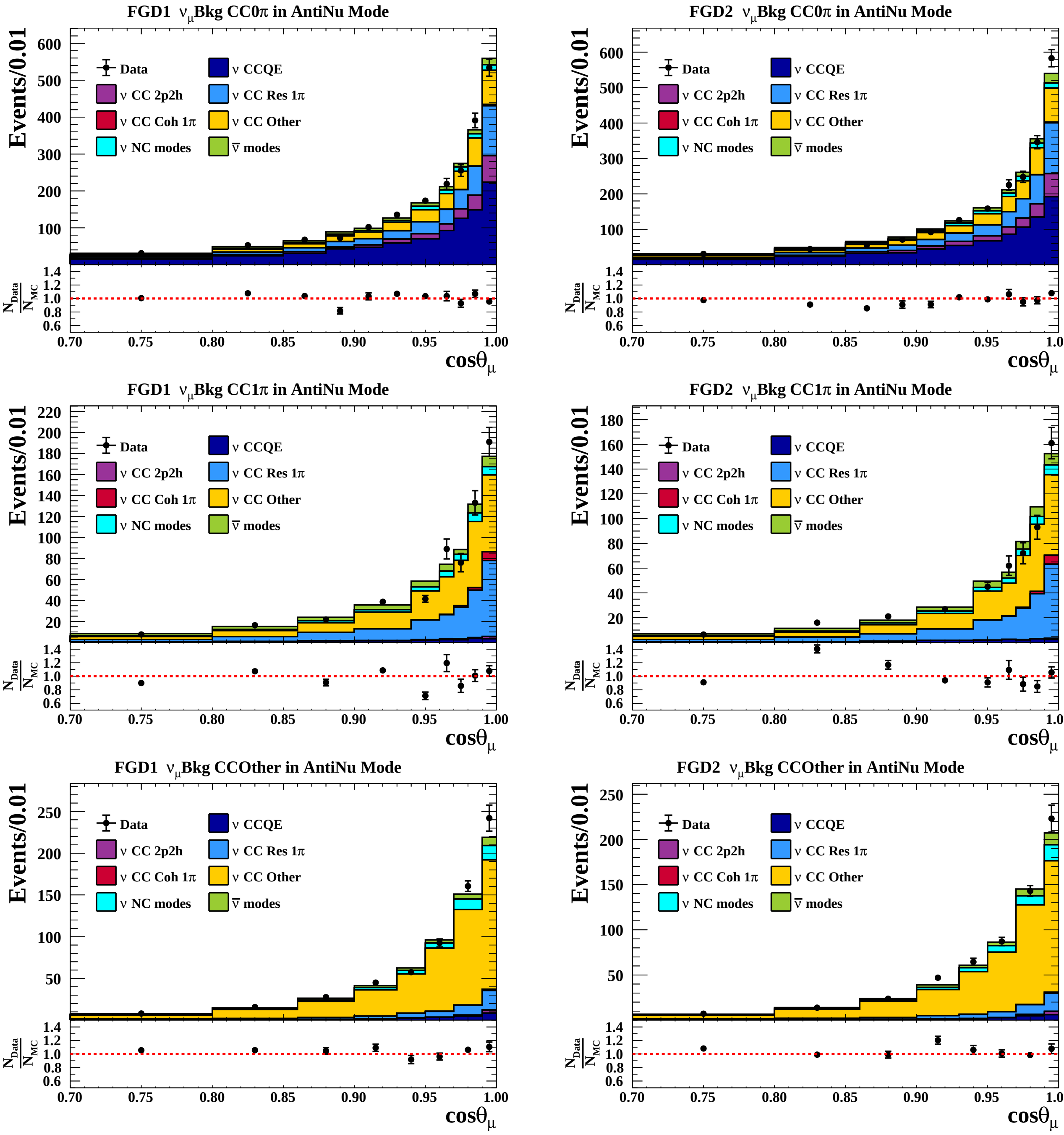

Figure 5.6: Data-MC comparisons for RHC ν_μ samples after the BANFF fit, projected as a function of $\cos\theta_\mu$.

Overall, the data-MC agreement has improved substantially compared to the pre-fit distributions presented in Section 3.2.3.4.
In order to better understand the results of the near detector fit, it is useful to look at the impact on different systematic categories.

5.1.1 Flux Parameters

Fig. 5.7 and Fig. 5.8 show the flux parameter values adjusted during the BANFF fit to ND280 data. The FHC ν_μ flux parameters, at both ND280 and SK, show an energy-dependent shape-like effect. At low energy values, they are increased by ∼10%, whereas at high energies the neutrino flux is suppressed by the same amount. All of the flux parameters' post-fit values are compatible to within one standard deviation with the prior errors of the flux model.
The flux parameters are all strongly correlated, both before and after the BANFF fit. As such, the total deviation with respect to the nominal flux model is of the order of 1-2σ, even though from Fig. 5.7 it would seem that the disagreement is larger. The flux parameter deviation from their nominal values is related to two types of effects. Firstly, the flux error model is not perfect, and there is an ongoing effort to include new NA61/SHINE data taken in 2010 with the T2K replica target, which should provide a more robust flux model. Second, as seen in Fig. 4.4, there are large anti-correlations between the flux and cross-section parameters. As a result, mis-modelled cross-section effects, particularly in CCQE-like samples, may be reabsorbed by the flux parameters. This could cause a bias in the near-to-far detector extrapolation. To gauge the size of this bias, we perform robustness studies under alternative cross-section models and tunes, which are detailed in Section 5.4.
Note that during the BANFF fit only the ND280 flux parameters are varied (since the fit only includes ND280 data), but the SK errors can be inferred and constrained thanks to the prior correlations. This is possible thanks to the strong correlations which exist between the ND280 and SK flux parameters (Fig. 3.11): especially at low energies, the flux is very strongly correlated between ND280 and SK, which makes the energy extrapolation quite reliable. Towards higher angles, however, the correlation becomes weaker and off-diagonal terms in the correlation matrix gain strength. This is due to the different angular acceptance between ND280 and SK of the flux, which is impacted by different pion kinematics at different angles.

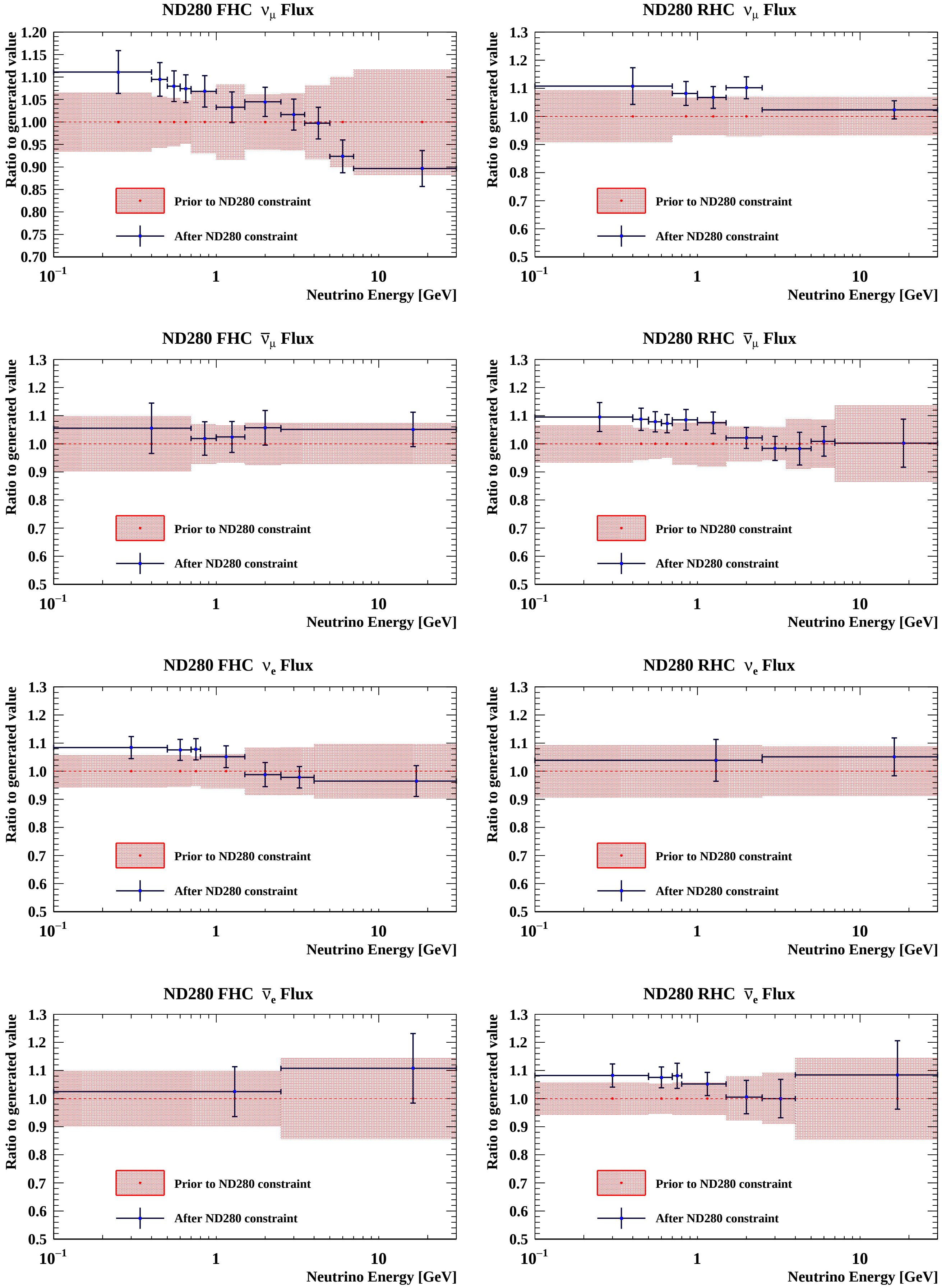

Figure 5.7: ND280 flux parameters after the BANFF fit, broken down by neutrino flux component and magnetic horn polarity.

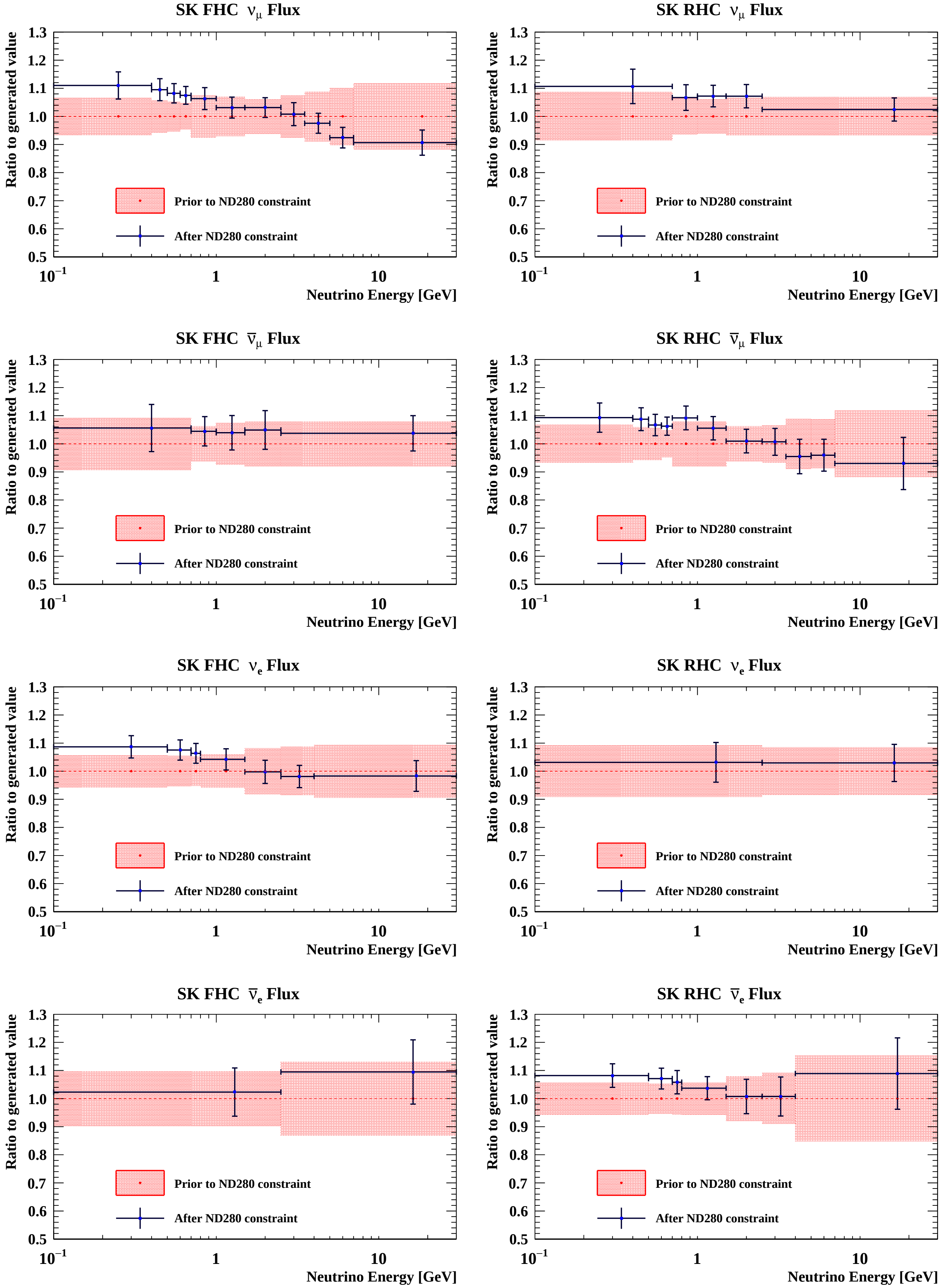

Figure 5.8: SK flux parameters after the BANFF fit, broken down by neutrino flux component and magnetic horn polarity.

5.1.2 Detector parameters

The post-fit values and errors of ND280 detector parameters are presented in Fig. 5.9, Fig. 5.10 and Fig. 5.11. As a reminder, the BANFF parametrization of detector parameters is via bin-content normalizations, whose ranges have been extracted after studying a large number of toy experiments in which individual, real detector parameters were varied[1]. The interpretation of these results is therefore very complex, as the detector parameters used in the near detector fit are a proxy for the real ND280 detector parameters.

Overall, the vast majority of detector parameters are within the 1σ error of their priors.

---

[1] For more details, see Section 3.3.3.

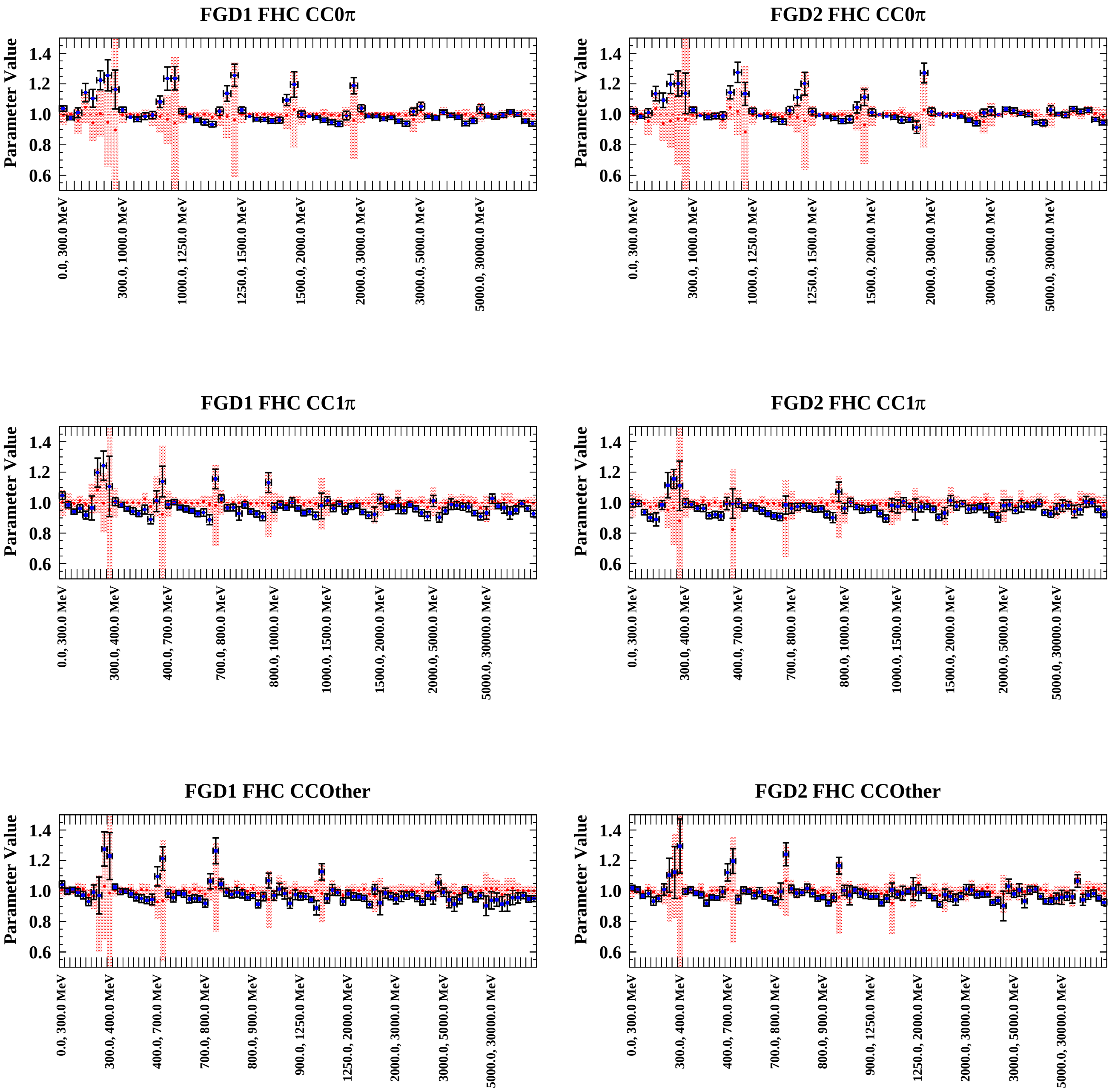

Figure 5.9: FHC ν_μ ND280 detector parameters after the BANFF fit. The labels correspond to the first p_μ bin in the momentum-angle bin labelling corresponding to detector parameters, as explained in Section 3.3.3.

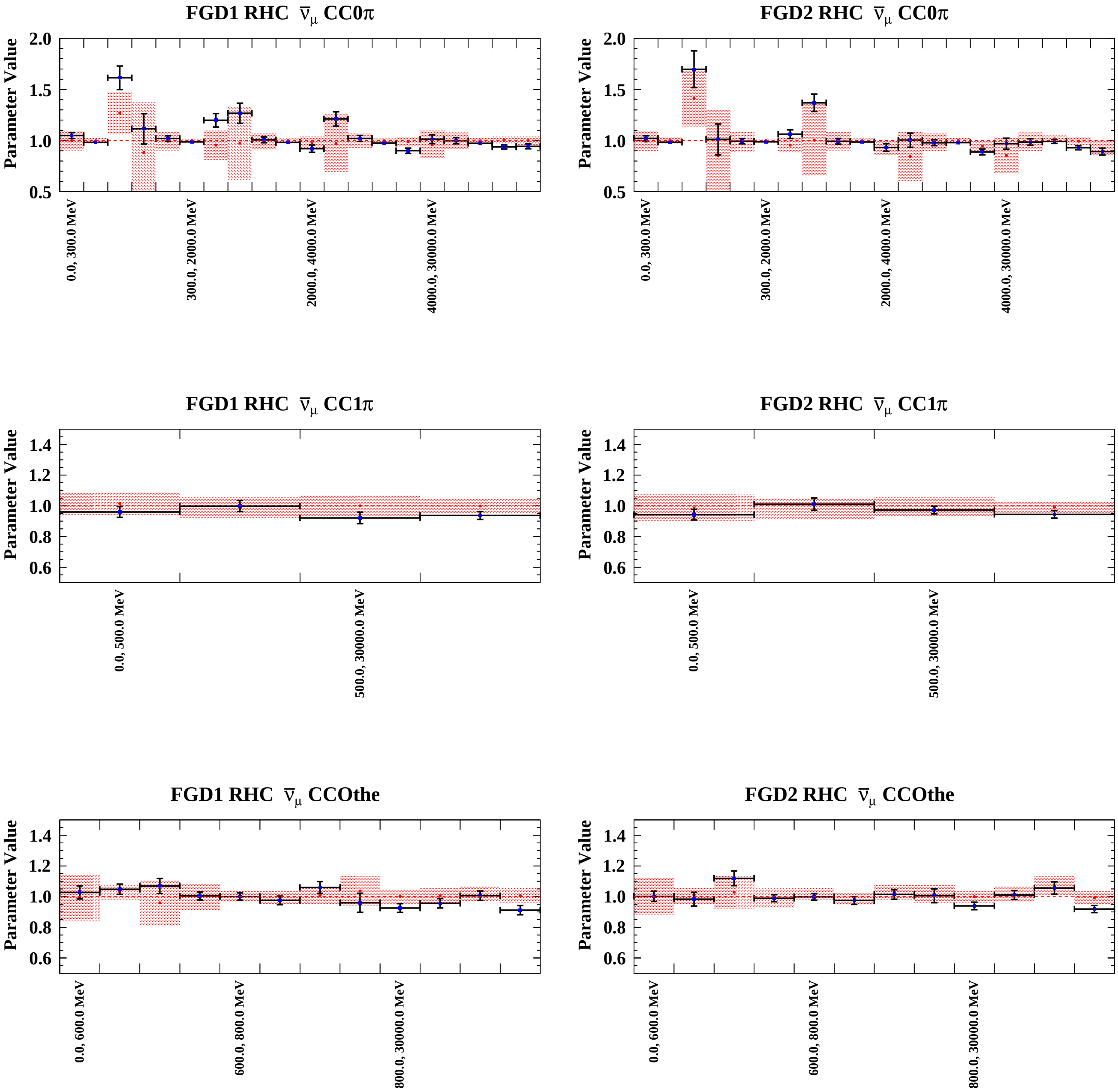
FGD1 RHC $\bar{\nu}_{\mu}$ CC0π

FGD2 RHC $\bar{\nu}_{\mu}$ CC0π

FGD1 RHC $\bar{\nu}_{\mu}$ CC1π

FGD2 RHC $\bar{\nu}_{\mu}$ CC1π

FGD1 RHC $\bar{\nu}_{\mu}$ CCOthe

FGD2 RHC $\bar{\nu}_{\mu}$ CCOthe

Figure 5.10: RHC $\bar{\nu}_{\mu}$ ND280 detector parameters after the BANFF fit. The labels correspond to the first p_{μ} bin in the momentum-angle bin labelling corresponding to detector parameters, as explained in Section 3.3.3.

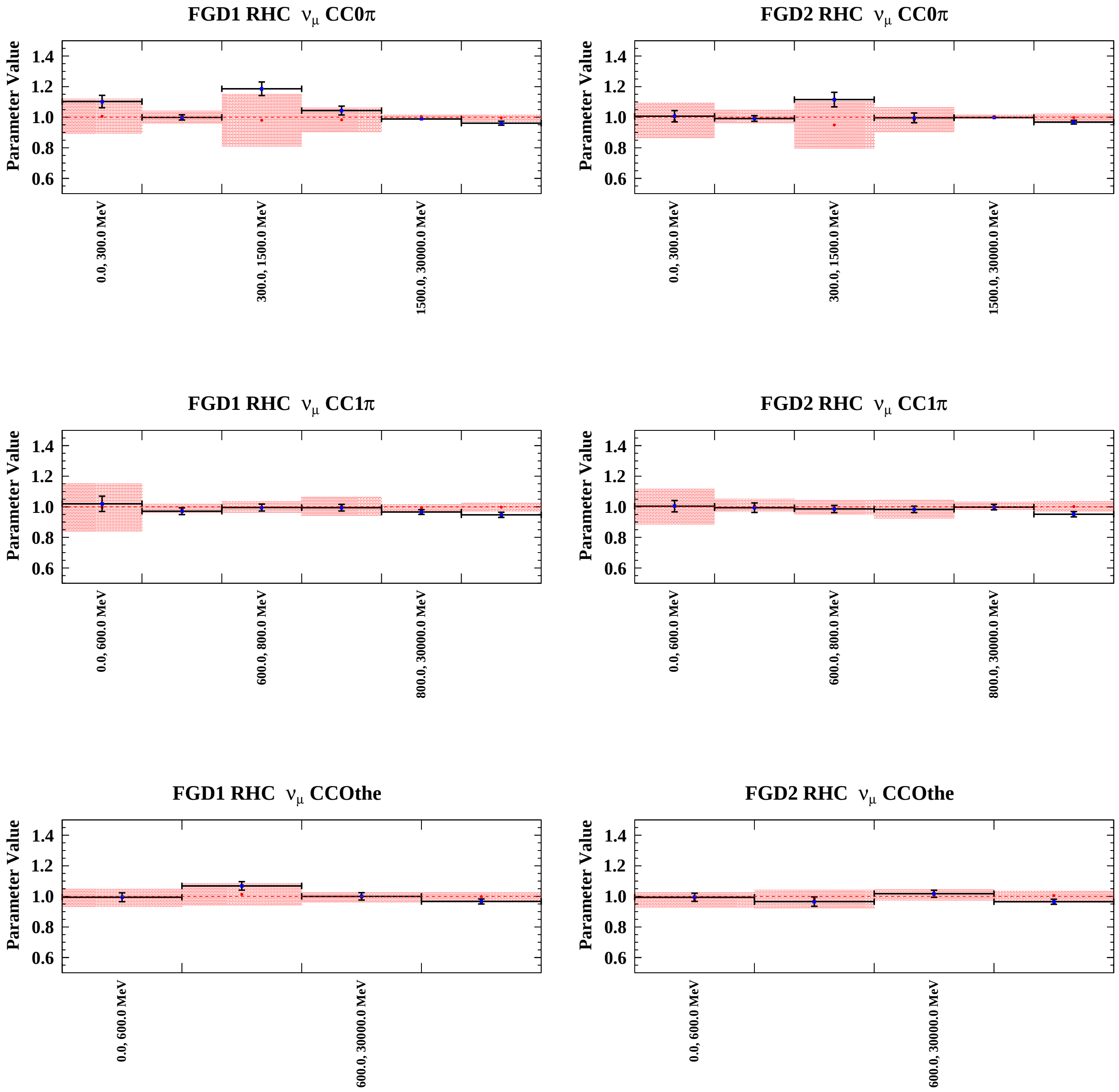

Figure 5.11: RHC ν_μ ND280 detector parameters after the BANFF fit. The labels correspond to the first p_μ bin in the momentum-angle bin labelling corresponding to detector parameters, as explained in Section 3.3.3.

5.1.3 Cross-section Parameters

The results of the cross-section parameters after the BANFF fit are presented in Fig. 5.12. Overall, most of the parameters are contained within their prior errors (if applicable). Several insights can be gained by looking at the cross-section parameters variations after the data fit.

5.1.3.1 CC0π parameters

This set of parameters impacts a large part of the data events (aiming to constrain the errors for the CCQE-like samples at SK). The first remarkable feature is the fact that the M_A^{QE} effective parameter is pulled upwards towards the NEUT nominal value of 1.2 GeV[2]. The increase in M_A^{QE} drives an enhancement of CCQE events across the entire spectrum, but it is interesting to note that the low-Q^2 parameters (parameters 0 through 5) indicate that there should be a suppression of events at low Q^2[3]. This effect is opposite to the one indicated by the M_A^{QE} parameter and low-energy flux parameters, and is due to the fact that M_A^{QE}, the low Q^2 parameters and the flux parameters are highly anti-correlated with one another (meaning their effects are of the same nature).
The 2p2h parameters are also correlated with M_A^{QE} and the flux parameters, and it is difficult to disentangle such interactions from CCQE interactions inside the 0π samples. The neutrino 2p2h normalization is consistent with that of the nominal Nieves et al. model, whereas the anti-neutrino normalization indicates the need for a suppression. This is probably a way to compensate the enhancement required by anti-neutrino flux parameters, bearing in mind that large correlations also exist between flux parameters and 2p2h normalization parameters (both have a normalization-like effect). The 2p2h shape dial for interactions on carbon is increased nearly two-fold with respect to the nominal prediction. This value corresponds to the "Δ-like" region described in Section 3.3.2. One of the consequences of the increase in this parameter is thus to shift the 2p2h population towards high q_0-high q_3 regions, while depopulating the low q_0 region corresponding to NN interactions. This effect is again correlated with the flux, M_A^{QE} and Q^2 parameters. The 2p2h shape parameter for oxygen interactions seems, on the other hand, entirely consistent with the nominal Nieves model.
Finally, the binding energy parameters (E_b) see their errors significantly reduced, while still being contained within their prior uncertainties.

5.1.3.2 CC1π parameters

The CC1π samples already had relatively good agreement with the data in the pre-fit distributions presented in Section 3.2.3.4. However, the MC over-estimates the data by about 5-10%.
The M_A^{RES} parameter is pulled downwards from its nominal value by about 3σ, which suppresses the CCRes cross-section across all energies. This probably indicated that M_A^{RES} is absorbing some of the deficiencies of the nuclear model[4]. C_5^A and the $I_{1/2}$ background are very close to their nominal values.
As a reminder, the low-momentum pion $I_{1/2}$ background is not fit at the near detector.

---

[2] As a reminder, a value of 1 on the parameter plots in Fig. 5.12 corresponds to the NEUT value used in the MC generation. The nominal value used for M_A^{QE} during the BANFF fit corresponds to a real value of 1.03 GeV, and this translates to a normalized parameter value of 0.86, seen in the priors.

[3] This suppression is consistent with the fact that the impulse approximation, on which the SF model is built, breaks down at low Q^2 values, so seeing this type of effect recovered in the data fit is quite encouraging.

[4] As M_A^{QE}, M_A^{RES} is an effective parameter, so it is prone to "soak up" other effects.

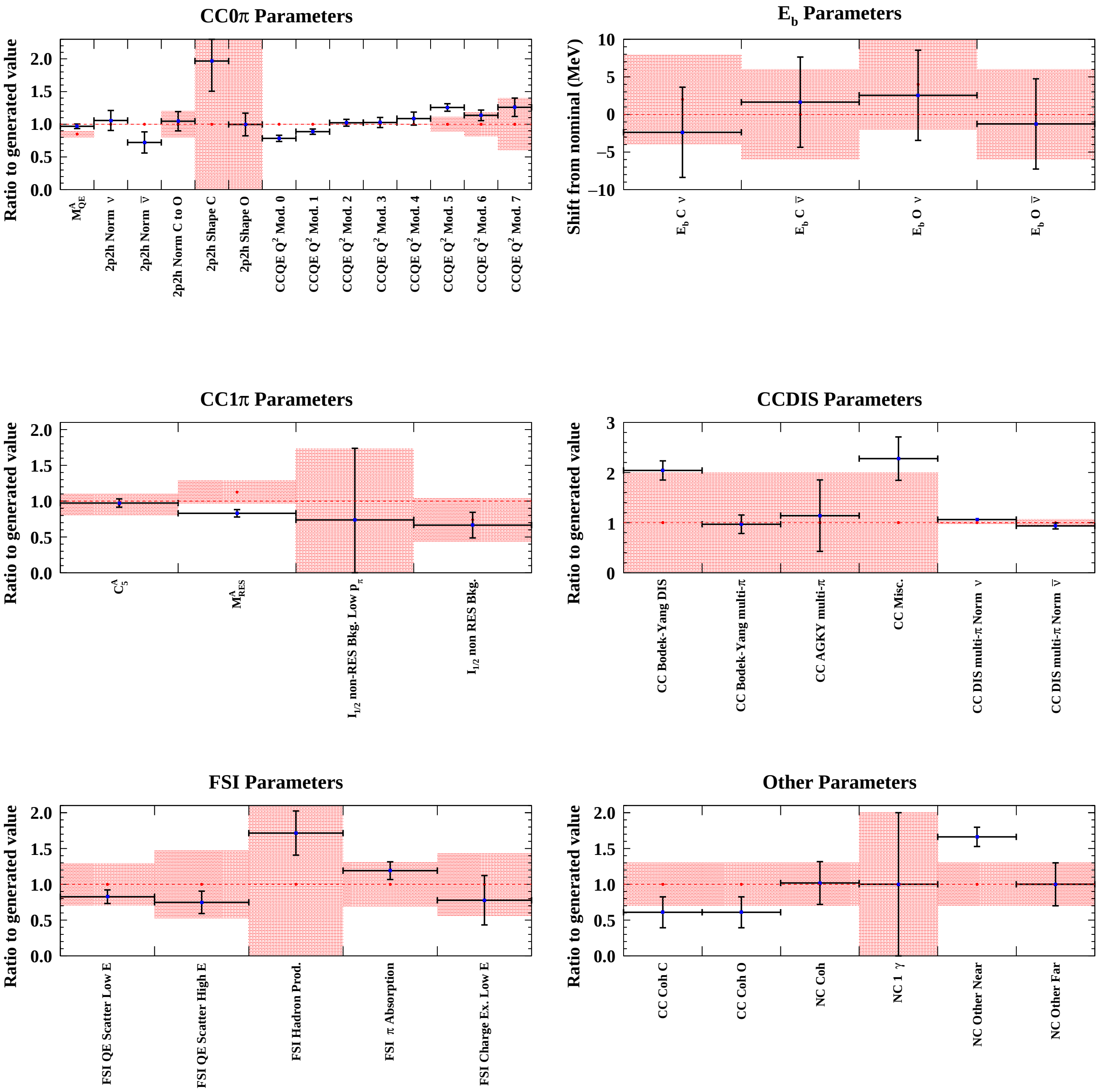

Figure 5.12: Cross-section parameters after the BANFF fit, separated by target interaction type.

5.1.3.3 CCDIS and CCOther parameters

The CCDIS parameters show some tension: the Bodek-Yang correction for DIS interactions is increased by about 100%, whereas the corresponding correction for multi-π interaction stays at its nominal value. This probably has to do with the fact the multi-π and DIS interactions are modelled via different mechanisms in NEUT.

The AGKY parameter is very close to its nominal input value.

The CC Misc. parameter, which targets a multitude of interactions, is increased more than two fold, but a large prior error has been foreseen for it, and its post-fit error is compatible with the prior assumptions. The knowledge on the interactions covered by it is currently very limited and further development is necessary.

In the "Other" parameters, both CC Coherent parameters indicate the need for a 40% suppression of coherent events. The NC coherent parameter is very close to its nominal input value. The largest discrepancy is seen in the NC Other parameter for the near detector. These types of interactions are very poorly known, so this is probably an indication that a more complete parametrization is needed.

5.1.3.4 FSI parameters

The FSI parameters are all within the 1σ prior errors. The largest impact is seen in the FSI parameter controlling hadron production.

5.1.3.5 Remarks

The post-fit values for the different cross-section parameters are a reflection of the model-dependent parametrization used in the T2K analysis. Where not enough information is available, large enough prior uncertainties have been applied in order to allow enough freedom in the error model. This does not mean that the analysis is fundamentally broken: rather, it implies that due to imperfect modelling, some biases may be introduced by the parametrization, and the size of the bias is estimated in Section 5.4.

While some degree of model dependence is inherent to any analysis, it is preferable to make the analysis as less model-dependent as possible. In the analysis presented in this thesis, only muon kinematics are used in the near detector fit. As a result, we must rely on inclusive models which predict the impact of nuclear effects on the outgoing muon kinematics.

A more model-independent approach would consists in using additional variables in the analysis, such as information about final state hadrons (and in particular protons and neutrons). For instance, the effect of some flux and cross-section parameters may be the same when considering muon kinematics, but the predictions for proton kinematics can be very different, so using hadronic information can make it possible to lift the degeneracy between correlated parameter categories. This will become particularly important as more data is collected, since the statistical precision will require a corresponding reduction on systematic uncertainties.

There is an ongoing effort to move towards such an analysis in the near detector fit[5]. The ND280 upgrade (Chapter 6) will make it possible to exploit proton kinematics, which as a result will pave the way to probing nuclear effects more precisely. In preparation for the upgrade, the oscillation

---

[5] This approach concerns only the near detector, as at Super-K the Cherenkov threshold for protons is too high in order to be able to exploit such variables at the far detector.

analysis framework is being updated in order to accommodate parameters which exploit proton kinematics, and new observables are being developed for the near detector fit.

5.1.4 Correlations

A large part of the power of the BANFF fit lies in extracting correlations between the different systematic parameter categories. The BANFF fit produces a covariance matrix between all of the parameters used in the fit (so flux, detector and cross-section parameters). This matrix is the inverse of the hessian[6] matrix calculated with the HESSE algorithm in MINUIT. The correlation matrix is then a normalized version of the covariance matrix.

For illustration purposes, Fig. 5.13 shows the correlations introduced after the BANFF fit between the different parameter categories. No correlations existed before the fit between flux, detector and cross-section parameters. After the fit, the detector parameters show an up to 20% anti-correlation with the flux parameters, and this effect is rather uniform.

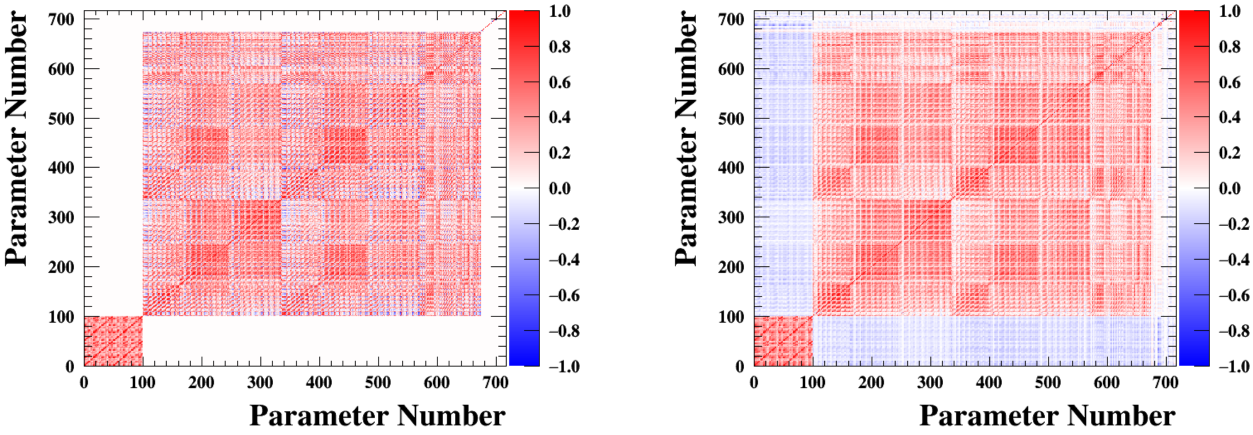

(a) Pre-fit

(b) Post-fit

Figure 5.13: Comparison of pre-fit (a) and post-fit (b) correlation matrices. The parameter numbers correspond to the following systematic categories: flux parameters, from 0 to 99; detector parameters from 100 to 673; and cross-section parameters from 674 to 716.

Fig. 5.14 shows a zoom on the flux and cross-section correlation introduced by the BANFF fit. There are large (up to 80%) anti-correlations between the flux parameters (particularly in the peak regions) and the CC0π parameters - namely M_A^{QE}, the Q^2 parameters and 2p2h normalization parameters. The presence of these strong correlations makes it difficult to interpret the exact meaning of CC0π parameters and is due to the fact that the flux parameters and the aforementioned CC0π parameters all have a normalization-like effect in similar regions of the phase space.

The correlations between cross-section parameters after the BANFF fit are presented in Fig. 5.15. We note that there are several regions with high correlations:

- The Q^2 parameters are all relatively highly correlated with each other. This is expected, since samples used in the near detector fit are binned in p_μ and cosθ_μ, which are not linear functions of Q^2. Several Q^2 parameters therefore act on the same p_μ-cosθ_μ bins.

---

[6] The hessian matrix is the matrix of second derivatives of parameters at their best-fit point.

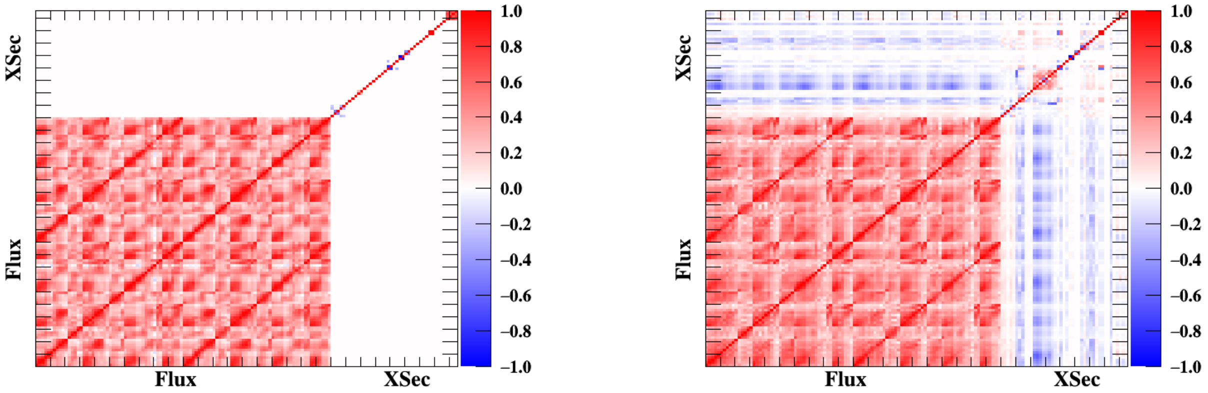

(a) Pre-fit (b) Post-fit

Figure 5.14: Comparison of pre-fit (a) and post-fit (b) correlation matrices for flux and cross-section parameters.

- The high Q^2 parameters (5, 6 and 7) have large anti-correlations with M_A^{QE}. This is also an expected effect, since M_A^{QE} controls the high-Q^2 region of the spectrum, but is known not to be a good model for this region. This is exactly the motivation for introducing the high Q^2 parameters, whose priors were extracted from other form factor parametrizations at large energies. These correlations, in particular, allow to partially decouple the effect of M_A^{QE} from that of low-Q^2 parameters.

- The 2p2h normalization parameters for neutrino and anti-neutrino events are positively correlated. This correlation is most probably acquired via the flux parameters.

- The Bodek-Yang correction parameters are anti-correlated, because they affect the event rate in the same way and because the multi-π and DIS regions populate overlapping regions in the p_μ-cosθ_μ phase space. These parameters also have a ∼10% correlation (for DIS) and anti-correlation (for multi-π) with the CC Coherent parameters.

- M_A^{RES} and C_5^A are strongly anti-correlated. This is expected because they affect overlapping regions of the spectrum and have a normalization-like effect, albeit with some shape features. For the same reasons, M_A^{RES} is negatively correlated with the CC Coherent parameters, whereas C_5^A is positively correlated with them.

- The binding energy parameters gain strong correlations among themselves, introduced via correlations with the flux and their own prior correlations. In addition, the $E_{b,\nu}^C$ parameter has a 20% anti-correlation with the 2p2h normalization for neutrino events, and the corresponding $E_{b,\bar{\nu}}^C$ parameter has a 14% anti-correlation with the 2p2h normalization for anti-neutrino events. This separation is expected - the interactions on carbon targets dominate the events at ND280, so the same type of correlation strength is less visible for the oxygen E_b parameters (though it is still present). This is yet another example of the difficulty to disentangle 2p2h and CCQE events within the CC0π samples.

- The FSI parameters have much smaller correlations than the ones in the pre-fit cross-section correlation matrix.

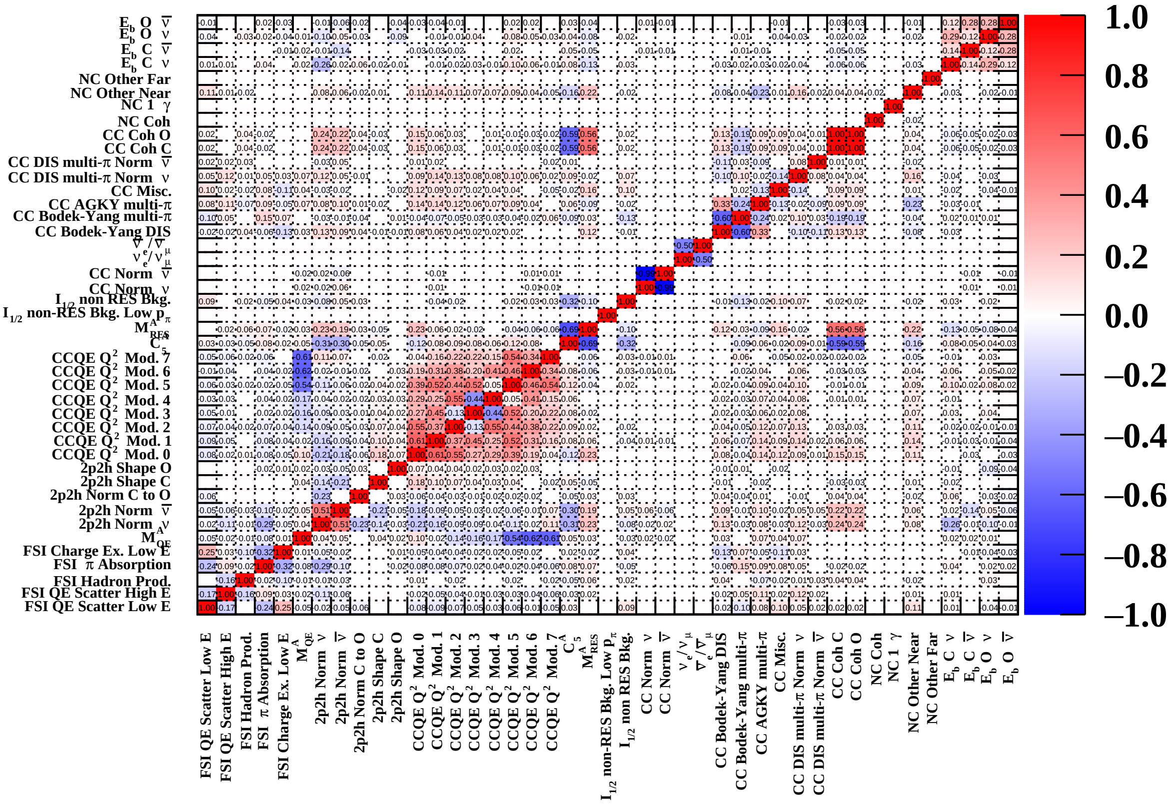

Figure 5.15: Post-fit correlation matrix for cross-section parameters.

5.2 P-Value calculation

After having performed the fit to the near detector data, it is possible to assess how well the pre-fit error model is capable of describing the data. To do this, we perform a *p-value* study.
We can define the following statement: $\mathbb{H}$ =“The model is compatible with the ND280 data” as the *null hypothesis*. We can then use the nominal error model to produce a large number of simulated data sets (“toy experiments”) which we fit with the same error model as used for the data. Each fit to a simulated data set will yield a minimized quantity $\Delta\chi^2$ (according to Eq. (4.4)). The data fit itself has a minimized $\Delta\chi^2_{Data} = 4736.94$. By looking at the distributions of the $\Delta\chi^2$ quantities of the simulated data fits, we define the p-value as the probability of the model to be compatible with the ND280 data ($\mathbb{H}$) or a more extreme data set (i.e. a data set whose $\Delta\chi^2$ is larger than that of the data), as follows:

$$p = \mathbb{P}(\Delta\chi^2 > \Delta\chi^2_{Data}|\mathbb{H}) = \frac{\int_{\Delta\chi^2_{Data}}^{+\infty} d\Delta\chi^2}{\int_0^{+\infty} d\Delta\chi^2} \tag{5.1}$$

A total of 895 toy experiments were created and fit with the BANFF nominal error model. Fig. 5.16 shows the $\Delta\chi^2$ distribution from the toy experiment fits, compared to the $\Delta\chi^2_{Data}$.

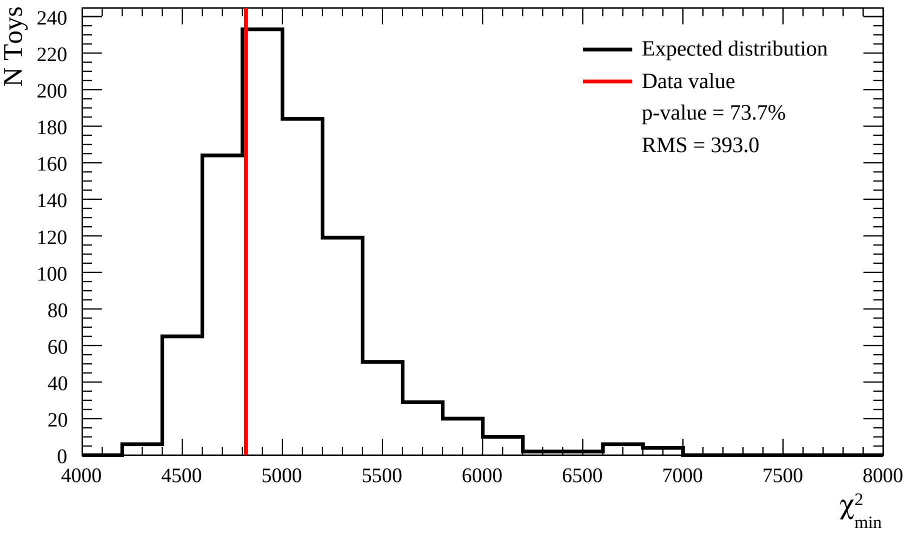

Figure 5.16: Distribution of total $\Delta\chi^2$ (here called χ^2_{min}) for the 895 toy experiment fits (black), compared to the $\Delta\chi^2_{Data}$ (red). The p-value calculated according to Eq. (5.1) and the RMS of the distribution are given in the legend.

The obtained p-value was of 73.7%, which indicates that the error model is largely capable of covering the data.

5.3 Effect on far detector samples

Not all of the systematic parameters used in the BANFF fit are propagated as constraints to the SK fitters. The ND280 detector parameters, the ND280 flux parameters, and some cross-section parameters specific to the near detector[7] are marginalized over. Their effect at the near detector is included in the post-fit errors on all the other parameters via the correlations seen in the previous section.

The systematic parameter best-fit values and errors are then used to reweight the SK MC prediction. Fig. 5.17 and Table 5.2 show the evolution of the SK MC with the BANFF tune. The event rate increases across all CCQE-like samples, and decreases in the 1Re1de sample, consistent with the BANFF prediction.

The reduction in the error from different systematic sources is further illustrated in Table 5.3. In order to obtain these numbers, the following procedure was applied for each SK sample:

- The SK MC is reweighted according to the nominal systematic parameter values either before or after the BANFF fit (for the errors before and after the constraint, respectively).
- The nominal distribution thus obtained is used to store the nominal total event rate, N.

---

[7] Namely, NC Other for near detector events, $E^C_{b,\nu}$, $E^C_{b,\bar{\nu}}$, the 2p2h shape for events on ^{12}C and the 2p2h shape parameter regulating the ratio of 2p2h events for ^{12}C and ^{16}O.

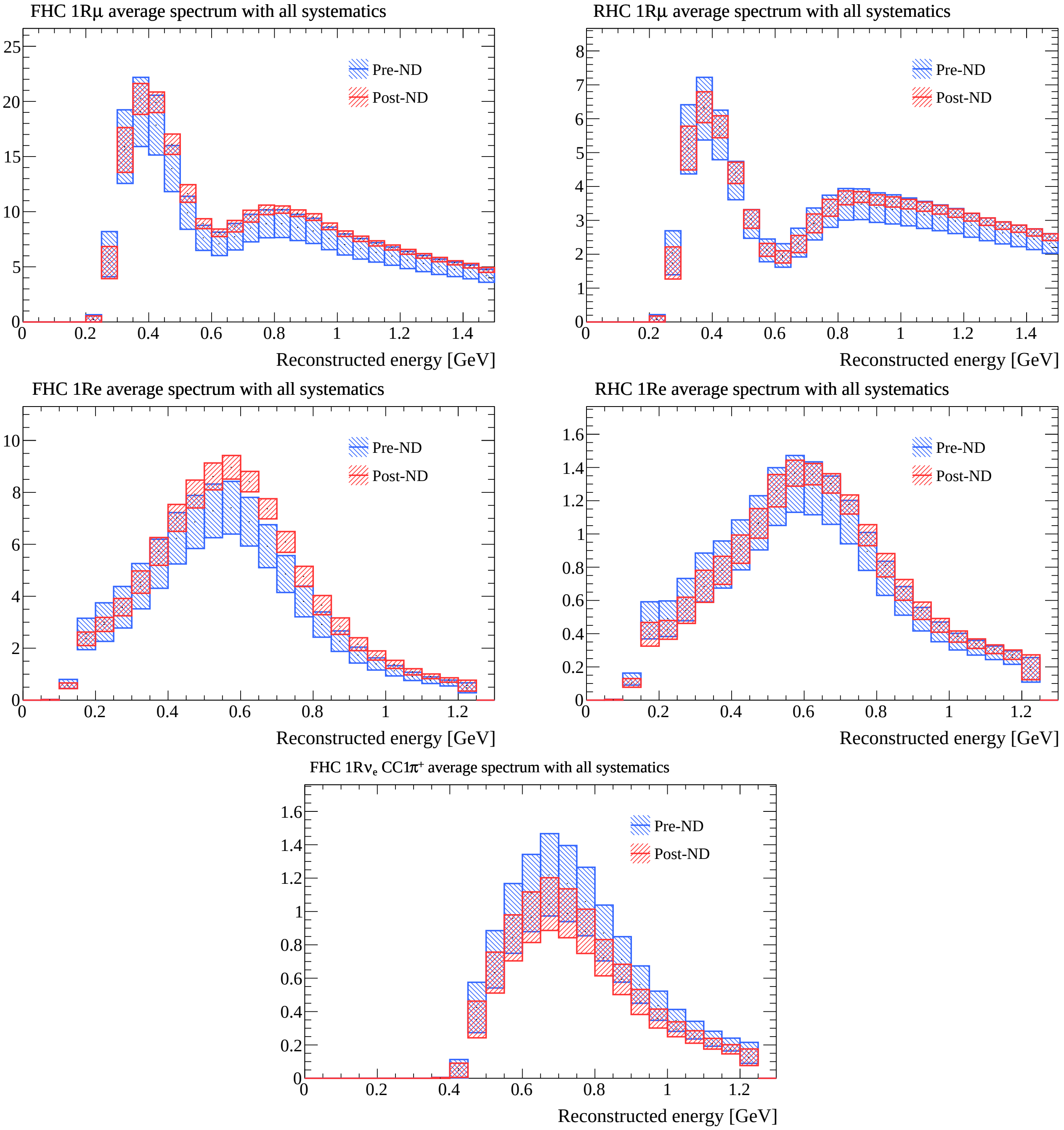

Figure 5.17: SK pre-fit MC as a function of reconstructed energy, before (blue) and after (red) the BANFF fit. The shaded regions show the 1σ error.

Sample	Predicted		Data
	before ND fit	after ND fit	
FHC 1Rμ	301.2	345.3	318
RHC 1Rμ	122.8	135.2	137
FHC 1Re	77.4	93.8	94
RHC 1Re	14.6	15.9	16
FHC 1Re1de	10.3	8.8	14

Table 5.2: Predicted event rates, before and after the BANFF fit, compared to the number of events in the data.

- For each of the systematic categories, the corresponding covariance matrix is used to throw the values of the systematic parameters. For flux and cross-section parameters, a different matrix is used depending on whether we are evaluating the pre- or post-ND fit errors. The SK detector systematic errors (also containing contributions from secondary interactions, SI, and photo-nuclear effects, PN[8]) are thrown from the same matrix, since the BANFF fit does not constrain these errors.
- Each throw will produce new nominal systematic parameter values, which are applied to the MC to create a new distribution, with N' events.
- The distribution of N' from all of the throws is fit with a gaussian function, and its RMS is taken as the absolute error, δN.
- The errors in Table 5.3 are calculated as $\delta N/N$, separately for each category, and once for all categories together to obtain the total error.

The error reduction after the near detector fit is apparent across all samples. The flux parameters have a post-fit error contribution of the level of just under 3% across all samples, reduced by about 40% from the pre-ND fit error.

The SK+SI+PN contributions are also slightly reduced, although they do not get directly constrained in the ND fit. The effect of the ND fit on this source of systematic errors is via the event rate itself: the SK MC is reweighted according to the BANFF best-fit values for systematic parameters, so even though the SK+SI+PN matrix does not change, the event rate does.

The cross-section parameters see a dramatic reduction in their error contribution. As previously mentioned, not all of the cross-section parameters described in Section 3.3.2 are constrained at the near detector. This is the case for the 2p2h energy dependence parameters, the NC Other parameter for the far detector, the NC 1γ background, and the $I_{1/2}$ non-resonant background for low-momentum pions. The effect of these cross-section parameters is evaluated separately (under “ND unconstr.” in the table), by throwing each of these parameters separately and then adding their effect on the event rate error in quadrature.

It is worth noting that the cross-section errors are the dominant source of systematic errors both before and after the ND constraint, particularly for the ratio of FHC to RHC 1Re samples. The latter is particularly important for δ_{CP} measurements, as the sensitivity to δ_{CP} comes from the asymmetry between ν_e and $\bar{\nu}_e$ appearance samples.

The total effect of the near detector fit is thus to reduce the total systematic error on CCQE-like

---

[8] See Section 3.3.3

	1Rμ		1Re			
Error source (units: %)	FHC	RHC	FHC	RHC	FHC 1d.e.	FHC/RHC
Flux (pre-ND)	5.0	4.7	4.8	4.7	4.9	2.6
Flux (post-ND)	**2.9**	**2.8**	**2.8**	**2.9**	**2.8**	**1.4**
SK+SI+PN (pre-ND)	2.7	2.3	3.2	4.2	13.4	1.3
SK+SI+PN (post-ND)	**2.1**	**1.9**	**3.1**	**3.9**	**13.4**	**1.2**
Xsec (pre-ND)	11.7	10.8	12.6	11.1	12.1	9.7
Xsec (post-ND) (ND constr.)	**3.1**	**3.0**	**3.2**	**3.1**	**4.2**	**1.5**
Xsec (post-ND) (ND unconstr.)	**0.6**	**2.5**	**3.2**	**3.6**	**2.8**	**3.8**
Total (pre-ND)	13.0	12.0	13.8	12.7	18.7	10.2
Total (post-ND)	**3.0**	**4.0**	**4.7**	**5.9**	**14.3**	**4.3**

Table 5.3: Summary of errors on SK samples, before (pre-ND) and after (post-ND) the BANFF fit. The entries are grouped according to the systematic error categories: flux; SK detector parameters, secondary interactions and photo-nuclear effects (SK+SI+PN); and cross-section parameters (Xsec). The cross-section parameters are further divided into two categories: constrained (ND constr.) and unconstrained (ND unconstr.) during the ND fit. The last column gives the error on the ratio of 1Re FHC and RHC samples.

samples (and in particular, on the signal 1Re appearance samples) from the level of 11-13% to the level of 3-6%. The 1Re1de systematic errors are dominated by the SK+SI+PN errors.

5.4 Robustness Studies

The validation tests described in Section 4.2 have proved that the tools used in the BANFF fit are working correctly, and the bias studies have shown a negligible impact on the far detector fit.

An additional set of tests are performed as part of the T2K oscillation analysis to test the robustness of the cross-section model itself. While the neutrino interaction model was designed with great care, it is by no means perfect, especially given our limited knowledge about neutrino interactions at T2K energies. We therefore perform a set of robustness studies using alternative interaction models and data-driven tunings to evaluate the capacity of both the near and the far detector fitters to account for such a discrepancy. This set of tests is usually performed when no neutrino interaction model is fully capable of predicting experimental data, or when a simplistic error model is used in the analysis with a plan to further develop it in future iterations of the OA.

The simulated data studies are performed in the following way:

- An alternative model or tune is chosen.
- The difference in the alternative model or tune with respect to the nominal MC prediction is applied as a set of weights to the nominal MC at the near detector, yielding a simulated data set.
- The simulated data set is fit with the nominal error model used in the OA.
- Independently, the far detector fit applies the same weights to the nominal SK MC prediction, obtaining a far detector simulated data set.

- The results of the BANFF fit to the simulated data are passed on to the far detector fit, which uses the constraints to reweight the nominal MC prediction according to the BANFF set of systematic parameters and errors.
- The far detector simulated data set is fit with the MC model modified under the BANFF simulated data fit.
- The oscillation parameters results of the far detector fit are compared to the nominal Asimov fit. If a bias is observed, different procedures are applied depending on the parameter and the size of the discrepancy.

A wide range of alternative models and tunes was tested in this OA. The rest of the chapter will describe the simulated data sets which have the largest impact on the oscillation parameters. At the end of this section, the quantitative impact of all of the simulated data sets will be summarized and the procedure to take possible biases into account will be described.
The complete description of all of the simulated data sets is documented in [148].

5.4.1 CC0π-focused simulated data set

The change from RFG to SF as a nuclear ground state model represents an important step towards future exclusive analyses, and is one of the most important improvements in the T2K oscillation analysis. The Q^2 normalization parameters described in subsubsection 3.3.2.1 were introduced to provide an ad-hoc freedom in the model, based on known discrepancies between the SF model and cross-section measurements. These normalization parameters currently affect only quasi-elastic events, since these are the events concerned by the SF ground-state model. However, this parametrization is purely empirical and does not have any strong theoretical grounding. In addition, these parameters are strongly correlated with CC0π flux parameters and the effective quasi-elastic axial mass M_A^{QE}. One way to test the robustness of this parametrization and its impact on oscillation parameters measurements is to assume that the data-MC discrepancy, absorbed in the data fit by the Q^2 parameters, is instead entirely due to non-quasielastic contributions to the CC0pi sample. We have devised a simulated data set to replicate this effect in the following way:

- The MC prediction *after* the ND280 data fit is taken and the post-fit values of the Q^2 parameters are set to 1 (i.e. the effect of the Q^2 parameters is cancelled).
- Both data events and the MC distribution obtained in the previous step are used to build reconstructed Q^2 distributions assuming QE kinematics (Q^2_{QE}), and the binning of these distributions is designed to match the ranges of the Q^2 parameters. This is only done for the 0π samples.
- The non-quasielastic (but of true CC0π topology) MC events are then varied until the modified MC distribution matches the data distribution. If varying the non-quasielastic contribution is not enough, QE events are varied as well.
- The resulting change in the non-quasielastic (but true CC0π) events is then applied as a set of weights to the nominal MC as a function of true Q^2_{QE} and gives the resulting simulated data set.

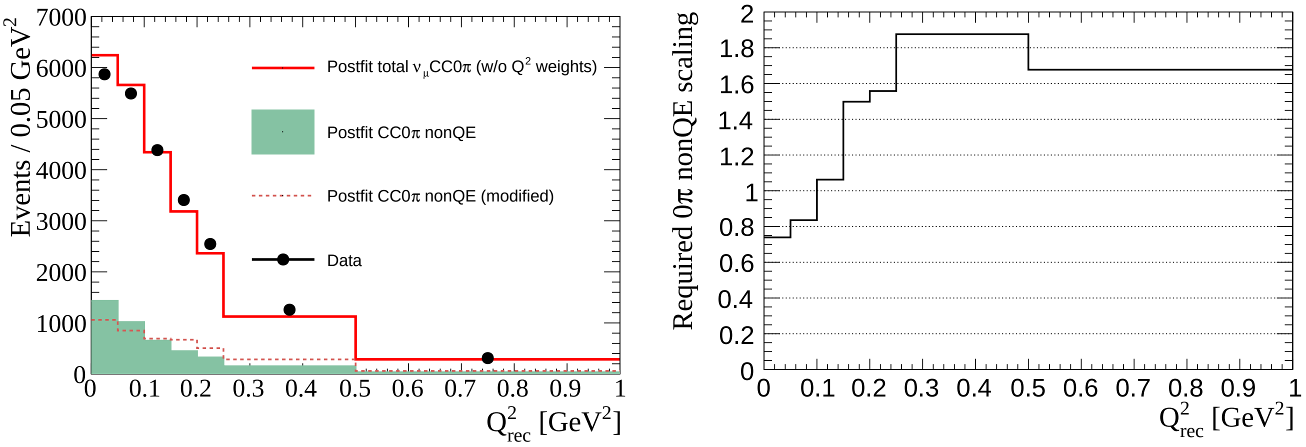

(a) (b)

Figure 5.18: (a) The post-fit near detector model *adjusted to set all the Q^2 scaling parameters to 1.0* is shown compared to the the FGD1 CC0π sample data, where the non-quasielastic (but true CC0π) contribution ("nonQE") is delineated by the shaded green region. The modification of this contribution that would be required to match the data is shown as the dotted red line. (b) The required weight to be applied to the non-quasielastic (but true CC0π) contribution to match the data. This is the scaling that was applied to obtain the simulated data set (in addition to resetting all Q^2 parameters to 1.0) as a function of true Q^2_{QE}.

This process has been applied separately to ν_μ and $\bar{\nu}_\mu$ samples, in order to extract different weights for neutrino and antineutrino events. The weight extraction process and the resulting weights for neutrino events is shown in Figure 5.18.

This is an example of a data-driven simulated data study: the weights to obtain the simulated data set were extracted from a data-MC discrepancy, rather than from an alternative nuclear model or other theoretical considerations. This simplistic simulated data set provides a conservative estimate of the maximum expected bias, by assuming that the entire CCQE mis-modelling is actually due to non-CCQE processes.

There are several limitations to this simulated data study. The weights shown in Figure 5.18 were extracted using the transferred 4-momentum reconstructed assuming quasi-elastic kinematics (Q^2_{QE}) as a proxy for the actual 4-momentum ($Q^2 = P_\nu - P_\mu$, where P_ν and P_μ are the neutrino and muon 4-momenta, respectively). Since the weights were extracted from a comparison with data, whose true Q^2 cannot be determined, by definition, Q^2_{QE} was used as a proxy for Q^2 even though it does not correspond entirely to events with non-quasi-elastic kinematics in the MC.

This study attempts to address the differences between neutrinos and anti-neutrinos by applying different weights for the two flavors. A more complete study should take into account the differences between interactions on carbon and oxygen targets.

5.4.1.1 Near Detector Fit Results

Figure 5.19 shows that the near detector systematic errors were globally recovered at the expected input value. The two parameters which deviate the most from the prediction are the last two Q^2 modifications, which control high-energy regions of the spectrum.

It is also worth noting that the high energy flux parameters are increased, which is an effect opposite to the high-Q^2 suppression seen in the cross-section parameters. The flux and Q^2 parameters are highly correlated, but the post-fit errors are still contained inside the allowed ranges of the nominal model.

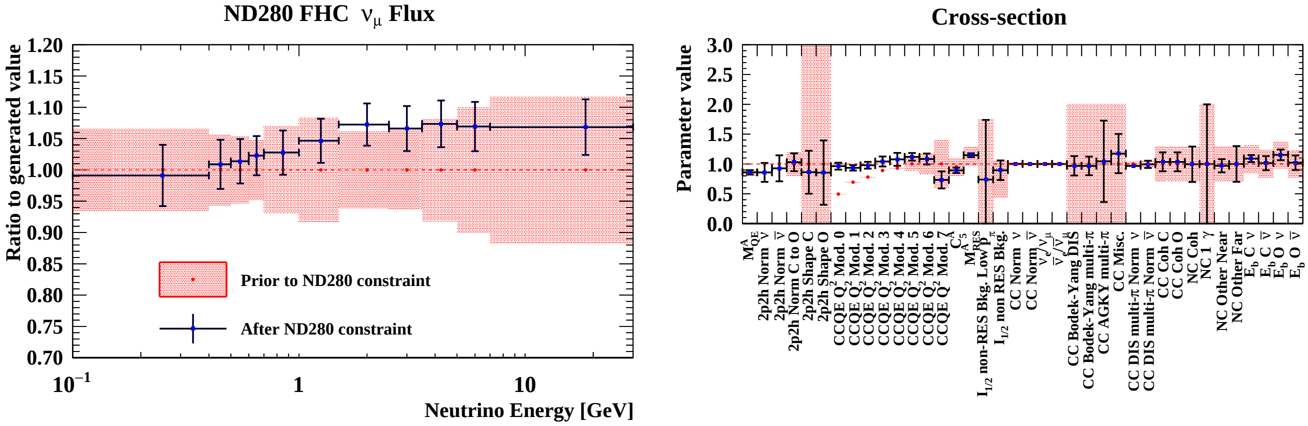

(a) (b)

Figure 5.19: Flux (a) and cross-section (b) systematic parameters as a result of the near detector fit to the CC0π-focused simulated data set. The red boxes show the nominal model prediction and errors.

5.4.1.2 Far Detector Fit Results

Fig. 5.20 shows how the obtained SK simulated data set compares to the nominal MC prediction and, especially, to the BANFF best fit prediction and errors. Ideally, the SK simulated data set (blue line) should be contained inside the BANFF errors for the fit to the corresponding near detector fake data set (red boxes). Any deviation from this agreement is an indication of a possible source of bias.

In Fig. 5.20, this is mostly the case. However, we do see a slight disagreement for the RHC 1Re sample. This is most probably due to the fact that the near detector fit is driven by FHC samples.

The effect of this simulated data set on the oscillation parameter contours can be seen in Fig. 5.21. $\sin^2\theta_{13}$ is largely unaffected by this fake data set. However, a small bias can be seen in the $\sin^2\theta_{23}$, Δm^2_{32} and δ_{CP} likelihoods. The simulated data set has a slightly smaller sensitivity to $\sin^2\theta_{23}$, consistent with the fact that 1Rμ samples see a shape-like shift compared to the Asimov data set, which drives the $\sin^2\theta_{23}$ sensitivity. On the other hand, the sensitivity to δ_{CP} and Δm^2_{32} improves for the simulated data set - the latter predicts an increase in the CCQE-like event rate (although driven by non-quasielastic events), which in turn increases the sensitivity to δ_{CP} by increasing the asymmetry between ν_e and $\bar{\nu}_e$ samples, and increases the sensitivity to Δm^2_{32} by decreasing the width of the disappearance dip.

5.4.2 Martini 2p2h simulated data set

As explained in Section 2.4.2.1, no available 2p2h model is entirely capable of fully describing experimental data. In this analysis, the baseline model for 2p2h interactions was chosen to be the Nieves et al. [94] model. The Martini et al. [95] model provides a 2p2h cross-section prediction which is almost double that of the Nieves et al. model for neutrino events, and about 50% larger

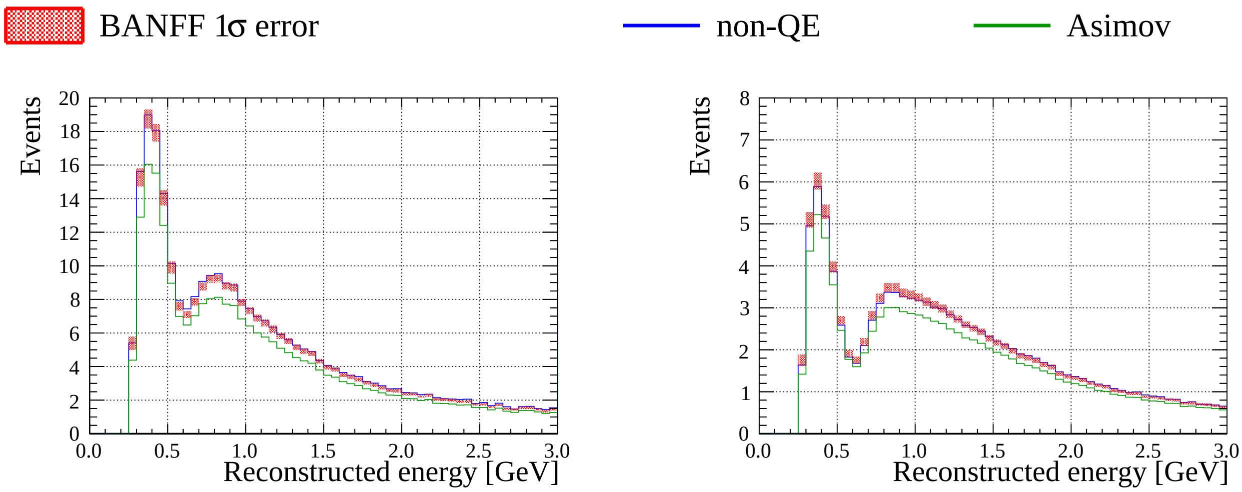

(a) FHC 1Rμ (b) RHC 1Rμ

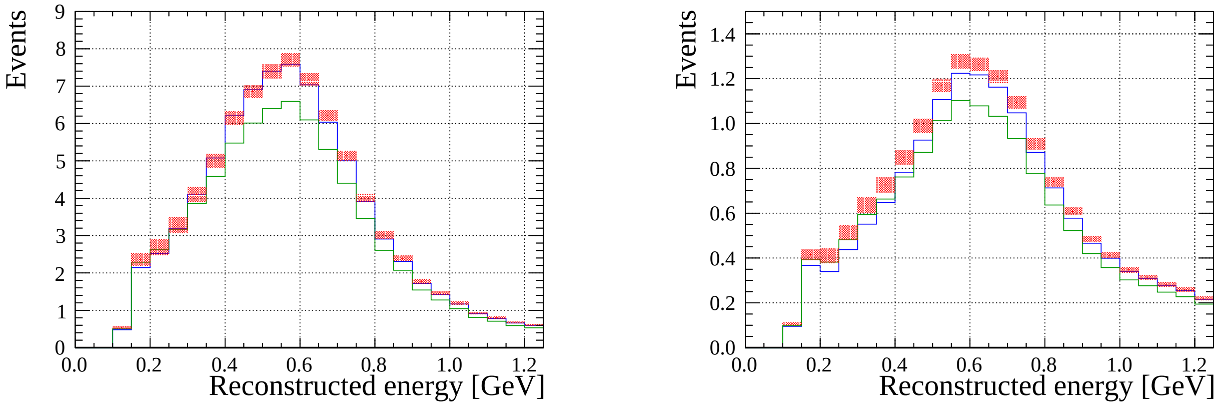

(c) FHC 1Re (d) RHC 1Re

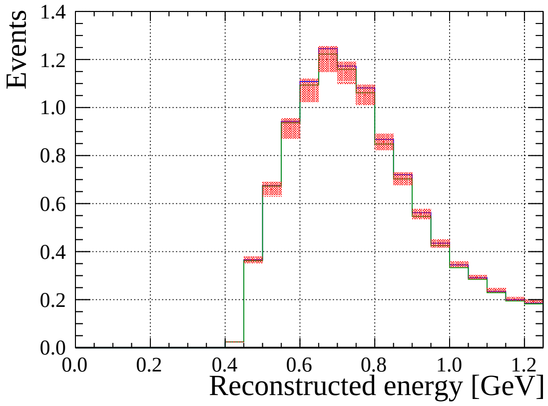

(e) FHC 1Re1de

Figure 5.20: SK predictions for the CC0π-focused simulated data set. The green line shows the nominal SK Asimov, with nominal BANFF Asimov best-fit systematic parameters. The blue line shows the SK prediction after applying the required weights to the nominal prediction - essentially, the SK simulated data set. The red shaded regions and their points show the errors and best-fit points from the BANFF fit to the simulated data set.

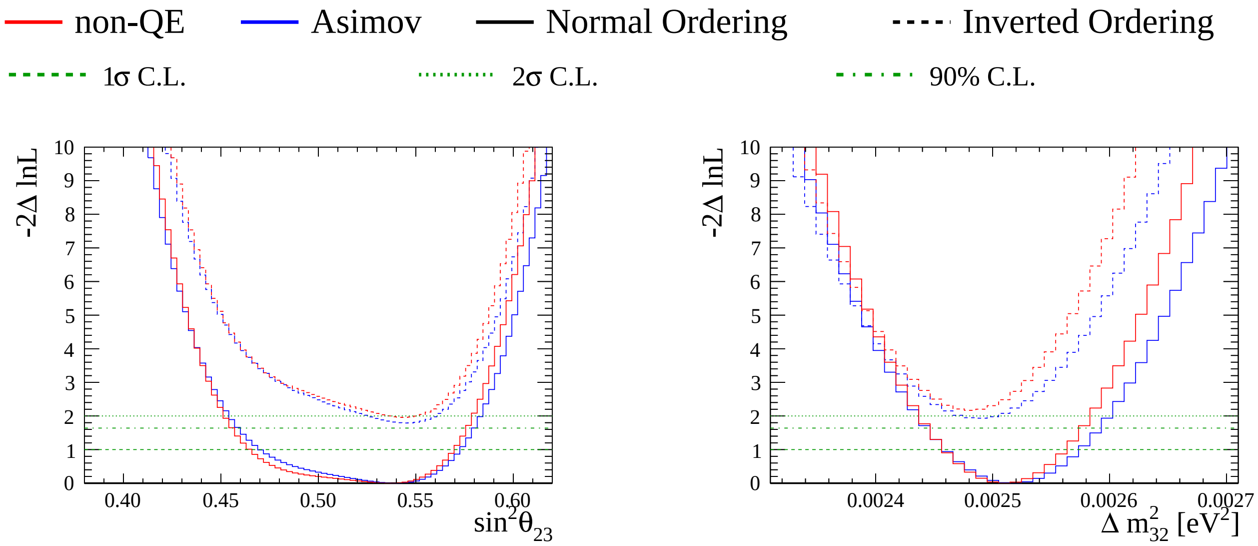

(a) $\sin^2\theta_{23}$ with reactor constraint

(b) Δm^2_{23} with reactor constraint

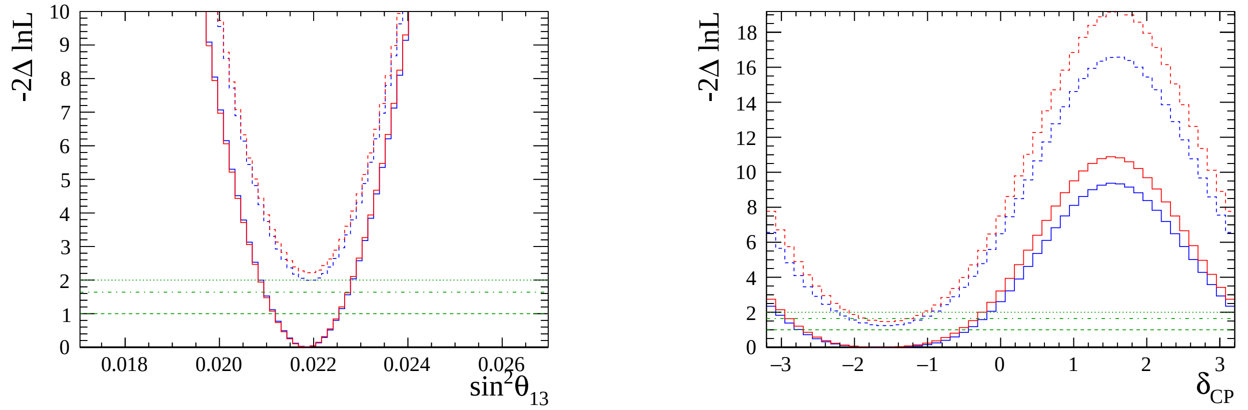

(c) $\sin^2\theta_{13}$ with reactor constraint

(d) δ_{CP} with reactor constraint

Figure 5.21: 1-D likelihood surfaces for all parameters, with the reactor constraint on $\sin^2\theta_{13}$, assuming normal hierarchy for the CC0π-focused simulated data set.

than that for anti-neutrino events. As such, testing the robustness of the oscillation analysis against such a large variation will show the extent of the bias we can expect due to 2p2h mis-modelling. As a reminder, 2p2h events populate a non-negligible part of the CCQE-like samples but do not have QE kinematics. They are therefore a source of bias in the energy reconstruction process, and need to be modelled as best as possible.

In order to generate a simulated data set mimicking the Martini et al. predictions for 2p2h events, we take the ratio of the NEUT cross-section predictions between the Martini et al. model and the Nieves et al. model, as a function of true neutrino energy, and apply them as separate weights for neutrino and anti-neutrino 2p2h events. Fig. 5.22 shows the behavior of the weights as a function of true neutrino energy (E_ν).

In reality, there is a caveat in the construction process of this simulated data set. Both the Nieves et al. model and the Martini et al. model give predictions up to 1.2 GeV in neutrino energy. Above this value, no prediction is available. In order to avoid having an unphysical cutoff, it was decided to extrapolate the last weight applied at 1.2 GeV until the end of the spectrum.

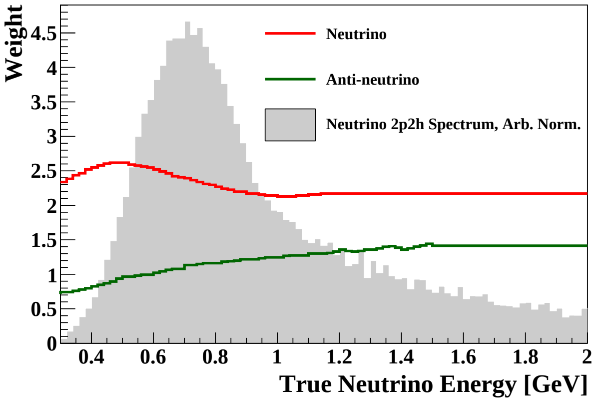

Figure 5.22: Weights applied to neutrino (red) and anti-neutrino (green) 2p2h events in the Martini 2p2h simulated data set.

5.4.2.1 Near Detector Fit Results

The results of the near detector fit[9] to the Martini et al. simulated data set (referred to as “Martini 2p2h”) are summarized in Fig. 5.23. The BANFF fit is capable of picking up the variation due to the Martini et al. model via the 2p2h normalization parameters, which are increased by ∼150% (∼15%) with respect to the nominal Nieves et al. predictions for neutrino (anti-neutrino) events. Due to the correlations between flux and 2p2h parameters, the low- to mid- energy flux parameters are also slightly increased, whereas the high-energy flux parameters are very slightly decreased. No other parameters are affected significantly.

5.4.2.2 Far Detector Fit Results

Fig. 5.24 shows the impact of the Martini 2p2h simulated data set on the SK samples. Unlike the previous CC0π-focused simulated data set, the Martini 2p2h simulated data set shows a relatively

---

[9] In order to be able to compare to the nominal Asimov sensitivity, the simulated data set was constructed with a nominal error model assuming priors different from unity for the low-Q^2 parameters.

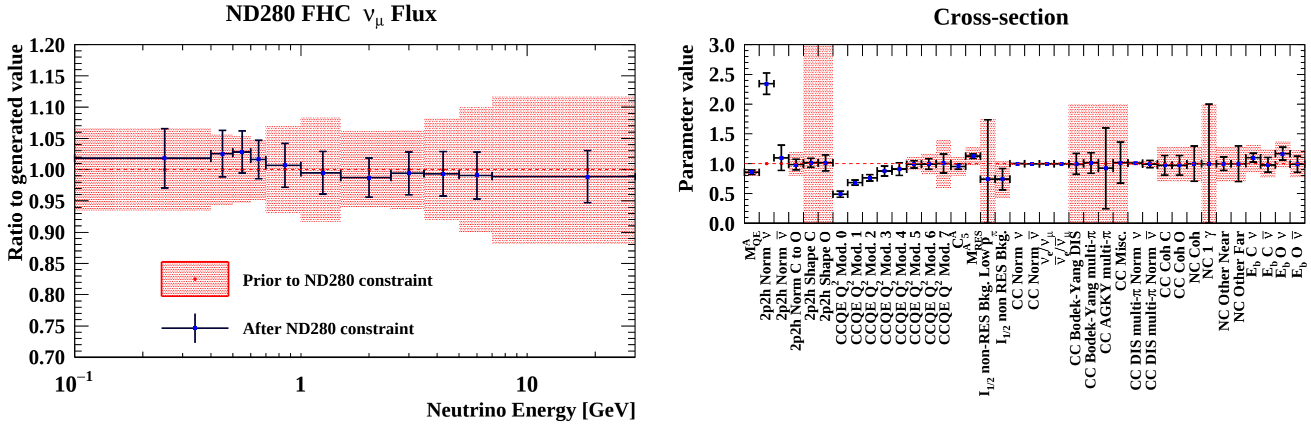

(a) (b)

Figure 5.23: Flux (a) and cross-section (b) systematic parameters as a result of the near detector fit to the Martini 2p2h simulated data set. The red boxes show the nominal model prediction and errors.

good agreement between the BANFF prediction and the SK simulated data. Based on this, we expect the bias on oscillation parameters to be small.

The impact of this simulated data set on the oscillation parameters is shown in Fig. 5.25. Due to the good agreement across CCQE-like samples, the sensitivity to $\sin^2\theta_{23}$, $\sin^2\theta_{13}$ and Δm^2_{32} is virtually unchanged. However, the sensitivity to δ_{CP} is improved for the Martini 2p2h simulated data set. This is due to the fact that the simulated data set impacts neutrino and anti-neutrino events in a different way, and thus the asymmetry between ν_e and $\bar{\nu}_e$ samples is larger. An increase in statistics alone can change the oscillation parameters results, but it does not quantify the bias due to the systematic uncertainty mis-modelling. To address this, when the final bias is calculated, the effect of statistics and systematics is separated, as will be detailed in Section 5.4.6.

5.4.3 MINERνA pion suppression tune

The MINERνA collaboration performed an extensive analysis of their pion production data, reported in [8]. This analysis included both single and multiple pion channels, as well as neutral pion production in neutrino and antineutrino beam data. The authors tuned the GENIE neutrino event generator to match both the MINERνA data and the pion production data from the ANL and BNL bubble chambers. They found that an additional suppression of pion production was needed at low Q^2, as shown in Fig. 5.26.

The pion suppression shown in red in Fig. 5.26 is applied at the near and far detectors according to equations 6 and 7 from [8]. This suppression is applied to charged-current resonant pion events only.

5.4.3.1 Near Detector Fit Results

The near detector fit results for the MINERνA pion suppression tune are shown in Fig. 5.27. As expected, this simulated data set modifies the post-fit values of CC1π parameters, namely M_A^{RES}

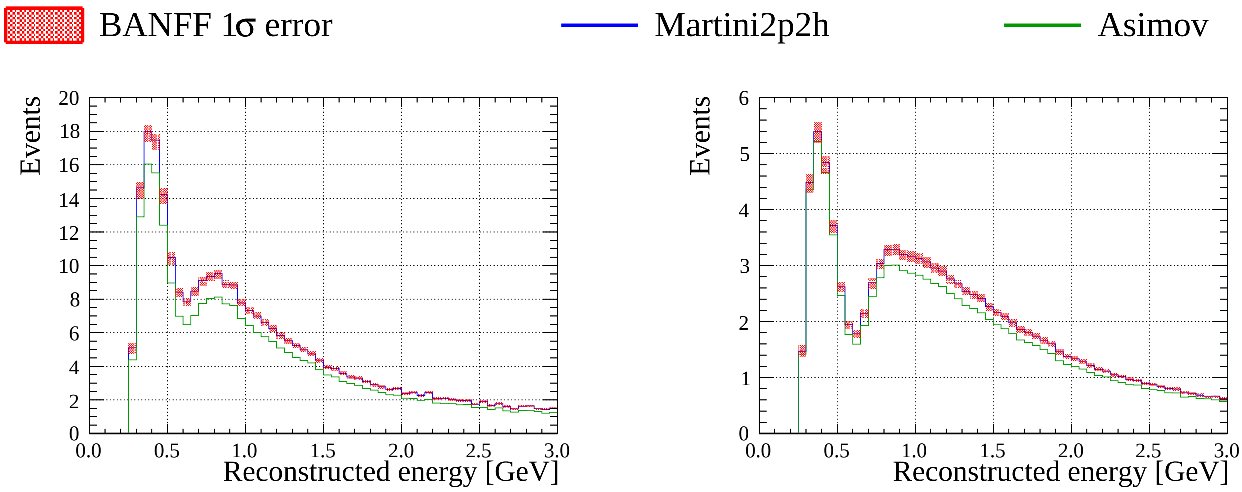

(a) FHC 1Rμ

(b) RHC 1Rμ

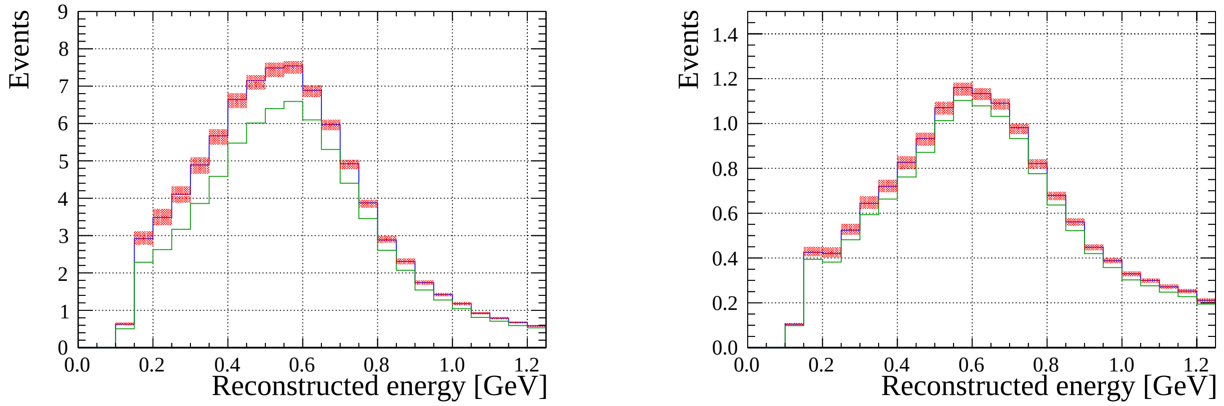

(c) FHC 1Re

(d) RHC 1Re

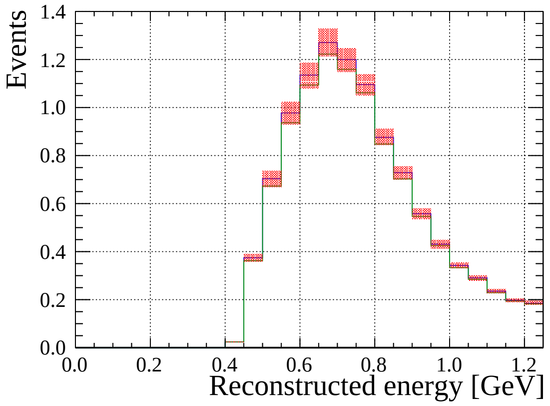

(e) FHC 1Re1de

Figure 5.24: SK predictions for the Martini 2p2h simulated data set. The green line shows the nominal SK Asimov, with nominal BANFF Asimov best-fit systematic parameters. The blue line shows the SK prediction after applying the required weights to the nominal prediction - essentially, the SK simulated data set. The red shaded regions and their points show the errors and best-fit points from the BANFF fit to the simulated data set.

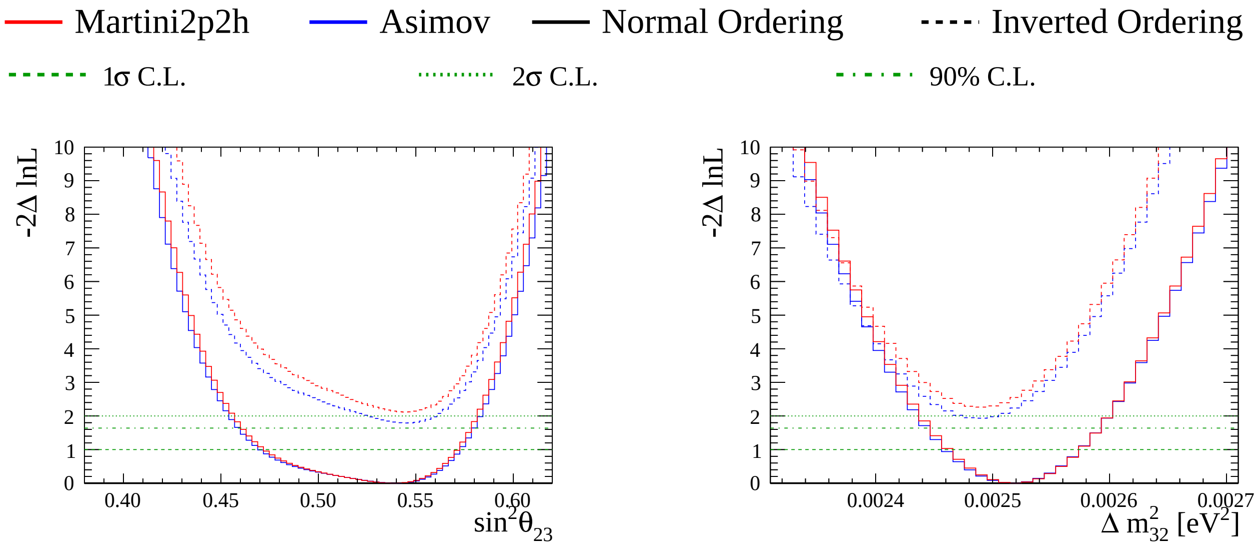

(a) $\sin^2\theta_{23}$ with reactor constraint

(b) Δm^2_{23} with reactor constraint

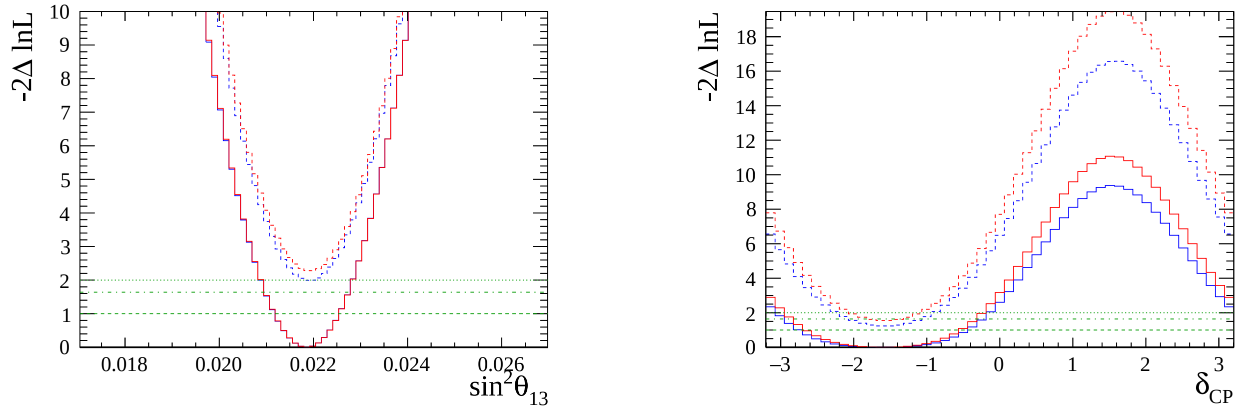

(c) $\sin^2\theta_{13}$ with reactor constraint

(d) δ_{CP} with reactor constraint

Figure 5.25: 1-D likelihood surfaces for all parameters, with the reactor constraint on $\sin^2\theta_{13}$, assuming normal hierarchy for the Martini 2p2h simulated data set.

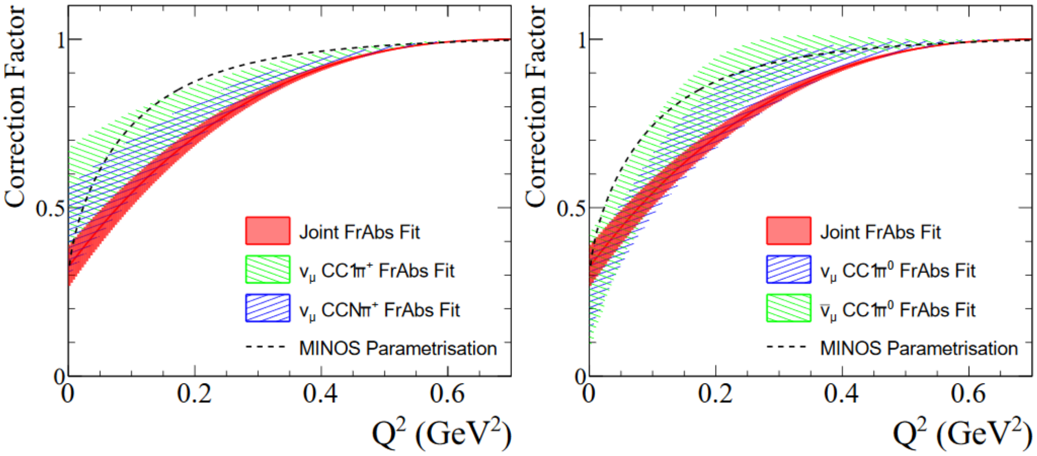

Figure 5.26: Extracted low-Q^2 suppression factors from the FrAbs + low-Q^2 tuning to each channel. The left and right plots compare the results for the charged and neutral pion production channels respectively. Shown in red is the uncertainty band extracted from the joint fit to all 4 channels simultaneously. Taken from [8].

and C_5^A. C_5^A, which controls the entire Q^2 spectrum, is slightly reduced as a result of the pion suppression at low Q^2 values, and as a consequence M_A^{RES} is slightly increase, to compensate for an over-reduction of the event rate at high Q^2 values. Some other parameters are affected: the CC Coherent parameters are reduced to their lowest limit allowed by the prior errors - coherent events also populate the low Q^2 region. The CCDIS parameters are modified slightly within their large errors, because some DIS background is still present in 1π samples. Finally, since some 2p2h events also populate the CC1π samples, the 2p2h normalization parameters are reduced as a consequence of the suppression as well. Overall, the BANFF fit was capable of capturing the modifications that the MINERνA pion suppression tune might induce.

5.4.3.2 Far Detector Fit Results

The MINERνA pion suppression tune affects CCRes events, which mostly populate the 1Re1de sample at SK. A significant impact on the CCQE-like samples is therefore not expected. This is confirmed by the SK spectra in Fig. 5.28. Although the BANFF prediction is systematically slightly underneath the SK simulated data, the two predictions agree within the near-detector systematic errors.
However, the disagreement between the near and far detector simulated data is particularly striking in the 1Re1de sample. This disagreement is a sign of an issue in the near-to-far detector extrapolation. The 1Re1de sample selects pions below Cherenkov threshold (Section 3.2.4), and the ND280 fit does not exploit pion kinematics during the fit. Even though the near detector fit correctly identifies the changes induced in the p_μ-cosθ_μ spectrum, the pion kinematic phase space is not the same at ND280 and SK. In particular, by selecting pions below Cherenkov threshold, the 1Re1de sample will see a larger suppression of events as a result of the MINERνA tune compared to the ND280 data.

The impact of the MINERνA pion suppression on the sensitivity to oscillation parameters is shown in Fig. 5.29. Since this simulated data set has a relatively low impact on the signal CCQE-

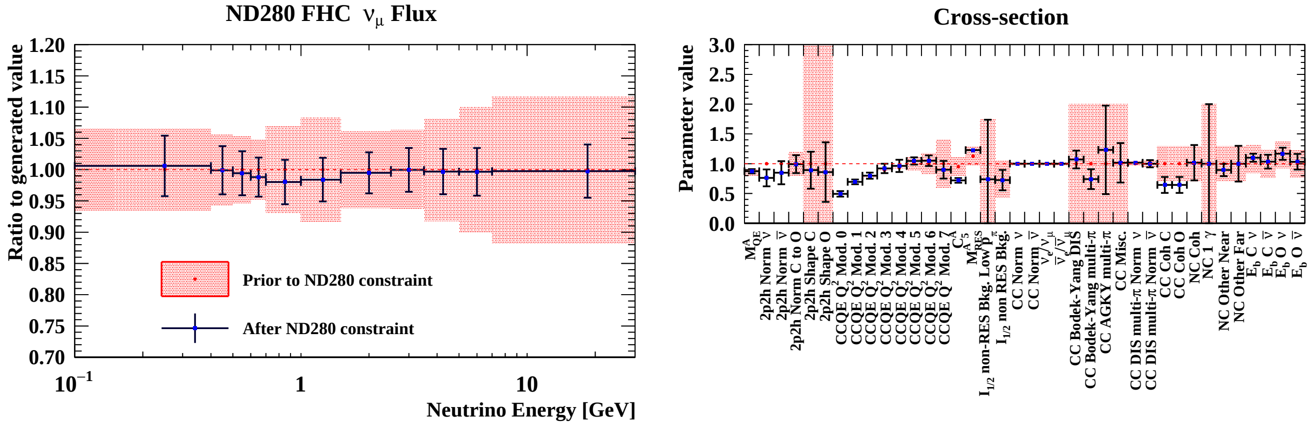

(a) (b)

Figure 5.27: Flux (a) and cross-section (b) systematic parameters as a result of the near detector fit to the MINERνA pion suppression tune simulated data set. The red boxes show the nominal model prediction and errors.

like samples, the change in sensitivity across all oscillation parameters is negligible. The largest change is seen in δ_{CP}, but it is much smaller compared to that induced by previous simulated data sets. Actually, the MINERνA pion suppression tune reduces the sensitivity to δ_{CP}, most notably because of its similar effect on ν_e and $\bar{\nu}_e$ samples, for which it slightly reduces the event rate.

Despite its limited effect on the sensitivity to oscillation parameter measurements, this simulated data set is nevertheless interesting as it highlights a discrepancy in the near-to-far detector extrapolation.

5.4.4 Data-Driven Pion Kinematics Simulated Data Set

The 1Re1de sample at SK only selects pions below Cherenkov threshold. However, the efficiency to select a pion is not flat across the pion momentum range, as is illustrated in Fig. 5.30.
In addition, the BANFF fit does not yet exploit pion kinematics in the near detector fit, and no dedicated pion systematics are included in the analysis yet. As a result, a sizable discrepancy can be seen in the pion momentum between the baseline model (i.e. after the ND280 data fit) and the ND280 data, as shown in Fig. 5.31.

The consequence of this is the introduction of a bias in the analysis, and the size of this bias on the oscillation parameters is estimated using a simulated data set. To create the simulated data set, the discrepancy between the data and post-ND fit MC observed at ND280 is applied as a single weight to the true SK 1Re1de events as a function of true pion momentum. In the $p_\pi^{reco} < 200$ MeV/c range, which roughly corresponds to the Michel tagging efficiency tipping point in true pion momentum at SK, the TPC pions have the largest data/MC ratio at 23% (closely followed by FGD1 $\bar{\nu}_\mu$ at 22.5%). FGD pions are underestimated by $\sim$ 10% in the same pion momentum range. The 23% from FGD1 CC1π TPC pions is applied without shape (i.e. as a single weight) to Super-Kamiokande events [10].

---

[10] Note that the the *reconstructed* pion candidate's *reconstructed* momentum at ND280 is applied to the *true* single pion's *true* momentum at SK. The assumption behind this is that the pion momentum is well-reconstructed, which is a justified assumption for the TPC pions used to extract this weight.

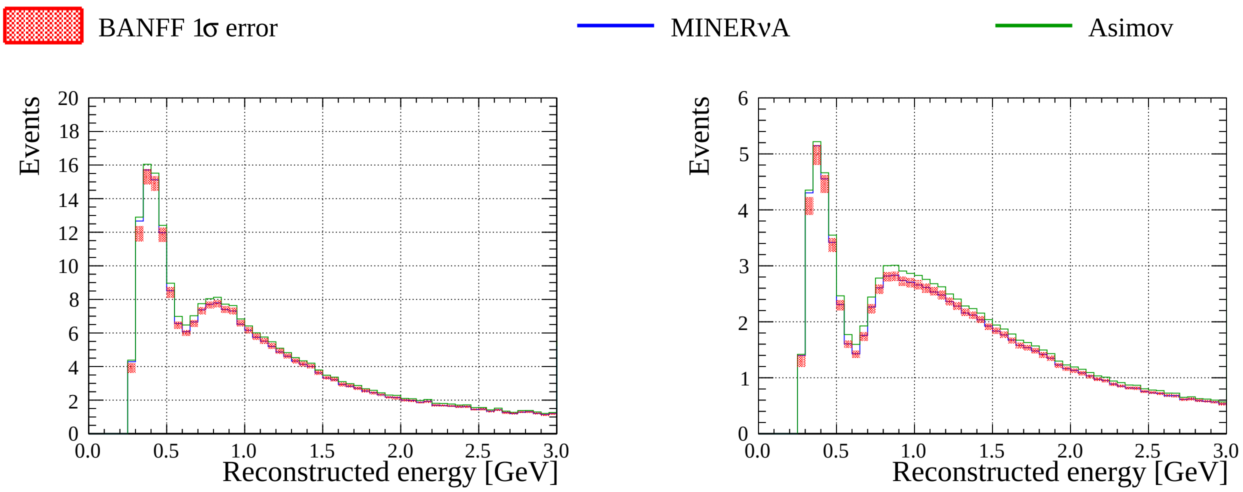

(a) FHC 1Rμ

(b) RHC 1Rμ

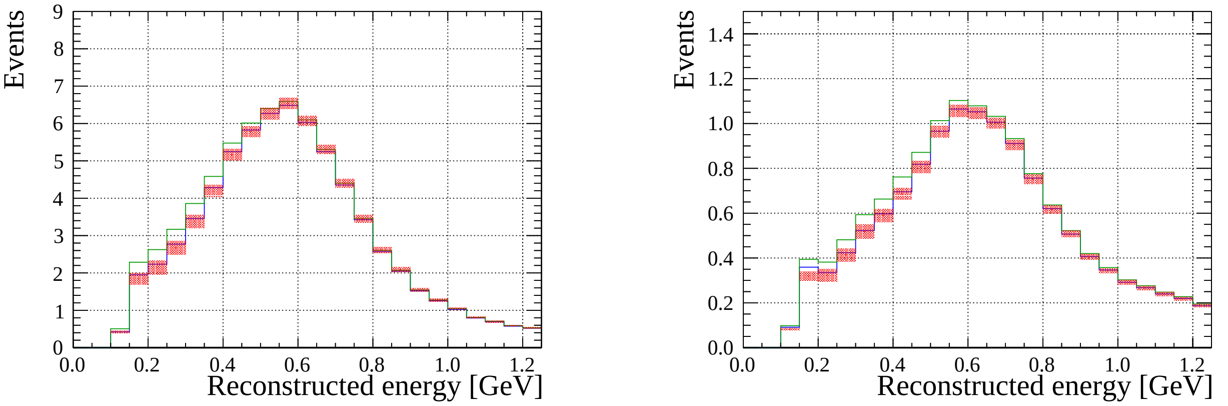

(c) FHC 1Re

(d) RHC 1Re

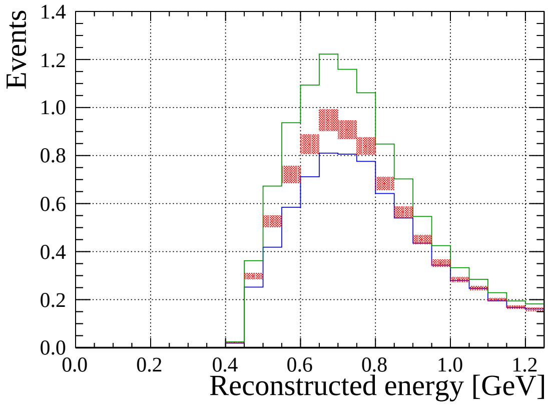

(e) FHC 1Re1de

Figure 5.28: SK predictions for the MINERνA pion suppression tune simulated data set. The green line shows the nominal SK Asimov, with nominal BANFF Asimov best-fit systematic parameters. The blue line shows the SK prediction after applying the required weights to the nominal prediction - essentially, the SK simulated data set. The red shaded regions and their points show the errors and best-fit points from the BANFF fit to the simulated data set.

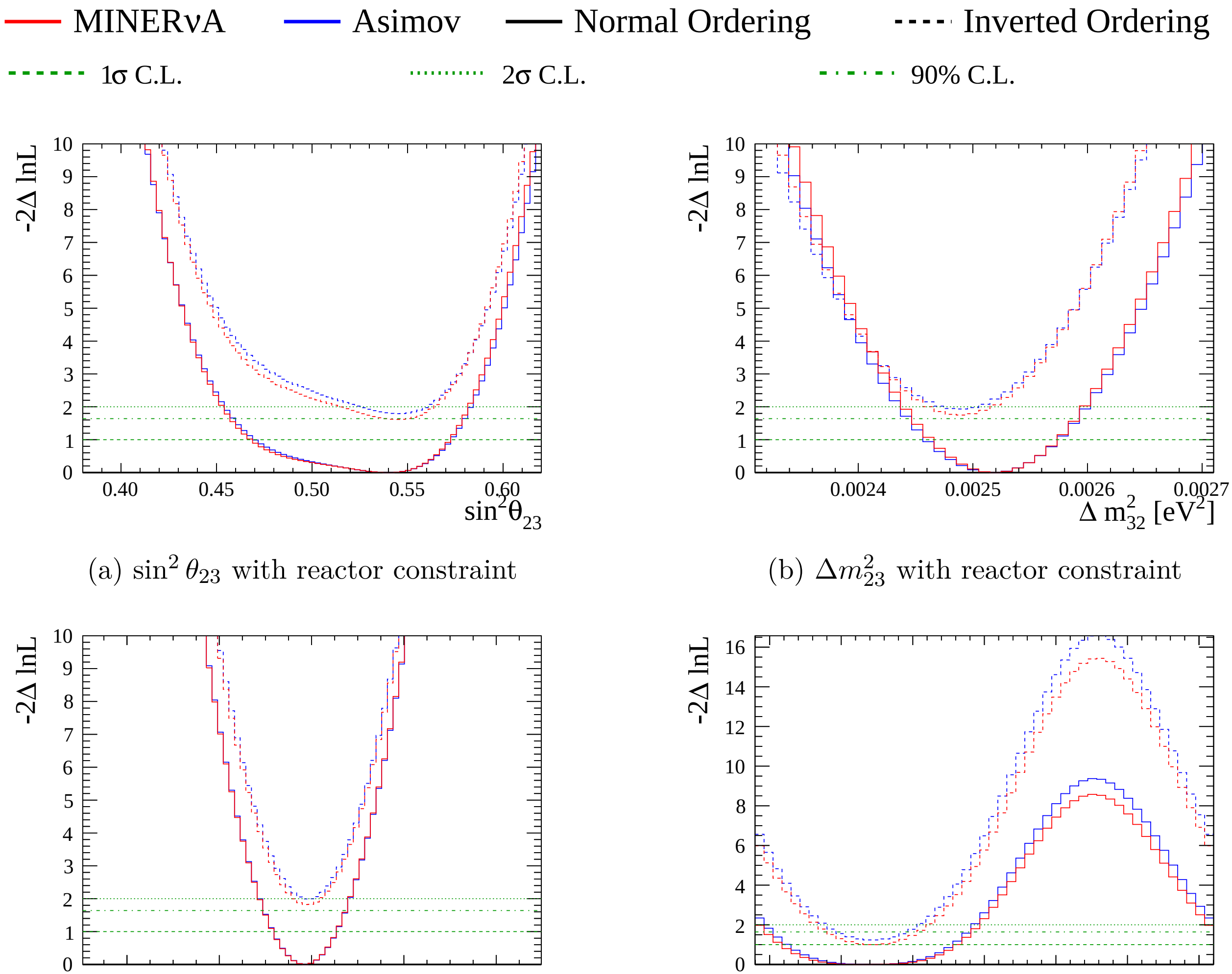

(a) $\sin^2\theta_{23}$ with reactor constraint

(b) Δm^2_{23} with reactor constraint

(c) $\sin^2\theta_{13}$ with reactor constraint

(d) δ_{CP} with reactor constraint

Figure 5.29: 1-D likelihood surfaces for all parameters, with the reactor constraint on $\sin^2\theta_{13}$, assuming normal hierarchy for the MINERνA pion suppression tune simulated data set.

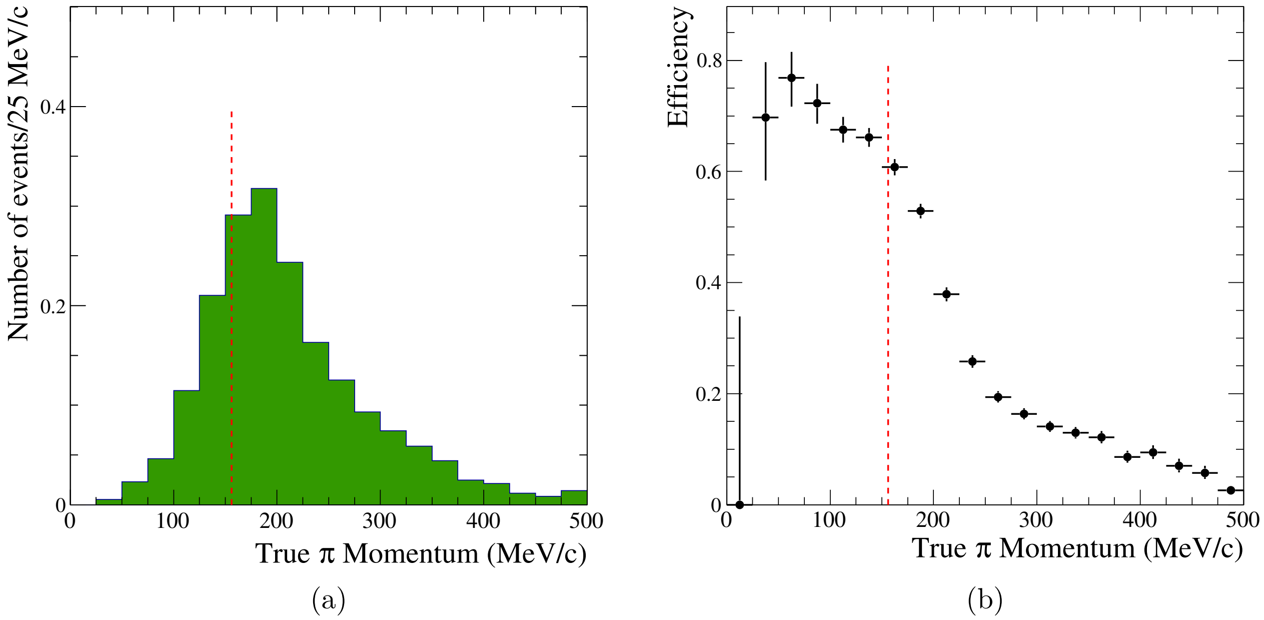

(a) (b)

Figure 5.30: The true momentum distribution for selected simulated signal events in the 1Re1de sample with 1 electron-ring and 1 Michel electron at SK (a) and the selection efficiency for these events (b). The red dashed line indicates the Cherenkov threshold for charged pions.

This simulated data study is the only one which did not have a corresponding ND280 fit (as the simulated data set itself was obtained from the ND280 fit to data). It was therefore only applied at SK.

5.4.4.1 Far Detector Fit Results

As expected, this simulated data set affects mostly the 1Re1de sample at SK. The impact on the SK samples is shown in Fig. 5.32. The bias on the oscillation parameters is very small, with the largest one being seen on δ_{CP}, due to slight event rate change in $\nu_e/\bar{\nu}_e$ samples. This simulated data study confirms that the pion kinematics mis-modelling is currently not a significant source of bias in the analysis.
However, the discrepancy between the data and MC as a function of pion momentum highlights a deficiency in the analysis. Although this does not bias the oscillation parameter measurements at the current level of statistics, it is important to develop appropriate samples and systematic uncertainties to reduce the data/MC discrepancy shown in Fig. 5.31 and to address the near-to-far detector extrapolation highlighted in the MINERνA simulated data study. There is an ongoing effort to further split the CC1π sample at the near detector into three sub-samples, according to the pion tag. In addition, multi-ring samples are being added to SK in order to better control the pion-production background channels.

The impact on the oscillation parameters contours is shown in Fig. 5.33.

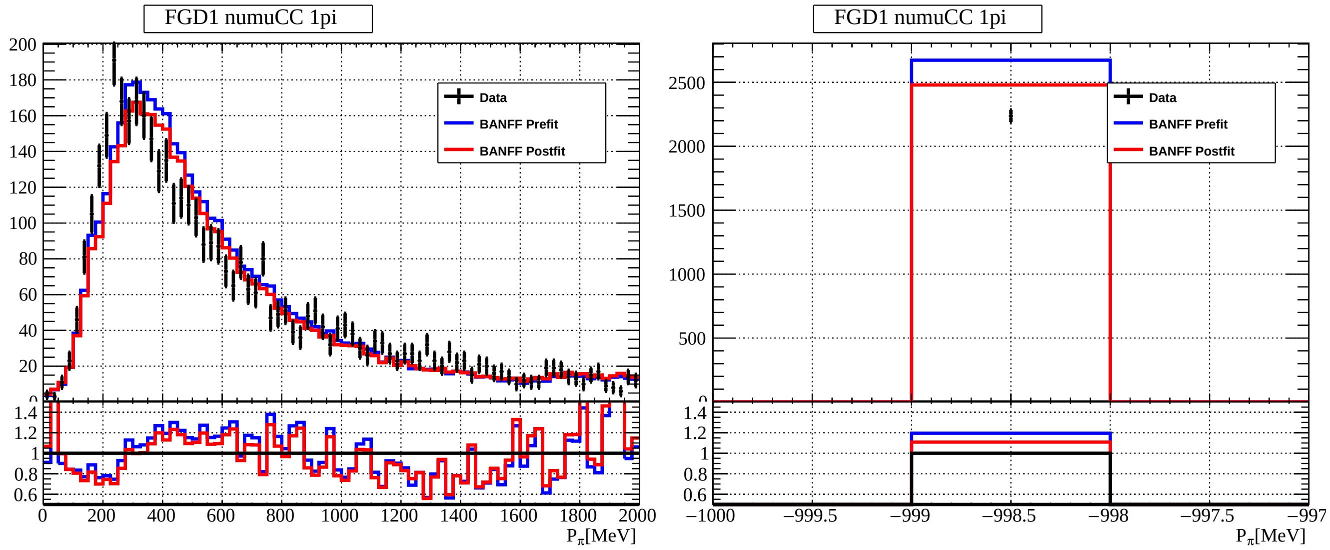

(a) TPC tagged pions

(b) Michel tagged pions

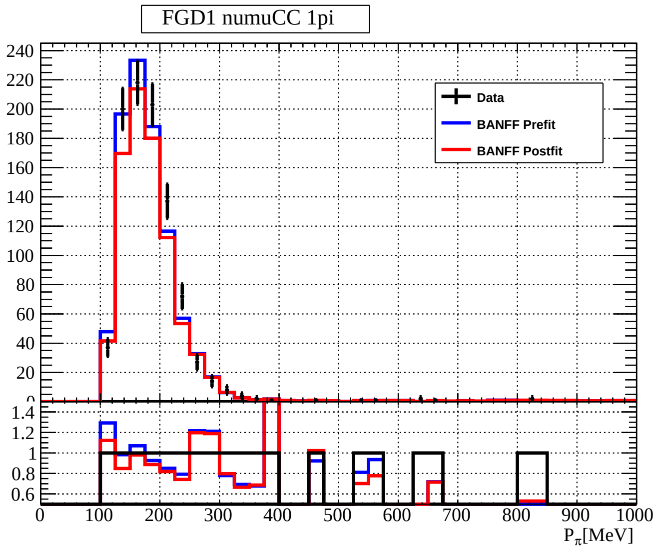

(c) FGD tagged pions

Figure 5.31: The observed data in the FGD1 CC1π sample as a function of reconstructed pion momentum at ND280 (black dots), overlaid with the prediction from the baseline model after tuning from the BANFF fit to ND280 data in muon kinematics (solid red) and the nominal model prediction (solid blue). The ratios of the prefit and postfit to data are included below the main distributions. Note: the Michel pion momentum value is not measured, and therefore a placeholder value of -999 has been assigned to all events which are tagged as Michel pions.

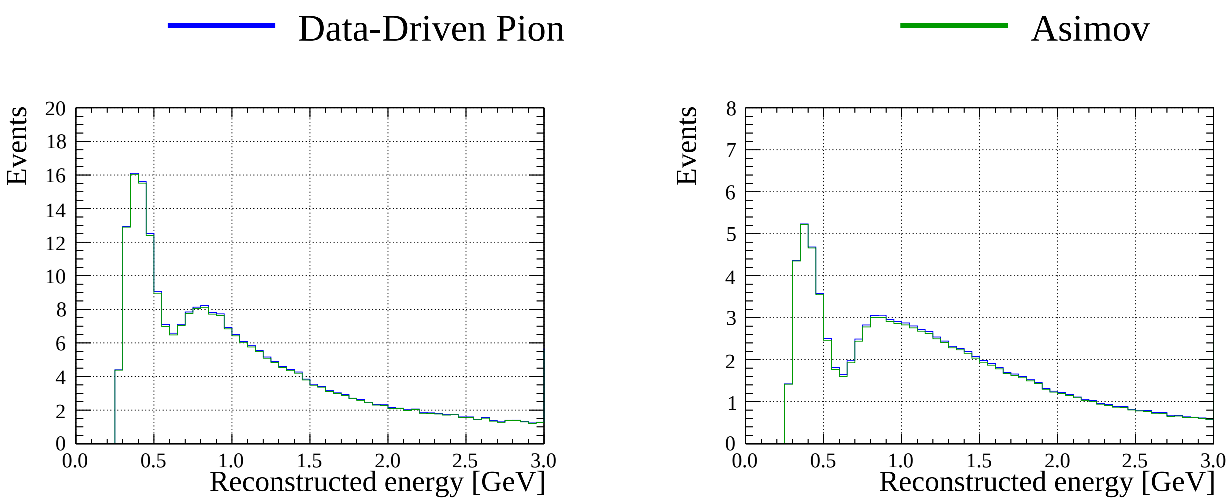

(a) FHC 1Rμ (b) RHC 1Rμ

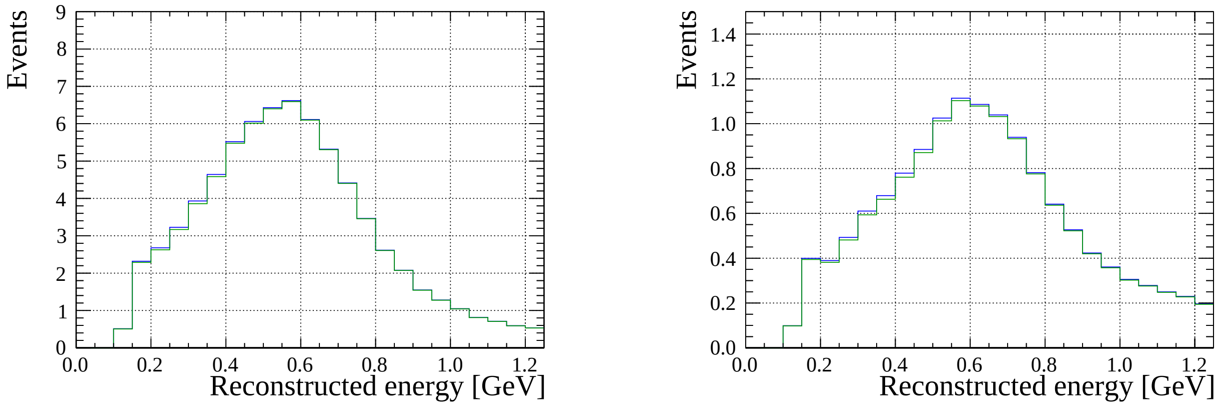

(c) FHC 1Re (d) RHC 1Re

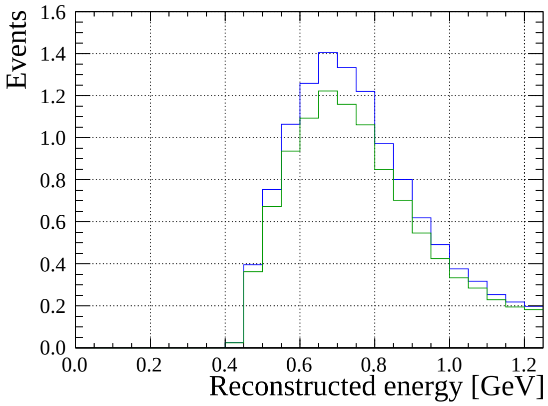

(e) FHC 1Re1de

Figure 5.32: SK predictions for the data-driven pion kinematics simulated data set. The green line shows the nominal SK Asimov, with nominal BANFF Asimov best-fit systematic parameters. The blue line shows the SK prediction after applying the required weights to the nominal prediction - essentially, the SK simulated data set.

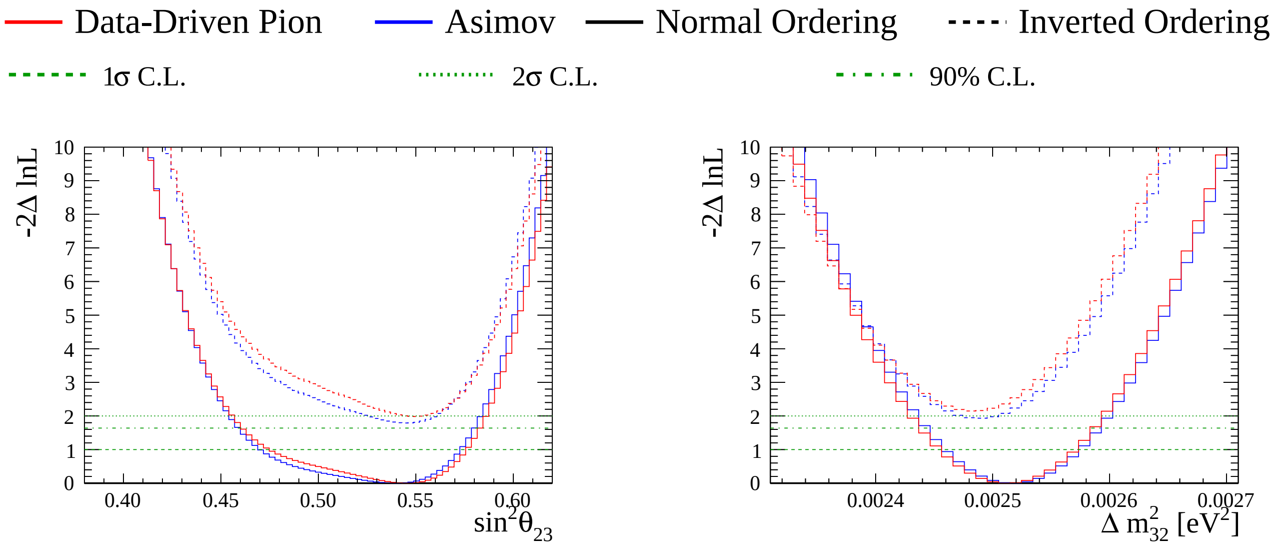

(a) $\sin^2\theta_{23}$ with reactor constraint

(b) Δm^2_{23} with reactor constraint

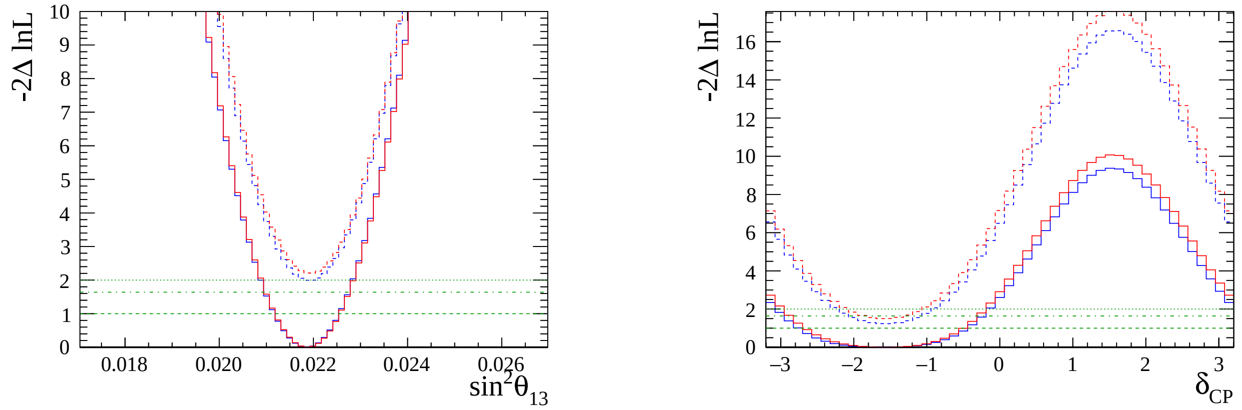

(c) $\sin^2\theta_{13}$ with reactor constraint

(d) δ_{CP} with reactor constraint

Figure 5.33: 1-D likelihood surfaces for all parameters, with the reactor constraint on $\sin^2\theta_{13}$, assuming normal hierarchy for the data-driven pion kinematics simulated data set.

5.4.5 Other simulated data sets

In addition to the simulated data sets described in detail in the sections above, alternative CCQE form factor parametrizations, based on the 3-component [124] and the Z-expansion models [91] were also tested. These alternative form-factor models are relevant since the current dipole parametrization of the M_A^{QE} form factor is known not to be a good description of the data at high Q^2 values. For each alternative form factor model, three simulated data sets were produced, corresponding to the nominal prediction of the alternative model, and to the upper/lower 1σ error prediction for each model.

Since these models affect CCQE interactions, it is expected that they will be able to test the robustness of the Q^2-dependent freedom in the ND fit. The results of these studies showed no significant bias on the oscillation parameter contours, and no significant issue in the near-to-far detector extrapolation. More information can be found in [148].

5.4.6 Criteria for error inflation as a result of robustness studies

The robustness studies described above allow us to assess the extent to which the sensitivity to oscillation parameters could be biased. If the observed bias is large enough, a revision of the cross-section error model may be in order.

For all 1D oscillation parameter contours, the mean and the 1σ and 2σ errors are extracted. The bias is defined as

$$\text{Bias} = \frac{|\text{Mean}_{Asimov} - \text{Mean}_{Sim.Data}|}{\sigma_{Asimov}} \tag{5.2}$$

with Mean_{Asimov} and $\text{Mean}_{Sim.Data}$ being the mean of the 1σ or 2σ Asimov and simulated data fit contours, respectively, and σ_{Asimov} is the 1σ or 2σ error of the Asimov fit. This bias accounts for both the systematic and statistical effect of each simulated data set.

The bias can also be compared to the size of the systematic errors alone, by replacing σ_{Asimov} in Eq. (5.2) with

$$1\sigma_{Asimov\ Syst.} = \sqrt{\sigma^2_{Asimov} - \sigma^2_{Asimov\ Stat.}} \tag{5.3}$$

where $\sigma_{Asimov\ Stat.}$ is calculated from an Asimov fit including only the statistical uncertainty on the predicted MC samples.

An observed bias is considered significant if it is larger than 50% of σ_{Asimov}. If this is the case, different actions may be in order, ranging from applying a smearing to the oscillation parameter(s) concerned by the bias, to including an additional uncertainty in the systematic error model accounting for the bias.

This procedure is applicable to most oscillation parameters, with the exception of δ_{CP}. The latter is a cyclical parameter, and its contours are not well-approximated by a gaussian. A conservative approach is to look at the change in the confidence limits interval with respect to the result from the data fit. The largest change with respect to the data result will then be used to extend the confidence limits obtained in the data fit to account for the effect of the simulated data studies.

The biases for all the simulated data sets tried during this analysis are presented in Table 5.4. No simulated data set introduced a bias larger than 50% of σ_{Asimov}. In order to take a conservative approach, the effect of all of the simulated data studies on Δm^2_{32} was added in quadrature and added as an additional smearing of 1.062×10^{-5} eV$^2/c^4$.

Simulated data set	Relative to	$\sin^2\theta_{23}$	Δm^2_{32}	δ_{CP}
CC0π-focused	Total	8.65%	12%	1.73%
	Syst.	21.3%	33%	6.92%
Martini 2p2h	Total	0.66%	2.60%	0.41%
	Syst.	1.61%	7.30%	1.62%
MINERνA pion tune	Total	2.92%	2.50%	0.87%
	Syst.	7.17%	6.80%	3.49%
Data-driven pion	Total	4.71%	6.50%	0.58%
	Syst.	11.60%	18%	3.94%
Nom. 3-comp.	Total	1.02%	0.40%	0.78%
	Syst.	2.50%	1.13%	3.07%
Upper 3-comp	Total	1.29%	0.65%	0.26%
	Syst.	3.17%	1.79%	1.06%
Lower 3-comp.	Total	0.68%	0.22%	0.20%
	Syst.	1.67%	0.62%	0.79%
Nom. Z-exp.	Total	2.49%	0.22%	0.56%
	Syst.	6.12%	0.61%	2.22%
Upper Z-exp.	Total	0.27%	2.10%	0.43%
	Syst.	0.67%	5.70%	1.71%
Lower Z-exp.	Total	3.05%	0.20%	0.14%
	Syst.	7.50%	0.55%	0.56%

Table 5.4: Bias for each simulated data set, for the main oscillation parameters, expressed as a fraction of $\sigma_{AsimovSyst.}$ (Syst.) or of σ_{Asimov} (Total).

5.5 Oscillation Analysis Results

Using the near-detector fit to data to constrain the systematic parameters, the far detector can be performed to the SK data.
Fig. 5.34 shows the best-fit spectrum, compared to the data, obtained as a result of the P-Theta fit [115]. The best-fit points for the oscillation parameters used to obtain this prediction are given in Table 5.5.

Parameter	Best Fit			
Data	T2K only		T2K+RC	
Mass Hierarchy	Normal	Inverted	Normal	Inverted
$\sin^2\theta_{23}$	0.467	0.466	0.561	0.563
$\sin^2\theta_{13}$	28.0×10^{-3}	31.0×10^{-3}	21.9×10^{-3}	22.0×10^{-3}
δ_{CP}	-2.22	-1.29	-1.97	-1.44
Δm^2_{32} (NH)/$\lvert\Delta m^2_{31}\rvert$ (IH) [eV^2/c^4]	2.495×10^{-3}	2.463×10^{-3}	2.494×10^{-3}	2.463×10^{-3}

Table 5.5: Best fit oscillation parameter values for the fit to T2K data (T2K only) and including the PDG2019 reactor constraint (RC) for $\sin^2\theta_{13}$ (T2K+RC).

The size of the ν_e and $\bar{\nu}_e$ data samples alone can be compared to different predictions for oscillation parameters. Fig. 5.35 shows a so-called “bi-event” plot, useful for illustrating at a glance the preferred regions of appearance parameters. Without making any quantitative statements, the bi-event plot shows that the amount of ν_e and $\bar{\nu}_e$ events in the data seem to be most compatible with a maximum CP violating phase δ_{CP} =-$\pi/2$, a $\sin^2\theta_{23}$ value in the higher octant (i.e. $\sin^2\theta_{23}$ >0.5) and the normal mass hierarchy.

In order to quantitatively evaluate the errors on oscillation parameters, the far detector fitter results are marginalized over all of the systematic parameters. Further marginalizing over oscillation parameters allows us to produce 1D and 2D contours for selected oscillation parameters.
Fig. 5.36a shows the confidence level contours for $\sin^2\theta_{23}$ and Δm^2_{32} (NH)/$|\Delta m^2_{31}|$ (IH). The best fit point is in the upper octant of $\sin^2\theta_{23}$, indicating a preference for maximal mixing. Fig. 5.36b shows the corresponding contours for $\sin^2\theta_{13}$ and δ_{CP}. Before applying the reactor constraint, it was found that the T2K only result was fully compatible with the PDG 2019 value for $\sin^2\theta_{13}$. The confidence levels indicate a preference for negative values of δ_{CP}.

Determining whether $\delta_{\mathrm{CP}} \neq 0, \pi$ is one of the fundamental questions neutrino oscillation experiments aim to answer. The $\Delta\chi^2$ contours for δ_{CP} present local extrema at $\pm\pi/2$, in addition to δ_{CP} having a cyclic interval. It is not appropriate to extract confidence limits on this parameter using the usual gaussian approximation, in which $\Delta\chi^2$ values correspond directly to the confidence level. Instead, the Feldman-Cousins approach [149] is used. The Feldman-Cousins method consists in computing appropriate critical $\Delta\chi^2$ values to determine the 90%, 1σ and 2σ confidence levels. The resulting confidence levels on the δ_{CP} measurement are illustrated in Fig. 5.37 and summarized in Table 5.6.

As a result, 35% of δ_{CP} values are excluded at the 2σ confidence level. CP conservation is excluded at a 90% confidence level.

It is interesting to compare the evolution of this result with that of the previous oscillation analysis [100]. In the 2018 OA, CP conservation was excluded at the 2σ level. In Section 4.3, the evolution of the *sensitivity* to δ_{CP} was illustrated as a function of incremental changes since the last

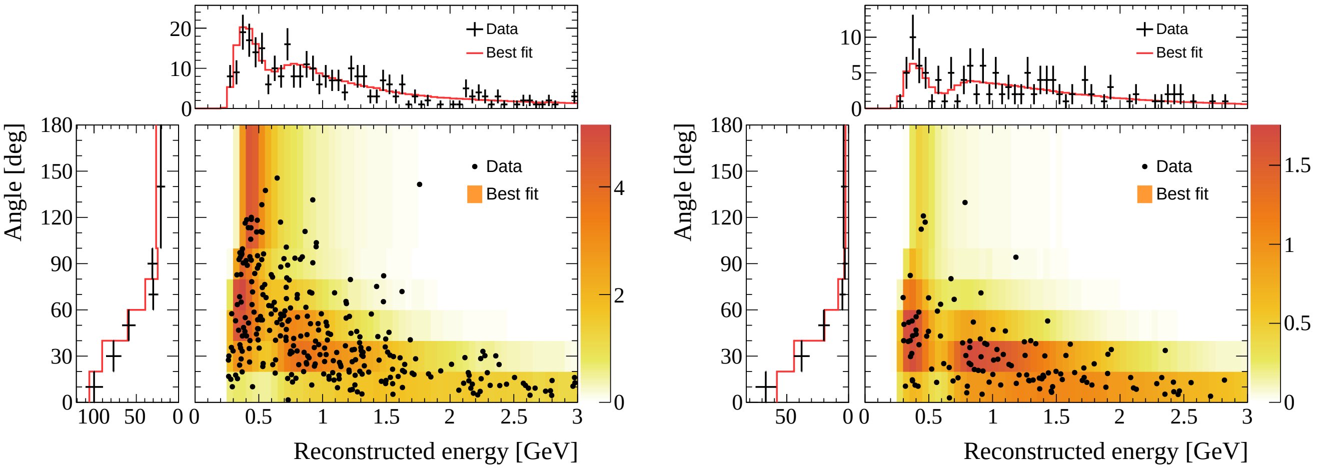

(a) FHC 1Rμ (b) RHC 1Rμ

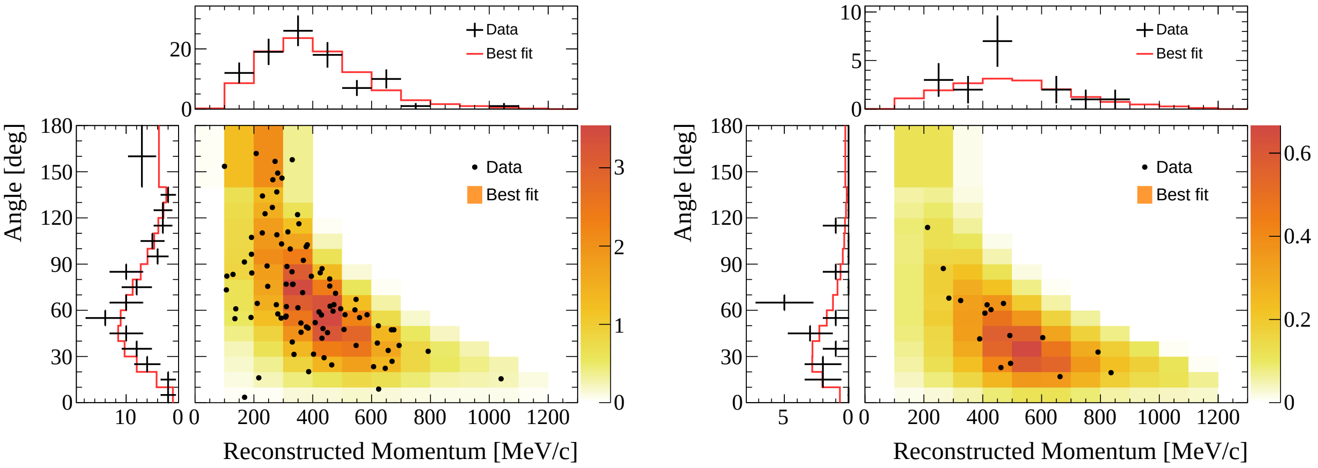

(c) FHC 1Re (d) RHC 1Re

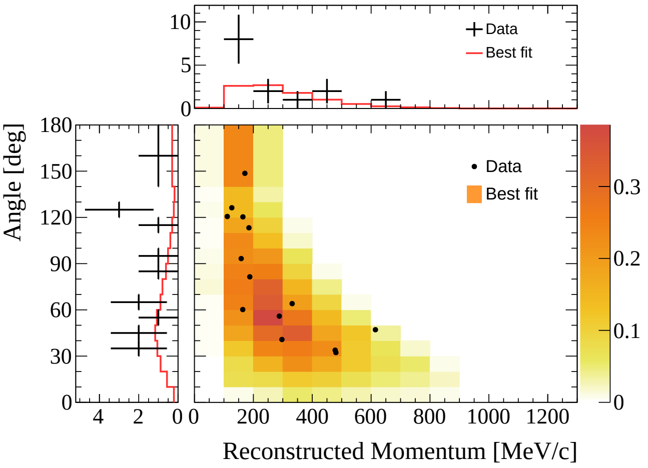

(e) FHC 1Re1de

Figure 5.34: Best-fit event rate (distribution, projections in red lines), compared to the data (black points) for the five SK samples.

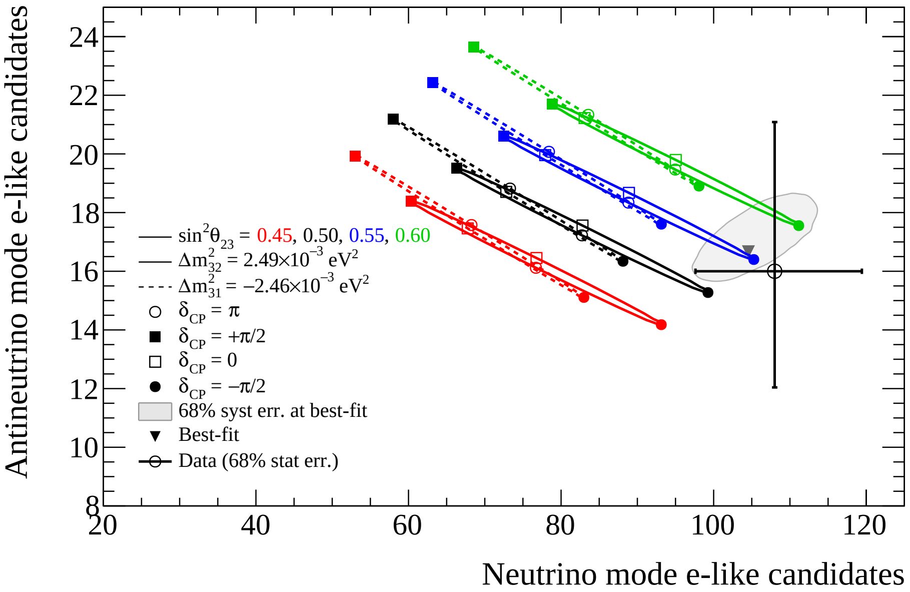

Figure 5.35: Number of ν_e and $\bar{\nu}_e$ events in the SK data (black point with error bars), compared to different oscillation parameter predictions. The colored ellipses represent different values for $\sin^2\theta_{23}$ and the mass hierarchy (solid for NH and dashed for IH). The different points on the ellipses represent different values of δ_{CP}. The best-fit point, along with its 1σ systematic error, is shown as the grey triangle on a grey shaded region.

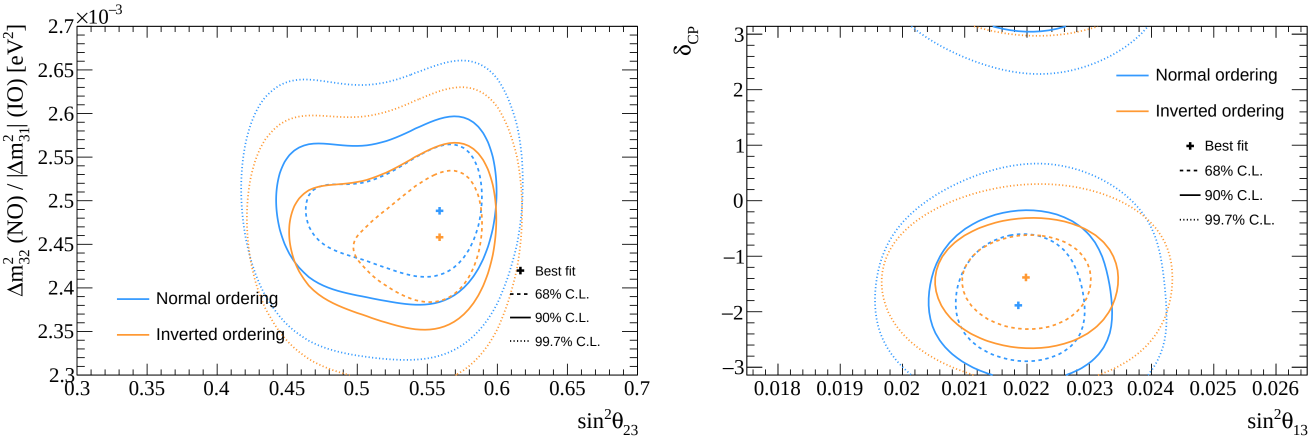

(a) $\sin^2\theta_{23}$ and Δm^2_{32} (NH)/$|\Delta m^2_{31}|$ (IH)

(b) $\sin^2\theta_{13}$ and δ_{CP}

Figure 5.36: Best fit points and confidence limits for different oscillation parameters. Both results include the PDG2019 reactor constraint.

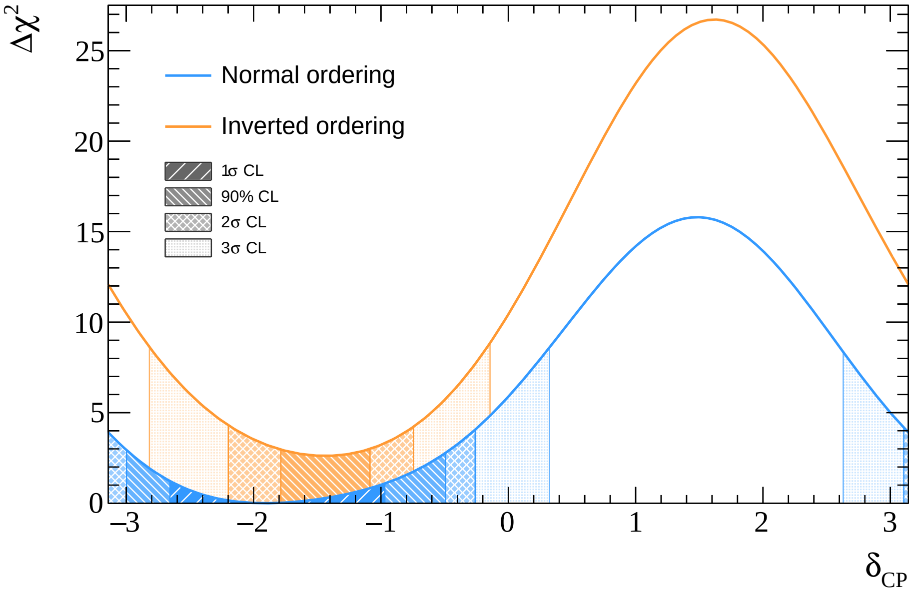

Figure 5.37: $\Delta\chi^2$ distribution as a function of δ_{CP} as a result of the T2K data fit, with the PDG 2019 reactor constraint applied. The shaded regions indicate different confidence levels.

Confidence level	Interval (NH)	Interval (IH)
1σ	[-2.66, -0.97]	
90%	[-3.00, -0.49]	[-1.79, -1.09]
2σ	[$-\pi$, -0.26]$\cup$[3.11, π]	[-2.20, -0.75]
3σ	[$-\pi$, -0.32]$\cup$[2.63, π]	[-2.82, -0.14]

Table 5.6: Confidence intervals for δ_{CP} computed with the Feldman-Cousins method, including the PDG 2019 reactor constraint.

OA. Fig. 4.10 showed that the changes in this analysis increase the sensitivity to δ_{CP}. Counter-intuitively, the results obtained as a result of the 2020 OA exclude a smaller fraction of δ_{CP} values. Fig. 5.38a presents the evolution of the δ_{CP} *measurement* in an analogous way to that of Fig. 4.10, with the addition of a data set D which includes the reprocessing of SK data. The effect of the data reprocessing on the electron-like samples was to move one event into the FHC 1Re sample, one event into the RHC 1Re sample, and one event out of the FHC 1Re1de sample, with respect to the Run 1-9 data used in [100].

Fig. 5.38a shows that the improved near detector and cross-section model, the PDG 2019 reactor constraint, and the SK data reprocessing account for about half of the reduction in the δ_{CP} sensitivity. Adding the SK run 10 data decreases the sensitivity about as much as all of the previous changed compounded.

Since the sensitivity to δ_{CP} mostly depends on the ν_e to $\bar{\nu}_e$ event rate, the stronger constraint on δ_{CP} obtained in the previous analysis was partly due to a statistical fluctuation of the data, which were, within statistical errors, in a favorable region for a stronger constraint. The reprocessing of SK data has changed the composition of 1Re and 1Re1de samples, and the addition of run 10 data did not yield global data in a region with a power to constrain δ_{CP} which is stronger than the last analysis. The new results are also more compatible with PMNS boundaries, unlike the 2018 analysis results, as evident in the bi-event plot of Fig. 5.38b.

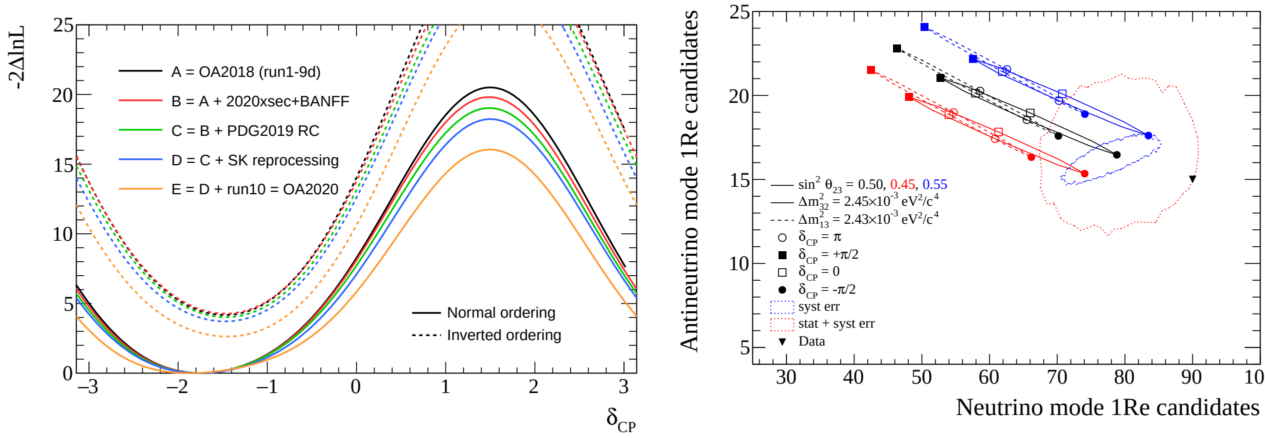

(a)

(b)

Figure 5.38: (a) Incremental evolution of δ_{CP} measurement with the various changes since the 2018 OA. (b) Bi-event plot for the 2018 OA.

To verify the robustness of the conclusions regarding the exclusion of CP conserving values, the simulated data fits described in Section 5.4 were used to evaluate the maximum extent to which the confidence limits on δ_{CP} could be extended. Table 5.7 summarizes the effect of all the simulated data sets on the δ_{CP} confidence intervals[11]. The largest extension on the 90% C.L. interval is induced by the CC0π-focused simulated data set and the data-driven pion tune. Extending the δ_{CP} intervals as a result does not affect the conclusions regarding the exclusion of CP conservation at a confidence level of 90%.

---

[11] The nominal interval edges in the table are computed assuming known NH.

	1 sigma		90% C.L.		2 sigma		3 sigma	
Interval Edges	-2.63	-0.961	-2.97	-0.518	-3.14	-0.286	2.66	0.302
Martini 2p2h	-0.0145	0.0314	-0.0233	0.0369	-0.0238	0.0407	-0.0442	0.0601
MINERvA	0.052	-0.027	0.058	-0.038	-0.060	-0.043	0.070	-0.058
Data-driven Pion	**-0.066**	0.027	-0.066	0.043	-0.050	0.047	-0.069	0.063
CC0π-focused	-0.0452	**0.0685**	-0.0636	**0.0858**	-0.0617	**0.0961**	**-0.1**	**0.131**
Eb (+ 5 MeV)	-0.003	-0.024	0.000	-0.020	0.001	-0.017	0.003	-0.012
Eb (+ 15 MeV)	-0.004	-0.013	-0.004	-0.010	-0.003	-0.009	-0.002	-0.005
Nom. 3-comp.	-0.032	0.005	-0.041	0.023	-0.040	0.032	-0.067	0.068
Upper 3-comp.	-0.056	0.034	**-0.070**	0.057	**-0.066**	0.070	**-0.100**	0.111
Lower 3Comp	-0.033	0.018	-0.044	0.035	-0.043	0.045	-0.074	0.083
Nom. Z-exp.	0.001	-0.016	0.000	-0.011	-0.001	-0.008	-0.002	-0.001
Upper Z-exp.	-0.026	0.009	-0.033	0.022	-0.031	0.030	-0.050	0.054
Lower Z-exp.	0.016	-0.016	0.016	-0.015	-0.015	-0.013	0.010	-0.007

Table 5.7: Net effect on the δ_{CP} intervals as a result of the simulated data studies. The largest impact in each column is highlighted.

Chapter 6

Towards T2K-II - the ND280 Upgrade

This chapter presents an overview of the ND280 Upgrade project. Section 6.1 gives a brief overview of the intended design for the ND280 upgrade, along with the strengths and limitations of the current detector. The different components of the upgraded ND280 detector are described in Section 6.1.1, Section 6.1.2 and Section 6.1.3. Finally, the impact of the ND280 Upgrade on the T2K physics program is described in Section 6.2, and Section 6.2.2 presents a study on the neutron detection capabilities of the SuperFGD. Section 6.3 concludes with the perspectives of using the ND280 in the future.

I have performed the charge spreading studies with the CERN test-beam data presented in Section 6.1.1. These studies, along with their application in Section 6.1.1.3, are the first time such studies were performed for the T2K experiment. In addition, I participated in the data taking for the DESY test-beam studies described in Section 6.1.1.3. I have also performed the physics sensitivity studies using transverse kinematic imbalances in Section 6.2.1 as well as the analysis presented in Section 6.2.2. These studies were the first to establish a way to obtain a hydrogen enriched sample using neutron measurements, and have applications beyond T2K: they are particularly relevant for future precision neutrino experiments like Hyper-K and DUNE.

Originally, the T2K experiment was intended to collect data until 2020, gathering a total of 7.8×10^{21} POT of data. Its success following the discovery of $\nu_\mu \to \nu_e$ oscillations, in particular the good sensitivity to the CP violation (δ_{CP}) and the $\sin^2\theta_{23}$ mixing angle, have motivated the T2K collaboration to put forward a proposal for an extended T2K run aiming to collect 20×10^{21} POT of data [150]. Future long baseline neutrino oscillation experiments, such as DUNE [60] and Hyper-Kamiokande [10] will begin data taking as soon as 2027. The extended T2K run will thus ensure continuous data taking, and will pave the way for future long baseline neutrino oscillation experiments.

Neutrino interactions are weak, by their nature. The first natural step in increasing the sensitivity to oscillation parameters is to increase the amount of statistics available. For this reason, the J-PARC accelerator facility plans an upgrade of the neutrino beamline. Fig. 6.1 shows the target beam power and accumulated POT as a function of time. As of 2020, the T2K beam has been operating stably at a power of 515 kW [1]. The MR facility will be upgraded in two stages, the first allowing to reach the design beam power of 750 kW through the upgrade of the MR power supply, and the second aiming to reach 1.3 MW, by upgrading the RF cavity. The 1.3 MW target is destined to produce a more powerful beam for the future Hyper-K experiment Chapter 7, which will collect an unprecedented amount of statistics.

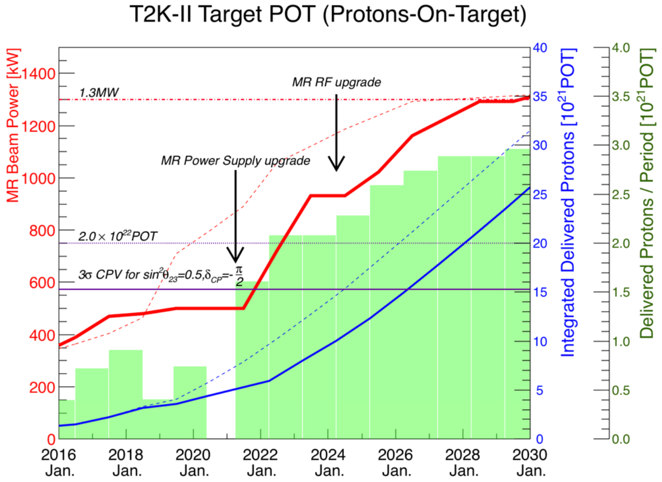

Figure 6.1: Target MR beam power (red) and accumulated POT (blue) as a function of Japanese Fiscal Year (JFY). Solid lines assume 6 months of the MR operation with the fast-extraction mode each year and a running time efficiency of 90%. Dashed lines show the expected MR beam power (red) and accumulated POT (blue) shown in T2K-II proposal [150] where the MR main power supply installation was scheduled in 2019. The 3σ line for CP violation was obtained using an improved systematic model (discussed later in the chapter). Figure from [151].

Increasing the statistics at T2K is particularly relevant for the measurement of δ_{CP} and determining if CP violation occurs. However, Fig. 6.2 shows that the impact of systematic errors cannot be neglected. The present level of systematics is highly limiting the sensitivity at higher statistics and they need to be reduced in order to cope with increased statistical precision.

The far detector systematic errors are well constrained with the help of the T2K near detector, ND280. The dominant sources of systematic errors are the neutrino flux and neutrino cross-section systematics, and these two sources are primarily constrained by the ND280 data. Therefore, an upgrade of the ND280 detector is proposed.

6.1 The ND280 Upgrade Design

The ND280 detector was designed before the measurement of the θ_{13} mixing angle. At the time, the rate of electron neutrino appearance in neutrino oscillations was completely unknown and the π^0 production in Neutral Current interactions could in principle constitute a limiting background for the measurement of electron neutrinos at the Super-K. As a consequence, ND280 was designed to perform a precise measurement of π^0 production in neutrino interactions. The (somehow unexpected) measurement of a relatively large value for θ_{13} (and correspondingly relatively large rate of electron neutrino appearance in oscillations) made the role of the π^0 background less crucial and enlarged the physics case of T2K, enabling the measurement of the δ_{CP} phase.

For the measurement of electron neutrino appearance (and thus δ_{CP}) the most relevant background is actually the rate of electron neutrinos produced in the beam itself by pion and kaon decays. To control this background and to minimize the uncertainty of electron-neutrino over electron-antineutrino cross-sections, which directly affects the measurement of δ_{CP}, the measurement of electron neutrino rate at ND280 is important. This requires good particle identification (PID) performances for muons versus electrons with the ND280 TPCs. The T2K collaboration has put forward a proposal for an

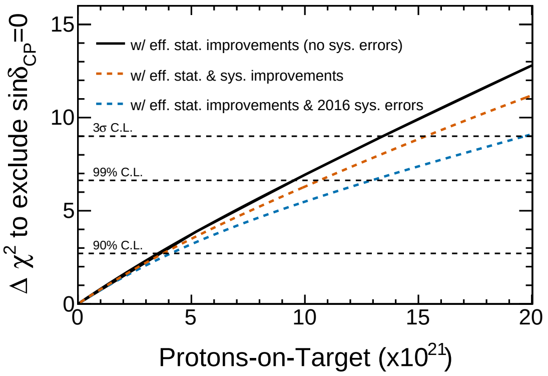

Figure 6.2: Sensitivity to exclude CP conserving values of δ_{CP} as a function of accumulated POT. All curves take into account the increase in statirstics ("w/ eff. stat. improvements") and different configurations are compared: assuming no systematic errors (solid black line), assuming the level of T2K systematic errors from the 2016 oscillation analysis [152] (blue dashed line) and assuming 50% improved systematic errors with respect to the 2016 level (orange dashed line). Notable confidence levels are indicated by black dashed lines. Figure from [153].

upgrade of the ND280 detector [154]. This upgrade aims to address the limitations the current ND280 detector has, as well as add new particle detection capabilities.

The T2K off-axis near detector (ND280) has been providing constraints for oscillation analyses and performing cross-section measurements since the beginning of T2K data taking. As described in Chapter 5, the constraints obtained with the ND280 detector have allowed a reduction of systematic uncertainties related to the flux and neutrino interaction modelling from ∼13% to ∼4% across SK signal samples. Thanks to its three TPCs, ND280 has excellent charge and momentum identification capabilities. In addition, unlike SK, ND280 is a magnetized detector, which allows it to perform charge identification with good precision. These capabilities should be preserved (and perhaps even enhanced), if possible, during the upgrade.

The current configuration of the ND280 subdetectors (two scintillating fine-grained detectors, FGDs, sandwiched between three TPCs) make it particularly well suited to measure horizontal tracks (i.e. particles travelling parallel to the neutrino beam axis). However, high angle tracks or backward going tracks are not reconstructed with good efficiency. Tracks originating in one of the FGDs which have very high angles may only produce scintillation light in a single bar (due to the FGD structure), whereas high angle tracks in the TPCs may not be selected because of the large number of TPC clusters required in the selection process, or may not even enter the TPCs at all if the angle is too high. (Section 3.2.3). Most events have only one visible track from a muon since the proton tracks are below the proton detection threshold. In such cases, the time difference between the origin and the end of the track is used in order to determine if the track is a positive forward-going muon or a negative backward-going muon. Only the FGDs and the P∅D can provide timing information, so tracks produced in FGD2 need to reach FGD1 and cross at least few scintillating bars, and similarly, tracks originating in FGD1 need to reach the P∅D. Because of the neutrino boost, the backward tracks are typically of low momentum, so the probability of crossing such a large amount of detector material is low, yielding a low detection efficiency. The efficiency of reconstructing different type of tracks is summarized in Fig. 6.3.

As a result, the coverage of the ND280 detector does not match the 4π acceptance of SK. This

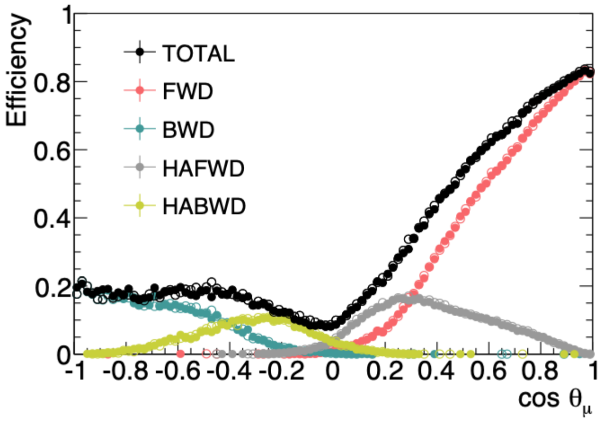

Figure 6.3: The efficiency of reconstructing different type of tracks, as a function of muon angle, using time-of-flight information at ND280. “HA” stands for “high-angle”, “FWD” and “BWD” stand for “forward” and “backward” with respect to the neutrino beam direction. Figure from [154].

can be seen in Fig. 6.4.

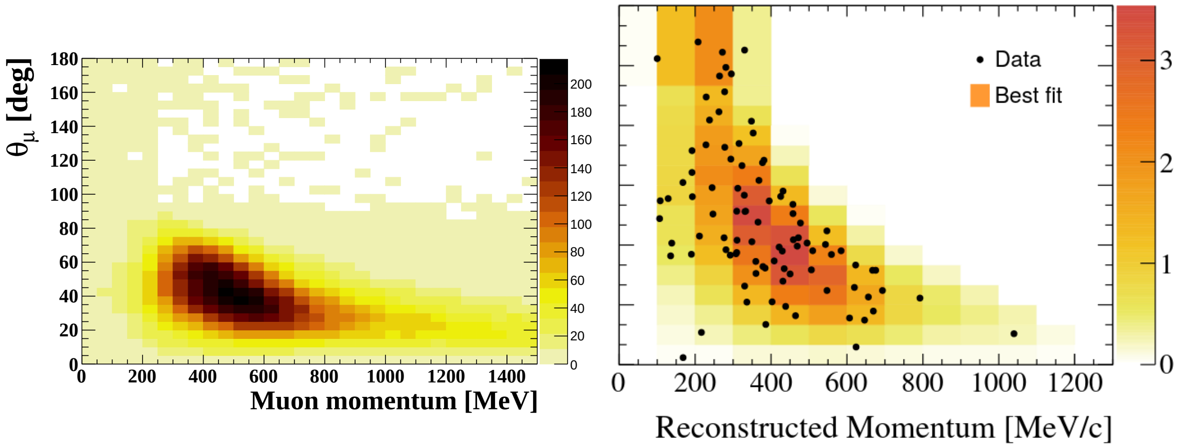

(a)

(b)

Figure 6.4: (a) Distribution of selected muons in the ND280 FGD1 ν_μ CC0π sample. (b) Distribution of signal ν_e events in the SK FHC 1Re sample as a function of electron angle and momentum - data (black dots) and best-fit MC prediction (colored background). The y-axis scale (for the angle) matches that of the plot on the left.

The second limitation of the current ND280 detector is related to particle detection thresholds. Currently, tracks fully contained in the FGD can only be reconstructed in two dimensions, and this implies that the momentum threshold for the reconstruction is relatively high. In order for its track to be reconstructed, a particle needs to cross at least 2 scintillating bars in the X direction and 2 bars in the Y direction. As a consequence, this imposes a threshold on the particle momentum, as a large energy is needed to cross this amount of material. This can be seen in Fig. 6.5 - the efficiency to detect low momentum protons is currently zero below 400 MeV in proton momentum. As can be seen from the proton momentum spectrum, the peak region of the spectrum cannot be reconstructed. Being able to detect final state protons (and hadrons in general) is particularly important in controlling nuclear effects which drive the largest systematic uncertainties for the oscillation analysis.

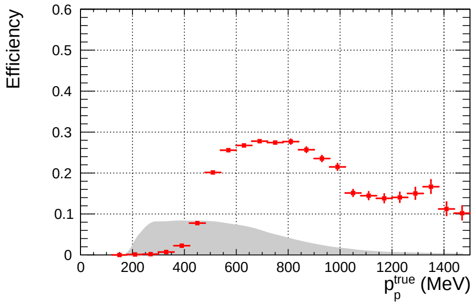

Figure 6.5: Current ND280 proton reconstruction efficiency as a function of proton momentum (red). For reference, the proton spectrum at ND280 generated with NEUT is shown in the background (grey, arbitrary normalization).

As such, the ND280 detector should be upgraded with the following requirements in mind:

- Full polar angle acceptance for muons produced in charged-current inclusive neutrino interactions, in order to match the acceptance of SK.
- Similar performance in terms of spatial resolution, momentum resolution, deposited energy and charge measurement as the current ND280.
- Large fiducial mass[1] (to increase the available statistics).
- High tracking efficiency for low momentum pions and protons, capable of determining event topology.
- High-efficiency Time-of-Flight detector, capable of reconstructing the direction of all particles crossing the TPCs.

In order to extend the capabilities of the ND280 detector and to make full use of the increased statistics which will be brought by the J-PARC beamline upgrade, the T2K collaboration put forward the ND280 Upgrade project [154]. The project consists in upgrading the upstream part of the ND280 detector, while maintaining the downstream TPCs and FGDs[2], as well as the ECal, the magnet and the SMRD (see Chapter 2).
Fig. 6.6 shows the design of the ND280 Upgrade. The upstream part, currently occupied by the P∅D detector, will be replaced by a set of three new sub-detectors: one 3D detector consisting of 1 cm scintillating cubes, called the “SuperFGD”, and two horizontal TPCs, above and below the SuperFGD, called High-Angle TPCs (HATPCs). A new, improved Time-of-Flight (ToF) detector will also be installed, surrounding the new subdetectors. Each of these subsystems will be described in the following sections, along with simulations and results from prototype tests.

---

[1] For reference, the two current ND280 targets have each a mass of about 1 ton

[2] Apart from the phase space coverage limitations, the current FGDs and TPCs are excellent detectors and will be kept in their current state.

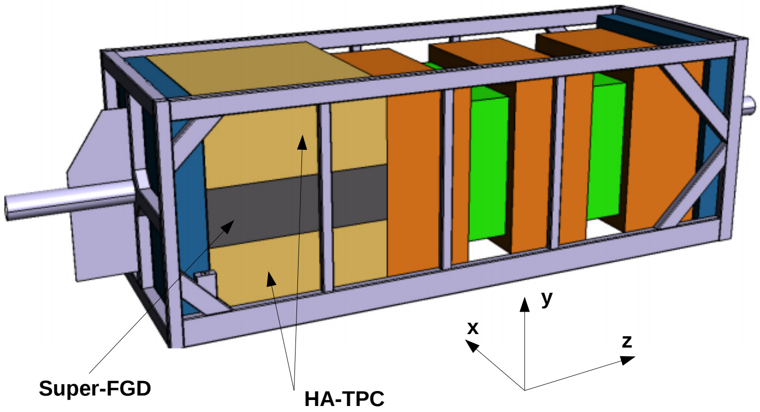

Figure 6.6: 3D model of the upgraded ND280 detector inside its basket (grey). In the upstream part (towards the left on the plot), three new sub-detectors will be installed: SuperFGD (drak gray) and two high angle TPCs (HA-TPC, light brown). The ToF detectors are not shown on this plot. The downstream part is the same as in the current ND280 configuration: three TPCs (orange) and two FGDs (green). In the lab coordinate system, the z-axis corresponds to the neutrino beam direction. Figure from [154].

6.1.1 High-Angle TPCs

The existing T2K TPCs (Section 2.2.2.2) provide accurate measurements of tracks emerging from neutrino interactions. The charge and momenta of particles are reconstructed thanks to the track curvature, and the particle are identified by measuring their energy loss as a function of distance (dE/dx). The current TPCs use the bulk Micromegas technology for charge readout [77].

Building up on the success of the T2K TPCs, two new horizontal TPCs are foreseen for the upgrade of the ND280 detector. The two High-Angle TPCs (HA-TPCs) will be placed above and below a new scintillating target (SuperFGD, described in Section 6.1.2) in order to provide the ability to track high-angle tracks with respect to the neutrino beam direction.

The new HA-TPCs must match the performances of the existing TPCs, the most important of which are:

- A momentum resolution of 10% or better for particles around 1 GeV/c, driven by the need to precisely reconstruct the neutrino energy. The 10% momentum resolution requirement is related to the Fermi motion of nucleons inside the nucleus. When using only muon kinematics (as is the case in the current analysis), the resolution is limited by the Fermi motion. The proton detection capabilities of the SuperFGD, however, will make it possible to add proton kinematics to the analysis, and thus improve the energy reconstruction. To this end, an even better momentum resolution is desirable. A 10% resolution at 1 GeV/c corresponds to a spatial resolution of 600-1000 μm resolution for the present TPCs, thus establishing a target for the spatial resolution of the HA-TPCs.
- Excellent e/μ separation ability. The current TPCs have an 8% energy resolution which allows to separate electrons from muons at the 4σ level.

In order to fulfill these requirements, the design of the new HA-TPCs will make use of the *resistive* Micromegas technology for its readout plane.

6.1.1.1 Resistive Micromegas

The resistive Micromegas technology is similar to the bulk Micromegas technology, but it contains an additional resistive layer on top of the anode. Fig. 6.7 illustrates the principle of the resistive Micromegas technology, compared to bulk Micromegas.

A track passing through the TPC ionizes the gas filling the chamber, producing free electrons. A uniform electric field is applied to the TPC, causing the electrons formed as a result of the ionization to drift towards the anode (readout plane). Before reaching the anode, the electrons encounter a mesh. The difference in potential between the anode and the mesh causes an avalanche which has the result of amplifying the electric signal and spreads out the charge over the surface of a pad, fixed on a printed circuit board (PCB). These characteristics are common to bulk and resistive Micromegas. The novelty of resistive Micromegas is the addition of a layer of resistive material and an insulator between the pads and the amplification gap. The resulting effect is a wider spreading of the amplified charge over multiple pads. Instead of reading out the signal of one avalanche in one pad, the signal is spread out over multiple pads.

There are three main advantages of using the resistive Micromegas technology, all of which rely on the enhanced charge spreading in the resistive layer:

- The charge spreading effect allows a precise spatial resolution while reducing the number of necessary pads, thus reducing the number of electronic readout channels.

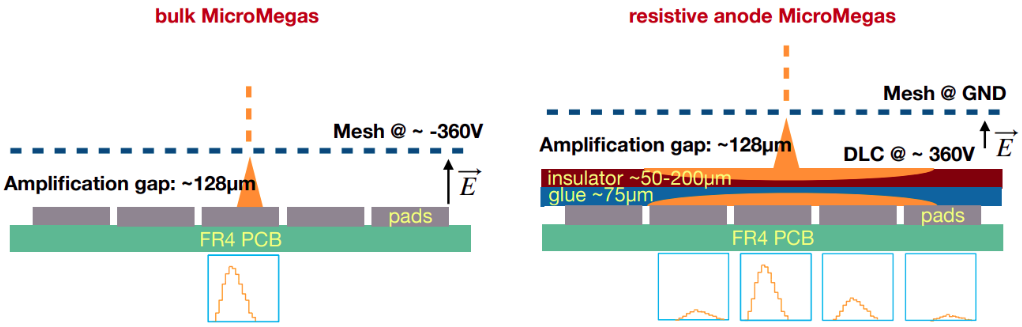

Figure 6.7: Comparison of bulk and resistive Micromegas. The printed circuit board (PCB) is shown in green, the dotted blue line represents the mesh, and the electron signal is shown in orange. For resistive Micromegas, the resistive insulator is shown in brown, and a glue layer is shown in dark blue. Under each of the pads (grey) reading an electric signal, a generic waveform (charge as a function of time) is shown.

- The uniform resistive layer significantly reduces the formation of sparks and their intensity.
- The amount of dead space on the readout plane is reduced - this comes from the fact that the increased spark protection provided by the uniform resistive layer no longer requires the addition of anti-spark circuitry.

Several prototypes for HA-TPCs have been tested with cosmic rays and controlled particle test-beams. The results obtained will be described in the following subsection.

6.1.1.2 Performance of HA-TPC prototypes

The design for the HA-TPCs is shown in Fig. 6.8. It shows the general configuration of the TPC components, but the exact parameters needed for optimal performance have to be determined experimentally. For this reason, several prototypes were built and tested at Saclay, CERN and DESY.

6.1.1.2.1 First test-beam study at CERN

A first prototype of a HA-TPC was initially tested at Saclay with a ^{56}Fe source and cosmic rays. The goal of these tests was to demonstrate that the charge spreading phenomenon occurred, that the device was robust to different voltages applied to the mesh, and to characterize the electronics response to the signal.

The results of these tests were satisfactory, and the prototype was further tested with a particle beam at CERN. The results of this test-beam study are published in [155] and summarized in this section.

The prototype was installed in the HARP field cage [156] and exposed to the T9 beamline at CERN with a copper target, to have a hadron-enriched composition. The TPC volume was filled with an $Ar:CF_4:iC_4H_{10}$ (95:3:2) gas mixture, which is the same as the one used in the ND280 TPCs. A 25 kV voltage was applied to the cathode of the field cage, generating an electric field of 167 V/m. The experimental setup allowed to test different drift distances, by moving the TPC with respect to the

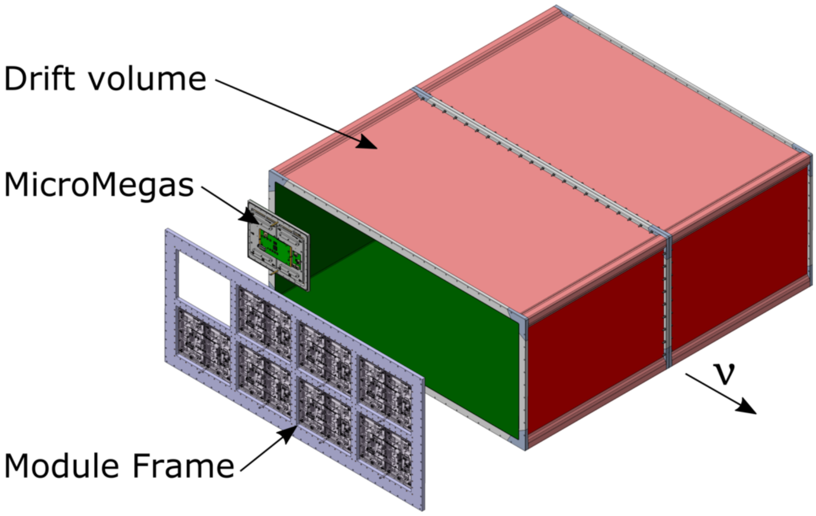

Figure 6.8: Schematic model of the HA-TPC.

beam. No magnetic field was applied, as the purpose of this test was to characterize the intrinsic detector performance, for which straight tracks are more suitable. During the beam test, a positively charged beam was used, with a set of triggers to discriminate between the particles forming the beam. The particles used during the beam test were protons, positive pions, and positrons, with momenta between 0.8-1.0 GeV/c. The prototype had a sensitive area of 36×34 cm^2, covered by 0.98×0.70 cm^2 pads, for a total number of 34×48 pads. The beam is intended to pass perpendicular to the side with the larger number of pads and parallel to the side with a smaller number of pads[3]. The gas quality in the TPC was assessed by looking at the stability of the drift velocity over time. Impurities such as water or oxygen can affect the drift velocity. Fig. 6.9 shows the evolution of the drift velocity for the CERN test-beam experimental setup. The velocity decreases over time, which indicates the presence of impurities. In this case, the reduction is consistent with the presence of water in the gas, which comes most probably from the HARP field cage which has been exposed to air during storage.

To analyze the collected test-beam data, a simple track reconstruction and selection algorithm was developed. The algorithm looks for signal in the pads at the beginning and at the end of the module, then constructs all possible combinations of tracks connecting the pads in the first and last columns. A track is retained if it is compatible with a straight line of hits between the two extrema. Fig. 6.10 illustrates a typical set of tracks in the TPC, before and after selection using the algorithm described above.

6.1.1.2.2 Charge Spreading

Taking the selected track in Fig. 6.10 as an example, we define the set of pads containing a signal in a column (i.e. in the long, vertical direction) as a “cluster”. In the selected track, it is clear that the charge of the track spreads perpendicular to the track direction, thus illustrating the charge

---

[3] For cosmics data, the situation is opposite: since most cosmic rays are vertical, they will pass along the axis containing more pads.

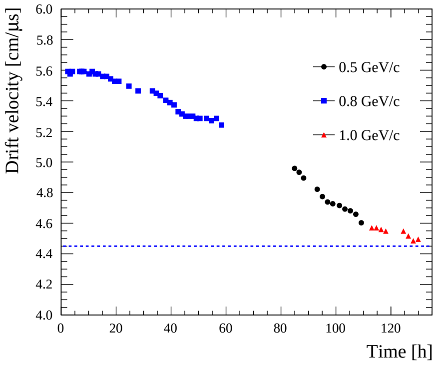

Figure 6.9: Drift velocity as a function of time, for the duration of the CERN beam test, and for different particle momenta.

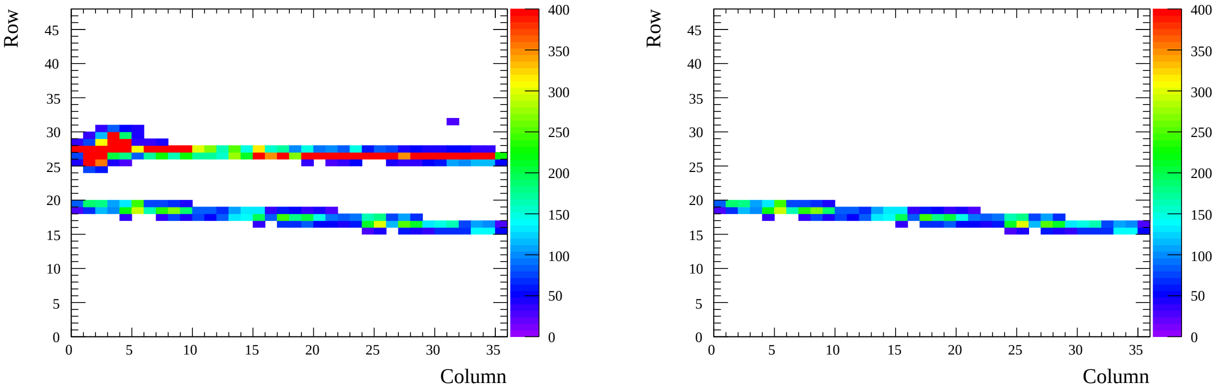

(a) (b)

Figure 6.10: Examples of tracks in the TPC prototype. (a) Raw tracks. (b) Track selected with the algorithm described in the text.

spreading phenomenon in action. The amount of pads in a column cluster defines the “cluster multiplicity” and is an important metric in characterizing the charge spreading.
In Fig. 6.11, the amount of charge collected as a function of time is presented for a typical three pad cluster.

Due to the charge spreading, the signal spreads to multiple pads, and arrives to sub-leading pads with a time delay which can be of the order of a few μs. A larger pad multiplicity is desirable, since it allows for a more precise reconstruction of the track position. Fig. 6.12 shows the cluster multiplicity for different particle tracks (left) and the fraction of charge deposited in the leading pad compared to the total charge of the cluster ($q_{max}/q_{cluster}$).

Most clusters have a multiplicity of 2-3 pads, and the leading pad contains ~80% of the charge. The $q_{max}/q_{cluster}$ distributions have a sharp cliff at 50%, due to geometrical reasons: most of the clusters contain two pads, and in this case the leading pad cannot contain less than 50% of the charge, since if it does, then it no longer is the leading pad. This can also be seen in the green distribution of two-pad clusters.
$q_{max}/q_{cluster}$ can actually be used as a first-order proxy for the track position with respect to the

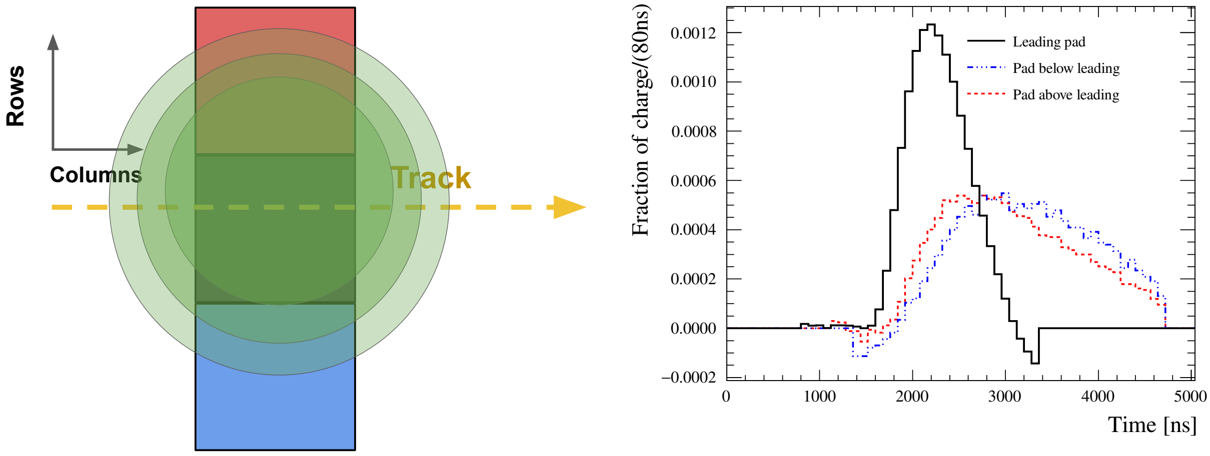

Figure 6.11: Example of waveforms as a function of time for the signal in a three-pad cluster: leading pad (black), pad above leading pad (red), pad below leading pad (blue). All three histograms are normalized to the area of the leading pad - in reality the blue and the red curves would have a much lower ADC count. A schematic definition of the pad categories is presented on the left, with pad colors corresponding to the color of their waveforms. The green transparent circles show different stages of the charge spreading in the resistive layer. The track is intentionally asymmetrical to highlight the difference between the charge in the pads above and below the leading pad.

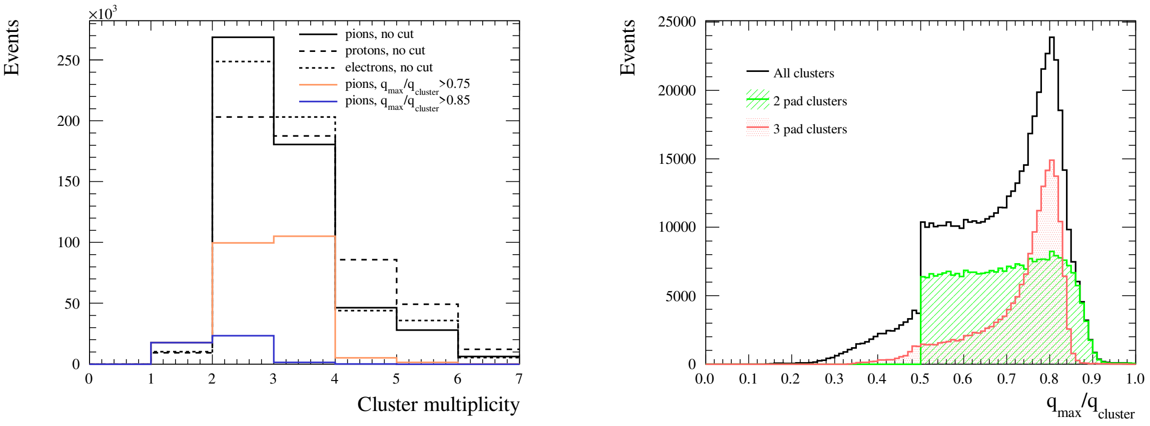

(a) (b)

Figure 6.12: Pad multiplicity in the cluster (a) and fraction of the cluster charge which is collected in the pad with largest signal (b). The histograms for pion, electron and proton clusters are normalized to the same area.

pad geometry: in an odd-numbered cluster, the higher the fraction of the charge carried by the leading pad, the closer the track passes with respect to the center of the pad. In two-pad clusters, the track is likely to have passed near the border between the two pads (otherwise, it would have produced a signal in a third pad, making it a three-pad cluster). This is confirmed in Fig. 6.12 (right), where it can be seen that selecting clusters with a $q_{max}/q_{cluster}$ >75% reduces the amount of two-pad clusters while increasing that of three-pad clusters[4].

Combining the information given by $q_{max}/q_{cluster}$ and that of the time delay of the peaks of the second (third) pads in a cluster with respect to the time when the leading pad charge reaches its maximum, it is possible to estimate the velocity of the spatial charge spreading in the resistive foil. The quantity $\delta t = t_{pad} - t_{max}$ represents this time difference, where t_{pad} is the time when the second or third leading pad reaches its maximum, and t_{max} is the time at which the leading pad reaches its maximum. For large values of $q_{max}/q_{cluster}$, the track passes close to the center of the central pad in three-pad clusters, the difference in time peak between the second and the third pad should converge to the same value, which corresponds to the time needed by the charge to spread along half a pad.

Fig. 6.13 shows that this is indeed the case: in the bottom left plot, at large values of $q_{max}/q_{cluster}$, the time difference between the leading pad and the second (third) pad tends towards a common value. For a pad size of 0.7 cm, this corresponds to a charge spreading velocity of the order of 0.6 cm/μs. This velocity is related to the product of the capacitance and the resistivity of the resistive layer (RC), which will be described in Section 6.1.1.3. With the installation of the HA-TPCs, T2K will become the first full-scale experiment to use the resistive Micromegas technology as a part of its detectors. As such, a good understanding of the charge spreading phenomenon is particularly important both for building realistic simulations and exploiting data.

6.1.1.2.3 Spatial Resolution

The spatial resolution is the precision with which the track position in a pad is determined. A simple approach is to determine the track position using the Center of Charge (CoC) or barycenter method. This method consists in weighting the positions of the center of each pad (x_{pad}) in a cluster by the fraction of the cluster charge deposited in each pad:

$$x_{track} = \frac{\sum (x_{pad} Q_{pad})}{\sum Q_{pad}} \tag{6.1}$$

where Q_{pad} is the charge deposited in the pad. However, a new method of determining the track position was proposed [157], and it has yielded improved spatial resolution when applied to ILC TPCs. The method consists in using the so-called “pad response function” (PFR), which describes the fraction of the cluster charge deposited in a particular pad versus the distance between the track position and the pad center:

$$Q_{pad}/Q_{cluster} = PRF(x_{track} - x_{pad}). \tag{6.2}$$

An analytical representation of the PRF [158] consists in taking the ratio of two 4-th degree polynomials:

$$PRF(x, \Gamma, \Delta, a, b) = \frac{1 + a_2 x^2 + a_4 x^4}{1 + b_2 x^2 + b_4 x^4}. \tag{6.3}$$

---

[4] Imposing a more stringent $q_{max}/q_{cluster}$ cut increases the relative amount of one-pad clusters, probably due to the fact that it selects clusters with a low charge deposition.

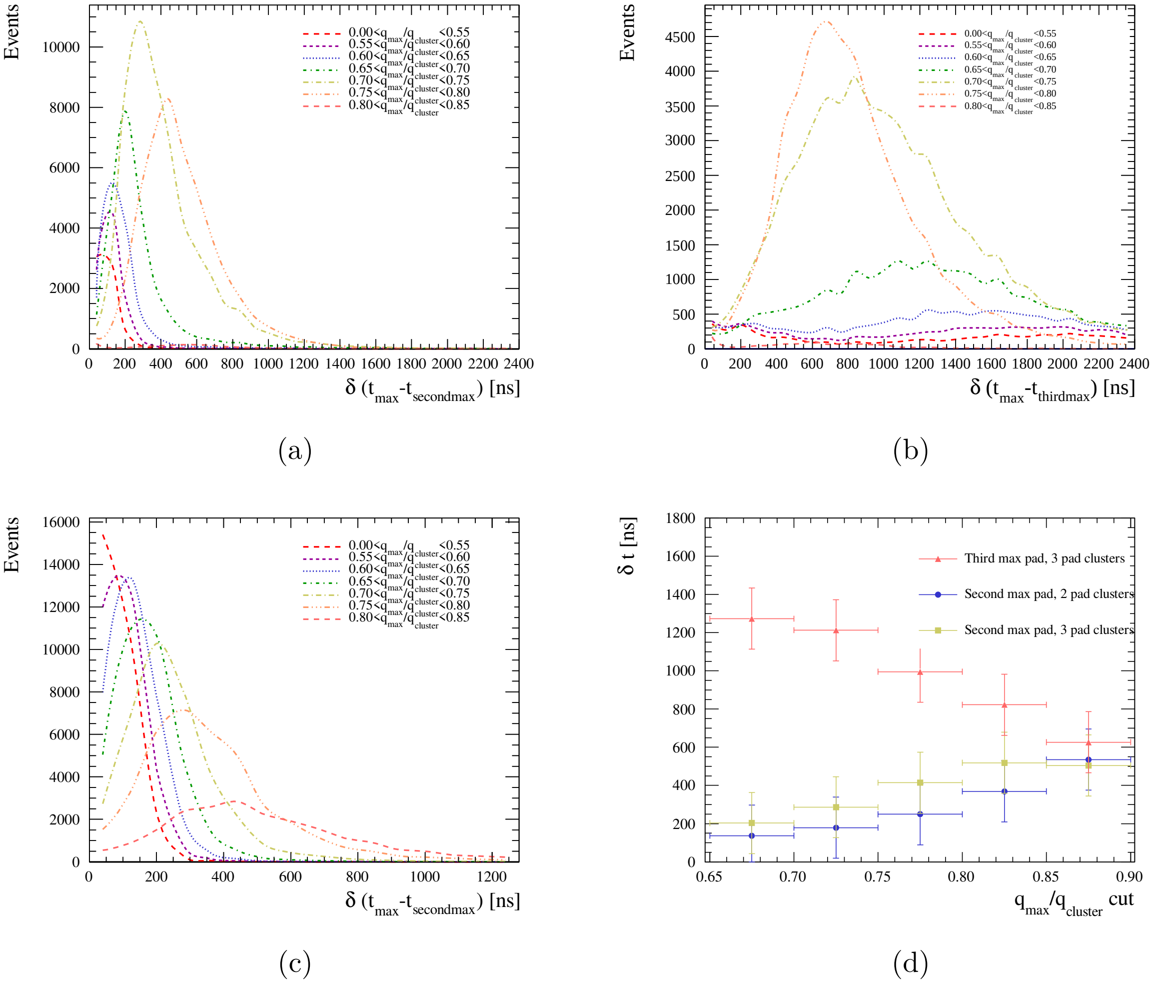

(a) (b)

(c) (d)

Figure 6.13: Distribution of peak-time differences between pads, for different cuts on the fraction of charge in the leading pad. Difference between the leading and the second (a) and third (b) pad in 3-pad clusters. (c) Difference between the leading and the second pad for 2-pad clusters. (d) Peak of the time difference distributions as a function of the cut value. The time is measured with a granularity of 80 ns. The error bars correspond to two time-bins.

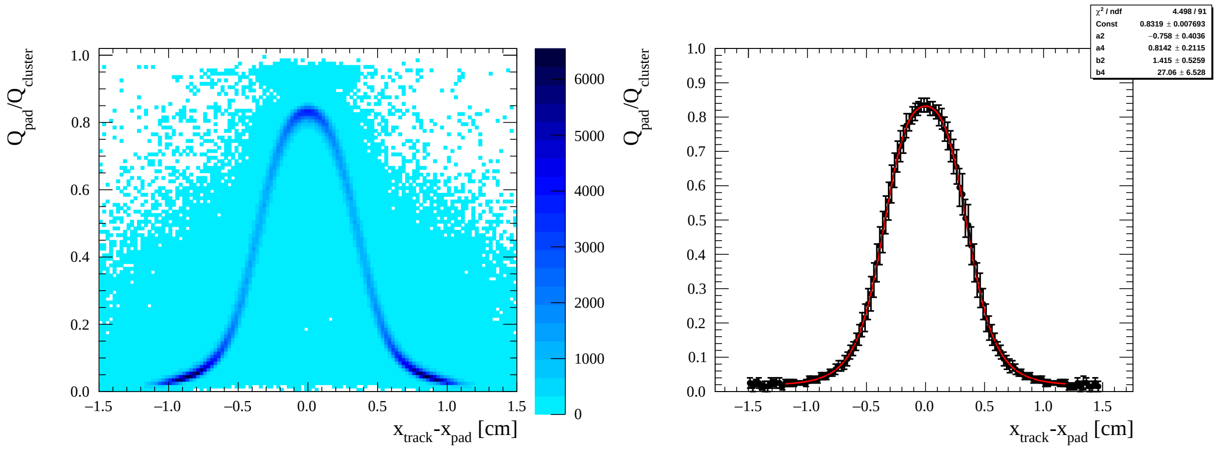

(a) (b)

Figure 6.14: (a) Distribution of $Q_{pad}/Q_{cluster}$ as a function of $x_{track} - x_{pad}$, where x_{track} is obtained with the CoC method to be used as a prior in the fit to determine the PRF. (b) Input to the PRF fit, for each bin, $Q_{pad}/Q_{cluster}$ is extracted as the mean and the error is the full width at half maximum for each $x_{track} - x_{pad}$ bin in the previous 2D plot. The results of the PRF fit are plotted in red and shown in the top-right inlay.

The coefficients a_2 and a_4, and b_2 and b_4 can be expressed in terms of the full width half maximum Γ, the base width Δ of the PRF, and two scale parameters a and b. This is just one possible parametrization, and others can be conceived and tested.
The position of the track is inferred by minimizing the following quantity, χ^2:

$$\chi^2 = \sum_{pads} \frac{Q_{pad}/Q_{cluster} - PRF\,(x_{track} - x_{pad})}{\sqrt{Q_{pad}/Q_{cluster}}} \tag{6.4}$$

Fig. 6.14 illustrates the process of extracting the PRF function. The method and its application to the CERN test-beam data are explained in detail in [159].

The PRF method yields much better results than the classic CoC method, as can be seen in Fig. 6.15.

The spatial resolution with the TPCs has been evaluated under different experimental conditions (drift distance, voltage, particle type and energy). For 1 GeV/c pions, the spatial resolution was found to be of about 300 μm [155].

6.1.1.2.4 Energy Resolution

TPCs identify particle types by comparing their energy loss (dE/dx) as a function of momentum to well known curves for different particle types. It is important that the new TPC be able to recover a dE/dx resolution comparable to that of current T2K TPCs (8% for electrons).
The truncated mean method was used to compute the energy loss in the TPC. This method consists in ordering the clusters (columns) in ascending order based on the deposited charge, and only retaining a fraction (truncation factor) of the clusters to compute the mean energy deposition. It was found that 62.8% was an adequate truncation factor, achieving a good resolution on dE/dx

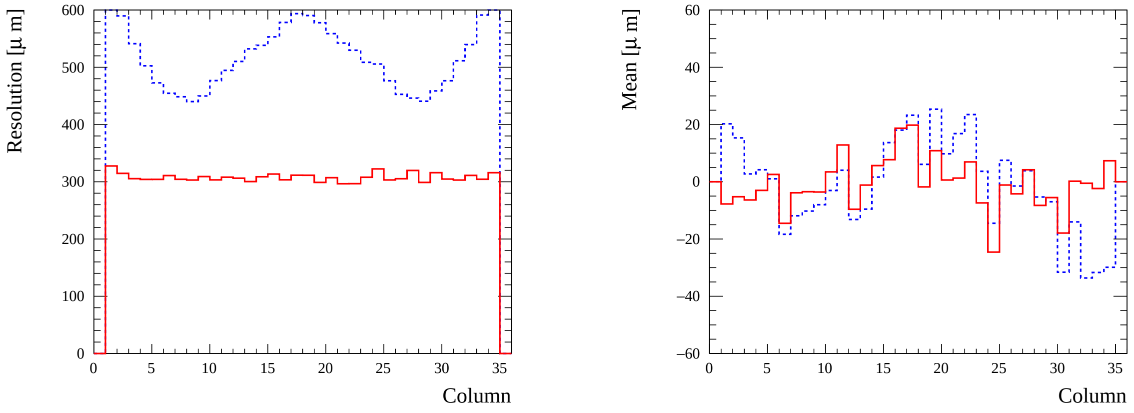

(a) (b)

Figure 6.15: (a) Spatial resolution obtained with the PRF method (red) and with the CoC method (blue). (b) Bias with respect to the track position in each column.

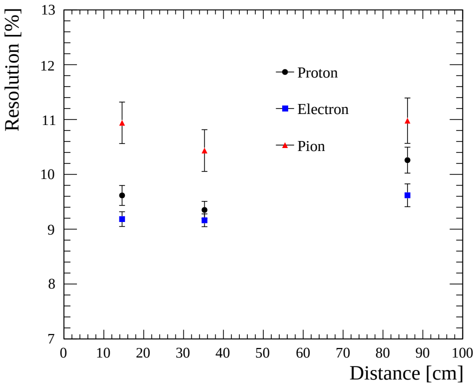

Figure 6.16: dE/dx resolution as a function of drift distance for different particle types with momenta of 0.8 GeV/c. For reference, the drift distance in the HA-TPC will be of 90 cm.

while keeping enough statistics.
Fig. 6.16 shows the evolution of the dE/dx resolution as a function of drift distance for various particle types. For electrons[5] a resolution compatible with 9% can be expected for a 90 cm drift distance, fully compatible with the one achieved by current T2K TPCs. The final dE/dx resolution is calculated by extrapolating the number of pads crossed by a track to the size of the whole TPC. For tracks perpendicular to the beam direction, two Micromegas modules will be crossed. Taking this into account, a final dE/dx resolution of 7% is obtained.

---

[5] All of the particle test beams used during these studies were positively charged. As such, here “electrons” actually means positrons. From the TPC’s perspective, as long as no magnetic field is applied, electrons and positrons are indistinguishable.

6.1.1.3 Second test beam study at DESY

The T2K HA-TPCs will have a different geometry than those tested with the CERN test-beam and characterized in [155]. In particular, the size of the pads is intended to be of 10×11 mm^2 [154]. A prototype with the final geometry of the modules was tested at the DESY test-beam facility in June 2019, where data with and without magnetic field was taken. Electron beams with momenta in the 0.5-5.0 GeV/c range were used.

The experimental setups of the CERN and DESY beam tests are compared in Table 6.1. The main difference, in addition to the pad geometry, is the presence of the 0.2 T magnetic field used in the beam test, which makes it possible to study curved tracks. In addition, it was possible to change the field cage orientation in order to study tracks which cross the module at an angle and thus investigate different clustering topologies.

The gas quality was also better during the DESY beam test than it was in the CERN beam test. Fig. 6.17 shows that the drift velocity was largely constant over time, with the only variation coming from the gas bottle changes. Apart from the gas bottle changes, the drift velocity V_{drift} under the electric field of $E = 275$V/cm varies less than 6‰, indicating an excellent gas quality. These measurements were performed with a Gas Monitoring Chamber identical to the ones used for the T2K TPCs.

	CERN	DESY
Test Area	T9	TB24/1
Magnet	—	PCMAG
Magnetic field (T)	—	0/0.2
Gas	Ar:CF$_4$:iC$_4$H$_{10}$	Ar:CF$_4$:iC$_4$H$_{10}$
Test beam particles	p, π^+, e^+	e^-
Momentum range (GeV/c)	0.8-1.0	0.5-5.0
MM Voltage (V)	340 (330-380)	360 (330-400)
Nominal electric field (V/cm)	167	275
Electronics sampling time (ns)	80	40
Electronics shaping time (ns)	100/200/400/600	116/200/412
Drift distance (cm)	10/30/80	15
Pad size (cm^2)	0.98×0.70	1.01×1.12

Table 6.1: Summary of CERN and DESY beam test setups.

Since this is a test-beam study and few interactions are expected to occur in the TPC gas, the tracks which are of interest are straight, single tracks crossing the detector. Showering or multi-particle tracks are rejected in the analysis. For these reasons, the DB-SCAN [160] algorithm was sufficient in the reconstruction. Due to the charge spreading, neighboring tracks may be reconstructed as a single track. In order to avoid this, a cut on the cluster multiplicity was applied. Fig. 6.18 shows an example of the track reconstruction algorithm and its ability to separate tracks.

The track position was estimated with the PRF method, like for the CERN test beam studies. The spatial resolution for horizontal tracks was found to be of 200-250 μm, with a very weak dependence on the presence of the magnetic field (Fig. 6.19, top left). For sloped tracks, a degradation of the spatial resolution is expected as the angle increases. Whereas for tracks parallel to one of the pad axes the definition of a cluster is unambiguous, several definitions of a cluster can be employed for sloped tracks. Fig. 6.19 (bottom) shows the different cluster definitions that were used to study

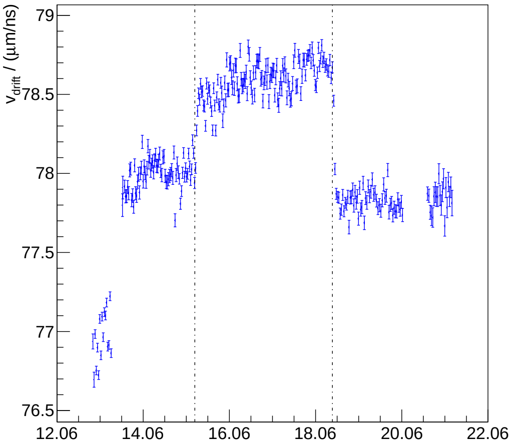

Figure 6.17: Drift velocity as a function of time (dates in June 2019). The dotted lines show the moments when the gas bottles were changed.

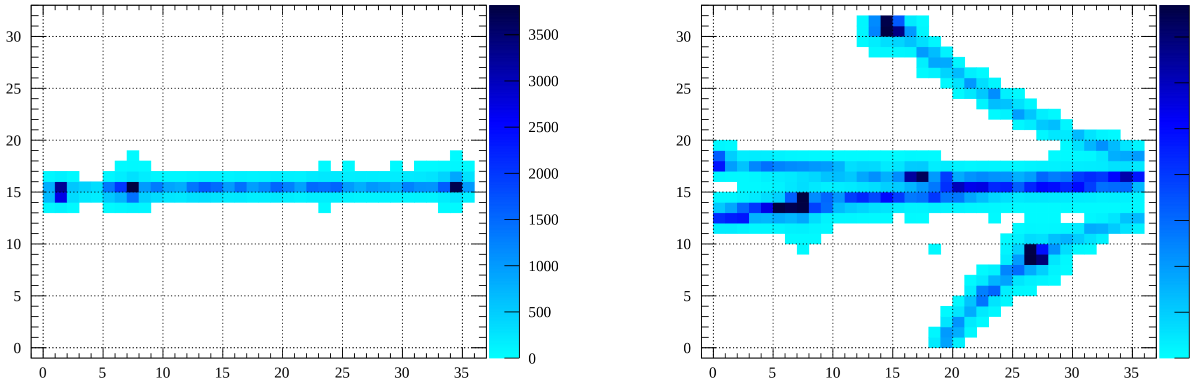

(a)

(b)

Figure 6.18: Event displays of a single track (a) and multi-track (b) in the prototype.

the dependence of the spatial resolution on the track angle. In the current T2K TPCs, the spatial resolution for sloped tracks degrades as a function of the track angle from 600 μm to ∼ 1 mm. The top right plot of Fig. 6.19 shows the performance of the DESY prototype for different track angles. For ∼45° tracks, the column clustering method provides the worst resolution, as expected. For such tracks, the “diagonal” cluster pattern provides the best spatial resolution. In the intermediate angle region (20°, 30°, 60°, 70°), the best results are achieved by using the “2 by 1” and “3 by 1” patterns. By using an adapted pattern for each angle region, the spatial resolution is always kept below 600 μm, for all track angles. A 600 μm resolution in a 0.2 T magnetic field corresponds to a momentum resolution of about 6%.

In terms of the deposited energy resolution, the DESY TPC prototypes performs better than the CERN prototype. The dE/dx resolution as a function of track angle is shown in Fig. 6.20. As for the spatial resolution, the dE/dx resolution improves when using an adapted clustering pattern.

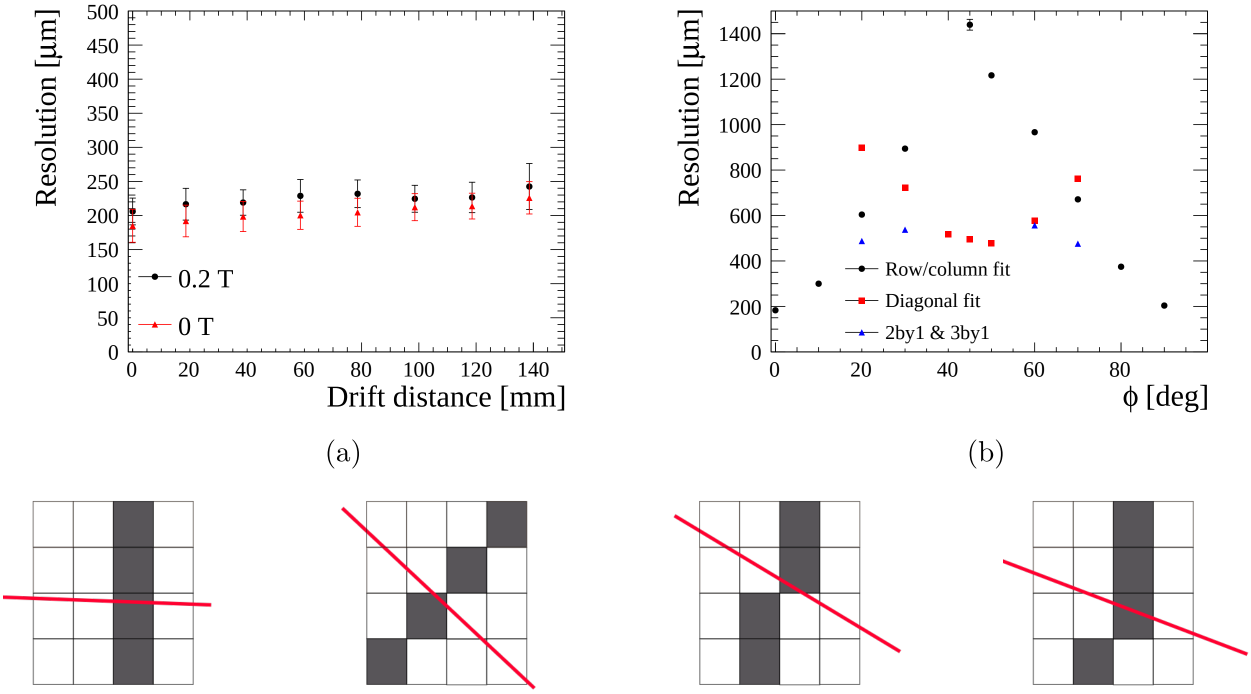

(a) (b)

(c) (d) (e) (f)

Figure 6.19: **Top:** Spatial resolution as a function of drift distance for horizontal tracks (a) and track angle (b). **Bottom:** The different cluster patterns that can be used depending on the track angle (red line): (c) column, (d) diagonal, (e) 2 by 1, (f) 3 by 1.

Overall, the dE/dx resolution is between 7% and 9%. The resolution will improve in the full scale TPC, as in the DESY beam test only one resistive MicroMegas module was used. It is expected that a track will cross at least two modules in the full-size TPC. As a result, a dE/dx resolution of 5.3% can be expected.

As previously noted, T2K will be the first full-scale experiment to use the resistive MicroMegas technology in its TPCs. As such, the charge spreading phenomenon needs to be well modelled and understood, both in order to understand its response and in order to simulate its behaviour. The quantity controlling the charge spreading over time is the product RC: R is the surface resistivity of the layer and C the capacitance determined by the spacing between the anode and readout planes. Dixit and Rankin have proposed a method [161, 162] to simulate charge spreading in Micro-Pattern Gaseous Detectors (MPGDs) which includes the response of the electronics. This model consists in developing a charge spreading profile, starting from the telegraph equation (in a 2D plane), assuming negligible inductance:

$$\rho(r,t) = \frac{1}{2t/RC}\exp\Big(-r^2/4t/RC\Big). \tag{6.5}$$

Eq. (6.5) thus gives the spatial (r) and temporal (t) profile of the charge density (ρ). The total charge profile is obtained by solving Eq. (6.5) and integrating the obtained charge density over the

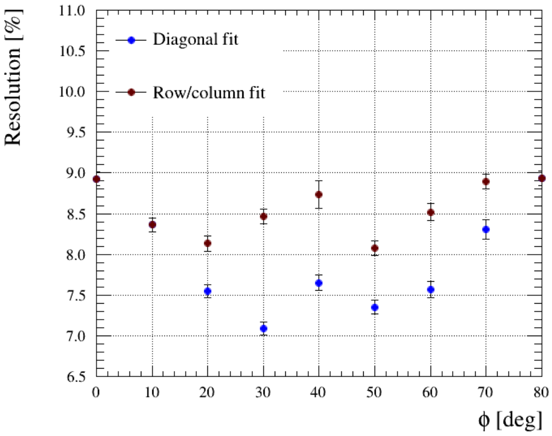

Figure 6.20: dE/dx resolution as a function of track angle, using two different clustering patterns. A 0.2 T magnetic field is applied.

pad area, yielding[161]:

$$S(t) = \frac{Q}{4}\left[erf(\frac{x_{\text{high}} - x_0}{\sqrt{2}\sigma(t)}) - erf(\frac{x_{\text{low}} - x_0}{\sqrt{2}\sigma(t)})\right]\left[erf(\frac{y_{\text{high}} - y_0}{\sqrt{2}\sigma(t)}) - erf(\frac{y_{\text{low}} - y_0}{\sqrt{2}\sigma(t)})\right] \tag{6.6}$$

with Q the initial amount of charge after the avalanche, (x_0,y_0) the track position, x_{high}, x_{low}, y_{high}, y_{low} the pad boundaries and in the denominator $\sigma(t) = \sqrt{(2t/\tau) + \omega^2}$. Here, $\tau = RC$ corresponds to the time constant characterizing the charge spread in the resistive layer. Finally, ω is associated to the longitudinal diffusion term. In the case of the DESY test beam prototype, the drift distance was small (15 cm), so the longitudinal diffusion can be neglected.

Using these considerations, the waveforms in each track can be fitted with the model described in Eq. (6.6) in order to extract the value of RC in each pad. However, the response of the electronics needs to also be taken into account. For this, a dedicated electronics simulation is used to obtain an electronics response function as a function of time $A(t)$ for a point-like charge deposition. The amount of charge in the leading pad completely dominates the shape of the waveform, and the charge spreading in the leading pad can be neglected. Thus, the leading pad is used to fix the parameters used in the electronics response function, and then the neighboring pads, where the charge spreading dominates, are fit with the convolution of Eq. (6.6) and $A(t)$, and the RC value for each pad is extracted. Fig. 6.21 shows the result of the fit to three pads in a cluster.

The RC values are used to construct an "RC map" for the module, shown in Fig. 6.22. A non-uniformity of RC values is seen in the downstream region of the module, of the order of 30%. The non-uniformity of the resistive layer is an important parameter to take into account when simulations are devised.

The analysis of the DESY test-beam data is ongoing, and a publication is under way.

6.1.2 SuperFGD

The current Fine-Grained Detectors (FGDs, Section 2.2.2.1) used by T2K are designed for interactions producing particles going along the neutrino beam direction. However, due to the limited phase-space coverage and particle detection thresholds listed in Section 6.1, a new target has been

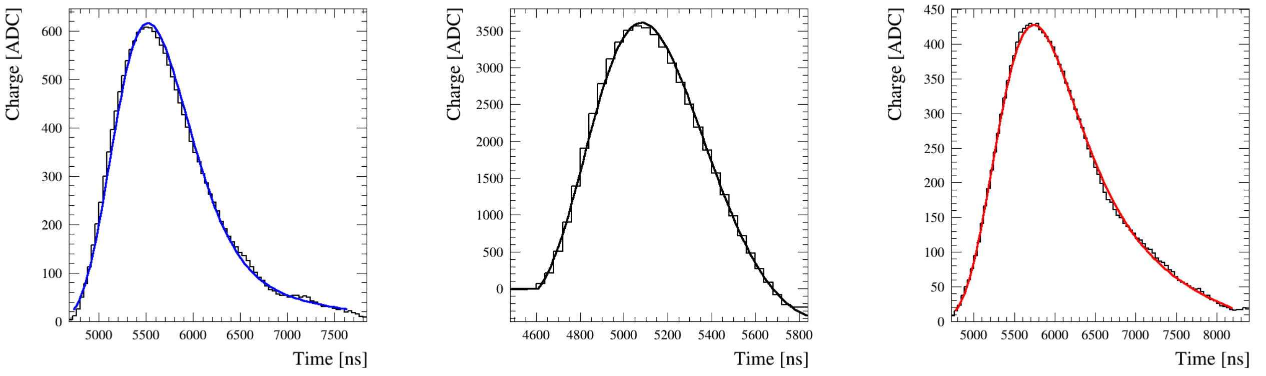

(a) Lower neighbor (b) Leading pad (c) Upper neighbor

Figure 6.21: Example of waveform fit results for the leading pad and its neighbors in a given cluster.

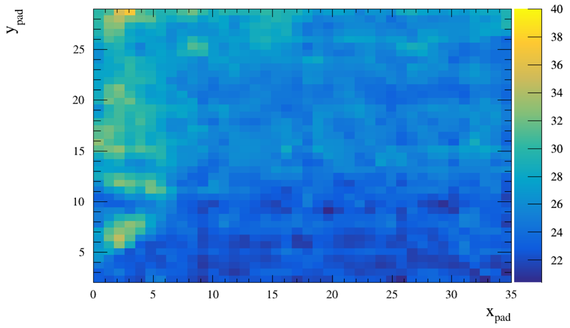

Figure 6.22: *RC* map obtained using an analytical fit, as described in the text. The colors correspond to the *RC* value.

designed with the following requirements in mind:

- The new target has to have a large active mass, in order to generate a number of neutrino interactions comparable to that of current FGDs. The total mass of the current FGDs is of 2 tons.
- It needs to be able to identify particles at high angle with respect to the neutrino beam direction.
- The target must be able to detect low-momentum hadrons produced in neutrino interactions, near the interaction vertex.

A 3D fully active target, comprised of 1 cm^3 plastic scintillating cubes, was proposed [163]. It consists of a large number of scintillating cubes, coated with an optically isolating layer. The cubes are assembled into a 3D structure, held together by three wavelength shifting (WLS) optical fibers, one along each axis. This detector is called the SuperFGD (for Super Fine Grained Detector) and will be an additional target at ND280, sandwiched between the two horizontal TPCs described in Section 6.1.1. A schematic view of the SuperFGD, obtained with GEANT4 [108], is shown in Fig. 6.23.

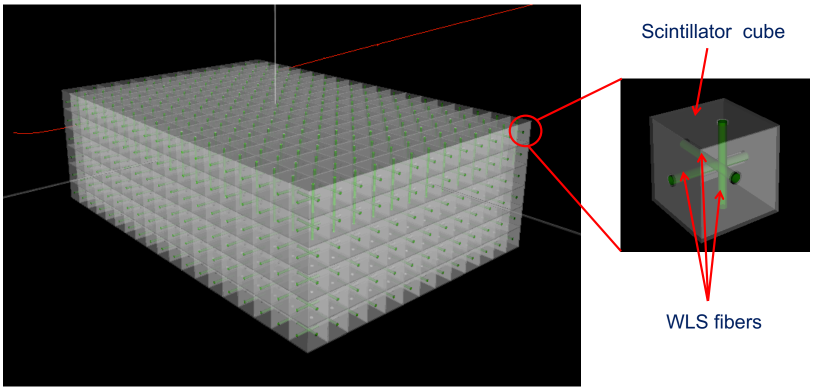

Figure 6.23: Schematic view of the SuperFGD detector, with a zoom on the structure of one cube.

The final detector will consist of 192×184×56 1 cm cubes, yielding a total of nearly 2 million cubes. The cubes are made of polystyrene doped with 1.5% of paraterphenyl (PTP) and 0.01% of POPOP [154]. As such, the detector will have a total active mass of nearly 2 tons. The main nuclear target participating in neutrino interactions will be carbon, like in the current FGDs. Carbon nuclei are close enough to oxygen nuclei present at SK, although some extrapolation is still necessary. It provides a good compromise for a large scale detector, while still being prone to similar neutrino interactions. The fiducial mass requirement of the detector is thus satisfied.

Providing individual read out for each cube would require a number of read-out channels of the order of 2 million, which is costly and difficult to maintain. For the SuperFGD, this issue is mitigated by the use of WLS fibers. As shown in Fig. 6.23, each cube has three orthogonal cylindrical 1.5 mm holes drilled along each axis, which can accommodate three WLS fibers with a diameter of 1 mm. Since the fibers can pass through an entire line of cubes, the total number of fibers does not scale with the volume (unlike the number of cubes), but rather corresponds to the number of cubes along the surface of each of the three cube planes. This allows to reduce the total amount of fibres, and thus of readout channels, to 58,368. Each WLS fiber is connected to a Multi-Pixel Photon Counter (MPPC). A signal in three WLS fibers makes it possible to reconstruct the position of the initial hit in 3D.

Thanks to its high granularity and 3D structure, the SuperFGD will be able to identify high-angle particles, achieving full polar angle coverage.

The size of individual cubes was chosen keeping in mind the requirement to detect low-momentum hadrons close to the interaction vertex. A 200 MeV/c proton, corresponding to the level of the Fermi momentum in a simple box-model description of the nucleus, has a range of about 5 cm in a carbon target.

Several SuperFGD prototypes of different sizes were tested using particle test-beams and simulations. One of the main challenges in constructing a full-size SuperFGD detector lies in its assembly. Several methods were tried [154], and the one retained was a preliminary assembly of the detector using fishing lines instead of WLS fibers. Once all of the cubes are assembled and the structure is stable, the fishing lines will be replaced with WLS fibres. This choice was made due to the fragility of WLS fibers. The assembly and production of cubes also takes a considerable amount of time - for example, producing 4000 cubes per day would take a minimum of around 1.5 years just to produce all the necessary cubes, without factoring in the drilling of the holes (12 000 holes can be drilled per day) and the actual assembly. Taking in these considerations, the installation of the SuperFGD, whose cube production started in January 2019, is scheduled to take place in 2022.

6.1.2.1 Performace of SuperFGD prototypes and simulations

The first prototype evaluated with a test beam was a small 5×5×5 cube prototype, shown in Fig. 6.24. The prototype was tested with at the T10 area of the CERN Proto-Synchrotron (PS) in the fall of 2017.

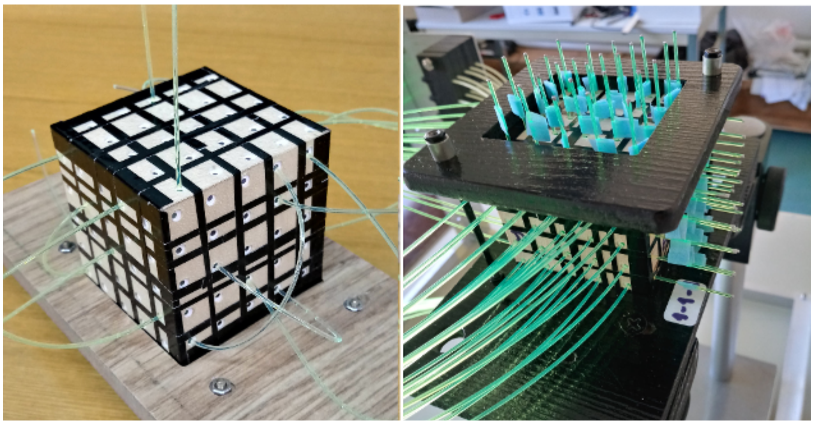

Figure 6.24: First SuperFGD small-scale prototype during assembly (left) and during the test-beam data taking.

The results of the first test-beam study were published in [164]. The goal of the test-beam study were to validate the technology and extract values for the light yield, amount of cross-talk, and timing resolution. The results are illustrated in Fig. 6.25.

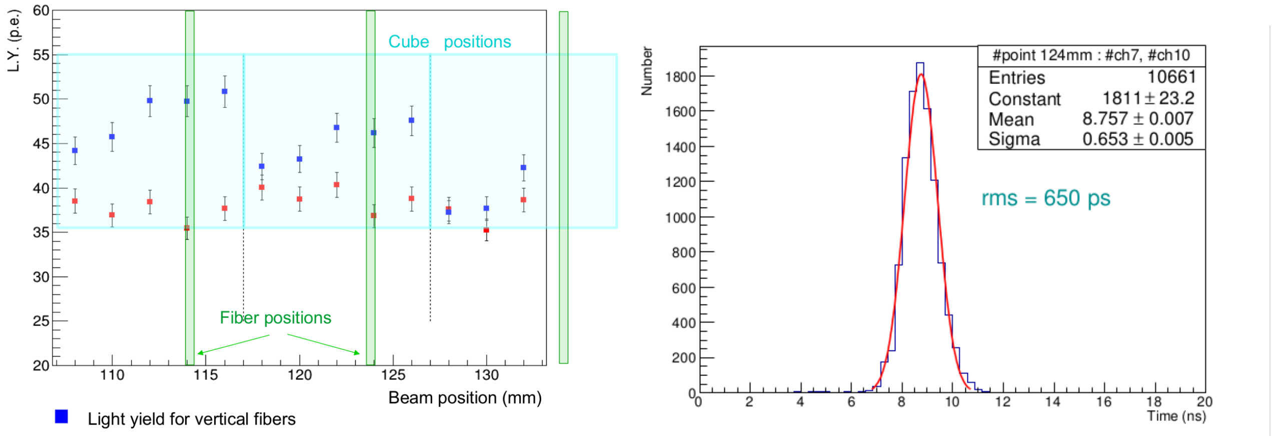

(a)

(b)

Figure 6.25: (a) Average light yield as a function of beam position relative to the 5×5×5 prototype size, for different types of fibers. (b) Distribution of average time between two fibers.

The average light yield for one fiber is between 36 and 50 p.e./MIP, and of 80 p.e. for two fibers. The amount of optical cross-talk is evaluated at 3.4% for each adjacent cube, yielding a total cross-talk of 13.7%. This corresponds to about 20% of the light emitted in a cube escaping through the reflecting walls. The timing resolution for a cube with a single fiber is of 0.95 ns, which is reduced when considering two fibers to 0.65-0.71 ns.

A second, larger prototype was constructed, and is shown in Fig. 6.26. The size of the second prototype is of 48×24×8 cubes, largely driven by the size of the CERN MNP17 magnet, and was tested at the T9 test-beam facility at CERN. This larger-scale prototype allowed to validated the assembly method using fishing lines, which is then used to assemble the final detector.

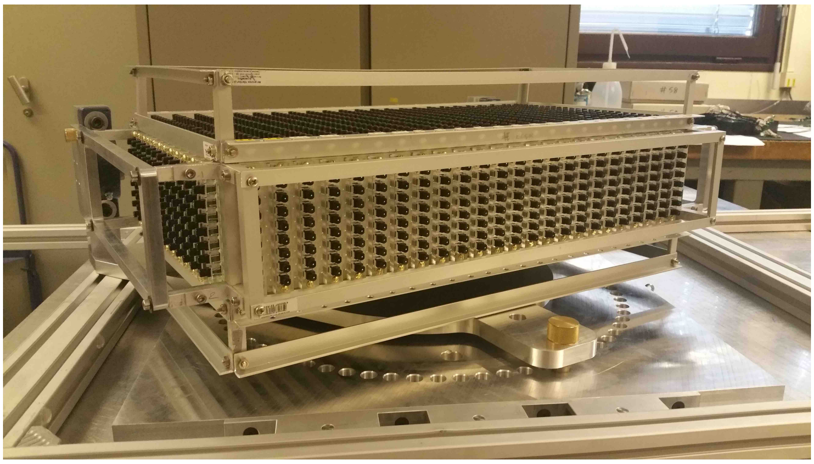

Figure 6.26: Second SuperFGD prototype, before being shipped to the CERN test-beam facility and adding MPPCs and electronic read-out.

The goal of the second test-beam study is to determine the actual performance of the detector and receive feedback which will help optimize the final detector parameters.

The test-beam study was performed with different particle beams with momenta ranging from 400 MeV/c to 8 GeV/c. Fig. 6.27 shows two examples of event displays using this prototype. The stopping protons (left) event display shows an event in which a proton from a 800 MeV/c test-beam[6] travels for a given range along the prototype z-axis (48 cubes, coinciding with the particle test-beam direction), and then stops and deposits the remainder of its energy in a small space. This type of test is useful in order to evaluate the detector performance for large energy depositions and to test detector simulations in which particle guns are used. It was found that the data and simulations were in good agreement [165]. The second event display (Fig. 6.27, right) shows an e^+e^- pair from a photon conversion, while a magnetic field is applied. The SuperFGD protoype can very well identify γ conversions, provided the tracks are long enough and a magnetic field is applied. This is an important asset to separate electron neutrino interactions from photon conversions, coming from π^0 particles.

The SuperFGD has particle discrimination capabilities, by using a dE/dx method similar to the TPCs. It can achieve a dE/dx resolution of the of the order of 10%. By looking at stopping protons, it was found that the prototype has the capacity to distinguish one proton from two protons (in the case of co-linear tracks). While particle identification is not the primary goal of the SuperFGD, it can significantly aid the HA-TPCs in this process. Particles which do not reach the TPC and are fully contained in the SuperFGD are measured using momentum-by-range.

In terms of detector performance, the average light yield in a cube for a MIP is of 58-59 p.e.. The amount of cross-talk with neighboring cubes is of 2.94% per side, lower than that obtained with the smaller prototype[7]. The time resolution of the detector was measured to be 1.14 ns for a single

---

[6] The proton actually has a smaller momentum, due to the fact that is passes a series of TPCs before entering the SuperFGD prototype.

[7] This is partly due to the fact that the 48×24×8 prototype had additional Tyvek reflector layers between the

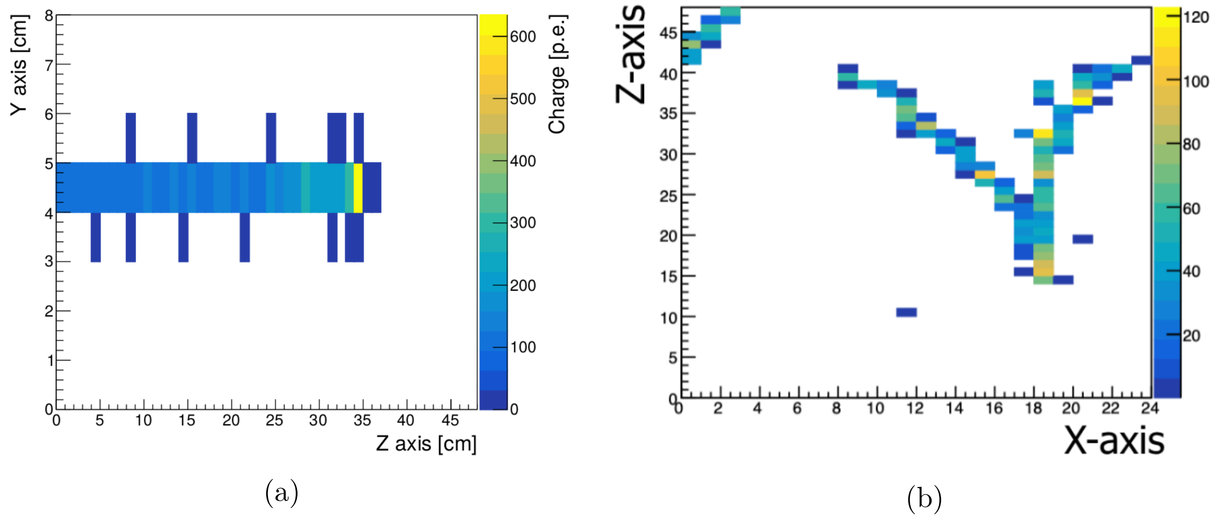

(a) (b)

Figure 6.27: Event displays for different types of events recorded with the 48×24×8 SuperFGD prototype. (a) Stopping proton. (b) e^+e^- pair from a photon conversion. In both cases, the z-axis shows the amount of p.e. recorded as an electric charge.

channel, but can be improved by considering multiple channels or scaling according to the light yield. The recovery time (i.e. the time required for a readout channel to be ready to receive a second hit) was estimated to be of order 200 ns, which is sufficient to record a Michel electron event following a muon decay in a cube[8].

The complete results of the test-beam study are published in [165].

As for the HA-TPCs, the installation of the SuperFGD is scheduled to take place in 2022.

6.1.3 Time-of-Flight Detectors

In addition to the SuperFGD and HA-TPCs, the ND280 upgrade foresees a Time-of-Flight (ToF) detector. The latter consists in six planes of plastic scintillating bars, coupled to an array of MPPCs. The six scintillator planes will fully enclose the HA-TPCs and the SuperFGD ensemble, as shown in Fig. 6.28.

The main purpose of the ToF detector is to reconstruct the direction of a particle with respect to the SuperFGD - i.e. whether it is going towards the target or whether it is exiting. In addition, the ToF detector will provide additional PID separation for particles whose energy loss is similar but with different masses and thus different ToF (e.g. protons and positrons).

A ToF prototype was tested at the CERN PS using test-beams, and displayed a timing resolution of 90 ps [154]. For comparison, a timing resolution of better than 500 ps is needed for unambiguous track direction measurements, and a resolution better than 100-200 ps can be used for particle identification.

---

horizontal cube planes.

[8] This is particularly useful for pion detection.

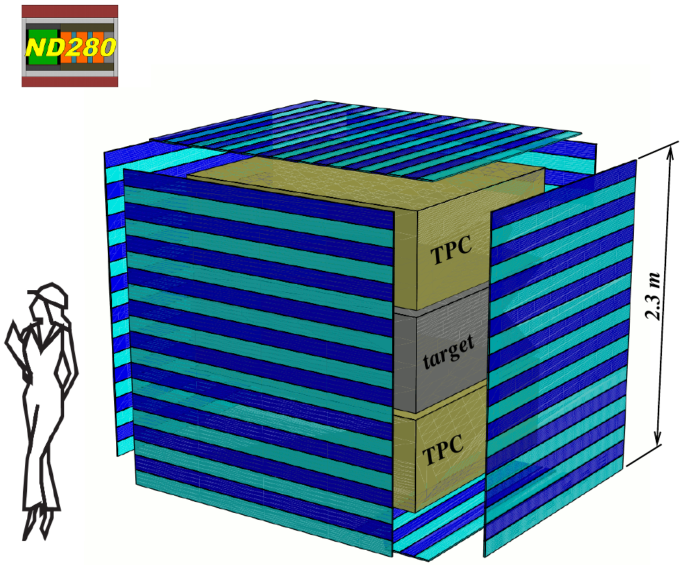

Figure 6.28: Schematic layout of the ToF planes (blue), surrounding the HA-TPCs and SuperFGD (target).

6.2 Physics impact

6.2.1 Impact of the SuperFGD using proton information

The impact of the ND280 Upgrade on the ND280 samples was gauged by performing simulations. The detector (SuperFGD + HA-TPCs + ToF) was simulated using GEANT4, and a sample of neutrino interactions was simulated with GENIE [166], using the 2016 T2K flux as an input [154]. By applying the same selections as described in Section 3.2.3, the total ν_μ CC-Inclusive coverage can be compared between the current ND280 configuration and that expected with the upgrade. Fig. 6.29 confirms that the upgraded configuration shows improvements in two previously deficient areas of phase space: high angle muons, thanks to the HA-TPCs, are better reconstructed, and backwards going muons now populate the spectrum thanks to the ToF information.

In terms of track reconstruction efficiencies, Fig. 6.30 shows the improvement thanks to the SuperFGD of proton and muon tracks. For an approximated comparison to the current FGDs, the efficiencies obtained with a two-readout view with the SuperFGD are also shown. The two-readout view consists in eliminating one of the planes used in the light readout (XY, XZ or ZY, with Z being the neutrino beam direction). Whereas with the previous FGD two-readout configuration the threshold for proton detection was at ~500 MeV/c, the three-readout SuperFGD allows to reduce it down to ~300 MeV/c. As shown in Fig. 6.5, this improvement will allow us to use nearly the entire proton spectrum at T2K energies. For muons, a two-readout view perpendicular to the beam direction (cases noXZ and noYZ in Fig. 6.30), the track reconstruction efficiency is almost uniform across the muon direction. For a lacking XY plane (like in current FGDs), there is a clear drop in efficiency at high angles with respect to the neutrino beam direction. The three-readout of the SuperFGD renders the efficiency across all muon directions uniform, thus mitigating the high-angle deficiency and increasing the overall track reconstruction efficiency.

The lower particle momentum thresholds and increased detection efficiencies were a requirement motivated by the need to reach a better control and understanding of nuclear effects. As shown in

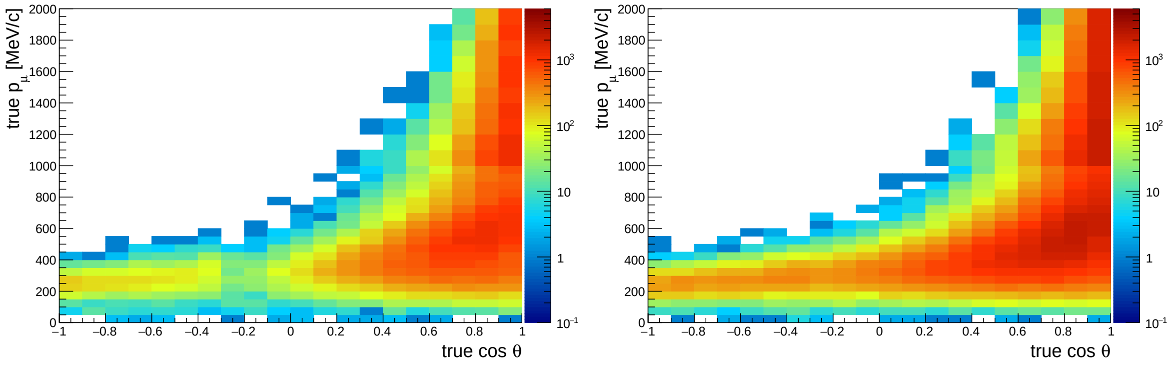

(a) (b)

Figure 6.29: Comparison of ν_μ events distribution for the current ND280 configuration (a) and using the ND280 Upgrade (b). The distributions are shown in p_μ-cosθ_μ, i.e. the reconstructed muon momentum and direction with respect to the beam direction.

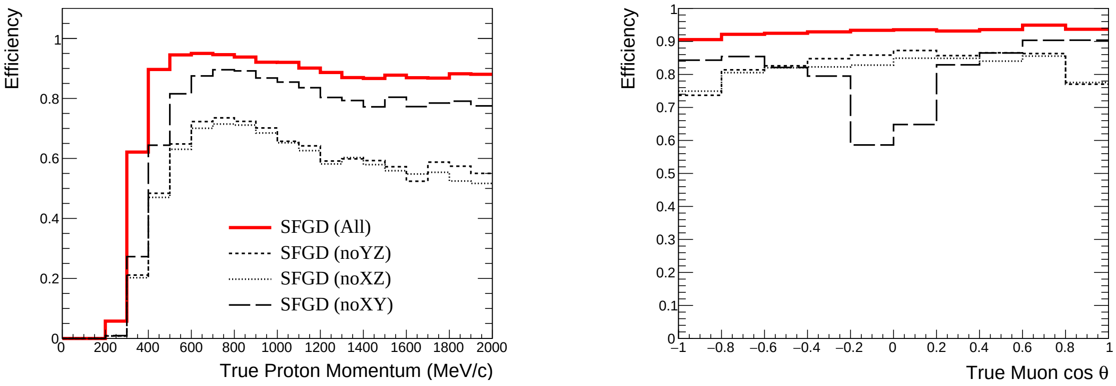

(a) (b)

Figure 6.30: Track reconstruction efficiencies in the SuperFGD with a three-readout view (red) compared with a two-readout view (dashed lines), for different particle types. (a) Protons as a function of true proton momentum. (b) Muons as a function of true cosθ_μ.

Chapter 5, neutrino interactions-related errors are the largest source of systematic uncertainty in the oscillation analysis, mainly due to the fact that neutrinos interact in a complex nuclear environment.

Due to the high momentum threshold for proton detection at SK, the neutrino energy in signal samples is estimated using the CCQE formula (Eq. (2.10)), using only outgoing lepton information. This has also been the case at the near detector. Nuclear effects causes a smearing o f the energy resolution and any nuclear effect which is not modelled or constrained properly biases the reconstructed neutrino energy.

Thanks to the lower particle detection thresholds made available by the upgrade, it will become possible to use information on final state protons at the level in the near detector analysis (Chapter 4). In order to do this, a novel and powerful approach is to exploit the kinematic imbalance in the transverse plane to the incoming neutrino beam.

For a quasi-elastic neutrino-nucleon interaction, a set of variables, called Single Transverse Variables

(STVs), can be defined in the plane transverse to the incoming neutrino direction as follows:

$$\delta p_{\mathrm{T}} = |\overrightarrow{p}^{l}_{T} + \overrightarrow{p}^{p}_{T}|, \tag{6.7}$$

$$\delta \alpha_{\mathrm{T}} = \arccos \frac{-\overrightarrow{p}^{l}_{T} \cdot \delta \overrightarrow{p}_{T}}{p^{l}_{T} \delta p_{\mathrm{T}}}, \tag{6.8}$$

$$\delta \phi_{\mathrm{T}} = \arccos \frac{-\overrightarrow{p}^{l}_{T} \cdot \overrightarrow{p}^{p}_{T}}{p^{l}_{T} p^{p}_{T}}. \tag{6.9}$$

where p^p and p^l are the (highest momentum) proton and lepton momenta, and the T index is the projection of the vector on the plane transverse to the incoming neutrino direction. The definition of these variables is summarized graphically in Fig. 6.31.

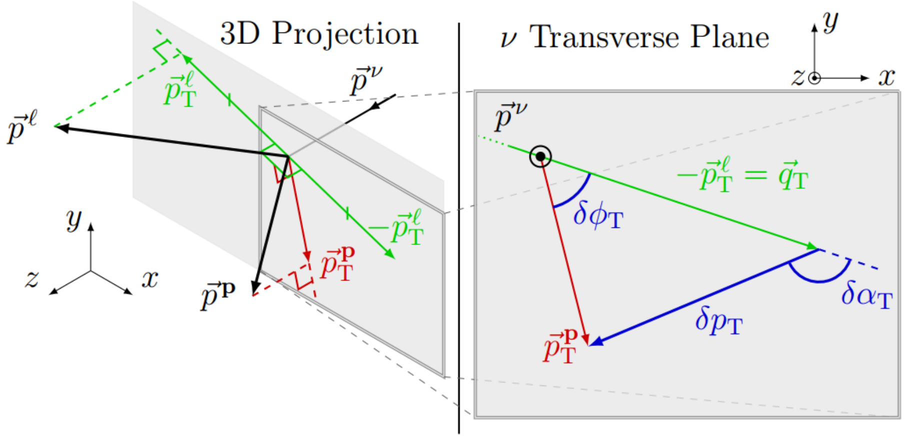

Figure 6.31: Schematic definition of STVs. The left side shows the momenta of the incoming neutrino, ν, and the outgoing lepton, ℓ, and proton p in black. The transverse plane is shown in light grey, and the projections of the outgoing particle momenta on this plane are shown in green. The right-hand side shows a rearrangement of the transverse momenta in the transverse plane and shows how the STVs are formed, in blue. Figure reproduced from [167].

STVs have been used in cross-section measurements by both the T2K [167] and MINERνA [168] collaborations. In the absence of nuclear effects, the outgoing particles are back-to-back in the transverse plan and thus δp_{T} and $\delta\phi_{\mathrm{T}}$ vanish, whereas $\delta\alpha_{\mathrm{T}}$ is undefined[9]. Any deviation from these values is a direct measurement of nuclear effect.

Nuclear effects can be broadly categorized into three types:

- The intial state motion of the nucleons inside a nucleus (Fermi motion), which is described by different nuclear ground state models (Section 2.4.1).
- Correlations between nucleons, usually leading to multi-nucleon interaction such as 2p2h interactions (Section 2.4.2.1).
- Final state interactions (FSI), which are re-interactions of the final state nucleon inside the nuclear medium - these can either alter the nucleon kinematics, or stimulate absorption or emission of other particles (such as nucleons and pions) and thus alter the final reconstructed topology (Section 2.4.4).

---

[9] In practice, this means that $\delta\alpha_{\mathrm{T}}$ has a uniform distribution, since no values are preferred.

In order to gauge the impact of the SuperFGD capabilities to discern nuclear effects, several NEUT 5.4.0 [101] simulations were produced using the T2K flux from the 2018 analysis [100]. Apart from the CCQE model, the same nuclear models as those used in the oscillation analysis presented in this thesis (see Section 3.2) were used in the simulations.
Several nuclear ground state models were compared:

- A Local Fermi Gas (LFG) model, based on the Nieves et al. [85] model.
- A Spectral Function (SF) model, by Benhar et al. [86].
- A Relativistic Fermi Gas (RFG) model, using the Llewellyn-Smith formalism [90].

The LFG model is the nominal NEUT 5.4.0 model, and it assumes an axial mass value of M_A^{QE} =1.05 GeV/c^2. The same axial mass value was retained in the other nuclear model simulations. The simulations assumed neutrino interactions in a hydrocarbon target (equal amounts of carbon and hydrogen[10]), which is the material from which the SuperFGD and current FGDs are made of. The detector effects of the SuperFGD (the target) were applied as a smearing and cuts in the following way:

- A conservative 4% smearing on each component of particle momentum vectors. This value comes from GEANT4 simulations of the SuperFGD, which estimated an overall 3% momentum resolution [154]. In order to be conservative, the overall momentum resolution was applied instead to each component of the particle momentum vector, with an additional 1%.
- Hard thresholds are applied to particle momenta: protons between 300 MeV/c and 1 GeV/c, and muons with a momentum larger than 50 MeV/c are retained.
- A full, 4π angular acceptance is assumed.

The studies were performed using only tracks contained in the SuperFGD (while including the samples of tracks reaching HA-TPC will further improve the performance) and only considering ν_μ interactions (i.e. a neutrino-mode beam). The simulated NEUT events were used to compare different model predictions as a function of STVs, and used to extract differential cross-sections. In order to extract these measurements, an approximate statistical error was applied by scaling the statistical error in the T2K STV measurement publication [167] by the square root of the ratio of the number of SuperFGD events expected with a 30% integrated efficiency[11]. The error bars include statistical uncertainties and a 5% systematic error, corresponding to the size of the cross-section and detector errors from the analysis in [167]. The total amount of statistics was assumed to correspond to 8×10^{21} POT. This number comes from the predictions in Fig. 6.1, by subtracting the expected statistics before the upgrade ($\sim 4 \times 10^{21}$ POT) from the total T2K+T2K-II statistics (20×10^{21} POT), and dividing the number by 2 (assuming half of the data is gathered in neutrino mode, and half in anti-neutrino mode). The total target mass was assumed to be of 2 tons of hydrocarbon. In addition to different nuclear ground state models, two more simulations were produced for the LFG ground state model: one in which it was assumed that no 2p2h interactions occur ("no 2p2h"), and one in which no FSI happened ("no FSI"). Although nonphysical, these additional simulations

---

[10] Note that a carbon nucleus has 6 protons, while a hydrogen atom only has one. Equal amounts of carbon and hydrogen atoms imply roughly six times as many interactions on carbon nuclei than on hydrogen atoms.

[11] This is a conservative estimate - the 30% efficiency is the same as the one achieved by the FGD1 detector in [167].

allow us to gauge the maximum extent of these nuclear effects. As a first step, only interactions which would fall into the CC0π samples are considered.

Fig. 6.32 shows the differential cross-sections as a function of δp_{T} and $\delta\phi_{\mathrm{T}}$. The different nuclear ground state models affect the bulk of the δp_{T} distribution, whereas nuclear effects such as 2p2h and FSI populate the tail of the distribution. In Fig. 6.32a, it is clear that with the SuperFGD there is a clear separation between the SF, RFG and LFG models towards the peak of the distribution, whereas the tail of the distribution shows a clear separation of the effect of FSI and 2p2h. The same type of effect can be seen in the tail of the $\delta\phi_{\mathrm{T}}$ distribution.

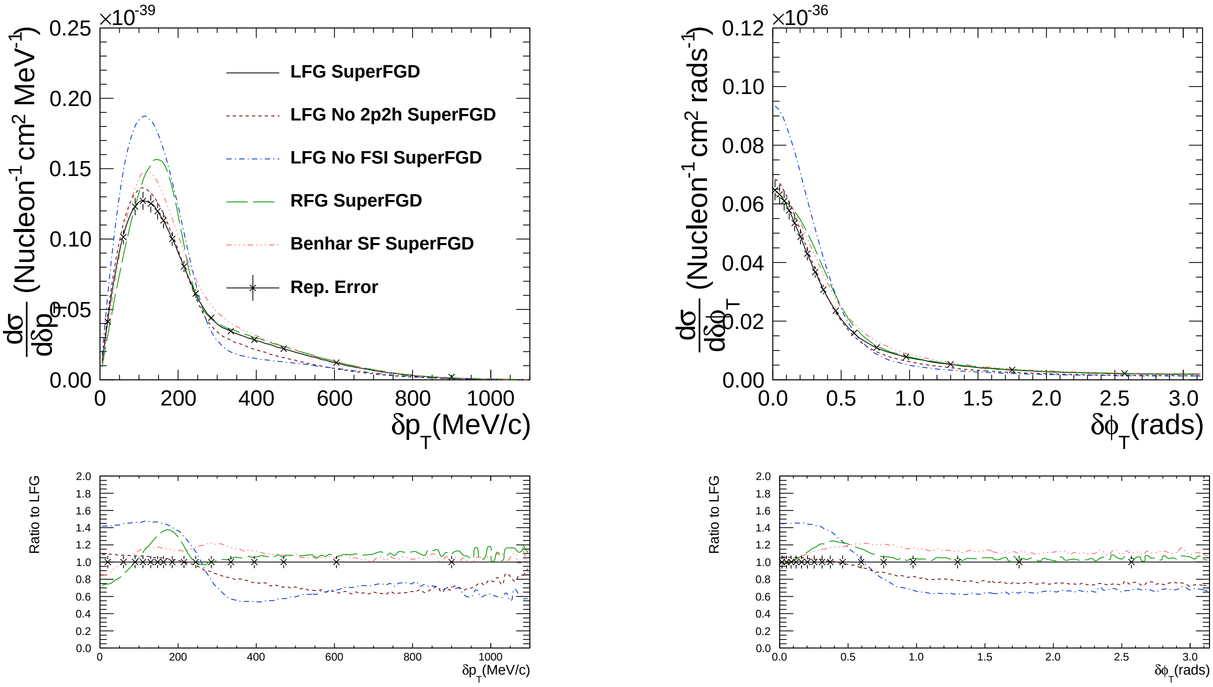

(a) (b)

Figure 6.32: The differential cross section of CCQE-like neutrino-hydrocarbon interactions in δp_{T} (a) and $\delta\phi_{\mathrm{T}}$ (b) for different nuclear models, smeared and acceptance-corrected based on the expected SuperFGD performance. The LFG prediction shows an approximate error based on assumptions discussed in the text. The lower figures present the same information as ratios to the LFG case.

Although it is possible to separate the no FSI and no 2p2h cases from the nominal model, the two are still degenerate. This degeneracy can be lifted with the help of $\delta\alpha_{\mathrm{T}}$, which has little sensitivity to any nuclear effect other than FSI. The effect of FSI is mostly to decelerate outgoing protons, while not affecting the outgoing lepton, and as a result it shifts $\delta\alpha_{\mathrm{T}}$ towards π. This is illustrated in Fig. 6.33. The only case which stands out is the LFG model with no FSI, which tends towards a constant cross-section as a function of $\delta\alpha_{\mathrm{T}}$. Exploiting the power of $\delta\alpha_{\mathrm{T}}$, we can define three regions of the spectrum:

- $0 < \delta\alpha_{\mathrm{T}} < \frac{\pi}{3}$: low FSI region;
- $\frac{\pi}{3} < \delta\alpha_{\mathrm{T}} < \frac{2\pi}{3}$: intermediate FSI region;
- $\frac{2\pi}{3} < \delta\alpha_{\mathrm{T}} < \pi$: high FSI region.

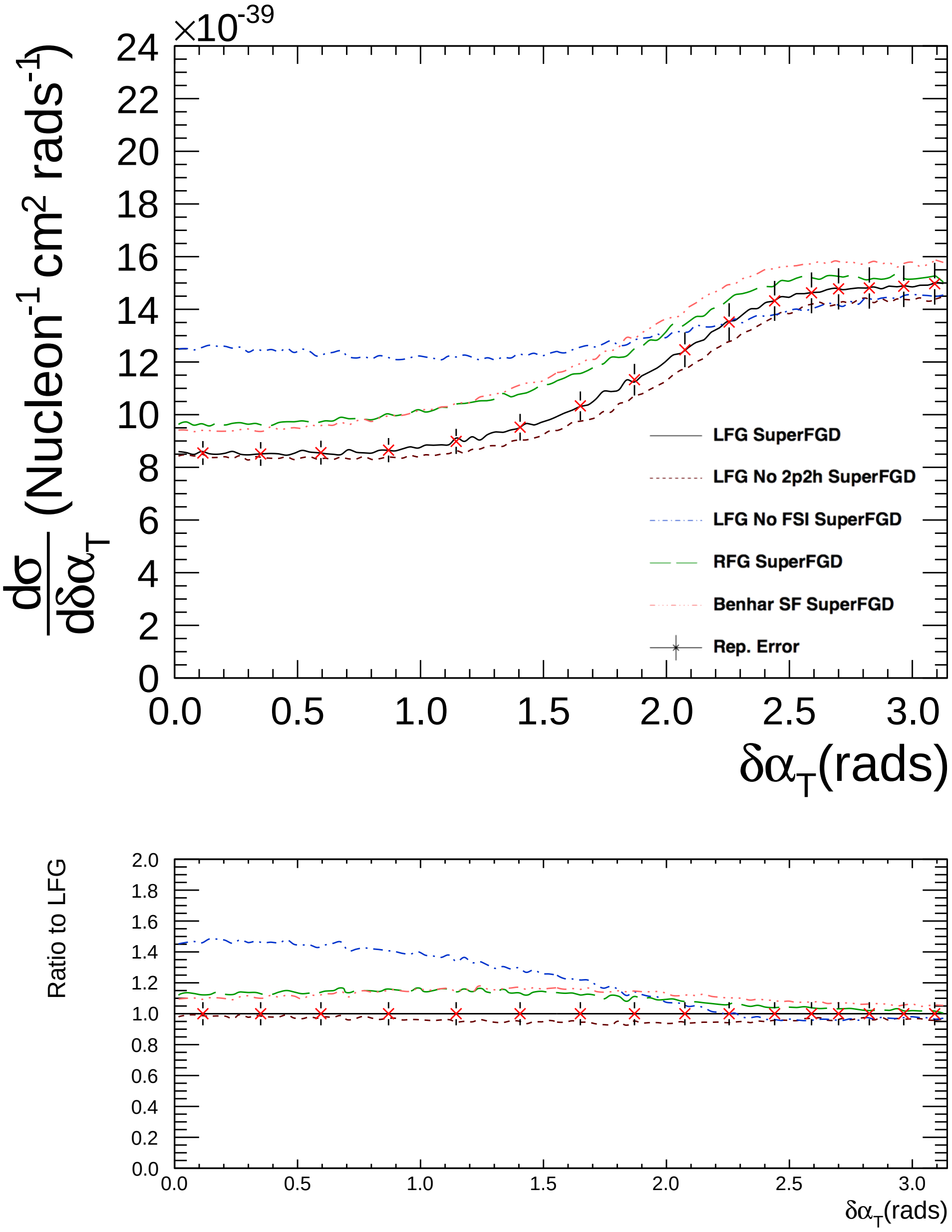

Figure 6.33: The differential cross section of CCQE-like neutrino-hydrocarbon interactions in $\delta\alpha_T$ for different nuclear models, smeared and acceptance corrected based on the expected SuperFGD performance. The LFG prediction shows an approximate error based on assumptions discussed in the text. The lower figures present the same information as ratios to the LFG case.

By selecting an appropriate region of $\delta\alpha_{\mathrm{T}}$, it is possible to isolate the effect of FSI and 2p2h (or other nuclear effects). This is illustrated in Fig. 6.34: a realistic LFG model (Fig. 6.34a and Fig. 6.34b) is compared to an nonphysical LFG prediction in which no FSI processes occur (Fig. 6.34c and Fig. 6.34d), broken down by interaction type. In the low FSI region ($0 < \delta\alpha_{\mathrm{T}} < \frac{\pi}{3}$), the tails of the distributions in Fig. 6.34a and Fig. 6.34c have almost the same composition, even though one case is a realistic model and the other is nonphysical. The SuperFGD thus opens the possibility to perform reliable, multi-differential analyses, using STVs, which are not possible with the current ND280 detector particle detection thresholds. This has positive consequences both for cross-section analyses and directly for the oscillation analysis. Cross-section analyses will be able to perform more reliable cross-section measurements and discriminate between different nuclear models. The increased statistics, as well as the addition of proton variables to constrain neutrino interactions systematics, will help lower current systematic uncertainties.

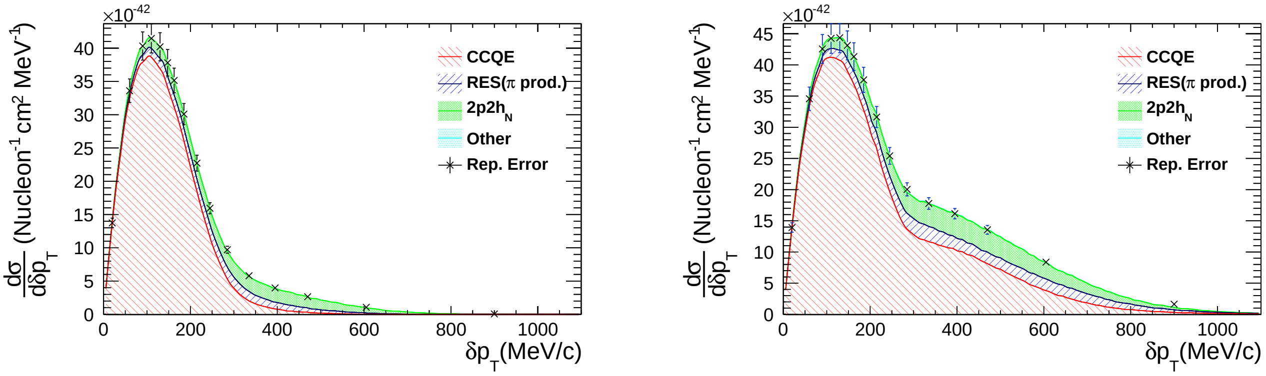

(a) LFG - Low $\delta\alpha_{\mathrm{T}}$ (b) LFG - High $\delta\alpha_{\mathrm{T}}$

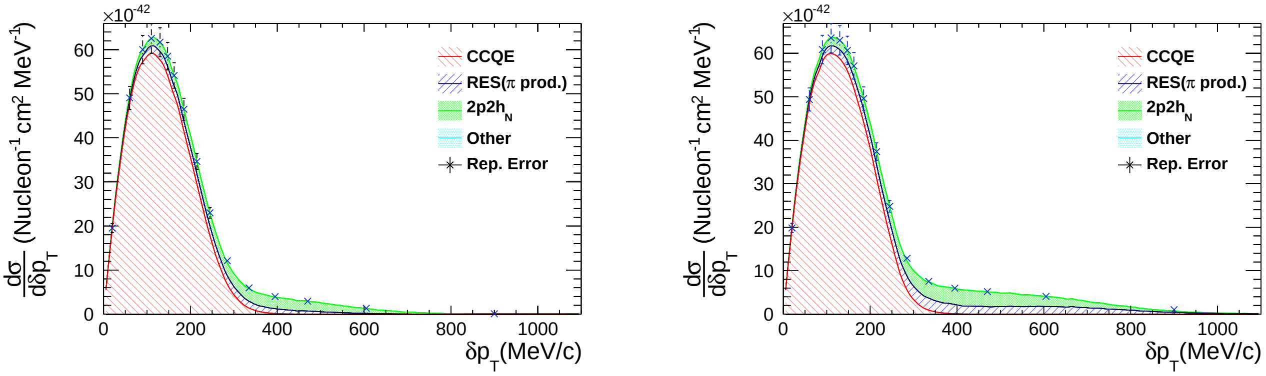

(c) LFG no FSI - Low $\delta\alpha_{\mathrm{T}}$ (d) LFG -no FSI - High $\delta\alpha_{\mathrm{T}}$

Figure 6.34: δp_{T} distributions broken down by interaction modes in different regions of $\delta\alpha_{\mathrm{T}}$. The upper row shows the sample which has no FSI processes, whereas the bottom row show a realistic LFG model.

6.2.2 Neutron measurement potential with the SuperFGD

A novel way in which the SuperFGD can help with the energy reconstruction is through the isolation of a sample with a low amount of nuclear effects. For neutrino interactions, STV information can be used in various ways to control the relative amount of nuclear effects. For anti-neutrino CCQE interactions, the situation is different: a typical CCQE anti-neutrino interaction is of the form $\bar{\nu}_\mu + p \rightarrow \mu^+ + n$, where p and n denote a proton and a neutron. There are no final state protons, but rather neutrons, which are notoriously difficult to detect.

On the other hand, whereas for neutrino interactions the initial nucleon involved is a neutron, which is not stable as an isolated particle, the proton in anti-neutrino interactions can exist as a separate particle - a hydrogen atom. Hydrogen atoms are by definition free of nuclear effects, since there is no nuclear medium in which the proton is bound. Being able to isolate a sample of (anti-)neutrino interactions on hydrogen will thus allow perfect energy reconstruction, only affected by the intrinsic detector resolution.

The power of using STVs in the case of anti-neutrino interactions is shown in Fig. 6.35a, where a NEUT 5.4.0 simulation was produced using the T2K flux, and no detector resolution was applied. For anti-neutrino interactions on carbon, the δp_{T} distribution has a similar shape as that shown in Section 6.2. For interactions on hydrogen, however, a clear peak can be seen at $\delta p_{\mathrm{T}} = 0$, consistent with the definition of δp_{T}. By selecting an appropriate region of δp_{T}, a nuclear effect-free sample can be obtained. Fig. 6.35b shows the evolution of the reconstructed anti-neutrino energy with different cuts in δp_{T}. A nuclear effect-free samples is also obviously independent on the nuclear model used for simulation.

The main challenge in applying this method is being able to measure neutrons. The SuperFGD can be used to detect fast neutrons (100 MeV/c-1 GeV/c in momentum), thanks to its granularity and timing resolution. A neutron can be detected indirectly through secondary interactions it undergoes in the detector. An example of such a process is shown in Fig. 6.36. In Fig. 6.36, a neutron is created in an anti-neutrino interaction at time t_1 at the primary interaction vertex where also a muon is emitted. The created neutron, which has a high penetrating power, travels for a certain distance before scattering of another nucleus at time t_2. As a result of the second scatter, the neutron knocks out particles from the struck nucleus (typically a proton, or a light ion such as an alpha particle). The struck particle deposits its energy in the vicinity of the secondary vertex. The energy transferred by the neutron to the struck particle depends very weakly on the initial neutron energy.

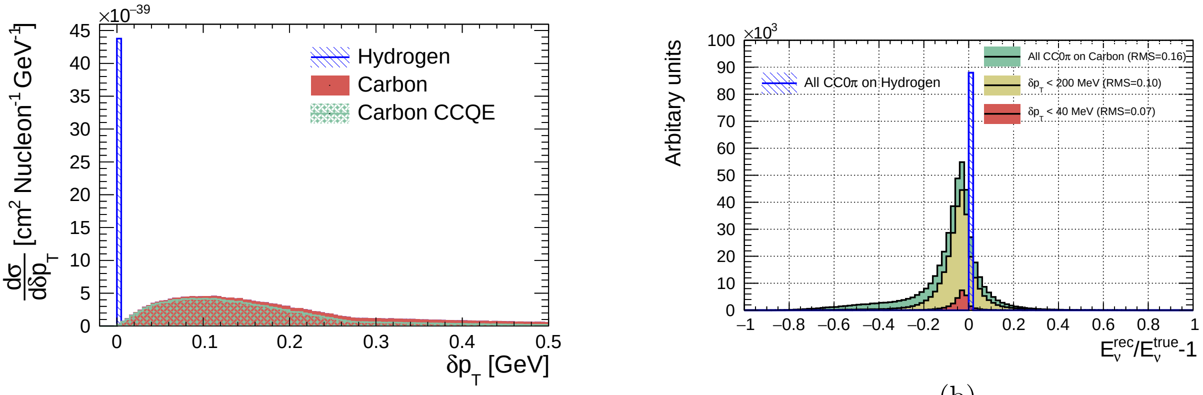

(a)

(b)

Figure 6.35: (a) Differential cross-section of anti-neutrino interactions on hydrocarbon (C and H nuclei), as a function of δp_{T}, separated by the interaction target. (b) Reconstructed anti-neutrino energy (E_ν^{rec}) bias with respect to the true anti-neutrino energy (E_ν^{true}) in the simulation. The shape of the spectrum is shown for different δp_{T} cuts.

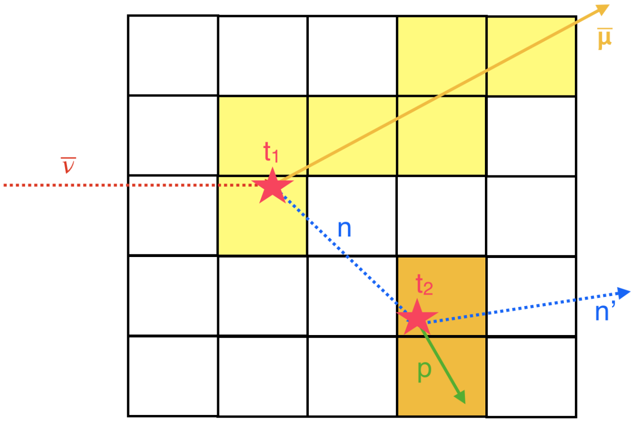

Figure 6.36: The process used to measure neutrons with the SuperFGD. The interaction vertices are represented with red stars. The charged particles resulting from both of these interactions produce hits in the SuperFGD cubes, shown by yellow and orange regions.

As a result, the neutron energy can be reconstructed using the time-of-flight (ToF) information between the primary and secondary vertices. The energy deposited by the recoil particle is used to tag the secondary vertex. This method has been used by the MINERνA collaboration [169], albeit with a two-plane readout. It is expected that the 3D readout of the SuperFGD will increase these capabilities.

To simulate the efficiency with which neutrons can be detected in the SuperFGD, a GEANT4 simulation of the full size detector[12] was done. An isotropic neutron particle gun was placed at the center of the detector. All relevant detector response effects, such as the light quenching in the plastic, the light capture efficiency and light attenuation in the fiber and the photo-detection efficiencies, are taken into account. The output of the detector response is given in terms of photo-electrons (p.e.). The neutron hits are grouped into a "neutron cluster" and a cut to omit all hits within a 3×3×3 cube volume around the neutron production point is applied to account for difficulties in separating neutron interaction-induced hits from those coming from the primary anti-neutrino interaction.

Fig. 6.37 shows the efficiency of detecting a neutron in the SuperFGD as a function of its kinematics, yielding a total integrated detection efficiency of 50%. High angle neutrons escape the detector faster because of the shorter size of SuperFGD in the vertical direction, and therefore have a lower detection efficiency. For simplicity, we consider a 2×2×2 m^3 detector in the following studies, which is equivalent to the first and last $\cos\theta_{neutron}$ bins in Fig. 6.37 for a cube detector and using an isotropic particle gun. The integrated efficiency for such a detector is of 71%.

The resolution on the reconstructed neutron kinetic energy depends on the timing resolution of the detector and the distance travelled by the neutron between its production point and its first interaction ("lever-arm"). Simulations were made with two different timing resolution assumptions. The timing resolution for a single WLS fiber is of 0.95 ns (as presented in Section 6.1.2), and is improved when considering the effect of multiple fibers used in the readout. As such, a possibility for the timing resolution σ_t^{ly} is:

$$\sigma_t^{ly} = \left\{0.95 \text{ ns}/\sqrt{3}\right\} \cdot \sqrt{40 \text{ PE/LY}}, \quad \sigma_t^{ly} > 200 \text{ ps} \qquad (6.10)$$

---

[12] The full SuperFGD size is 2×0.6×2 m^3.

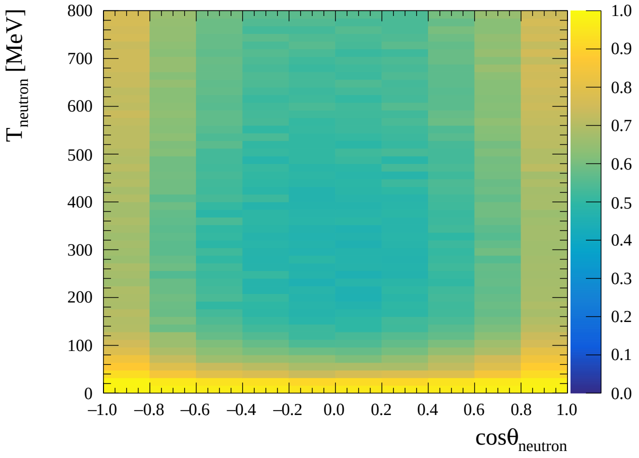

Figure 6.37: Neutron detection efficiency as a function of neutron kinetic energy ($T_{neutron}$) and direction ($\cos\theta_{neutron}$) in the full size SuperFGD simulation.

in which the 0.95 ns single-fiber time resolution is divided by $\sqrt{3}$ on account of three fibers being used in the 3D readout. The resolution is then weighted by the ratio of the total light yield in the cluster (LY), in units of p.e., divided by 40 p.e., which is the light yield of a single readout channel for a MIP crossing one cube. A more conservative time resolution σ_{ch}^{ly} can be obtained using the following equation:

$$\sigma_{ch}^{ly} = \left\{ 0.95 \text{ ns}/\sqrt{\#\text{channels}} \right\}, \quad \sigma_{t}^{ch} > 200 \text{ ps} \tag{6.11}$$

in which the 0.95 ns resolution is weighed by the number of readout channels that measured more than one p.e.. Both timing resolutions also require that the measured light yield occur within 200 ps of the neutron interaction, and both are artificially limited to a lower value of 200 ps to effectively simulate an arbitrary limitation due to some front-end electronics sampling rate. Both Eq. (6.10) and Eq. (6.11) are used in simulations.

These timing resolutions apply to the t_2 time in Fig. 6.36. The resolution on t_1 is neglected in this study, as it is assumed that the muon track produced at the primary vertex will allow a precise determination of the primary vertex time.

An additional step to improve the neutron kinetic energy resolution is to select tracks which have travelled a large enough distance between the neutron production point and the first neutron interaction - this is referred to as a “lever-arm cut”. Fig. 6.38 shows the evolution of the resolution on the neutron kinetic energy for different lever-arm cuts and time resolution assumptions. The neutron kinetic energy can be measured with a resolution between 10% and 20% for energies up to about 300 MeV. To study the impact on the anti-neutrino energy reconstruction, a NEUT 5.4.0 simulation was produced using an LFG model [85] for CCQE interactions, and the nominal model used in the oscillation analysis Section 3.3.2 for other interactions. A sample of CC0π anti-neutrino interactions was selected and an additional threshold on the muon momentum was applied at 100 MeV/c (to represent the SuperFGD thresholds). The kinematics of the neutrons from such processes are then smeared according to the neutron kinetic energy resolution obtained via the GEANT4 simulation. Only the highest-momentum neutrons are considered, if more than one is present in the simulated event. For each neutron, its travelled distance before the first interaction is also stored. An additional 4% smearing on the muon momentum and a 1° smearing on the muon angle were applied.

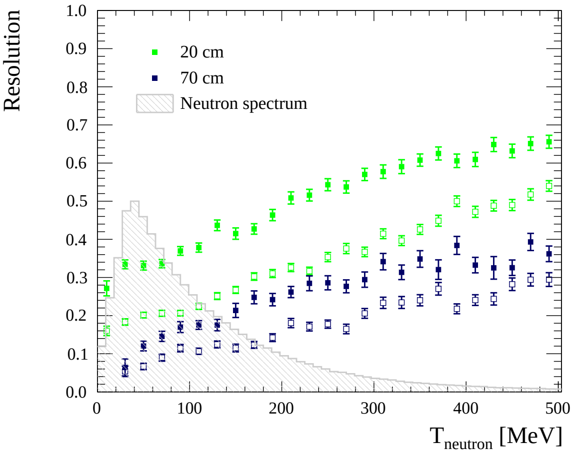

Figure 6.38: Neutron kinetic energy resolution as a function of its kinetic energy, for different time resolution assumptions and lever-arm cuts. The filled markers apply the timing resolution according to Eq. (6.11), and hollow markers use Eq. (6.10). Lever-arm cuts of 20 cm (green) and 70 cm (blue) are shown, corresponding to the rejection of events with a travelled distance before the first interaction of less than the lever-arm cut value. The grey distribution in the background shows the NEUT 5.4.0 neutron spectrum shape using the T2K anti-neutrino flux, for CC0π interactions, with the efficiencies from Fig. 6.37 applied.

After applying the detector smearing, the STVs can be computed. The relevant variable to consider in order to separate interactions on carbon and hydrogen is δp_{T}, as a peak towards low δp_{T} values is expected. Fig. 6.39 shows the δp_{T} distribution after applying the detector smearing described above. A clear peak can be seen for hydrogen events. The goal of the study is to obtain a sample which is nuclear effect-free (as is the case for interactions on hydrogen), or minimally influenced by nuclear effects (as is the case for low δp_{T} carbon interactions). The strategy to do this is to select events below a certain δp_{T} threshold. The obtained sample has to have a good purity of hydrogen interactions, while maintaining an adequate efficiency. Several δp_{T} cuts and lever-arm cuts were considered.

The optimization process is shown in Fig. 6.40. The "hydrogen purity" is computed as the fraction of selected interactions[13] below a δp_{T} threshold which actually occur on hydrogen nuclei. The "hydrogen efficiency" is defined as the number of selected interactions which occur on hydrogen divided by the total number of interactions on hydrogen. It was found that the optimal δp_{T} cut is of 40 MeV/c. It is interesting to note in Fig. 6.40 that increasing the lever-arm cut significantly worsens the efficiency of the selection (as more events are rejected), but it does not improve the purity for a fixed δp_{T} cut value. A stronger lever-arm cut improves the neutron kinetic energy resolution as seen in Fig. 6.38, but as a consequence it also selects faster neutrons, which means they have smaller times-of-flight for the same travelled distance. A 10 cm lever-arm cut was chosen for the rest of the studies.

For a 40 MeV/c δp_{T} cut and a 10 cm lever-arm cut, a purity of 61% and an efficiency of 22% can be expected. This corresponds to approximately 988 anti-neutrino interactions with either hydrogen or carbon per ton of detector mass per 10^{21} POT. Assuming that during T2K-II 8×10^{21} POT are

---

[13] The δp_{T} cut selects interactions with occur on hydrogen and carbon nuclei.

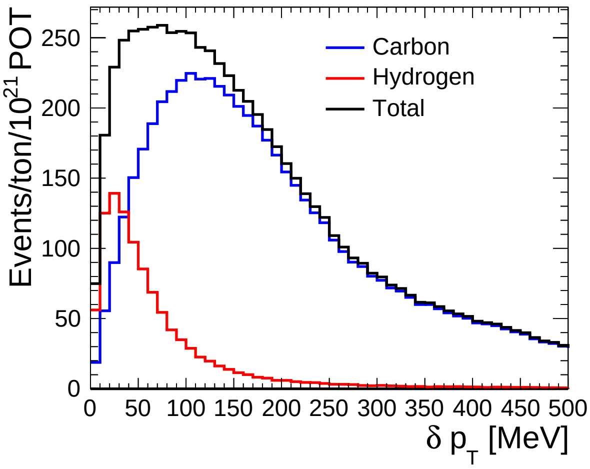

Figure 6.39: δp_{T} distribution for a 10 cm lever-arm cut and using the time resolution in Eq. (6.10). The total (black) distribution is shown, and separated by interaction target - carbon (blue) and hydrogen (red). The event rate is expressed per ton of detector mass and per $10^{2}1$ POT for scalability.

collected in anti-neutrino mode (half of the expected POT), a SuperFGD of two tons would expect to collect a sample of ∼15800 hydrogen-enriched events. For reference, the current FGD1+FGD2 antineutrino CC0π samples contain a total of ∼16600 events. The events selected as a result of

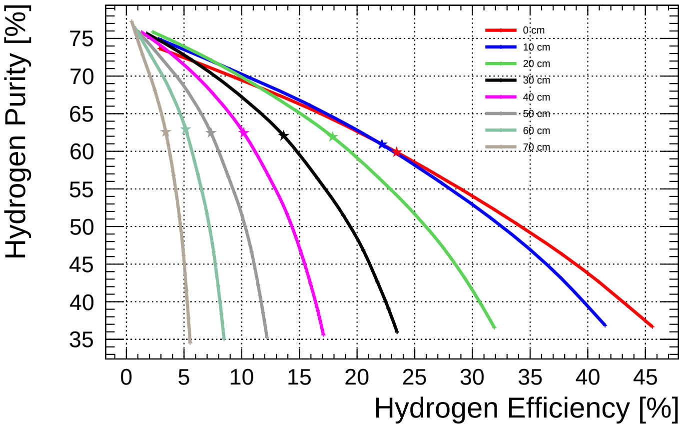

Figure 6.40: The antineutrino hydrogen purity vs efficiency for different δp_{T} and lever-arm cuts. The first (top left) marker on each line corresponds to a 10 MeV/c cut and then the star corresponds to the chosen δp_{T} cut of 40 MeV/c. Each line corresponds to a different lever-arm cut and is made using Eq. (6.10) to determine the time resolution.

the 40 MeV/c δp_{T} cut and the 10 cm lever arm cut are then used to compute the reconstructed anti-neutrino energy. Fig. 6.41 shows the evolution of the energy resolution before (Fig. 6.41a) and after (Fig. 6.41b) the optimal cuts described above. When no cuts are applied, energy resolution is of 15%, and is reduced to 7% after applying the cuts[14]. In Fig. 6.41a, a secondary distribu-

---

[14] A similar resolution is achieved using both Eq. (6.10) and Eq. (6.11) for the time resolution.

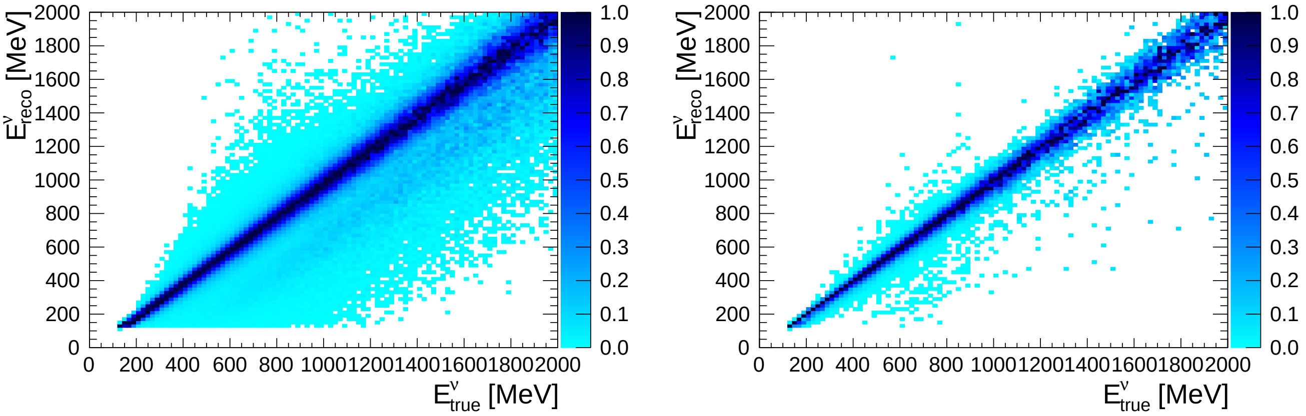

(a) No cut

(b) With 40 MeV/c δp_{T} cut

Figure 6.41: Reconstructed anti-neutrino energy (E^{ν}_{reco}) as a function of true anti-neutrino energy (E^{ν}_{true}), before (a) and after (b) the δp_{T} cut. The distributions are normalized column-wise to the largest entry per column.

tion can be seen weakly alongside the main distribution - this secondary population corresponds to non-quasi-elastic events which contaminate the CC0π samples, such as 2p2h events. When applying the δp_{T} cut, this population is completely removed. This method of improving the energy reconstruction is robust under nuclear ground state model variations and poorly constrained nuclear effects. Fig. 6.42a shows that the energy resolution is reduced by a similar amount, regardless of the nuclear ground state model used[15]. Some model dependence can still be seen in the peaks of the bias distributions, due to the carbon events which contaminate the samples. The impact of 2p2h interactions was also studied in the following way: the nominal 2p2h model used in NEUT (by Nieves et al. [94]) was used to gauge a reference amount of 2p2h interactions. The amount of 2p2h interactions was then artificially enhanced or suppressed (from 0% to 200% of the original amount[16]), and the bias on the neutrino energy was computed. The results are shown in Fig. 6.42b - unlike when comparing different ground state models, the resulting energy distributions after the cuts are virtually indistinguishable. This confirms that the method described in this analysis is capable of removing one of the dominant sources of nuclear effects, even in interactions on carbon targets.

A test-beam study of a SuperFGD prototype was performed using a neutron beam at Los Alamos National Laboratory. The aim of this test is to determine the actual neutron detection capabilities of the SuperFGD and use the data to construct improved simulations. The analysis of the data is ongoing. The results of the neutron tagging abilities of the SuperFGD, in a general context, were published in [170].

---

[15] The same models as in Section 6.2 were compared here, namely a Local Fermi Gas model [85], a Relativistic Fermi Gas model [90], and the Spectral Function model developed by Benhar et al. [86].

[16] A two-fold enhancement actually corresponds roughly to the strength of 2p2h interactions in the Martini et al. model [95].

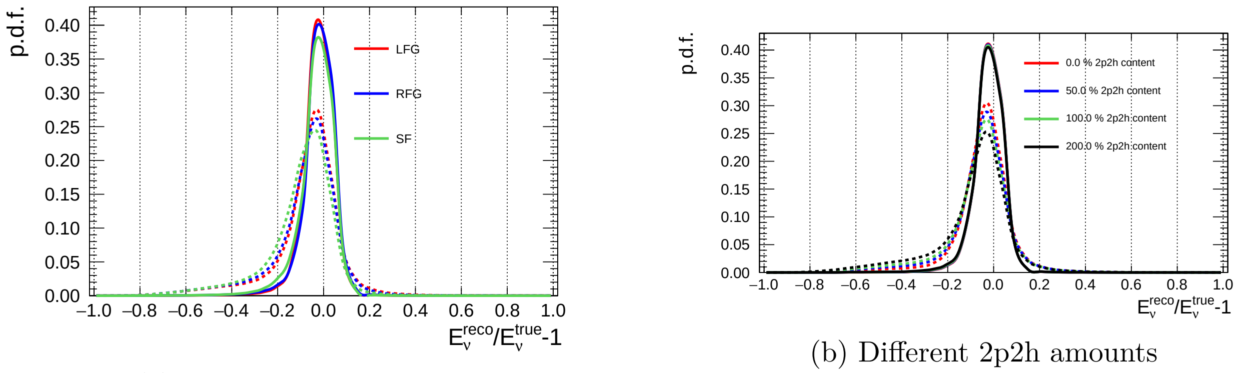

(a) Different nuclear models

(b) Different 2p2h amounts

Figure 6.42: Reconstructed energy bias, before (dashed lines) and after (solid lines) applying the δp_{T} and lever arm cuts. (a) Comparison of different nuclear ground state models used in the NEUT simulation. (b) Comparison of the LFG ground state model with varying 2p2h event fractions.

6.3 Perspectives

Further studies to include these capabilities in the T2K OA are on-going. Preliminary and conservative estimates based on these studies show that this corresponds to an improvement of a factor 2.5-3 (2) on the constraints of systematic uncertainties for neutrino (antineutrino) with respect to the performances of present ND280 design for the same POT (as will be shown in Section 7.3).
The three new detectors for the ND280 Upgrade are scheduled to be installed at J-PARC in 2022. In addition to opening the way to numerous possibilities in terms of physics at T2K, the ND280 Upgrade and its technologies have applications beyond the scope of T2K and T2K-II.
The DUNE experiment is considering a near detector which is conceptually similar to the SuperFGD+TPC ensemble [171]. The impact of neutron detection capabilities for neutrino energy reconstruction have a direct application for the DUNE oscillation physics program [170].
The entire T2K near detector complex will also serve as the near detector for the future Hyper-Kamiokande experiment. The requirements in terms of particle thresholds and detector acceptance have thus been established while also keeping in mind the need to enable systematic error reduction for the Hyper-Kamiokande oscillation analysis.

Chapter 7

CP violation with the Hyper-Kamiokande Experiment

Building up on the success of the T2K and Super-Kamiokande experiments, the Hyper-Kamiokande (HK, Hyper-K) experiment was proposed as a a natural successor [10]. The Hyper-K experiment is based on the same technology as the Super-Kamiokande experiment, i.e. it is a water Cherenkov neutrino detector. As such, its physics program spans a wide range:

- Long-baseline neutrino oscillation measurements
- Atmospheric neutrino oscillation measurements
- Proton decay
- Astrophysical neutrino measurements.

This chapter focuses on the long baseline neutrino oscillation program of Hyper-K. Section 7.1 presents an overview of the Hyper-K long baseline neutrino oscillations program. Section 7.2 provides a description of the Hyper-Kamiokande detector itself, along with its expected performance. The near detectors to be used in the HK long-baseline program are described in Section 7.3. Section 7.4 provides an overview of the sensitivity of the HK experiment to CP violation and precision measurements of oscillation parameters. Finally, Section 7.5 offers some perspectives on the future of the Hyper-K experiment.

7.1 The Hyper-Kamiokande Long-Baseline Neutrino Program

The Hyper-Kamiokande detector is a water Cherenkov neutrino detector, which will be built under Mt. Nijugo, in the Tochibora mine in the Gifu prefecture of Japan. Hyper-K will be located at the same off-axis angle as Super-K with respect to the J-PARC neutrino beam. As such, the Hyper-K detector will be able to serve a long-baseline neutrino oscillations program in much of the same way as Super-Kamiokande is serving today in the T2K experiment. In addition, the J-PARC beamline will be upgraded, obtaining a beam power of 1.3 MW, which will enable unprecedented statistics. Due to the large size of the Hyper-K detector and its improved detection techniques (as will be detailed in Section 7.2), the long-baseline neutrino oscillations program with the Hyper-K detector will benefit from an improved sensitivity to neutrino oscillation parameters, inaccessible to the current T2K experiment, most notably enabling a 5σ sensitivity to CP violation discovery for a large portion of δ_{CP} values.

Hyper-K will also be used to study atmospheric neutrino oscillations, which are produced isotropically in the atmosphere and thus span a wide range of angles and distances through the earth's crust. A longer baseline through the earth means that neutrino oscillations will be more affected by matter effects in the earth, which offer sensitivity to the mass hierarchy. The 295 km baseline between Tokai (where the J-PARC accelerator complex is located) and the Hyper-K detector is relatively short compared to the baselines of experiments such as DUNE or NOνA. The accelerator neutrino physics program of Hyper-K on its own will not have an improved sensitivity to the mass hierarchy. However, a combined fit of accelerator neutrinos produced at J-PARC, along with a sample of atmospheric neutrinos, will make it possible to determine the mass hierarchy, if other experiments will not have determined it before.

7.2 The Far Detector: Hyper-Kamiokande

The Hyper-Kamiokande detector consists of a cylindrical tank filled with pure water. A schematic representation of the tank is shown in Fig. 7.1. The size of the structure enclosing the tank is of 78 m in height and 74 m in diameter, with the actual water tank having a 60 m height. Hyper-K will employ the Cherenkov ring imaging technique (Section 2.3) by detecting the Cherenkov light emitted by particles with the help of photo-multiplier tubes (PMTs). As for Super-Kamiokande, the interior of the HK tank (Inner Detector, ID) will be lined with a dense array of 40,000 50 cm ⌀ PMTs, whose role is to collect the Cherenkov light emitted by particles produced in neutrino interactions. The outer detector (OD) will be lined with 6,700 20 cm ⌀ PMTs, whose role is to

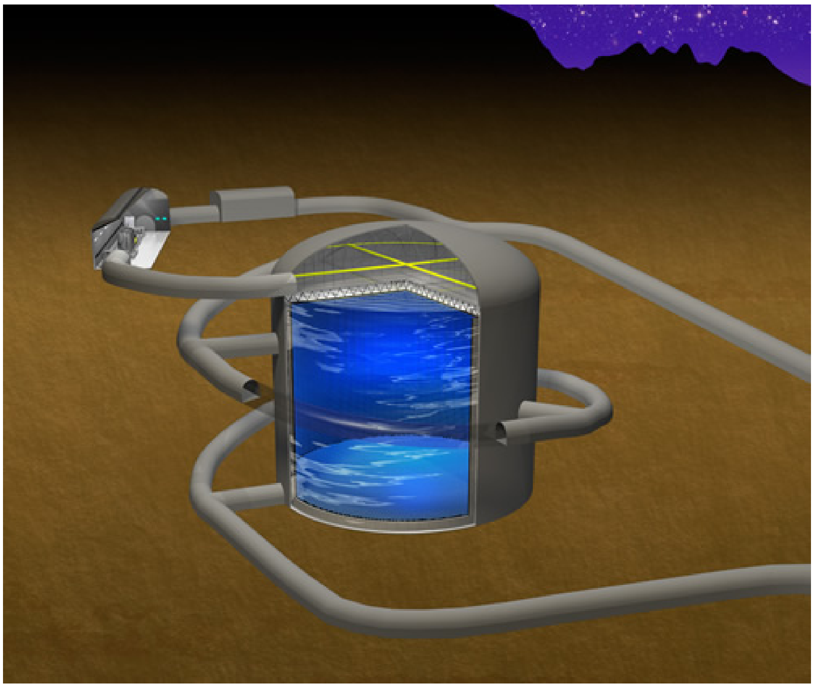

Figure 7.1: Schematic representation of the Hyper-Kamiokande detector. Image credit: http://www.hyper-k.org.

reject background events.

Alternative designs are also under investigation, with 20000 PMTs and a few thousands of multi-PMTs (modules composed of an array of small 3” PMTs), as well as the possibility to load the detector water with Gadolinium (Gd) in order to tag neutrons.

Neutrino detectors are generally located deep underground, in order to shield the inside of the detector from cosmic ray backgrounds. Hyper-K will be located under an overburden of 650 meters of rock or 1,750 meters-water-equivalent (m.w.e.).

The water filling the detector plays two roles - it provides a target for neutrino interactions, and a nucleon decay source. Rare events such as neutrino interactions need a very large interaction mass to accumulate sufficient statistics - for instance, in order to reach a precision of the order of a few % on δ_{CP}, an order of 1,000 electron neutrino signal events are needed, which corresponds to a target mass of the order of 100 kton, assuming a beam power of 1.3 MW. The total (fiducial) volume of the Hyper-K detector will be of 258 (187) kton, meeting this requirement.

For its long-baseline (LBL) neutrino oscillation physics program, Hyper-K plans to use the J-PARC neutrino beam facility currently used by the T2K experiment, described in Section 2.1. Hyper-K will be located at a 2.5° off-axis angle with respect to the J-PARC neutrino beam. As described in Chapter 6, the J-PARC neutrino beamline will be upgraded to enhance the amount of statistics available for both T2K and Hyper-K [151]. The beam power is expected to reach at least 1.0 MW by 2026, and operate stably at 1.3 MW starting 2028 (Fig. 6.1).

Assuming a beam power of 1.3 MW, 10 years of data taking, the oscillation parameter values in Table 7.1 and a $\nu : \bar{\nu}$ ratio of 1:3 (i.e. three times as much time spent taking data in $\bar{\nu}$ beam mode than in ν beam mode), the expected number of events in the appearance and disappearance channels at HK was simulated using NEUT for the neutrino interactions and GEANT3 for the Hyper-K detector response (assuming similar efficiencies to those of Super-Kamiokande). The same selections as described in Section 3.2.4 were applied. For δ_{CP} measurements, the signal samples are single-ring $\nu_e/\bar{\nu}_e$ samples, whose expected event rate is shown in Table 7.2.

Parameter	$\sin^2 2\theta_{13}$	δ_{CP}	$\sin^2 \theta_{23}$	Δm^2_{32}	mass hierarchy	$\sin^2 2\theta_{12}$	Δm^2_{21}
Value	0.10	0	0.50	2.4×10^{-3} eV^2	Normal	0.8704	7.6×10^{-5} eV^2

Table 7.1: Oscillation parameters used in the HK Design Report [10].

		signal		BG						Total
		$\nu_\mu \to \nu_e$	$\bar{\nu}_\mu \to \bar{\nu}_e$	ν_μ CC	$\bar{\nu}_\mu$ CC	ν_e CC	$\bar{\nu}_e$ CC	NC	BG Total	
ν mode	Events	1643	15	7	0	248	11	134	400	2058
	Eff.(%)	63.6	47.3	0.1	0.0	24.5	12.6	1.4	1.6	—
$\bar{\nu}$ mode	Events	206	1183	2	2	101	216	196	517	1906
	Eff. (%)	45.0	70.8	0.03	0.02	13.5	30.8	1.6	1.6	—

Table 7.2: The expected number of $\nu_e/\bar{\nu}_e$ candidate events and efficiencies with respect to FCFV events. Normal mass hierarchy with $\sin^2 2\theta_{13} = 0.1$ and δ_{CP} =0 are assumed. Background is categorized by the flavor before oscillation.

Table 7.2 shows that the dominant background in ν_e samples comes from the intrinsic $\nu_e/\bar{\nu}_e$ component of the beam. The $\nu_e/\bar{\nu}_e$ event rate as a function of reconstructed energy (assuming CCQE kinematics, Eq. (2.10)) is shown in Fig. 7.2.

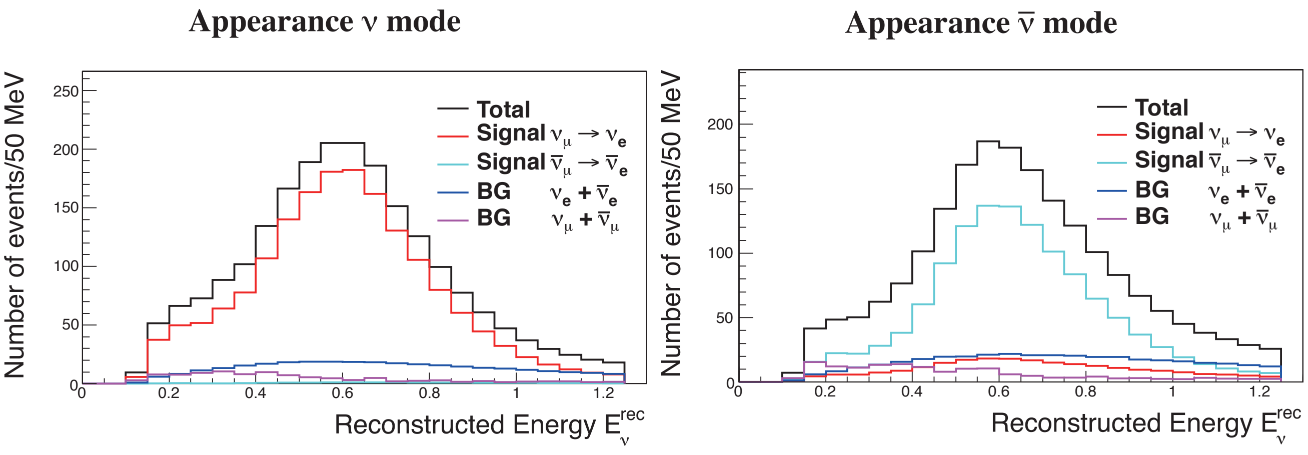
Appearance ν mode

Appearance ν̄ mode

(a) Neutrino beam mode

(b) Anti-neutrino beam mode

Figure 7.2: Reconstructed neutrino energy distribution of the ν_e candidate events. Compositions of appearance signal, $\nu_\mu \rightarrow \nu_e$ and $\bar{\nu}_\mu \rightarrow \bar{\nu}_e$, and background events originating from $(\nu_\mu + \bar{\nu}_\mu)$ and $(\nu_e + \bar{\nu}_e)$ are shown separately. Taken from [10].

Similarly, for the disappearance channel, the signal is formed by signal-ring $\nu_\mu/\bar{\nu}_\mu$ events. The expected event rates are summarized in Table 7.3 and Fig. 7.3.

		ν_μCCQE	ν_μCC non-QE	$\bar{\nu}_\mu$CCQE	$\bar{\nu}_\mu$CC non-QE	$\nu_e + \bar{\nu}_e$ CC	NC	$\nu_\mu \rightarrow \nu_e$	total
ν mode	Events	6043	2981	348	194	6	480	29	10080
	Eff. (%)	91.0	20.7	95.6	53.5	0.5	8.8	1.1	—
$\bar{\nu}$ mode	Events	2699	2354	6099	1961	7	603	4	13726
	Eff. (%)	88.0	20.1	95.4	54.8	0.4	8.8	0.7	—

Table 7.3: The expected number of $\nu_\mu/\bar{\nu}_\mu$ candidate events and efficiencies (with respect to FCFV events) for each flavor and interaction type.

In neutrino mode, the purity of ν_μ CC events is of 89% for energies below 1.5 GeV. In anti-neutrino mode, the purity is lower because of the significant contribution of wrong-sign ν_μ CC events.

At this level of statistics, the signal ν_e samples have enough statistical power to discriminate between different values of $\delta_{\rm CP}$. Fig. 7.4 shows the event rate predictions for different values of $\delta_{\rm CP}$. It thus becomes possible not only to distinguish between the two CP-violating cases, but also to distinguish CP-conserving values of $\delta_{\rm CP}$ of 0 and 180°. Although Hyper-K will be able to accumulate enough statistics, the impact of systematic errors will become a limiting factor for its physics program. Fig. 7.5 shows the impact of systematic parameters on the exclusion of CP conserving values at Hyper-K as a function of time. Using accelerator neutrinos alone, and assuming the mass hierarchy is known, CP violation can be established in the first few years of Hyper-K, but the necessary time depends on the size of the systematic uncertainties assumed in the model.

7.3 Near Detectors

As seen in the previous section, the statistical power of HK is unprecedented. The LBL neutrino oscillations program at Hyper-K will be carried out following much of the same philosophy as the

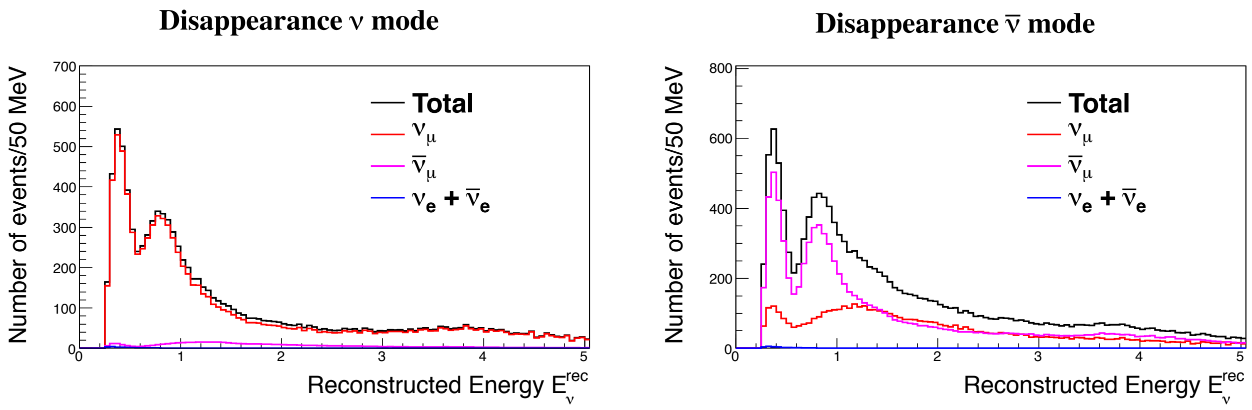

(a) Neutrino beam mode.

(b) Anti-neutrino beam mode.

Figure 7.3: Reconstructed neutrino energy distribution of the $\nu_\mu/\bar{\nu}_\mu$ candidate events after oscillation. Taken from [10].

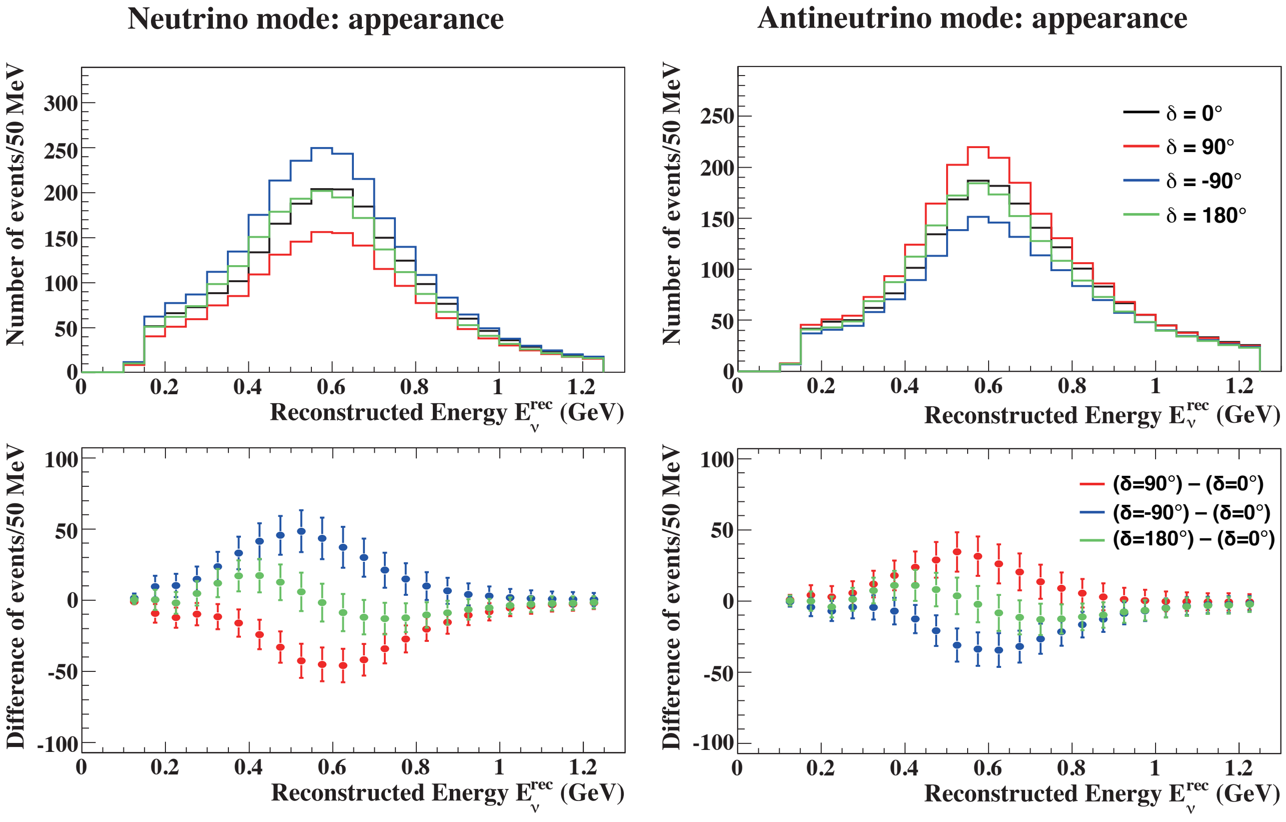

(a) Neutrino beam mode.

(b) Anti-neutrino beam mode.

Figure 7.4: Reconstructed neutrino energy distribution for several values of δ_{CP}. $\sin^2 2\theta_{13} = 0.1$ and normal hierarchy is assumed. The difference of the reconstructed neutrino energy distribution from the case with $\delta_{CP} = 0°$ is shown below each distribution. The error bars represent the statistical uncertainties of each bin.

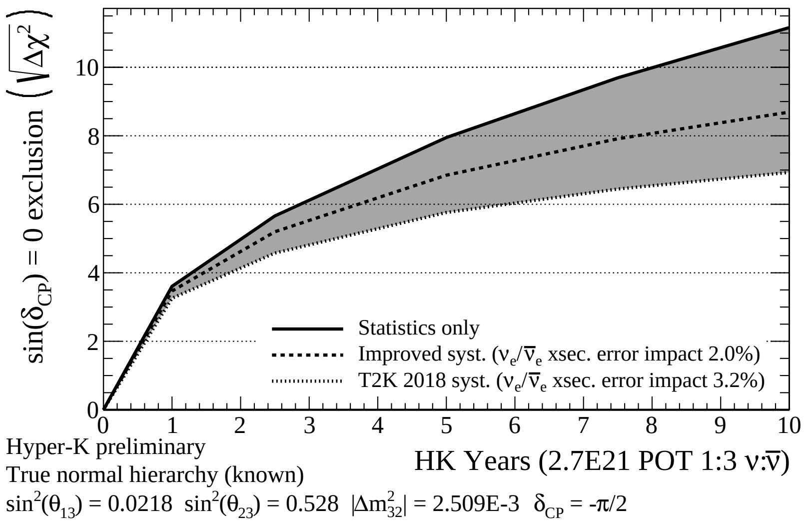

Figure 7.5: Hyper-K sensitivity to exclude CP conserving values, assuming no systematic errors (statistical error only, solid line), the systematic errors obtained in the 2018 T2K oscillation analysis [100] (dotted), and an improved systematic error model, described in the Hyper-Kamiokande Technical Design Report [10] (dashed).

T2K oscillation analysis. In particular, this implies constraining the systematic errors in Hyper-K data from oscillated beam neutrinos with unoscillated spectrum data close to the neutrino beam production point. As shown in Chapter 5, the T2K near detector data in its current form reduces the systematic uncertainties across signal samples at Super-Kamiokande from the level of 15% to the level of 4%.

However, using this strategy has its limitations. This method relies on the use of models for the neutrino flux and neutrino interaction model. Effects which are not correctly modelled may introduce biases in the oscillation parameters measurements. In addition, particularly in the case of neutrino interactions, no current model is capable of describing the full range of know interactions. Currently, only lepton information (from muons) is used at ND280, in order to match the observables accessible to the far detector. However, adding information from final state hadron variables (protons, neutrons and pions) in the near detector analysis would help disentangle flux and cross-section effects. For instance, flux and cross-section effects may be indistinguishable in muon kinematics, but have a different impact on the hadronic energy.

In addition, the neutrino energy spectra are different between the near detector and the far detector - the energy extrapolation needs to be modelled precisely. The targets (carbon versus oxygen) and neutrino species (ν_μ versus ν_e) also differ between the near and far detectors and thus the near-to-far detector extrapolation also relies on the use of models to build the far detector prediction.

As was seen in the T2K oscillation analysis, the dominant source of systematic errors comes from the neutrino interaction model. With the increase of statistics expected at Hyper-K, the systematic errors will become a limiting effect in the determination of CP-violation.

Following these considerations, the facility to monitor the event rate before oscillations needs to meet the following requirements:

- Precisely monitor the neutrino flux, composition and beam position, with an on-axis detector.
- Offer an image of the final state of neutrino interactions which is as complete as possible: this includes the possibility to precisely measure final state hadrons.

- Have an angular acceptance which matches that of the far detector - Hyper-K will have a 4π acceptance.
- Have the ability to measure interactions on water targets.
- The near detector facility must be able to measure electron neutrino cross-sections using the intrinsic ν_e component of the beam.

No single detector technology can achieve all of these goals, so the strategy for the Hyper-K LBL neutrino oscillations program is to use three near detectors.
The first one is the existing INGRID detector (Section 2.2.1) to monitor the beam position and precisely measure the neutrino flux.
The remaining requirements will be met by two detector facilities: the ND280 detector complex, following the upgrade described in Chapter 6, and an intermediate water Cherenkov detector (IWCD), placed at ∼1 km from the beam source, which will have the possibility to take data at various off-axis positions. These two detectors will be briefly described in this section.

7.3.1 Upgraded ND280

The upgrade of the ND280 detector is described in Chapter 6. A notable feature of the ND280 detector is that it is a magnetized detector, and will be the only such detector to be used in the Hyper-K LBL program. This is an essential feature, since it makes it possible to distinguish final state particles by their charge, which is needed to monitor the wrong-sign component of the neutrino flux.
The main strength of the upgraded ND280 detector for the Hyper-K LBL program lies in its low particle detection thresholds and increased angular acceptance. As shown in Section 6.2, the Super-FGD has a low threshold for proton detection, opening the way for more exclusive measurements of final state particles. This will also address the main limitation in a model-dependent oscillation analysis such as done in T2K today, namely the limited capability of constraining nuclear effects by using exclusively outgoing lepton kinematics information.

As explained in Section 6.2, nuclear effects bias the reconstructed neutrino energy, which needs to be precisely modelled in order to avoid biases on oscillation parameter measurements. In order to maximize the near detector resolution on the neutrino energy, one approach consists in exploiting the hadronic information made available at ND280 thanks to the upgrade. Information about final state protons gives access to a range of new and powerful variables to control nuclear effects: single transverse variables (STVs, described in Section 6.2), but also p_n, the reconstructed total momentum of the initial nucleon using muon and proton/neutron kinematics (introduced in [172]), and the sum of the muon and highest-momentum proton kinetic energies as an estimator for the neutrino energy ($E_{vis} = E_\mu + E_p$). An example illustrating the power of the E_{vis} variable to improve the reconstructed neutrino energy resolution can be seen in Fig. 7.6. In addition to improving the neutrino energy reconstruction, the variables made available though proton measurements can be used in a multi-dimensional analysis, as each type of variable is sensitive to different types of nuclear effects. For instance, p_n offers a direct probe of the Fermi motion of nucleons in the nucleus. The combination of E_{vis} and the reconstructed energy using the CCQE formula, E_{rec} makes it possible to identify non-QE events in CC0π samples, while $\delta\alpha_\mathrm{T}$ is sensitive to the presence of FSI. A large dimensionality of the analysis also requires enough statistics to populate a dense phase space using both muon and proton kinematic variables.

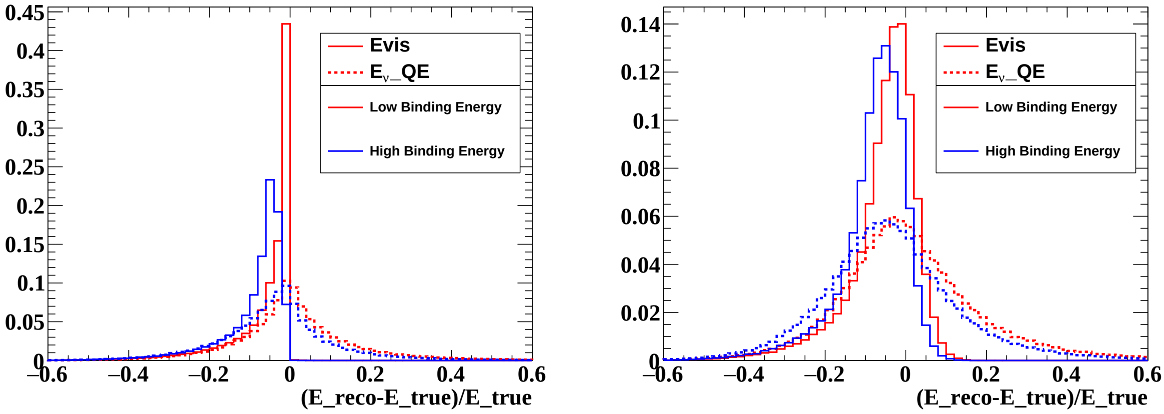

(a) (b)

Figure 7.6: Comparison of reconstructed neutrino energy using E_{vis} (solid lines) and the CCQE formula using only muon kinematics (dashed lines). The different line colors indicate different values for the binding energy - 15 MeV, "low" (35 MeV, "high") in red (blue). (a) Without detector smearing. (b) With SuperFGD smearing as described in Section 6.2.

A simple two-dimensional analysis using p_n and E_{vis} from CC0π samples can already offer insights on the sensitivity improvements that the upgraded ND280 detector can bring to a Hyper-K oscillation analysis.

Fig. 7.7 shows the evolution of the constraints on several systematic parameters affecting CC0π samples as a function of POT. With 20×10^{21} POT and assuming a ratio of $\nu : \bar{\nu}$ beam modes of 1:1, the CCQE systematic errors can be reduced at the level of 3%, 2p2h errors to the level of 5%, and the error on the binding energy[1] reduced to 1 MeV. Using the neutron detection capabilities of the SuperFGD (Section 6.2.2), a similar study can be performed for anti-neutrino events.

The preliminary expected systematic errors for 20×10^{21} POT are summarized in Table 7.4.

Parameter	ν mode	$\bar{\nu}$ mode
CCQE normalization	3.2%	4.6%
2p2h normalization	5%	10%
Binding energy	$<$ 1 MeV	1 MeV
Proton FSI	$<$ 1%	1%
Pion Absorption	4%	14%
Pion Background	5%	14%
Hydrogen normalization	—	5%

Table 7.4: Sensitivity to cross-section parameters using proton and lepton information with the ND280 Upgrade, with 20×10^{21} POT.

---

[1] Assuming a Spectral Function [86] nuclear ground state model.

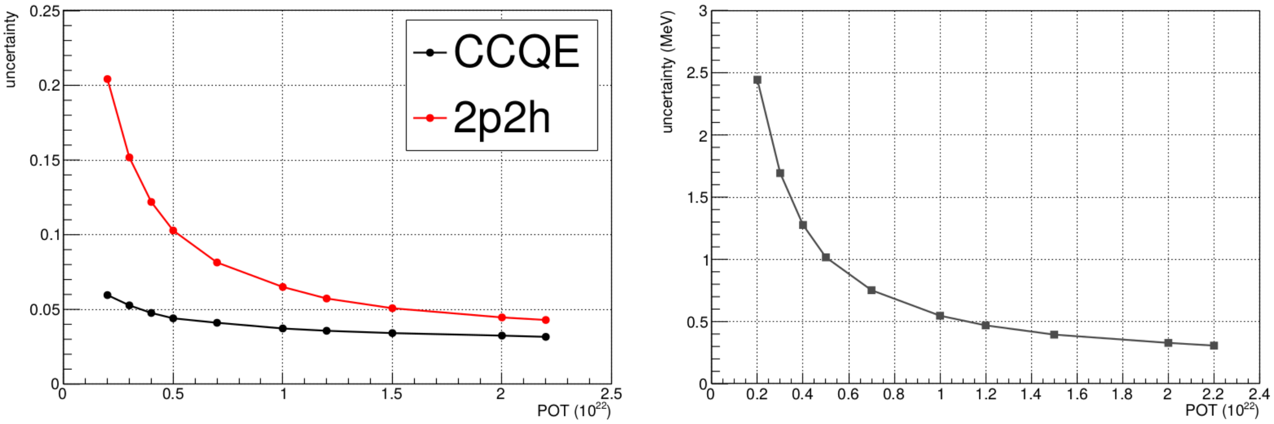

(a) (b)

Figure 7.7: Error reduction as a function of POT, for neutrino mode samples, as a result of a two dimensional p_n versus E_{vis} fit obtained with the ND280 upgrade expected performance. (a) Relative error reduction for CCQE and 2p2h components. (b) Absolute error reduction (in MeV) on the binding energy.

7.3.2 Intermediate Water Cherenkov Detector

The second near detector in the HK LBL physics program will be a water Cherenkov detector, placed at a distance of ∼1 km from the neutrino beam production point[2].

The Intermediate Water Cherenkov Detector (IWCD) design concept is shown in Fig. 7.8. The detector itself will be located in a 50 m shaft, filled with water up to the top of the instrumented detector region. The detector itself will be filled with ultra-pure water, which will constitute the interaction target for neutrino interactions, and will therefore match the target and detection technology at Hyper-K. The detector itself is buoyant, so it can span different positions in the shaft determined by the water level. The detector has a 10 m diameter, with an inner detector diameter of 8 m. Multiple detector heights have been studied, with heights ranging from 6 m to 10 m, depending on the chosen location and the expected event rate at this location. The inside of the detector is lined with photo-sensors following the “multi-PMT” concept. A multi-PMT sensor consists of an array of small PMT photo-sensors (3” ⌀) housed in a transparent, water tight pressure vessel along with readout electronics and monitoring devices. A schematic representation of a multi-PMT detector can be seen in Fig. 7.9. This type of design offers several advantages for a small-scale water Cherenkov detector. By replacing a single, large 20” PMT with an array of small 3” PMTs, the Cherenkov rings produced in the detector can be sampled with a much more efficient granularity. This is particularly important for a small-scale Cherenkov detector, as rings travel smaller distances compared to those produced in the Super-K or Hyper-K detectors, so a finer resolution is needed. In addition, housing multiple PMTs along with their readout electronics inside a single vessel reduces the issues related to water-proofing and cabling which arise from increasing the number of readout channels needed for a fine granularity. The dome of the PMTs will be made of acrylic, which is capable of withstanding the relatively low water pressure in the IWCD.

One of the main design features of the IWCD detector is its ability to move inside the shaft, thus spanning a range of off-axis angles with respect to the J-PARC neutrino beam. The measured

---

[2] Several locations are under consideration and are being investigated for their compatibility with the Hyper-K physics program.

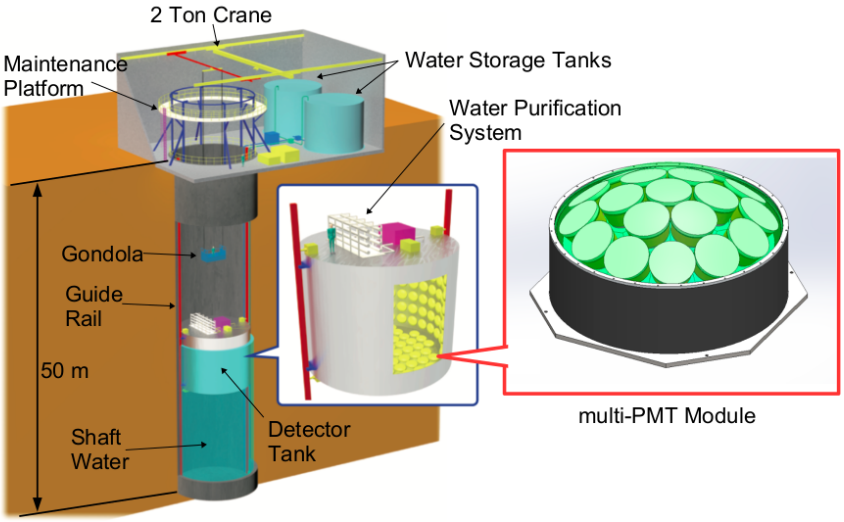

Figure 7.8: Schematic representation of the IWCD design.

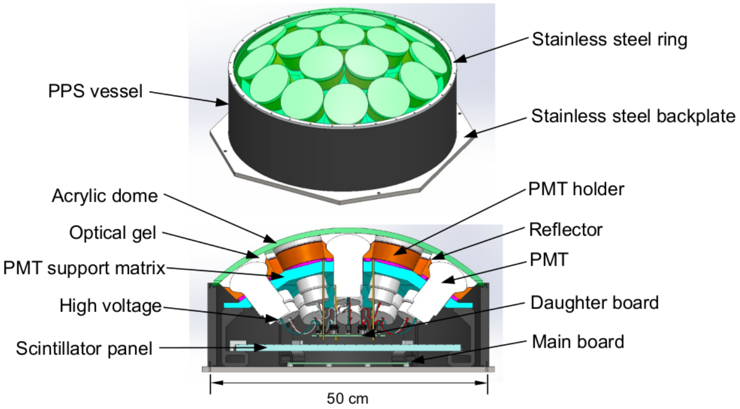

Figure 7.9: The design of multi-PMT modules, with labeled components.

spectra at different off-axis angles (OAA) can further be used in a linear combination which makes it possible to reproduce any flux energy shape: for instance very narrow (almost mono-energetic) energy fluxes can be built, or an energy spectrum reproducing the oscillated spectrum at Hyper-K. A functional form $G(E_\nu)$, can be defined as

$$G(E_\nu) = \sum_{i=1}^{N_{OAA}} A_i \Phi_i(E_\nu) \tag{7.1}$$

where N_{OAA} is the number of off-axis angles that the data is divided into, A_i are coefficients which weigh the predicted neutrino spectra $\Phi_i(E_\nu)$ at each off-axis position. This linear combination method is used to study measurements with narrow band beams (termed "pseudo-monochromatic"). Another advantage of this method is the fact that linear combinations of off-axis angles can be used to reproduce the energy spectrum observed at HK, after oscillation, thus reducing errors related to the extrapolation of the neutrino interaction model at different energies. The main challenge of this method is a precise determination of the off-axis angle and flux, since the neutrino flux changes with the angle according to the kinematic considerations described in Section 2.1.2.

The "pseudo-monochromatic" beams method will provide accurate measurements of ν_e cross sections. The IWCD will also be able to predict the intrinsic ν_e flux with 3% precision. The increased precision to the ν_e flux comes from the fact that the relative rates of ν_μ and ν_e events change as a function of the OAA. For instance, at larger OAA, the ν_e component of the beam increases. In addition, the possibility of moving on-axis makes it possible to increase the statistics for both ν_e and ν_μ measurements.

7.4 Sensitivities

The sensitivity of Hyper-K to neutrino oscillation measurements has to be evaluated before its operation. This exercise is needed to both gauge the capabilities of the experiment, but also to study the impact of different systematic errors on oscillation parameter measurements and inform the detector design.

7.4.1 Samples and Simulation

7.4.1.1 Beam Samples

The samples containing events from neutrinos coming from the J-PARC beam are the same as those used in the SK event selections described in Section 3.2.4. The NEUT event generator is used to model neutrino interactions, and the Hyper-K detector response is assumed identical to that of SK, using a GEANT3 simulation. The main difference with respect to the SK MC is that the Hyper-K beam samples are scaled to 10 years of Hyper-K data taking with a 1.3 MW beam, amounting to a total of 2.7×10^{22} POT.

7.4.1.2 Atmospheric Samples

For its atmospheric samples, Hyper-K used the SK atmospheric MC, which is scaled to the HK fiducial volume.

The atmospheric samples are separated into three categories: fully-contained (FC), partially-contained

(PC) and upward-going muons (UP-μ).

FC and PC events are neutrino events which occur inside the detector fiducial volume. If no signal is seen in the outer detector (OD), the event is classified as FC. If an additional signal is seen in the OD, the event is classified as PC. UP-μ events are neutrino events which have occurred in the rock surrounding the detector or in the OD water, and then travel upward through the detector.

After a number of reduction cuts (aiming to reduce background events), the FC samples are further divided based on the number of Cherenkov rings, the PID of the most energetic ring, the amount of visible energy (E_{vis}) and the number of decay electrons. The PC and UP-μ samples are categorized based on the stopping point of the muon inside the detector, into through-going (the muon does not stop in the detector) and stopping muon (the muon stops inside the fiducial volume). Finally, the UP-μ through-going samples are further divided based on whether the event produces an electromagnetic shower while traversing the FD into “showering” and “not showering”.

The main signal used in the atmospheric analysis to determine the mass hierarchy comes from FC, upward going electrons. The PC and Up-μ samples are background control samples.

Further details about the SK atmospheric selections can be found in [173].

7.4.2 Statistical Framework

In order to evaluate the sensitivity to oscillation parameters, the expected Hyper-K data is simulated by applying a set of “true” oscillation parameters. The obtained spectrum is then fit with a MC prediction, which may use the same oscillation parameters in the assumption (an Asimov fit), or a different set of oscillation parameters.

The flow of the process is as follows:

- A “true” spectrum is built using a certain combination of oscillation parameters
- An MC prediction is built without applying any oscillations.
- The uncertainties on each of the expected oscillation parameter values (priors) are used to build a multi-dimensional grid, in which each dimension corresponds to the range of an oscillation parameter, and is divided into equally spaced intervals spanning the parameter uncertainty.
- For each set of oscillation parameters in the grid, the unoscillated MC prediction is modified given the oscillation parameter combination.
- Each oscillated MC spectrum is adjusted to the “true” spectrum, by varying the event rate under the effect of parameters describing systematic effects related to the neutrino flux modelling, the detector response, and the neutrino interaction model, until a χ^2 test statistic is minimized (the fit and minimization procedure are described below). The best-fit set of systematic parameters is retained.
- This process is repeated at each oscillation parameter combination in the grid. Once completed, different χ^2 contours can be extracted as a function of one or two oscillation parameters.

The process described above depends on the granularity of the oscillation parameter space, and can thus become computationally expensive. For Hyper-K analyses, the oscillation parameter space is four-dimensional, corresponding to the $\sin^2\theta_{23}$, $\sin^2\theta_{13}$, Δm^2_{32} and δ_{CP} parameters. The nominal values, and ranges used to define each parameter dimension, are summarized in Table 7.5. The nominal values in this table will be referred to as the “Asimov A” set. The size of the parameter

Parameter	Nominal	Range	Points
$\sin^2\theta_{23}$	0.528	[0.426, 0.579]	19
$\sin^2 2\theta_{13}$	0.085	[0.070, 0.100]	13
Δm^2_{32}	2.509	[2.464, 2.554]	13
δ_{CP}	$-\pi/2$	$[-\pi, \pi]$	61

Table 7.5: Oscillation parameter values and ranges.

grid is thus of 19 × 13 × 13 × 61 = 195871 points. In order to speed up the computation, the fits are performed in parallel.

We can define the likelihood of an expected spectrum (E) under the observed spectrum (O) using a Poissonian distribution:

$$\mathcal{L}(E, O) = \prod_n \frac{e^{-E_n} E_n^{O_n}}{O_n!} \tag{7.2}$$

where n is the index spanning the bins of each distribution. The E_n and O_n predictions are each built using a different set of oscillation parameter values, Θ. In other words, O_n is the spectrum built with the "nominal" values in Table 7.5, whereas E_n is the spectrum built using a set of oscillation parameters on the grid defined in the same table. The χ^2 test statistic is defined therefore as:

$$\chi^2(\Theta) = -2\log\left[\frac{\mathcal{L}(E_n, O_n)}{\mathcal{L}(O_n, O_n)}\right] = 2\sum_n \left[E_n - O_n + O_n \log\left(\frac{O_n}{E_n}\right)\right] \ . \tag{7.3}$$

The effect of the systematic parameters on the expected distribution is included via their "pulls" on the event rate:

$$E_n \ \longrightarrow \ E_n \prod_j \left(1 + f_j^n \varepsilon_j\right) \ , \tag{7.4}$$

where ε_j represent the systematic parameters and the f_j^n terms are defined as the fractional variation on the event rate in bin n induced by a 1σ variation of the j-th systematic parameter. As such, the effect of systematic parameters is assumed to be linear.

There is one exception to this rule: the energy scale systematic. As described in Section 3.3.3.2, the energy scale uncertainty modifies the absolute energy scale, having the effect of moving events in and out of energy bins. To avoid the costly operation of re-defining the samples at each variation of the energy scale systematic, its effect is applied analytically after all other linear systematic parameters in the following way:

$$E'_n = \sum_m \frac{E_m \prod_i (1 + \varepsilon_i f_m^i)}{4\,(1 + \hat{\varepsilon}\sigma)\,\Delta b_m} \beta_{n,m}(1 + \hat{\varepsilon}\sigma) \ . \tag{7.5}$$

The numerator in the sum is the same as in Eq. (7.4), while

$$\begin{aligned} \beta_{n,m}(x) &= (1 + s_\beta)\left(\Delta b_n + x\Delta b_m - |b_n - x b_m| - |b_{n+1} - x b_{m+1}|\right) \\ s_\beta &= \mathrm{sign}\left(\Delta b_n + x\Delta b_m - |b_n - x b_m| - |b_{n+1} - x b_{m+1}|\right) \end{aligned} \tag{7.6}$$

is a "mask" function that quantifies the overlap between two axes, each defined by a different energy scaling (n indices stand for the nominal axis, whereas m indices are for the "stretched" axis under the effect of the energy scale change). In Eq. (7.6), b_n and b_m are the bin edges on the nominal axis and the shifted axis, respectively, Δb_n is the width of bin n (i.e. $\Delta b_n = b_{n+1} - b_n$, and correspondingly for m indices), $\hat{\varepsilon}$ is the amount of the energy scale shift in units of sigma, and x is the “stretch factor”, which quantifies by how much the energy scale has been modified. It may be useful to think of the two axes as an elastic ruler, which can be stretched or compressed.

Finally, the prior errors on the systematic parameters are included through a gaussian penalty term taking into account the correlations between all the systematic parameters (the correlation matrix, ρ_{kj} and its inverse, the Hessian matrix ρ^{-1}_{kj}), yielding the final χ^2:

$$\chi^2_{\mathrm{tot}}(\Theta) = 2\sum_n \left[E'_n - O_n - O_n \log\frac{E'_n}{O_n}\right] + \sum_{kj} \varepsilon_k \rho^{-1}_{kj} \varepsilon_j \ . \tag{7.7}$$

The χ^2 is minimized using the Levenberg–Marquardt algorithm [174, 175], which allows to speed up the fitting process compared to classical gradient descent minimization.

7.4.3 Systematic parameters

The systematic errors used in the Hyper-K sensitivity analysis are structured in the same way as those used in the T2K oscillation analysis Chapter 3, i.e. they account for effect related to the neutrino flux, cross-sections and the detector efficiency. They are used in the analysis via the BANFF correlation matrix obtained in the T2K 2018 oscillation analysis.

In this chapter, three sets of systematic error models are exploited. They are:

- **Statistics only** - In this model, no systematic errors are considered. It therefore represents the ideal (and unrealistic) case in which the measurements are not affected by systematic effects.

- **T2K 2018** - This systematic error model assumes the same level of systematic uncertainites as in the 2018 T2K oscillation analysis [100], with the exception of the binding energy uncertainty. With the improvements described in Section 3.3.2, the treatment of the binding energy is expected to improve (and has improved in the current analysis), so the large error on the binding energy was deemed too conservative.

- **Improved error mode/Hyper-K error model** - This systematic error model was obtained starting from the T2K error model, and then accounting for the expected improvements which will be brought by the Hyper-K statistics and the improved near detector constraints from the ND280 upgrade. Also, improved ν_e errors are tested to mimic the capabilites of the IWCD.

The Hyper-K error model was obtained starting from the T2K error model by scaling down the systematic errors in the interaction model according to the expected performance of the upgrade and of the IWCD. In addition, the errors were modified to take into account the increase in statistics, which scales them by a factor of $\sqrt{N}$, where N is the relative increase in statistics between Hyper-K and T2K. A single scaling factor is considered, corresponding to the statistics expected with 10 years of HK data (no further dependence as a function of HK statistics is considered). Each of the parameters constrained in the near detector fit was also capped at a lower limit of 1%.

Table 7.6 summarizes the impact of the uncertainties in the two systematic models on the far detector samples.

Model	Error source	1Rμ		1Re			
		FHC	RHC	FHC 0 d.e.	RHC 0 d.e.	FHC 1 d.e.	FHC/RHC 0 d.e.
T2K 2018	Flux+xsec (constrained)	3.24%	2.93%	4.14%	3.46%	4.90%	4.23%
	NC1γ	0.00%	0.00%	1.06%	2.55%	0.24%	1.46%
	NC Other	0.24%	0.24%	0.13%	0.27%	0.87%	0.14%
	E_b	—	—	—	—	—	—
	$\sigma(\nu_e)\&\sigma(\bar{\nu}_e)$	0.00%	0.00%	2.63%	1.56%	2.63%	3.22%
	Detector+FSI	3.24%	2.78%	4.16%	4.39%	17.75%	2.05%
	All Systematics	4.62%	4.06%	6.03%	6.30%	18.45%	4.99%
Hyper-K	Flux+xsec (constrained)	0.81%	0.72%	0.79%	0.87%	1.15%	0.74%
	NC1γ	0.00%	0.00%	0.47%	1.12%	0.11%	0.66%
	NC Other	0.07%	0.07%	0.03%	0.07%	0.24%	0.04%
	E_b	0.03%	0.03%	0.02%	0.03%	0.01%	0.01%
	$\sigma(\nu_e)\&\sigma(\bar{\nu}_e)$	0.00%	0.00%	1.83%	1.22%	1.83%	2.03%
	Detector+FSI	1.71%	1.60%	1.53%	1.70%	5.26%	0.95%
	All Systematics	1.89%	1.74%	2.56%	2.53%	5.63%	2.45%

Table 7.6: Summary of systematic error models investigated in this thesis.

7.4.4 Sensitivity to CP violation

The main short-term goal for the Hyper-K experiment is determining whether CP violation occurs. CP conservation can be excluded at the $3\sigma(5\sigma)$ level, for 78%(57%) of δ_{CP} values [10].
The sensitivity of the Hyper-K experiment to do this is performed by running fits using the statistical framework described in the previous section. To evaluate the sensitivity to exclude CP-conservation as a function of the assumed "true" value of δ_{CP}, the process is repeated for a different "true" value of δ_{CP} until the full range is scanned. The sensitivity itself is calculated as

$$\sigma = \sqrt{\chi^2_{trial} - \chi^2_{\delta_{CP}=0,\pi}}, \tag{7.8}$$

in which χ^2_{trial} and $\chi^2_{\delta_{CP}=0,\pi}$ are the χ^2 calculated according to Eq. (7.7), for a δ_{CP} value under trial, and for the CP-conserving cases, respectively. The smaller value of the difference with respect to $\delta_{\mathrm{CP}}=0$ or $\delta_{\mathrm{CP}}=\pi$ is retained. The results are shown in Fig. 7.10.

The limiting factors in the CP-asymmetry measurement are those which affect the relative rate of $\nu_e/\bar{\nu}_e$ candidates, as it is these samples which have the largest sensitivity to determine the value of δ_{CP}. This is illustrated in Fig. 7.11, which shows how the sensitivity changes as a function of the uncertainty on the $\nu_e/\bar{\nu}_e$ cross-section ratio.

Aside from the systematic error limitations, the sensitivity to exclude CP-conservation is limited by the knowledge of the mass hierarchy. In most sensitivity studies, it is assumed that the mass hierarchy will be determined sometime before the operation of Hyper-K by other experiments, such as JUNO [176]. However, if the mass hierarchy is unknown, this can cause a loss of sensitivity to CP-violation if only accelerator neutrinos are used, due to a degeneracy between the effect of the mass hierarchy and δ_{CP} on the $\nu_e/\bar{\nu}_e$ oscillated spectra.
To lift this degeneracy and have an enhanced MH sensitivity, atmospheric neutrino information can be used. Hyper-Kamiokande is also designed to accommodate a rich atmospheric neutrino physics

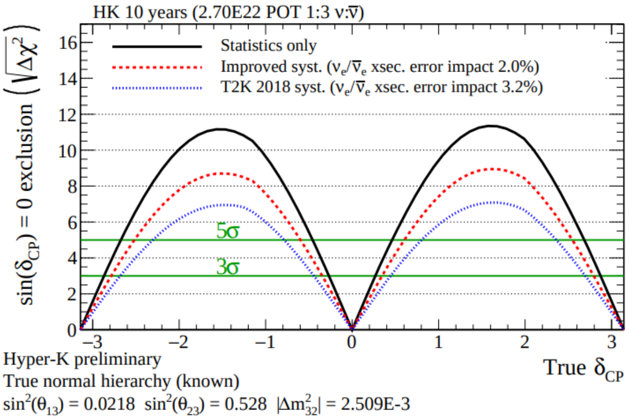

Figure 7.10: Sensitivity to exclude sin$\delta_{\rm CP}$ =0, using accelerator neutrinos, and assuming 10 years of Hyper-K data taking and normal hierarchy (known), as a function of the true value of $\delta_{\rm CP}$. Three cases are compared: statistics only (i.e. no systematic errors) in solid black, the T2K 2018 level of systematic errors (dotted blue) and the improved HK error model (dashed red).

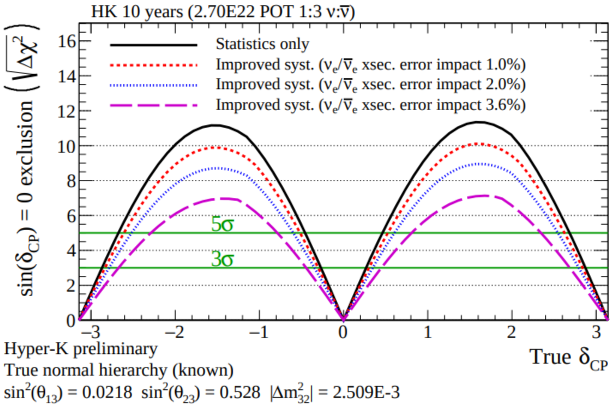

Figure 7.11: Sensitivity to exclude sin$\delta_{\rm CP}$ =0, using accelerator neutrinos, and assuming 10 years of Hyper-K data taking and normal hierarchy (known), as a function of the true value of $\delta_{\rm CP}$. Comparison of the impact of different systematic errors on the total $\nu_e/\bar{\nu}_e$ cross section ratio.

program, building on the experience of Super-K. Since the sensitivity to mass hierarchy comes from matter effects, atmospheric neutrinos crossing large portions of the earth have sensitivity to it. Assuming the values in Table 7.5 for the MC prediction, if the mass hierarchy is known, equal sensitivities will be obtained for $\delta_{\rm CP}$ <0 and $\delta_{\rm CP}$ >0. If, on the other hand, the mass hierarchy is unknown, the predicted spectrum changes, and there will be a loss of sensitivity for $\delta_{\rm CP}$ >0 values for a true NH scenario, and for $\delta_{\rm CP}$ <0 for a true IH scenario. The addition of atmospheric samples makes it possible to recover part of this lost sensitivity, as shown in Fig. 7.12. These sensitivities improve when evaluated under an improved systematics scenario, as can be seen in the bottom line of Fig. 7.12.

7.4.5 Precision measurements

The precise measurement of Δm^2_{32} and $\sin^2\theta_{23}$ (and its octant determination) are also major goals of the Hyper-K experiment. As the oscillation probability depends on $\sin^2\theta_{23}$, $\delta_{\rm CP}$ and Δm^2_{32} at

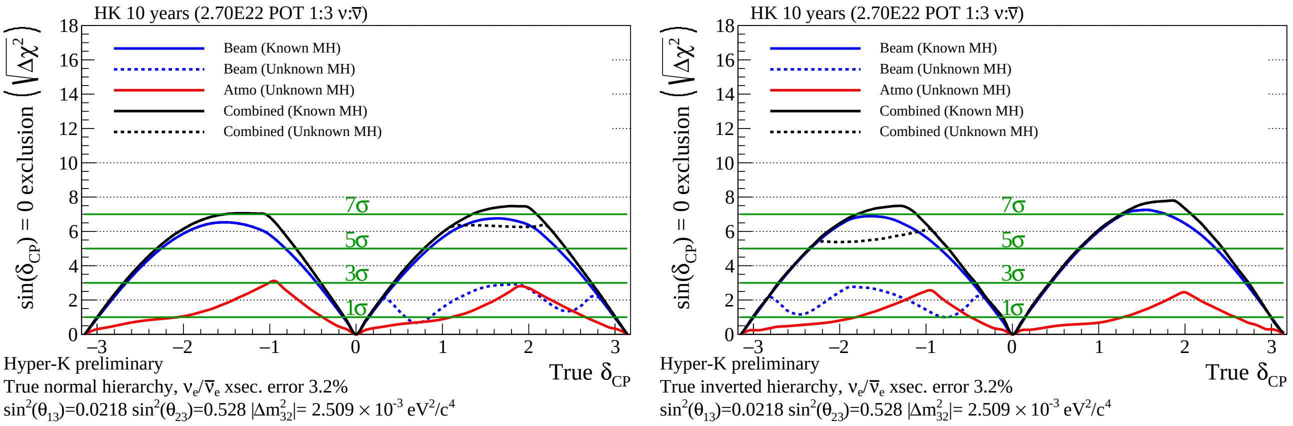

(a) T2K 2018 model - True NH (b) T2K 2018 model - True IH

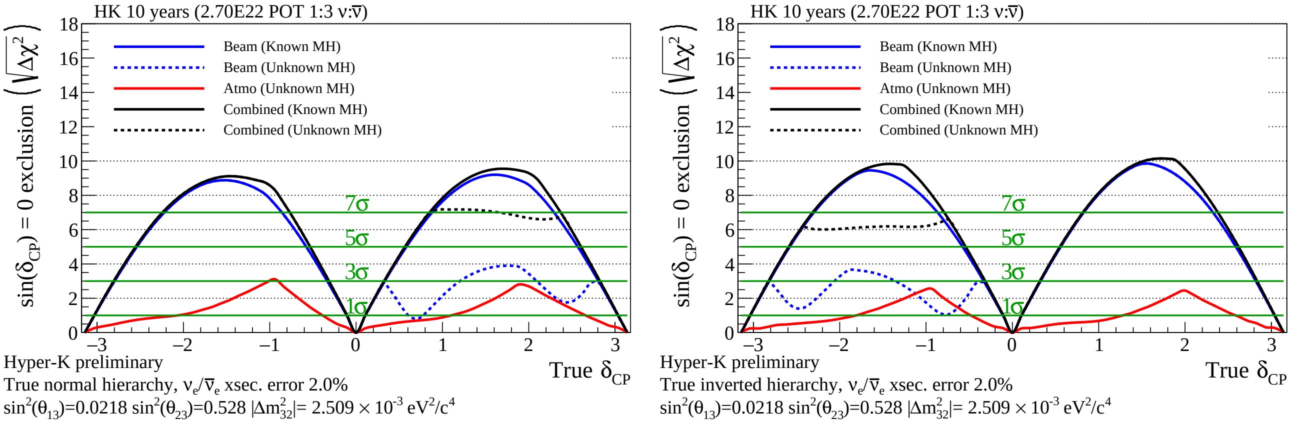

(c) HK improved model - True NH (d) HK improved model - True IH

Figure 7.12: Sensitivity to exclude CP conservation, assuming T2K 2018 systematic errors (top line), HK improved systematic errors (bottom line) and 10 years of HK operation (2.7×10^{22} POT, 1:3 $\nu : \bar{\nu}$), for different samples used in the analysis: accelerator (beam) neutrino samples (blue), atmospheric neutrino samples (red) and a combined fit to atmospheric and beam samples (black). The results of a combined sample without systematic errors is shown in gray. The solid lines assume the mass hierarchy is known, whereas the dashed lines assume the mass hierarchy is unknown.

once, the precise determination of each parameter will improve the precision on the remaining ones. The value of the δ_{CP} angle also needs to be determined with precision, and this is a task which is even more challenging than establishing whether CP violation occurs. In general, the precise determination of physics parameters is at the core of experimental physics. For PMNS parameters, the precise values of the mixing angles and the δ_{CP} phase are essential to identify underlying symmetries in the neutrino mixing pattern, and thus discriminate between different neutrino mixing model predictions. Two obvious examples are whether $\sin^2\theta_{23}$ is maximal (i.e. 0.5), or if the CP violating phase is maximal (i.e. $\delta_{\mathrm{CP}} = \pm\pi/2$). These values would indicate the presence of hidden symmetries in the neutrino mixing pattern, which any model trying to explain flavor mixing must be able to predict.

The dominant sources of systematics affecting the precision on δ_{CP} depend on the true value of δ_{CP}. When $\sin\delta_{\mathrm{CP}}$ is close to 0, the oscillation probability is dominated by CP-odd terms, and so the main systematic error sources are the same as those for CP-violation search, i.e. the statistics of ν_e and $\bar{\nu}_e$ samples and the systematics affecting their relative rate. However, when $|\sin\delta_{\mathrm{CP}}\,|$ is close to 1 (maximal CP violation), the oscillation probability becomes driven by the CP-even term cosδ_{CP}. The effect of this term is to enhance or suppress the event rate above the flux peak, with the opposite effect below the peak. Therefore, in this case, the δ_{CP} precision is limited in large part by the precision on the $\nu_e/\bar{\nu}_e$ spectrum shape and shape effects/systematics on the $\nu_e/\bar{\nu}_e$ spectrum become important limiting factors.

In HK the ultimate precision on δ_{CP}, assuming 10 years of Hyper-K data taking and the effect of improved systematic errors coming from the ND280 upgrade, is of 7° if sin$\delta_{\mathrm{CP}} \sim 0$ and 19° if sin$\delta_{\mathrm{CP}} \sim 1$ [10]. These assumptions do not take into account the probable improvement in flux uncertainties which is expected to come with the addition of new NA61/SHINE data, which will further improve the flux constraints.

However, the effect of the CP-even term can be similar, and thus degenerate, to that of other systematic parameters. As an example, Fig. 7.13 shows the similar effect that a 12° (slightly better than the target precision) shift on δ_{CP} and a 0.5% shift in the energy scale have on the electron neutrino spectra.

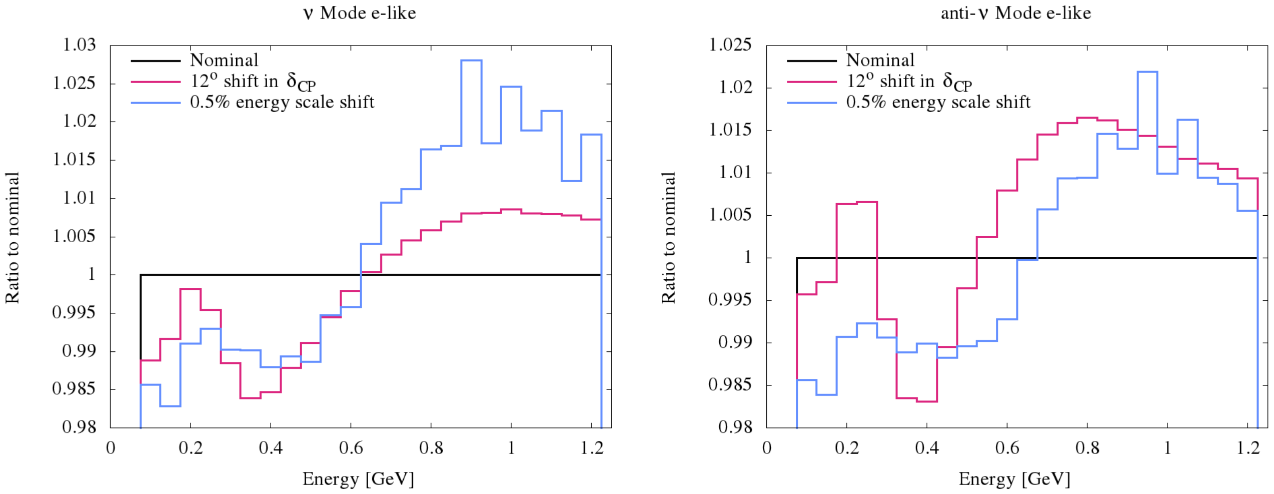

(a) (b)

Figure 7.13: Ratio of energy spectrum predicted with δ_{CP} =-78° (magenta) and δ_{CP} =-90°, and the ratio to nominal with a 0.5% energy scale shift (blue) applied to reconstructed electron neutrino (a) and antineutrino (b) candidates.

The 1σ uncertainty on energy scale is of 2.4% in Super-K today, while the target uncertainty at HK is 1% for this systematic parameter. Currently, the same (fully correlated) energy scale uncertainty is used for both μ-like and e-like samples: Fig. 7.14 shows contributions to the χ^2 in Eq. (7.7) that a 0.5% shift in the energy scale has in μ-like samples and e-like samples. The effects of energy scale changes, obviously, are mostly visible as shifts on the rising and falling edges of the spectrum. In addition to having much more statistics, the μ-like samples have three slope-changing regions, unlike the e-like samples, which only have two. As a result, the μ-like samples will drive the constraint on the energy scale parameter. This is also confirmed by Fig. 7.15, which shows the constraint on the energy scale parameter from the two samples, when no other systematic parameters are varied. Accordingly, Fig. 7.16 shows that the δ_{CP} resolution is not significantly impacted by a change in the energy scale uncertainty, when using the same parameter for μ-like

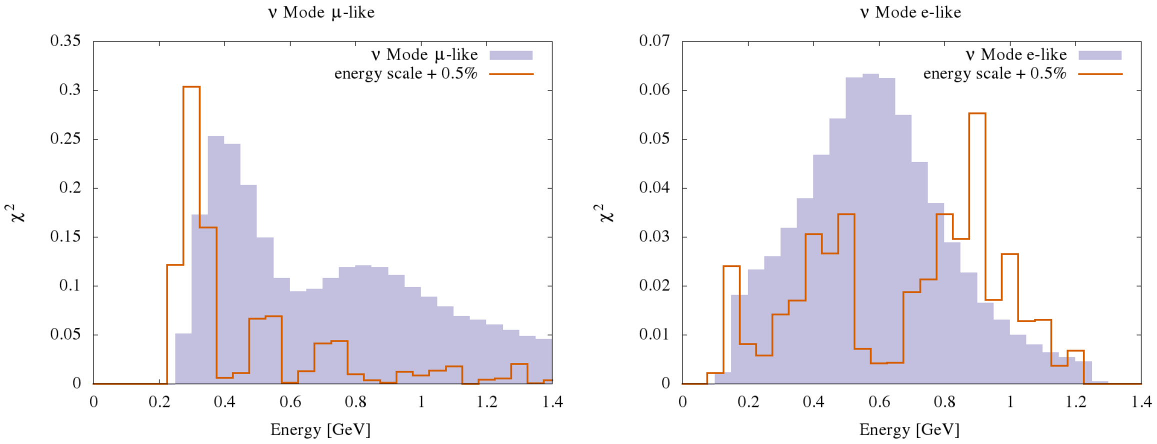

(a) (b)

Figure 7.14: Contribution to the total χ^2 of a 0.5% shift in the energy scale, as a function of neutrino energy, for neutrino-mode μ-like (a) and e-like (b) samples. The oscillated neutrino flux is shown in gray, with an arbitrary normalization.

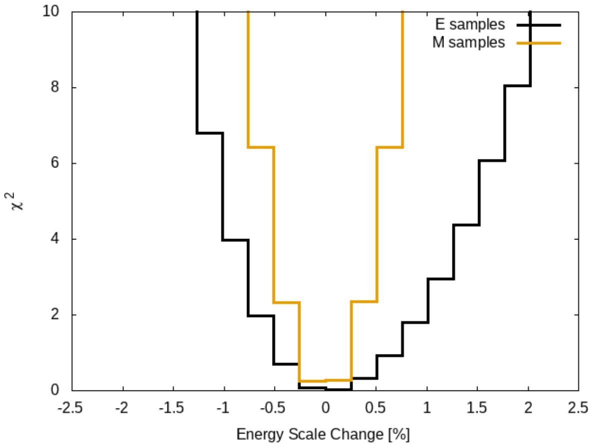

Figure 7.15: Contribution to the total χ^2 as a function of the change in energy scale. The contributions are calculated for μ-like and e-like samples, separately.

and e-like samples (left). However, there is a slight loss in δ_{CP} sensitivity when using two separate dials for the two samples (right). It is expected that, in reality, at the 1% level, the energy scale systematic will only be partially correlated between ν_e and ν_μ samples, due to different methods being used to estimate this systematic uncertainty for each type of sample. A more detailed model of energy calibration is needed to develop a precise estimation of ν_e-ν_μ correlation for the energy scale.

δ_{CP} is not the only parameter which presents some degeneracy with the energy scale uncertainty. In μ-like samples, the effect of the energy scale is similar to that of a Δm^2_{32} shift, as can be seen in Fig. 7.17. The effect of Δm^2_{32} is to shift the position of the disappearance dip, thus mimicking the effect of an energy scale shift.

This degeneracy has an effect on the Δm^2_{32} resolution, shown in Fig. 7.18. Since the majority of the constraint comes from μ-like samples, using a single parameter does not change the Δm^2_{32} resolution. However, using separate parameters slightly degrades the Δm^2_{32} resolution, as the e-like

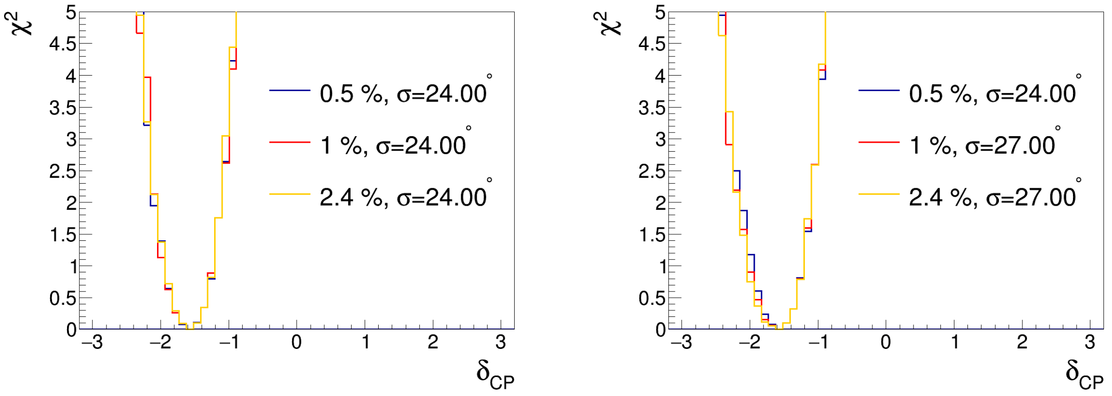

(a) (b)

Figure 7.16: δ_{CP} 1σ contours near $\delta_{\mathrm{CP}} = \pi/2$, for fits assuming different energy scale errors, and using one energy scale parameter (a) or two separate energy scale parameters (b) for μ-like and e-like samples. The percentage in the legend corresponds to the energy scale uncertainty, and σ is the resolution on δ_{CP}.

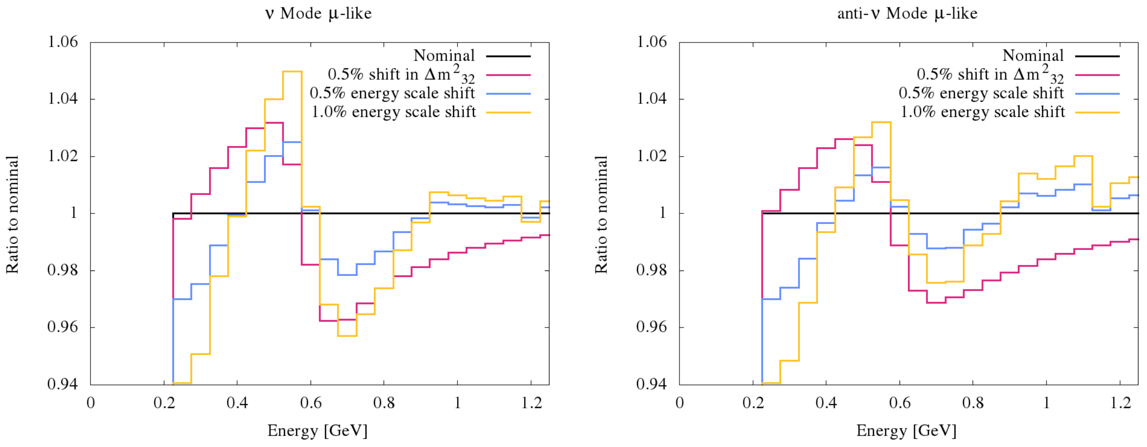

(a) (b)

Figure 7.17: Ratio to nominal of energy spectrum predicted with a 0.5% shift on the Δm^2_{32} value from Table 7.5 (magenta), and with a 0.5%(1%) energy scale shift in blue (yellow) applied to reconstructed muon neutrino (a) and antineutrino (b) candidates.

samples have a smaller power of constraining it. It is worth noting that in these studies, a well controlled linearity of the energy scale uncertainty as a function of particle energy is assumed, since a single energy scale shift is applied for all energies. Further uncertainty on the energy scale linearity may impact the Δm^2_{32} sensitivity, and therefore more precise models of the calibration process are needed to inform such studies.

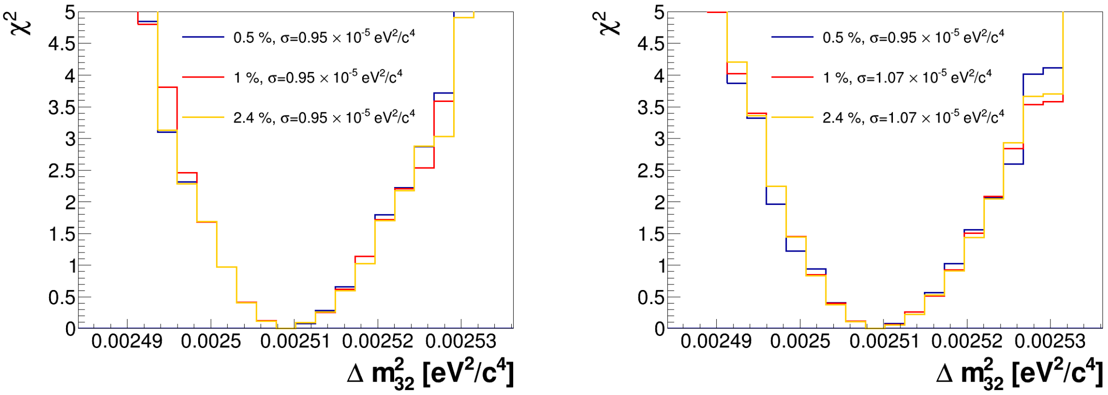

(a) (b)

Figure 7.18: Δm^2_{32} contours for fits assuming different energy scale errors, and using one energy scale parameter (a) or two separate energy scale parameters (b) for μ-like and e-like samples. The percentage in the legend corresponds to the energy scale uncertainty, and σ is the resolution on Δm^2_{32}.

7.5 Conclusion and Perspectives

The Hyper-Kamiokande experiment has a rich physics program, including a competitive long-baseline neutrino oscillations program. As a result, Hyper-K is expected to rule on CP violation within the first three years of its operation and provide world-leading precision on the neutrino oscillation parameters. Hyper-K will be able to reduce the statistical uncertainty on samples used in neutrino oscillation analyses to the percent level. As a result, systematic errors of the same level need to be achieved.

The use of three near detectors (INGRID, upgraded ND280 and IWCD) will be instrumental in this effort. Since the ND280 detector will have been in use for nearly 20 years during Hyper-K operation, the detector maintenance will become increasingly challenging, especially as replacement parts become more and more obsolete. This will provide an opportunity to further improve the near detector complex, an "upgrade of the upgrade" of ND280, taking full advantage of the modularity of ND280. Possible improvements under consideration are the idea of including more water targets in the near detector complex, and building up on the 3D scintillating technology developed for the SuperFGD, e.g. by using a larger mass with the SuperFGD technology in order to enable precision ν_e measurements.

Chapter 8

Conclusion

The discovery of neutrino oscillations has opened a new field in particle physics. Current, past and future experiments aim to elucidate the mechanisms which enable neutrinos to oscillate, by measuring the physical parameters which govern this process. At this stage, the neutrino mass hierarchy is still unknown, yet it is an important physical parameter. In addition, neutrino oscillations have provided us with a hint of charge-parity violation in the lepton sector. In order to establish whether this occurs, a fundamental parameter of the PMNS paradigm, δ_{CP}, needs to be measured. Present accelerator neutrino experiments are collecting data and new experiments are being developed in order to measure the amount of CP violation occurring in neutrino oscillations. This thesis has presented the latest oscillation parameters measurements of the T2K experiment.

T2K produces a muon neutrino beam, which is measured using a suite of detectors near the beam production point, and then measured 300 km away from the production point by the Super-Kamiokande detector. After nearly 10 years of data taking, the far-detector samples are limited by the amount of available statistics, and by systematic uncertainties. To reduce the systematic uncertainties on the oscillated spectrum, T2K used its near detector, ND280, to constrain systematic parameters which affect the neutrino flux and neutrino-nucleus interactions.

This thesis had a major focus on the role of the near detector in the oscillation analysis. The ND280 detector is an excellent tracking device, and the inclusion of its data in the oscillation analysis has enabled a reduction of systematic uncertainties from the level of 15% to the level of 4% across all far-detector samples. The role of the near detector in constraining systematic uncertainties is therefore essential in order to obtain precise measurements of oscillation parameters.

For the analysis presented in this thesis, many improvements in the near detector analysis were introduced. The amount of neutrino data collected at the near detector since the last published analysis [100] has nearly doubled, whereas the anti-neutrino data has tripled. A new and improved flux uncertainty model, using external constraints obtained from the NA61/SHINE experiment with a full-size replica of the T2K target was included for the first time in a T2K oscillation analysis.

One of the main limiting systematic errors in neutrino oscillation physics comes from our limited knowledge of neutrino-nucleus interactions. So far, simplistic models have been used to describe the interactions neutrinos undergo on complex nuclear targets. The analysis presented in this thesis is the first full-scale experiment oscillation analysis to use a sophisticated Spectral Function model to model the nuclear ground state. Thanks to the implementation of this model, one of the major sources of systematic uncertainty in the previous T2K analysis (the uncertainty on the nucleon removal energy) was reduced to a negligible level. Although in this analysis only part of the neutrino interaction final state is used (outgoing leptons), future detectors will aim to precisely measure hadronic final states. The Spectral Function model lays the ground work for more exclusive analyses, in which the full interaction final state can be exploited.

As a result, T2K has provided world-leading measurements of neutrino oscillation parameters. The oscillation analysis conducted at T2K has, like any analysis, a certain degree of model dependence. Given the limited knowledge of neutrino-nucleus interactions, there is always a possibility that the oscillation results will be biased due to mis-modelling effects. In order to assess the robustness of the analysis against such possible biases, a multitude of studies were performed and described in this thesis. The systematic uncertainty error model used in the T2K oscillation analysis was found to be robust enough to accommodate a wide range of alternative models and tunes.

In 2022, T2K plans a major upgrade of its beamline and near detector complex. The J-PARC neutrino beamline will begin a series of upgrades, aiming to increase the neutrino beam power from its current value of 515 kW, to 750 kW, and finally to 1.3 MW by 2026. This will enable an unprecedented amount of statistics to be collected, and the T2K detectors need to be upgraded in order to make the most of this improvement.

As a result, the ND280 Upgrade project was proposed, and will be installed in 2022 at J-PARC. The development of the upgrade provided a very fruitful R&D endeavour. The ND280 detector will be upgraded by adding an additional 2t fully-active target, with a 3D structure composed of scintillating cubes with optical read-out channels (SuperFGD). This will double the available target mass at ND280, and will enable a fully 3D track reconstruction process. Thanks to its 3D structure, the SuperFGD will have improved particle detection capabilities, in particular regarding the detection of low momentum protons and neutrons. Protons produced in the final state of neutrino interactions are an essential ingredient in controlling neutrino-nucleus interaction systematics, and will enable a powerful reduction in the model dependence of the analysis. The neutron detection capabilities of the SuperFGD have also been examined in this thesis, and an analysis to improve the anti-neutrino energy reconstruction using neutron information was described.

Another novel detection technology employed by the upgraded ND280 detector is the resistive MicroMegas technology. With the installation of the upgrade, T2K will be the first full-scale experiment to make use of the latter. The resistive MicroMegas technology will be part of two horizontal Time Projection Chambers, sandwiching the new SuperFGD target, and will enable excellent particle reconstruction, in particular for high-angle tracks. The resistive MicroMegas technology relies on the charge spreading phenomenon in a resistive layer. It is important to model this effect in order to correctly characterize the detector and simulate its response. Several studies on the charge spreading in resistive MicroMegas are described in this thesis. The combined effect of the SuperFGD and new TPCs will make the ND280 detector acceptance match that of the far detector.

The scope of the ND280 Upgrade project goes beyond the T2K experiment. In 2027, the Hyper-K experiment, a natural successor to the Super-K experiment, will begin operation. Hyper-K has a rich physics program, and one of its main axes will be studying long-baseline accelerator neutrino oscillations. As a result, Hyper-K will also use the ND280 Upgrade in its physics program. In this thesis, the impact of the upgraded ND280 detector on the Hyper-K oscillation analysis was shown to provide a large reduction in the largest sources of systematic uncertainties.

In addition, Hyper-K will have a prolific atmospheric neutrino program. The inclusion of atmospheric neutrino samples in the Hyper-K oscillation analysis will allow to lift the degeneracy between the mass hierarchy and the CP violating phase δ_{CP}. As a result, Hyper-K will be able to rule on CP violation within the first three years of its operation. Moreover, sensitivity studies have allowed us to gauge the impact of detector systematic parameters, such as the Hyper-K energy calibration, on the Hyper-K oscillation analysis. This is an essential step in the design of a new experiment, setting the goals for the detector design and performance.

In conclusion, numerous advances in neutrino physics were made, both concerning particle detection techniques, and the theoretical and statistical devices used in neutrino oscillation analyses. The work presented in this thesis has helped gauge the impact of novel detector technologies, as well as develop more robust analysis methods for current (T2K) and future (Hyper-K, DUNE) neutrino oscillation experiments.

Bibliography

[1] P. Dunne, "Latest Neutrino Oscillation Results from T2K." The XXIX International Conference on Neutrino Physics and Astrophysics, 2020.

[2] A. Himmel, "New Oscillation Results from the NOvA Experiment," July 2020.

[3] Y. Nakajima, "Recent results and future prospects from Super-Kamiokande," June 2020.

[4] M. G. Aartsen *et al.*, "Measurement of Atmospheric Neutrino Oscillations at 6–56 GeV with IceCube DeepCore," *Phys. Rev. Lett.*, vol. 120, p. 071801, Feb 2018.

[5] J. Nieves, I. Ruiz-Simo, and M. J. Vicente-Vacas, "The Nucleon axial mass and the MiniBooNE CCQE neutrino-nucleus data," *J. Phys. Conf. Ser.*, vol. 408, p. 012040, 2013.

[6] W. M. Alberico, M. Ericson, and A. Molinari, "The Role of Two Particles - Two Holes Excitations in the Spin - Isospin Nuclear Response," *Annals Phys.*, vol. 154, p. 356, 1984.

[7] I. Ruiz Simo, J. E. Amaro, M. B. Barbaro, A. De Pace, J. A. Caballero, and T. W. Donnelly, "Relativistic model of 2p-2h meson exchange currents in (anti)neutrino scattering," *J. Phys. G*, vol. 44, no. 6, p. 065105, 2017.

[8] P. Stowell *et al.*, "Tuning the GENIE pion production model with MINERvA data," *Phys. Rev. D*, vol. 100, p. 072005, Oct 2019.

[9] I. Esteban, M. C. Gonzalez-Garcia, M. Maltoni, T. Schwetz, and A. Zhou, "The fate of hints: updated global analysis of three-flavor neutrino oscillations," *JHEP*, vol. 09, p. 178, 2020.

[10] K. Abe *et al.*, "Hyper-Kamiokande Design Report," 5 2018.

[11] W. Pauli, "Pauli letter collection: letter to Lise Meitner." Typed copy. Translation available at https://microboone-docdb.fnal.gov/cgi-bin/RetrieveFile?docid=953;filename=pauli%20letter1930.pdf.

[12] J. Chadwick, "Intensitätsverteilung im magnetischen Spectrum der β-Strahlen von radium B + C," *Verhandl. Dtsc. Phys. Ges.*, vol. 16, p. 383, 1914.

[13] F. A. Scott, "Energy Spectrum of the Beta-Rays of Radium E," *Phys. Rev.*, vol. 48, pp. 391–395, Sep 1935.

[14] J. Chadwick, "Possible Existence of a Neutron," *Nature*, vol. 129, p. 312, 1932.

[15] E. Fermi, "Versuch einer Theorie der β-Strahlen. I," *Zeitschrift fur Physik*, vol. 88, pp. 161–177, Mar. 1934.

[16] F. Reines and C. L. Cowan, “The neutrino,” *Nature*, vol. 178, pp. 446–449, 1956.

[17] F. Reines and C. L. Cowan, “Detection of the free neutrino,” *Phys. Rev.*, vol. 92, pp. 830–831, Nov 1953.

[18] C. L. Cowan, F. Reines, F. B. Harrison, H. W. Kruse, and A. D. McGuire, “Detection of the free neutrino: A Confirmation,” *Science*, vol. 124, pp. 103–104, 1956.

[19] G. Danby *et al.*, “Observation of high-energy neutrino reactions and the existence of two kinds of neutrinos,” *Phys. Rev. Lett.*, vol. 9, pp. 36–44, Jul 1962.

[20] M. L. Perl *et al.*, “Evidence for anomalous lepton production in $e^+ - e^-$ annihilation,” *Phys. Rev. Lett.*, vol. 35, pp. 1489–1492, Dec 1975.

[21] K. Kodama *et al.*, “Observation of tau neutrino interactions,” *Phys. Lett. B*, vol. 504, pp. 218–224, 2001.

[22] S. Schael *et al.*, “Precision electroweak measurements on the Z resonance,” *Phys. Rept.*, vol. 427, pp. 257–454, 2006.

[23] G. Altarelli, “The Standard model of particle physics,” 10 2005.

[24] M. Goldhaber, L. Grodzins, and A. W. Sunyar, “Helicity of neutrinos,” *Phys. Rev.*, vol. 109, pp. 1015–1017, Feb 1958.

[25] M. Aker *et al.*, “Improved Upper Limit on the Neutrino Mass from a Direct Kinematic Method by KATRIN,” *Phys. Rev. Lett.*, vol. 123, no. 22, p. 221802, 2019.

[26] N. Majorana, “A symmetric theory of electrons and positrons,” *Ettore Majorana Scientific Papers: On occasion of the centenary of his birth*, pp. 201–233, 01 2006.

[27] N. Aghanim *et al.*, “Planck 2018 results. VI. Cosmological parameters,” *Astron. Astrophys.*, vol. 641, p. A6, 2020.

[28] F. T. Avignone, III *et al.*, “Double Beta Decay, Majorana Neutrinos, and Neutrino Mass,” *Rev. Mod. Phys.*, vol. 80, pp. 481–516, 2008.

[29] J. N. Bahcall, W. A. Fowler, I. Iben, Jr., and R. L. Sears, “Solar neutrino flux,” *Astrophys. J.*, vol. 137, pp. 344–346, 1963.

[30] R. Davis, D. S. Harmer, and K. C. Hoffman, “Search for neutrinos from the sun,” *Phys. Rev. Lett.*, vol. 20, pp. 1205–1209, May 1968.

[31] M. Cribier, “Results of the whole GALLEX experiment,” *Nucl. Phys. B Proc. Suppl.*, vol. 70, pp. 284–291, 1999.

[32] J. N. Abdurashitov *et al.*, “Solar neutrino flux measurements by the Soviet-American Gallium Experiment (SAGE) for half the 22 year solar cycle,” *J. Exp. Theor. Phys.*, vol. 95, pp. 181–193, 2002.

[33] K. S. Hirata *et al.*, “Observation of ^{8}B solar neutrinos in the Kamiokande-II detector,” *Phys. Rev. Lett.*, vol. 63, pp. 16–19, Jul 1989.

[34] Q. R. Ahmad *et al.*, “Direct Evidence for Neutrino Flavor Transformation from Neutral-Current Interactions in the Sudbury Neutrino Observatory,” *Phys. Rev. Lett.*, vol. 89, p. 011301, Jun 2002.

[35] B. Pontecorvo, “Inverse beta processes and nonconservation of lepton charge,” *Zh. Eksp. Teor. Fiz.*, vol. 34, p. 247, 1957.

[36] B. Pontecorvo, “Neutrino Experiments and the Problem of Conservation of Leptonic Charge,” *Zh. Eksp. Teor. Fiz.*, vol. 53, pp. 1717–1725, 1967.

[37] M. Aglietta *et al.*, “Experimental study of atmospheric neutrino flux in the NUSEX experiment,” *Europhys. Lett.*, vol. 8, pp. 611–614, 1989.

[38] C. Berger *et al.*, “Study of Atmospheric Neutrino Interactions with the Frejus Detector,” *Phys. Lett. B*, vol. 227, p. 489, 1989.

[39] R. Becker-Szendy *et al.*, “IMB-3: A Large water Cherenkov detector for nucleon decay and neutrino interactions,” *Nucl. Instrum. Meth. A*, vol. 324, pp. 363–382, 1993.

[40] Y. Fukuda *et al.*, “Atmospheric muon-neutrino / electron-neutrino ratio in the multiGeV energy range,” *Phys. Lett. B*, vol. 335, pp. 237–245, 1994.

[41] Y. Fukuda *et al.*, “Evidence for oscillation of atmospheric neutrinos,” *Phys. Rev. Lett.*, vol. 81, pp. 1562–1567, Aug 1998.

[42] Z. Maki, M. Nakagawa, and S. Sakata, “Remarks on the unified model of elementary particles,” *Prog. Theor. Phys.*, vol. 28, pp. 870–880, 1962.

[43] K. Eguchi *et al.*, “First Results from KamLAND: Evidence for Reactor Antineutrino Disappearance,” *Phys. Rev. Lett.*, vol. 90, p. 021802, Jan 2003.

[44] S. Abe *et al.*, “Precision Measurement of Neutrino Oscillation Parameters with KamLAND,” *Phys. Rev. Lett.*, vol. 100, p. 221803, Jun 2008.

[45] Y. Abe *et al.*, “First Measurement of θ_{13} from Delayed Neutron Capture on Hydrogen in the Double Chooz Experiment,” *Phys. Lett. B*, vol. 723, pp. 66–70, 2013.

[46] F. P. An *et al.*, “Observation of Electron-Antineutrino Disappearance at Daya Bay,” *Phys. Rev. Lett.*, vol. 108, p. 171803, Apr 2012.

[47] J. K. Ahn *et al.*, “Observation of Reactor Electron Antineutrinos Disappearance in the RENO Experiment,” *Phys. Rev. Lett.*, vol. 108, p. 191802, May 2012.

[48] H. J. Lipkin, “Quantum theory of neutrino oscillations for pedestrians: Simple answers to confusing questions,” *Phys. Lett. B*, vol. 642, pp. 366–371, 2006.

[49] K. Abe *et al.*, “Observation of Electron Neutrino Appearance in a Muon Neutrino Beam,” *Phys. Rev. Lett.*, vol. 112, p. 061802, 2014.

[50] S. P. Mikheev and A. Y. Smirnov, “Neutrino Oscillations in an Inhomogeneous Medium: Adiabatic Regime,” *Sov. Phys. JETP*, vol. 65, pp. 230–236, 1987.

[51] L. Wolfenstein, “Neutrino oscillations in matter,” *Phys. Rev. D*, vol. 17, pp. 2369–2374, May 1978.

[52] C. Giganti, S. Lavignac, and M. Zito, “Neutrino oscillations: The rise of the PMNS paradigm,” *Prog. Part. Nucl. Phys.*, vol. 98, pp. 1–54, 2018.

[53] V. Barger, K. Whisnant, S. Pakvasa, and R. J. N. Phillips, “Matter effects on three-neutrino oscillations,” *Phys. Rev. D*, vol. 22, pp. 2718–2726, Dec 1980.

[54] T. Katori and M. Martini, “Neutrino–nucleus cross sections for oscillation experiments,” *J. Phys. G*, vol. 45, no. 1, p. 013001, 2018.

[55] M. H. Ahn *et al.*, “Measurement of Neutrino Oscillation by the K2K Experiment,” *Phys. Rev. D*, vol. 74, p. 072003, 2006.

[56] P. Adamson *et al.*, “Measurement of Neutrino and Antineutrino Oscillations Using Beam and Atmospheric Data in MINOS,” *Phys. Rev. Lett.*, vol. 110, p. 251801, Jun 2013.

[57] P. Adamson *et al.*, “The NuMI Neutrino Beam,” *Nucl. Instrum. Meth. A*, vol. 806, pp. 279–306, 2016.

[58] K. Abe *et al.*, “Evidence of Electron Neutrino Appearance in a Muon Neutrino Beam,” *Phys. Rev. D*, vol. 88, no. 3, p. 032002, 2013.

[59] D. S. Ayres *et al.*, “NOvA: Proposal to Build a 30 Kiloton Off-Axis Detector to Study $\nu_\mu \to \nu_e$ Oscillations in the NuMI Beamline,” 3 2004.

[60] R. Acciarri *et al.*, “Long-Baseline Neutrino Facility (LBNF) and Deep Underground Neutrino Experiment (DUNE): Conceptual Design Report, Volume 1: The LBNF and DUNE Projects,” 1 2016.

[61] K. Abe *et al.*, “Constraint on the matter–antimatter symmetry-violating phase in neutrino oscillations,” *Nature*, vol. 580, no. 7803, pp. 339–344, 2020. [Erratum: Nature 583, E16 (2020)].

[62] K. Abe *et al.*, “The T2K Experiment,” *Nucl. Instrum. Meth. A*, vol. 659, pp. 106–135, 2011.

[63] M. H. Ahn *et al.*, “Indications of neutrino oscillation in a 250 km long baseline experiment,” *Phys. Rev. Lett.*, vol. 90, p. 041801, 2003.

[64] “Accelerator technical design report for J-PARC,” 3 2003.

[65] T. Sekiguchi *et al.*, “Development and operational experience of magnetic horn system for T2K experiment,” *Nucl. Instrum. Meth. A*, vol. 789, pp. 57–80, 2015.

[66] K. Abe *et al.*, “T2K neutrino flux prediction,” *Phys. Rev. D*, vol. 87, no. 1, p. 012001, 2013. [Addendum: Phys.Rev.D 87, 019902 (2013)].

[67] Ferrari, Alfredo and Sala, Paola R. and Fasso, Alberto and Ranft, Johannes, “FLUKA: A multi-particle transport code (Program version 2005),” 10 2005.

[68] R. Brun, F. Bruyant, F. Carminati, S. Giani, M. Maire, A. McPherson, G. Patrick, and L. Urban, "GEANT Detector Description and Simulation Tool," 10 1994.

[69] A. Fasso, A. Ferrari, J. Ranft, and P. Sala, "FLUKA: Present status and future developments," *Conf. Proc. C*, vol. 9309194, pp. 493–502, 1993.

[70] N. Antoniou *et al.*, "Study of hadron production in collisions of protons and nuclei at the CERN SPS," 1 2006.

[71] K. Abe *et al.*, "Measurement of neutrino and antineutrino oscillations by the T2K experiment including a new additional sample of ν_e interactions at the far detector," *Phys. Rev. D*, vol. 96, no. 9, p. 092006, 2017. [Erratum: Phys.Rev.D 98, 019902 (2018)].

[72] K. Abe *et al.*, "Measurement of the muon neutrino inclusive charged-current cross section in the energy range of 1–3 GeV with the T2K INGRID detector," *Phys. Rev. D*, vol. 93, no. 7, p. 072002, 2016.

[73] K. Abe *et al.*, "Measurement of the ν_μ charged-current cross sections on water, hydrocarbon, iron, and their ratios with the T2K on-axis detectors," 4 2019.

[74] S. Aoki *et al.*, "The T2K Side Muon Range Detector (SMRD)," *Nucl. Instrum. Meth. A*, vol. 698, pp. 135–146, 2013.

[75] P. A. Amaudruz *et al.*, "The T2K Fine-Grained Detectors," *Nucl. Instrum. Meth. A*, vol. 696, pp. 1–31, 2012.

[76] N. Abgrall *et al.*, "Time Projection Chambers for the T2K Near Detectors," *Nucl. Instrum. Meth. A*, vol. 637, pp. 25–46, 2011.

[77] I. Giomataris, R. De Oliveira, S. Andriamonje, S. Aune, G. Charpak, P. Colas, A. Giganon, P. Rebourgeard, and P. Salin, "Micromegas in a bulk," *Nucl. Instrum. Meth. A*, vol. 560, pp. 405–408, 2006.

[78] B. Jamieson, "Experience with the Time Projection Chambers for the T2K Near Detectors," *Physics Procedia*, vol. 37, pp. 535–542, 2012. Proceedings of the 2nd International Conference on Technology and Instrumentation in Particle Physics (TIPP 2011).

[79] H. Bethe, "Zur Theorie des Durchgangs schneller Korpuskularstrahlen durch Materie," *Annalen der Physik*, vol. 397, no. 3, pp. 325–400, 1930.

[80] Y. Fukuda *et al.*, "The Super-Kamiokande detector," *Nucl. Instrum. Meth. A*, vol. 501, pp. 418–462, 2003.

[81] Y. Fukuda *et al.*, "The Super-Kamiokande detector," *Nucl. Instrum. Meth. A*, vol. 501, pp. 418–462, 2003.

[82] H. Zhang *et al.*, "Supernova Relic Neutrino Search with Neutron Tagging at Super-Kamiokande-IV," *Astropart. Phys.*, vol. 60, pp. 41–46, 2015.

[83] L. Alvarez-Ruso *et al.*, "NuSTEC White Paper: Status and challenges of neutrino–nucleus scattering," *Prog. Part. Nucl. Phys.*, vol. 100, pp. 1–68, 2018.

[84] J. A. Formaggio and G. P. Zeller, “From eV to EeV: Neutrino Cross Sections Across Energy Scales,” *Rev. Mod. Phys.*, vol. 84, pp. 1307–1341, 2012.

[85] J. Nieves, I. Ruiz Simo, and M. J. Vicente Vacas, “The nucleon axial mass and the MiniBooNE Quasielastic Neutrino-Nucleus Scattering problem,” *Phys. Lett. B*, vol. 707, pp. 72–75, 2012.

[86] O. Benhar, A. Fabrocini, and S. Fantoni, “The Nucleon Spectral Function in Nuclear Matter,” *Nucl. Phys. A*, vol. 505, pp. 267–299, 1989.

[87] T. Golan, C. Juszczak, and J. T. Sobczyk, “Effects of final-state interactions in neutrino-nucleus interactions,” *Phys. Rev. C*, vol. 86, p. 015505, Jul 2012.

[88] L. Pickering, “Examining nuclear effects in neutrino interactions with transverse kinematic imbalance,” *JPS Conf. Proc.*, vol. 12, p. 010032, 2016.

[89] S. Bolognesi *et al.*, “NIWG model and uncertainties for 2017 oscillation analysis,” Tech. Rep. 315, T2K, 2017.

[90] C. H. Llewellyn Smith, “Neutrino Reactions at Accelerator Energies,” *Phys. Rept.*, vol. 3, pp. 261–379, 1972.

[91] B. Bhattacharya, R. J. Hill, and G. Paz, “Model independent determination of the axial mass parameter in quasielastic neutrino-nucleon scattering,” *Phys. Rev. D*, vol. 84, p. 073006, 2011.

[92] V. Bernard, L. Elouadrhiri, and U.-G. Meissner, “Axial structure of the nucleon: Topical Review,” *J. Phys. G*, vol. 28, pp. R1–R35, 2002.

[93] A. A. Aguilar-Arevalo *et al.*, “First Measurement of the Muon Neutrino Charged Current Quasielastic Double Differential Cross Section,” *Phys. Rev. D*, vol. 81, p. 092005, 2010.

[94] R. Gran, J. Nieves, F. Sanchez, and M. J. V. Vacas, “Neutrino-nucleus quasi-elastic and 2p2h interactions up to 10 GeV,” *Phys. Rev. D*, vol. 88, p. 113007, Dec 2013.

[95] M. Martini, M. Ericson, G. Chanfray, and J. Marteau, “A Unified approach for nucleon knock-out, coherent and incoherent pion production in neutrino interactions with nuclei,” *Phys. Rev. C*, vol. 80, p. 065501, 2009.

[96] R. Gonzaléz-Jiménez, G. D. Megias, M. B. Barbaro, J. A. Caballero, and T. W. Donnelly, “Extensions of Superscaling from Relativistic Mean Field Theory: the SuSAv2 Model,” *Phys. Rev. C*, vol. 90, no. 3, p. 035501, 2014.

[97] C. Berger and L. M. Sehgal, “PCAC and coherent pion production by low energy neutrinos,” *Phys. Rev. D*, vol. 79, p. 053003, 2009.

[98] D. Rein and L. M. Sehgal, “Neutrino Excitation of Baryon Resonances and Single Pion Production,” *Annals Phys.*, vol. 133, pp. 79–153, 1981.

[99] S. Gollapinni, “Neutrino Cross section Future,” in *Prospects in Neutrino Physics*, 2 2016.

[100] K. Abe *et al.*, “Improved constraints on neutrino mixing from the T2K experiment with 3.13×10^{21} protons on target,” 1 2021.

[101] Y. Hayato, "A neutrino interaction simulation program library NEUT," *Acta Phys. Polon. B*, vol. 40, pp. 2477–2489, 2009.

[102] R. A. Smith and E. J. Moniz, "Neutrino reactions on nuclear targets," *Nucl. Phys. B*, vol. 43, p. 605, 1972. [Erratum: Nucl.Phys.B 101, 547 (1975)].

[103] K. M. Graczyk and J. T. Sobczyk, "Form factors in the quark resonance model," *Phys. Rev. D*, vol. 77, p. 053001, Mar 2008.

[104] C. Berger and L. M. Sehgal, "PCAC and coherent pion production by low energy neutrinos," *Phys. Rev. D*, vol. 79, p. 053003, 2009.

[105] A. Bodek and U.-K. Yang, "Update to the Bodek-Yang Unified Model for Electron- and Neutrino- Nucleon Scattering Cross Sections," *PoS*, vol. ICHEP2010, p. 292, 2010.

[106] T. Sjostrand, "High-energy physics event generation with PYTHIA 5.7 and JETSET 7.4," *Comput. Phys. Commun.*, vol. 82, pp. 74–90, 1994.

[107] K. Fusshoeller *et al.*, "FHC muon neutrino charged current multiple pion samples in the ND280 tracker for the 2020 oscillation analysis inputs: Run 2+3+4+8 with P6T NEUT_D MC," Tech. Rep. 407, T2K, 2020.

[108] S. Agostinelli *et al.*, "GEANT4–a simulation toolkit," *Nucl. Instrum. Meth. A*, vol. 506, pp. 250–303, 2003.

[109] P. Bartet *et al.*, "ν_μ CC event selections in the ND280 tracker using Run 2+3+4 data," Tech. Rep. 212, T2K, 2015.

[110] J. Albert *et al.*, "Study on SK ν_e candidates and systematic errors with T2K 3.23×10^{19} POT data," Tech. Rep. 028, T2K, 2011.

[111] K. Iwamoto *et al.*, "Inelastic single pion signal study in ν_e appearance using modified decay electron cut," Tech. Rep. 233, T2K, 2016.

[112] K. Abe *et al.*, "Measurements of neutrino oscillation in appearance and disappearance channels by the T2K experiment with 6.6×10^{20} protons on target," *Phys. Rev. D*, vol. 91, no. 7, p. 072010, 2015.

[113] E. Atkin *et al.*, "Measuring PMNS parameters in a joint ND280-SK analysis using MCMC," Tech. Rep. 393, T2K, 2020.

[114] C. Andreopoulos *et al.*, "VALOR Run 1-10 Analysis," Tech. Rep. 394, T2K, 2021.

[115] L. Berns *et al.*, "P-theta 2020 run 1-10 joint-fit analysis," Tech. Rep. 397, T2K, 2020.

[116] N. Abgrall *et al.*, "Measurements of $\pi^\pm$, $K^\pm$, K^0_S , Λ and proton production in proton–carbon interactions at 31 GeV/c with the NA61/SHINE spectrometer at the CERN SPS," *Eur. Phys. J. C*, vol. 76, no. 2, p. 84, 2016.

[117] N. Abgrall *et al.*, "Measurements of $\pi^\pm$, $K^\pm$ and proton double differential yields from the surface of the T2K replica target for incoming 31 GeV/c protons with the NA61/SHINE spectrometer at the CERN SPS," *Eur. Phys. J. C*, vol. 79, no. 2, p. 100, 2019.

[118] T. Vladisavljevic *et al.*, “Flux Prediction and Uncertainty with NA61/SHINE 2009 Replica-Target Data,” Tech. Rep. 354, T2K, 2020.

[119] E. Atkin *et al.*, “NIWG model and uncertainties for 2019-2020 oscillation analysis,” Tech. Rep. 344, T2K, 2019.

[120] A. M. Ankowski, O. Benhar, and M. Sakuda, “Improving the accuracy of neutrino energy reconstruction in charged-current quasielastic scattering off nuclear targets,” *Phys. Rev. D*, vol. 91, no. 3, p. 033005, 2015.

[121] K. Abe *et al.*, “Simultaneous measurement of the muon neutrino charged-current cross section on oxygen and carbon without pions in the final state at T2K,” *Phys. Rev. D*, vol. 101, no. 11, p. 112004, 2020.

[122] P. A. Rodrigues *et al.*, “Identification of nuclear effects in neutrino-carbon interactions at low three-momentum transfer,” *Phys. Rev. Lett.*, vol. 116, p. 071802, 2016. [Addendum: Phys.Rev.Lett. 121, 209902 (2018)].

[123] A. M. Ankowski, “Breakdown of the impulse approximation and its consequences: The Low-Q^2 problem,” *PoS*, vol. NUFACT08, p. 118, 2008.

[124] C. Adamuscin, E. Tomasi-Gustafsson, E. Santopinto, and R. Bijker, “Two-component model for the axial form factor of the nucleon,” *Phys. Rev. C*, vol. 78, p. 035201, 2008.

[125] D. Dutta *et al.*, “A Study of the quasielastic $(e, e'p)$ reaction on C-12, Fe-56 and Au-97,” *Phys. Rev. C*, vol. 68, p. 064603, 2003.

[126] A. Bodek and T. Cai, “Removal Energies and Final State Interaction in Lepton Nucleus Scattering,” *Eur. Phys. J. C*, vol. 79, no. 4, p. 293, 2019.

[127] C. Colle, O. Hen, W. Cosyn, I. Korover, E. Piasetzky, J. Ryckebusch, and L. B. Weinstein, “Extracting the mass dependence and quantum numbers of short-range correlated pairs from $A(e, e\prime p)$ and $A(e, e\prime pp)$ scattering,” *Phys. Rev. C*, vol. 92, no. 2, p. 024604, 2015.

[128] K. Abe *et al.*, “Characterization of nuclear effects in muon-neutrino scattering on hydrocarbon with a measurement of final-state kinematics and correlations in charged-current pionless interactions at T2K,” *Phys. Rev. D*, vol. 98, no. 3, p. 032003, 2018.

[129] G. D. Megias *et al.*, “Meson-exchange currents and quasielastic predictions for charged-current neutrino-^{12}C scattering in the superscaling approach,” *Phys. Rev. D*, vol. 91, no. 7, p. 073004, 2015.

[130] G. D. Megias, J. E. Amaro, M. B. Barbaro, J. A. Caballero, and T. W. Donnelly, “Inclusive electron scattering within the SuSAv2 meson-exchange current approach,” *Phys. Rev. D*, vol. 94, p. 013012, 2016.

[131] M. Dunkman *et al.*, “Updated recommendation of the 2014-5 oscillation parameters,” Tech. Rep. 265, T2K, 2015.

[132] A. Higuera *et al.*, “Measurement of Coherent Production of $\pi^{\pm}$ in Neutrino and Antineutrino Beams on Carbon from E_ν of 1.5 to 20 GeV,” *Phys. Rev. Lett.*, vol. 113, no. 26, p. 261802, 2014.

[133] M. Glück, E. Reya, and A. Vogt, "Dynamical parton distributions revisited," *Eur. Phys. J. C*, vol. 5, pp. 461–470, 1998.

[134] T. Yang, C. Andreopoulos, H. Gallagher, K. Hoffmann, and P. Kehayias, "A Hadronization Model for Few-GeV Neutrino Interactions," *Eur. Phys. J. C*, vol. 63, pp. 1–10, 2009.

[135] M. Tanabashi *et al.*, "Review of Particle Physics," *Phys. Rev. D*, vol. 98, no. 3, p. 030001, 2018.

[136] P. Gueye *et al.*, "Coulomb distortion measurements by comparing electron and positron quasielastic scattering off C-12 and Pb-208," *Phys. Rev. C*, vol. 60, p. 044308, 1999.

[137] E. Wang, L. Alvarez-Ruso, Y. Hayato, K. Mahn, and J. Nieves, "Photon emission in neutral current interactions at the T2K experiment," *Phys. Rev. D*, vol. 92, no. 5, p. 053005, 2015.

[138] P. de Perio *et al.*, "Neut nuclear effects (fsi)," Tech. Rep. 033, T2K, 2012.

[139] L. L. Salcedo, E. Oset, M. J. Vicente-Vacas, and C. Garcia-Recio, "Computer Simulation of Inclusive Pion Nuclear Reactions," *Nucl. Phys. A*, vol. 484, pp. 557–592, 1988.

[140] K. Nakamura *et al.*, "Review of particle physics," *J. Phys. G*, vol. 37, p. 075021, 2010.

[141] T. Feusels *et al.*, "Tuning of the NEUT Cascade Model using $\pi^{\pm}$-A Scattering External Data to Improve Final State Interaction and Secondary Interaction Systematic Uncertainties," Tech. Rep. 365, T2K, 2017.

[142] E. S. Pinzon Guerra *et al.*, "Measurement of σ_{ABS} and σ_{CX} of π^{+} on carbon by the Dual Use Experiment at TRIUMF (DUET)," *Phys. Rev. C*, vol. 95, no. 4, p. 045203, 2017.

[143] D. Barrow *et al.*, "Super-Kamiokande Data Quality, MC, and Systematics1in Run 10," Tech. Rep. 399, T2K, 2020.

[144] R. Akutsu *et al.*, "Super-Kamiokande data quality for T2K Run 9," Tech. Rep. 355, T2K, 2019.

[145] R. Akutsu *et al.*, "Super-Kamiokande events and data quality studies for T2K Run 8," Tech. Rep. 317, T2K, 2017.

[146] L. Munteanu *et al.*, "Constraining the Flux and Cross Section Models with Data from ND280 using FGD1 and FGD2 for the 2020 Oscillation Analysis," Tech. Rep. 395, T2K, 2021.

[147] M. Tanabashi *et al.*, "Review of Particle Physics," *Phys. Rev. D*, vol. 98, no. 3, p. 030001, 2018.

[148] S. Bolognesi *et al.*, "Assessing the effect of cross-section model uncertainties on the T2K oscillation analyses with simulated data studies using the BANFF and P-Theta fit frameworks," Tech. Rep. 396, T2K, 2021.

[149] G. J. Feldman and R. D. Cousins, "A Unified approach to the classical statistical analysis of small signals," *Phys. Rev. D*, vol. 57, pp. 3873–3889, 1998.

[150] K. Abe *et al.*, "Proposal for an Extended Run of T2K to 20×10^{21} POT," 9 2016.

[151] K. Abe *et al.*, "J-PARC Neutrino Beamline Upgrade Technical Design Report," 8 2019.

[152] K. Abe *et al.*, "Combined Analysis of Neutrino and Antineutrino Oscillations at T2K," *Phys. Rev. Lett.*, vol. 118, no. 15, p. 151801, 2017.

[153] K. Abe *et al.*, "Sensitivity of the T2K accelerator-based neutrino experiment with an Extended run to 20×10^{21} POT," 7 2016.

[154] K. Abe *et al.*, "T2K ND280 Upgrade - Technical Design Report," 1 2019.

[155] D. Attié *et al.*, "Performances of a resistive Micromegas module for the Time Projection Chambers of the T2K Near Detector upgrade," *Nucl. Instrum. Meth. A*, vol. 957, p. 163286, 2020.

[156] G. Prior, "The HARP time projection chamber," *Nucl. Phys. B Proc. Suppl.*, vol. 125, pp. 37–42, 2003.

[157] D. Attie, "Beam tests of Micromegas LC-TPC large prototype," *JINST*, vol. 6, p. C01007, 2011.

[158] K. Boudjemline, M. S. Dixit, J. P. Martin, and K. Sachs, "Spatial resolution of a GEM readout TPC using the charge dispersion signal," *Nucl. Instrum. Meth. A*, vol. 574, pp. 22–27, 2007.

[159] S. Suvorov, *Search for heavy neutrinos in the T2K experiment and upgrade of the near detector ND280.* PhD thesis, Université Paris-Saclay, 2020.

[160] M. Ester, H.-P. Kriegel, J. Sander, and X. Xu, "A density-based algorithm for discovering clusters in large spatial databases with noise," in *Proceedings of the Second International Conference on Knowledge Discovery and Data Mining*, pp. 226–231, AAAI Press, 1996.

[161] M. S. Dixit and A. Rankin, "Simulating the charge dispersion phenomena in micro pattern gas detectors with a resistive anode," *Nucl. Instrum. Meth. A*, vol. 566, pp. 281–285, 2006.

[162] M. S. Dixit, J. Dubeau, J. P. Martin, and K. Sachs, "Position sensing from charge dispersion in micropattern gas detectors with a resistive anode," *Nucl. Instrum. Meth.*, vol. A518, pp. 721–727, 2004.

[163] A. Blondel *et al.*, "A fully active fine grained detector with three readout views," *JINST*, vol. 13, no. 02, p. P02006, 2018.

[164] O. Mineev *et al.*, "Beam test results of 3D fine-grained scintillator detector prototype for a T2K ND280 neutrino active target," *Nucl. Instrum. Meth. A*, vol. 923, pp. 134–138, 2019.

[165] A. Blondel *et al.*, "The SuperFGD Prototype Charged Particle Beam Tests," *JINST*, vol. 15, no. 12, p. P12003, 2020.

[166] C. Andreopoulos, "The GENIE neutrino Monte Carlo generator," *Acta Phys. Polon. B*, vol. 40, pp. 2461–2475, 2009.

[167] K. Abe *et al.*, "Characterization of nuclear effects in muon-neutrino scattering on hydrocarbon with a measurement of final-state kinematics and correlations in charged-current pionless interactions at T2K," *Phys. Rev. D*, vol. 98, no. 3, p. 032003, 2018.

[168] X. G. Lu *et al.*, "Measurement of final-state correlations in neutrino muon-proton mesonless production on hydrocarbon at $\langle E_\nu \rangle = 3$ GeV," *Phys. Rev. Lett.*, vol. 121, no. 2, p. 022504, 2018.

[169] M. Elkins *et al.*, "Neutron measurements from antineutrino hydrocarbon reactions," *Phys. Rev. D*, vol. 100, no. 5, p. 052002, 2019.

[170] L. Munteanu, S. Suvorov, S. Dolan, D. Sgalaberna, S. Bolognesi, S. Manly, G. Yang, C. Giganti, K. Iwamoto, and C. Jesús-Valls, "New method for an improved antineutrino energy reconstruction with charged-current interactions in next-generation detectors," *Phys. Rev. D*, vol. 101, no. 9, p. 092003, 2020.

[171] G. Yang, "3D Projection Scintillator Tracker in the DUNE Near Detector," *PoS*, vol. ICHEP2018, p. 868, 2019.

[172] A. P. Furmanski and J. T. Sobczyk, "Neutrino energy reconstruction from one muon and one proton events," *Phys. Rev. C*, vol. 95, no. 6, p. 065501, 2017.

[173] M. Jiang *et al.*, "Atmospheric Neutrino Oscillation Analysis with Improved Event Reconstruction in Super-Kamiokande IV," *PTEP*, vol. 2019, no. 5, p. 053F01, 2019.

[174] K. Levenberg, "A method for the solution of certain non-linear problems in least squares," *Quarterly of Applied Mathematics*, vol. 2, p. 164–168, Jul 1944.

[175] D. W. Marquardt, "An algorithm for least-squares estimation of nonlinear parameters," *Journal of the Society for Industrial and Applied Mathematics*, vol. 11, no. 2, pp. 431–441, 1963.

[176] F. An *et al.*, "Neutrino Physics with JUNO," *J. Phys. G*, vol. 43, no. 3, p. 030401, 2016.

universite PARIS-SACLAY

ÉCOLE DOCTORALE
Particules, hadrons, énergie et noyau :
instrumentation, imagerie, cosmos
et simulation (PHENIICS)

Titre: Vers la mesure de la violation de la symétrie CP dans les oscillations de neutrinos avec l'expérience T2K

Mots clés: T2K, oscillations de neutrinos, violation CP

Résumé: La découverte des oscillations de neutrinos a montré que ceux-ci ont une masse, et ce fait ne peut pas être expliqué par le Modèle Standard. Les expériences d'oscillations de neutrinos actuelles et de prochaine génération se focalisent sur la mesure de la phase de violation de la symétrie charge-parité (CP), δ_{CP}, et cherchent à déterminer si la symétrie CP est violée dans les oscillations de neutrinos.

L'expérience T2K (Tokai-to-Kamioka) mesure les différences de masse et le mélange des saveurs de neutrinos en mesurant leurs oscillations. Le spectre avant oscillation, mesuré avec le détecteur proche de T2K (ND280), est utilisé pour contraindre les incertitudes systématiques liées à la modélisation du flux de neutrinos et de leurs interactions. Plusieurs améliorations à l'analyse d'oscillations avec le détecteur proche sont décrites, en particulier concernant le modèle des incertitudes systématiques liées aux interactions des neutrinos. Les résultats de l'analyse d'oscillations sont discutés, et la robustesse de l'analyse est examinée en effectuant plusieurs études avec des données simulées en utilisant des modèles alternatifs d'interaction.

T2K envisage une mise à niveau de son détecteur proche en 2022. Les capacités de la mise à niveau en terme de physique sont examinées. Un aperçu de la sensibilité de l'expérience Hyper-Kamiokande à la violation de la symétrie CP est également donné. Comme la physique des neutrinos est entrée dans une époque de mesures de précision, l'impact des paramètres systématiques sur la précision de Hyper-Kamiokande est discuté.

Title: Towards the measurement of CP violation in neutrino oscillations with the T2K experiment

Keywords: T2K, neutrino oscillations, CP violation

Abstract: The discovery of neutrino oscillations has demonstrated that neutrinos have mass, which cannot be explained in the framework of the Standard Model. The focus of current and next-generation long-baseline neutrino experiments is the determination of the charge-parity (CP) violating phase δ_{CP} and establishing whether neutrino oscillations violate CP symmetry.

The T2K (Tokai-to-Kamioka) experiment probes the mass differences and mixing of neutrinos by measuring neutrino oscillations. The unoscillated spectrum, measured at the T2K near detector (ND280), is used to constrain the systematic uncertainties stemming from the flux and cross-sections models. Several improvements in the oscillation analysis framework with the T2K near detector, with a focus on updates to the neutrino interaction error model, are presented. The results on the oscillation parameters are discussed, and the robustness of the analysis is examined by performing simulated data studies using alternative neutrino interaction models.

T2K plans an upgrade of its near detector, to be installed in 2022. The capabilities of the upgrade in terms of physics performance are examined. An overview of the sensitivity of the next-generation Hyper-Kamiokande experiment is also given. As neutrino physics has now entered an era of precision measurements, the impact of systematic parameters on the Hyper-Kamiokande precision is discussed.